

ELECTROSTATIC INSTABILITIES AND TURBULENCE IN A TOROIDAL MAGNETIZED PLASMA

THÈSE N° 3849 (2007)

PRÉSENTÉE LE 29 JUIN 2007
À LA FACULTÉ DES SCIENCES DE BASE
CRPP Association Euratom
SECTION DE PHYSIQUE

ÉCOLE POLYTECHNIQUE FÉDÉRALE DE LAUSANNE

POUR L'OBTENTION DU GRADE DE DOCTEUR ÈS SCIENCES

PAR

Francesca Maria POLI

Laurea di dottore in Fisica, Università degli Studi di Roma, Italie
et de nationalité italienne

acceptée sur proposition du jury:

Prof. G. Gremaud, président du jury
Prof. A. Fasoli, directeur de thèse
Dr S. Brunner, rapporteur
Prof. E. Lazzaro, rapporteur
Prof. F. Skiff, rapporteur



ÉCOLE POLYTECHNIQUE
FÉDÉRALE DE LAUSANNE

Lausanne, EPFL

2007

Contents

1	Introduction and motivation	3
2	Linear drift instabilities in a toroidal plasma	7
2.1	Elementary properties of drift instabilities	8
2.2	The interchange mechanism	10
2.3	The dispersion relation for inhomogeneous plasmas	12
2.3.1	The equilibrium distribution function	13
2.3.2	The perturbed distribution function	15
2.4	Analytical solution for drift waves	16
2.4.1	Drift waves in straight magnetic fields	17
2.4.2	Drift waves in curved magnetic fields, interchange limit	19
2.5	Summary and discussion	21
3	The TORPEX device	23
3.1	Geometrical parameters	24
3.2	Magnetic field configuration	25
3.3	Particle Confinement	27
3.4	Plasma production by microwaves	28
4	Diagnostics	31
4.1	Electrostatic Langmuir Probes	32
4.2	Probe design and specifications	33
4.3	LPs for the measurement of the background parameters	35
4.4	LPs for the measurement of fluctuations	36
4.5	Typical parameters of TORPEX plasmas.	39
5	Measurement of the linear properties of fluctuations	43
5.1	Stationary and homogeneous processes	44
5.2	Measurement of fluctuations rms	44
5.2.1	Measurement of density fluctuations	45
5.2.2	Measurement of electrostatic potential fluctuations	46
5.2.3	Measurement of the phase between \tilde{n} and $\tilde{\phi}_p$	46
5.3	Reconstruction of the 2D profile of fluctuations rms	47
5.4	Measurement of the dispersion relation	50
5.4.1	Estimate of $P(k_z, \omega)$	51

5.4.2	Statistical dispersion relation	52
5.4.3	Phase velocity	54
5.4.4	Measurement of the parallel wavenumber	55
6	Measurement of the nonlinear properties of fluctuations	59
6.1	Spectral evolution of fluctuations due to nonlinear interactions	60
6.1.1	Nonlinear dynamics in the laboratory frame	60
6.1.2	Spatial versus temporal representation	61
6.2	Spectral power transfer	62
6.3	Estimate of the quadratic coupling coefficients	64
6.3.1	Test of convergence	66
6.4	Measurement of the wavenumber from two probes	70
7	General properties of the instabilities observed on TORPEX	73
7.1	Ion mass	75
7.1.1	Spectral features	76
7.2	Microwave power	77
7.2.1	Spectral features	78
7.3	Toroidal magnetic field	79
7.3.1	Spectral features	80
7.4	Vertical magnetic field	80
7.4.1	Spectral features	82
7.5	Neutral gas pressure	84
7.5.1	Spectral features	84
7.6	Summary and discussion	87
8	Identification and characterization of drift-interchange instabilities	89
8.1	Background and fluctuation profiles	90
8.2	Spectral properties	92
8.2.1	Reconstruction of the profile of spectral amplitude	92
8.3	Measurement of the dispersion relation	94
8.3.1	Perpendicular wavenumbers	95
8.3.2	Phase velocity	97
8.3.3	Parallel wavenumber	97
8.4	Comparison with linear theory	99
8.5	Drift instabilities in Argon plasmas	102
8.6	Summary and discussion	104
9	Identification and characterization of interchange instabilities	107
9.1	Time-averaged profiles	107
9.2	Power spectrum of fluctuations	108
9.3	Dispersion relation	111
9.3.1	Dispersion relation across B	111
9.3.2	Radial profile of the phase velocity	112
9.3.3	Dispersion relation along B	114

9.4	Comparison with theory	115
9.5	Drift-interchange vs interchange instabilities	118
9.6	Summary and discussion	119
10	Development of turbulence from drift-interchange instabilities	123
10.1	Nonlinear coupling	125
10.2	From nonlinear coupling to energy cascade	127
10.2.1	Hypotheses and limits of the model	128
10.2.2	Estimate of the nonlinear coupling coefficients	129
10.2.3	Spectral power transfer	130
10.3	From frequency to wavenumber cascade	132
10.4	Nonlinear interactions between pure interchange and drift-interchange instabilities	133
10.5	Spectral features versus spatio-temporal dynamics	138
10.6	Summary and discussion	140
11	Conclusions and outlook	143
A	Typical plasma parameters on TORPEX	147
B	Normalizations used in the dispersion relation	149
C	Complements to Chap. 4	151
C.1	The FLP arrays	151
C.1.1	Transfer function of the FLP electronic modules	152
C.2	Transfer function of LP modules and HEX TIP modules	157
D	Geometrical effects on the measurement of k_{\parallel}	159
E	Corrections due to temperature fluctuations	163
E.1	Corrections to the measurement of $\tilde{\phi}_p$	164
E.2	Corrections to the measurement of \tilde{n}	164
E.3	Corrections to the phase between \tilde{n} and $\tilde{\phi}_p$	165
E.4	Corrections to the wavenumber associated with $\tilde{\phi}_p$	167

Abstract

This Thesis aims at characterizing the linear properties of electrostatic drift instabilities arising in a toroidal plasma and the mechanisms leading to their development into turbulence. The experiments are performed on the TORoidal Plasma EXperiment (TORPEX) at CRPP-EPFL, Lausanne.

The first part of the Thesis focuses on the identification of the nature of the instabilities observed in TORPEX, using a set of electrostatic probes, designed and built for this purpose. The global features of fluctuations, analyzed for different values of control parameters such as the magnetic field, the neutral gas pressure and the injected microwave power, are qualitatively similar in different experimental scenarios. The maximum of fluctuations is observed on the low field side, where the pressure gradient and the gradient of the magnetic field are co-linear, indicating that the curvature of the magnetic field lines has an important role in the destabilization of the waves. The power spectrum is dominated by electrostatic fluctuations with frequencies much lower than the ion cyclotron frequency. Taking advantage of the extended diagnostics coverage, the spectral properties of fluctuations are measured over the whole poloidal cross-section. Both drift and interchange instabilities develop and propagate on TORPEX, with the stability of both being affected by the curvature of the magnetic field. It is shown that modes of different nature are driven at separate locations over the plasma cross-section and that the wavenumber and frequency spectra, narrow at the location where the instabilities are generated, broaden during convection, suggesting an increase in the degree of turbulence.

The transition from coherent to turbulent spectral features and the role of nonlinear coupling between modes in the development of turbulence are treated in the second part of this work. It is found that nonlinear mode-mode coupling is responsible for the redistribution of spectral energy from the dominant instabilities to other spectral components and that this mechanism is independent of the nature of the instabilities. Nonlinear interactions between the mode and its nonlinearly generated harmonics are responsible for the filling of the spectral regions between harmonics. Later in the development along the convection path, the unstable mode transfers energy to spectral components with significantly larger frequencies. This transfer of energy can be interpreted in the investigated plasma scenarios as a forward cascade in wavenumbers, with transfer of energy from large to small scales.

Keywords: electrostatic fluctuations, instabilities, drift waves, interchange, turbulence, nonlinear, toroidal, plasma, Volterra.

Version abrégée

La caractérisation des propriétés linéaires des instabilités électrostatiques présentes dans un plasma toroïdal ainsi que la mise en évidence des mécanismes conduisant à leur développement en turbulence constituent l'objectif de cette thèse. Les expériences sont réalisées sur TORPEX (TORoidal Plasma EXperiment) au Centre de Recherches en Physique des Plasmas de Lausanne. La première partie de ce travail est dédiée à l'identification de la nature des instabilités observées dans TORPEX. Les fluctuations de densité, température et potentiel sont analysées pour divers valeurs des paramètres de contrôle, tels que le champ magnétique, la pression de gaz neutre et la puissance micro-onde injectée. Les caractéristiques globales de ces fluctuations sont similaires pour les différents scénarios expérimentaux explorés. Les fluctuations sont maximales dans la région où le gradient de pression et le gradient du champ magnétique sont co-linéaires, indiquant que la courbure des lignes de champ magnétique joue un rôle important dans la déstabilisation des ondes. Le spectre de puissance est dominé par des fluctuations électrostatiques, dont les fréquences sont nettement plus basses que la fréquence cyclotronique des ions. Les propriétés spectrales des fluctuations sont également mesurées sur toute la section poloidale du plasma, montrant que des instabilités de dérive et d'interchange se développent et se propagent, en étant toutes deux affectées par la courbure du champ magnétique. Des modes de différente nature apparaissent dans des endroits distincts de la section du plasma et les spectres en nombre d'onde et en fréquence des fluctuations sont étroits dans les régions où se forment les instabilités, puis s'élargissent pendant la convection, suggérant une augmentation du niveau de turbulence. La transition d'un comportement spectral cohérent vers un comportement spectral turbulent ainsi que le rôle des couplages non linéaires entre les modes dans le développement des turbulences sont traités dans la deuxième partie de ce travail. Nous avons montré que les couplages non linéaires entre modes sont responsables de la redistribution d'énergie spectrale des instabilités dominantes vers les autres composantes spectrales et que ce mécanisme est indépendant de la nature des instabilités. Les interactions non linéaires entre le mode et ses harmoniques provoquent le remplissage des régions spectrales situées entre les harmoniques. Le long de la trajectoire de convection, le mode instable transfère l'énergie aux composantes spectrales de fréquence significativement plus élevée. L'observation d'une relation linéaire entre nombre d'onde et fréquence permet d'interpréter ce transfert d'énergie comme un transfert d'énergie des grandes vers petites échelles.

Mots-clés : fluctuations électrostatiques, instabilités, ondes de dérive, interchange, turbulence, non linéaire, plasma.

Chapter 1

Introduction and motivation

Most plasma magnetic confinement schemes are affected by levels of particle and heat flux across the magnetic field much higher than those induced by collisional processes [1]. Drift waves and related turbulence have received increasing attention over the past two decades, due to their role in the regulation of such ‘anomalous’ cross-field transport [2][3]. Drift waves are driven by gradients in the equilibrium pressure profile, a feature that makes them universally present in laboratory plasmas, and are characterized by low frequencies and long wavelengths. In low- β plasmas, drift waves have electrostatic character, leading to perturbations in density and plasma potential, but not in the magnetic field. Although it is at present generally accepted that plasma transport across the magnetic field is controlled by low-frequency drift wave fluctuations, a complete understanding of the mechanisms leading from linearly unstable modes to turbulence and the link between turbulence and transport is still missing. To explain how drift waves, initially unstable in a limited frequency range, give rise to a broad spectrum, nonlinear mechanisms based on three-wave coupling are invoked [4]. Theoretical models for drift wave induced turbulence have been developed for non-collisional [5][6] and collisional [7] regimes. For ion Larmor radius much smaller than the density gradient scale length, the dominant nonlinearities in the continuity equation for the ion dynamics arise from the $\tilde{\mathbf{E}} \times \mathbf{B}$ term in the convective derivative applied to density and vorticity [5][6][8][9].

A systematic comparison of theoretical results with experimental data in fusion devices is not possible due to the intrinsic difficulty, in high performance tokamaks or stellarators, to diagnose the plasma with adequate coverage, and spatial and temporal resolution. Density gradients are often extremely steep close to the plasma edge, where the level of density fluctuations can be as high as 10%-100% of the background density, compared to 0.1%-1% measured in the central regions [2]. Direct measurements of fluctuating quantities are often limited to the Scrape Off Layer (SOL) plasma where the wavenumber and frequency spectra have evolved to a strongly turbulent stage. Although some coherent features are still detectable in the measured spectra, it is difficult to trace the source of turbulence to any linear wave or instability underlying the turbulence [10][11]. These intrinsic difficulties motivate the development of basic plasma physics experiments dedicated to fluctuations, turbulence and transport studies.

Since the first detailed observations in Q machines [12], drift waves have been exten-

sively studied in linear devices in collisionless [13][14] and collisional [15][16] regimes. In these experiments the pressure profile is centered on the axis of the device and is radially symmetric. Drift waves are therefore excited at a well defined radial position, where the density gradient is maximum, then propagate perpendicularly to the magnetic field, along the azimuthal direction. As the absence of magnetic field curvature limits the development of turbulence, an *ad hoc* electric field is in some cases applied externally, to introduce an effective gravity term and investigate its effects [17].

Although some aspects of the physics of drift waves and turbulence related transport can be addressed in linear devices, toroidal geometry is important in order to have the ingredients that drive turbulence in fusion experiments, namely magnetic field line curvature in combination with plasma gradients [18][19]. The gradient of the magnetic field intensity and the curvature of the field lines contribute to the destabilization of low frequency fluctuations in bad curvature regions, where the pressure and the gradient of the magnetic field are co-linear. Basic plasma physics experiments in toroidal geometry offer the possibility of investigating electrostatic instabilities, their development into turbulence and their implications for anomalous transport in fusion plasmas in well controlled and reproducible experimental scenarios with extensive diagnostic coverage.

Aspects of the physics of low frequency fluctuations have been studied in a number of experiments with simple magnetized toroidal plasmas, namely a toroidal magnetic field with a superimposed small vertical field component. The combined effect of pressure gradient and interchange drive on the dispersion relation was investigated in Ref. [20]. The resistive drift turbulence was shown to be dominated by the interchange effect in the long wavelength limit, but measurements could be taken and compared with predictions only in limited regions of the plasma, at the plasma edge. Recently, several experiments addressed the spatio-temporal evolution of density and potential fluctuations [21][22][23], mainly using cross-correlation techniques.

For a complete investigation of the nature of the instabilities, the analysis of the spatio-temporal dynamics of the fluctuations needs to be integrated with measurements of their spectral properties. The dispersion relation should be measured in both perpendicular and parallel directions, over extended regions of the plasma. The results should then be compared with a theory that takes into account the combined effects of pressure gradient and interchange drive. Such a comprehensive investigation has not been undertaken so far, to our knowledge, in any toroidal experiment with simple magnetic configuration, and constitutes the main goal of the first part of this work. The role of nonlinear coupling in the development of turbulence has been investigated in linear devices, both in the frequency [15] and in the wavenumber [24] domain. First comparisons of the measured spectral and spatial features of electrostatic turbulence with the predictions of a nonlinear fluid model were attempted in a basic toroidal device [25][26]. Up to date, no systematic measurements of the nonlinear properties of fluctuations leading to the development of turbulence from an initial drift-interchange instability have been performed in a simple magnetized toroidal plasma. Of particular interest is the study of the evolution of the spectra during convection. These aspects constitute the motivation for the second part of this work.

This Thesis contributes to the characterization of the linear and nonlinear properties of electrostatic instabilities that develop in toroidal plasmas, via a number of

experiments performed on the simple magnetised toroidal plasma TORPEX [27][28].

A local kinetic dispersion relation for electrostatic instabilities is derived in slab geometry in the limit for drift waves in Chap. 2. Inhomogeneities in the density and temperature profiles are allowed in the equilibrium distribution function of ions and electrons. The effect of the magnetic field curvature and of the gradient in the magnetic field magnitude are included as external forces. The numerical solution of this dispersion relation constitutes our main reference for the identification of the nature of the observed instabilities.

Arrays of electrostatic probes have been designed and built to measure fluctuation levels and the dispersion relation at fixed locations along the azimuthal direction. The distance between the probes is sufficiently small to resolve wavelengths of approximately 3 mm and the dedicated electronics has been designed to guarantee low phase distortion up to the largest frequencies acquired (*i.e.* 125 kHz). This set of probes is integrated with movable probe arrays for the measurement of the radial profile of fluctuations in the density, electron temperature and electrostatic plasma potential, and of the dispersion relation parallel and perpendicular to the magnetic field. Almost 200 electrostatic Langmuir probes are installed on TORPEX. They are described in Chap. 4, while the TORPEX experimental setup is described in Chap. 3.

To isolate the driving mechanism for instabilities it is necessary to identify the plasma location where instabilities are excited by measuring the fluctuating quantities over most of the plasma cross-section. The location where the fluctuation amplitude is maximum is expected to correspond to the location where the drive is the largest. In order to treat efficiently the very large amount of data from such a comprehensive set of probes, a semi-automatic method for the reconstruction of the profile of the amplitude of fluctuations and their distribution in frequency has been developed (Sec. 5.3). Based on the measurement of the power spectra over the whole plasma cross-section and taking advantage of the reproducibility of the plasma discharges, this method allows one to separate the regions where individual modes are driven. When instabilities of different nature coexist in the same plasmas, the determination of the driving mechanism is an essential step for the identification of their nature.

The dispersion relation is reconstructed by means of statistical techniques, described in Sec. 5.4. Particular care is taken in the measurement of the parallel wavenumber (Sec. 5.4.4), which is important for the discrimination between pure interchange and drift instabilities. This measurement is particularly delicate and affected by many factors, due to the low ratio of the parallel to the perpendicular wavenumber (Sec. 5.4.4 and App. D). The width of the parallel and perpendicular wavenumber spectra, related to the degree of turbulence and to the correlation length, is measured for each frequency component. Chapter 6 describes the spectral techniques used to quantify the nonlinear coupling among spectral components. An equation for the nonlinear dynamics of fluctuations in the laboratory frame is derived and used to quantify the transfer of energy in mode-mode interactions.

The general properties of the instabilities observed on TORPEX and the dependence of their spectral features on selected control parameters is discussed in Chap. 7. It is shown that density fluctuations peak on TORPEX on the low field side, where the pressure gradient and the magnetic field gradient are co-linear, indicating that the

curvature of the magnetic field is essential for their destabilization. Both drift and interchange instabilities can develop in TORPEX plasmas. Drift modes with $k_{\perp}\rho_i < 0.1$, where ρ_i is the ion Larmor radius and k_{\perp} the wavenumber perpendicular to the magnetic field, are strongly affected by the curvature of the magnetic field lines. Chapter 8 focuses on the characterization of the linear properties of these modes, which are referred to as *drift-interchange*. The linear properties of pure interchange instabilities are described in Chap. 9.

The second part of the Thesis is dedicated to the identification of the mechanisms leading to electrostatic turbulence from linear drift instabilities. This represents the subject of Chap. 10, aimed at characterizing the evolution of the nonlinear properties of fluctuations at different stages of the development of turbulence. The extended diagnostics coverage is an important tool also for this part of the research. Fluctuations are measured at different locations over the plasma cross-section, starting from the region where the instabilities are generated and following the direction of convection. The wavenumber and frequency spectra broaden during convection indicating development of turbulence. By measuring the strength of the nonlinear coupling at different locations along the convection path, the role of three-wave interactions in the broadening of the spectrum has been elucidated. The development of turbulence begins with a phase where harmonics of the unstable modes are generated. The strong nonlinear coupling among the lowest order harmonics is at this stage responsible for the filling of the spectral regions at frequencies intermediate to the harmonics themselves. At subsequent stages, the unstable modes interact nonlinearly with spectral components with significantly larger frequencies and energy is transferred in the frequency domain away from the modes. These mechanisms leading to turbulence seem to be independent of the nature of the instabilities. The transfer of energy from the frequency of the unstable mode to spectral components with larger frequencies can be interpreted as a forward cascade in wavenumber space, with transfer of energy from large to small scales. This extension is justified by the strong $\mathbf{E}_0 \times \mathbf{B}$ drift in TORPEX plasmas and by the measurement of a linear dispersion relation along the direction of convection in an extended range of frequencies. Chapter 11 summarizes the main results achieved and their implication, and outlines some of the possible future lines of research on TORPEX.

Chapter 2

Linear drift instabilities in a toroidal plasma

Plasmas that are inhomogeneous across the magnetic field are subject to a large class of instabilities, which go under the name of *gradient instabilities* [29][18]. The instabilities are considered universal because gradients in the density, temperature and, in particular configurations, also in the magnetic field, are inevitable in laboratory plasmas. This Thesis work will address the case of weak inhomogeneities, *i.e.* plasmas in which the ion Larmor radius is small compared to the typical scale length of the inhomogeneities. Instabilities driven in such plasmas are called *drift instabilities* and the corresponding propagating perturbations *drift waves* [18].

In this Thesis the term *drift* will therefore be used in general to indicate all those instabilities developing in weakly inhomogeneous plasmas, in the presence of gradients in the background pressure profile combined to a curved magnetic field. However, a distinction will be made between drift waves with $\mathbf{k} \cdot \mathbf{B}_0 \simeq 0$, which represent the interchange limit, and can be called interchange modes, and drift waves with $\mathbf{k} \cdot \mathbf{B}_0 \neq 0$ (see Table 2.2). In toroidal geometry the stability of drift waves is affected by the presence of a curved magnetic field, which contributes to the destabilization of modes in regions where the density gradient is co-linear to the magnetic field gradient. Drift modes whose stability properties are strongly affected by the interchange mechanism can be referred to as *drift-interchange*.

Resonance phenomena between particles and waves are important for the stability of drift waves. For this reason the stability will be analyzed using a Vlasov equation, rather than the moments equations. The properties of drift waves in presence of a density gradient and the effect of collisions on their stability will be briefly summarized in Sec. 2.1. The interchange mechanism will be discussed in Sec. 2.2. Section 2.3 will provide a description of the kinetic dispersion relation used in the next Chapters to compare the measured dispersion relation and to identify the nature of the instabilities observed on TORPEX. The contribution of a gradient in the amplitude of the magnetic field and the curvature of the field lines are included as an external force parallel to the background pressure profiles. Numerical solutions will be derived in the limit of straight magnetic field (Sec. 2.4.1) and in the interchange limit (Sec. 2.4.2), and calculated for the typical plasma parameters on TORPEX. The implications of these results will be

summarized at the end of the Chapter.

2.1 Elementary properties of drift instabilities

Drift waves are collective low frequency oscillations in the ion and electron population, existing in the presence of a gradient in the background density profile. While the propagation is essentially perpendicular to the magnetic field, a small component of the phase velocity is usually allowed along \mathbf{B} , with $k_{\parallel}/k_{\perp} \ll 1$. If the phase velocity along the magnetic field is sufficiently low ($\omega \ll k_{\parallel}v_{the}$) the electrons can respond adiabatically and the linearized Boltzmann distribution applies in the form:

$$\tilde{n}_e = n_0 \frac{e\tilde{\phi}}{T_{e0}}. \quad (2.1)$$

Here n_0 and T_{e0} are the background density and electron temperature, having assumed quasi-neutrality $Zn_{i0} = n_{e0} = n_0$, while \tilde{n}_e and $\tilde{\phi}$ represent the fluctuating density and electrostatic potential. Assuming that perturbations propagate across the magnetic field and are of the form $e^{i(k_y y - \omega t)}$, the dispersion relation $\omega_{*e} = k_y v_{de}$ is obtained from the linearized ion continuity equation. Under the hypothesis of adiabaticity, \tilde{n}_e and $\tilde{\phi}$ are in phase and the perturbations propagate with the electron diamagnetic velocity \mathbf{v}_{de} :

$$\mathbf{v}_{de} = \frac{T_{e0}}{eB_0^2} \nabla \ln n_0 \times \mathbf{B} = \frac{T_{e0}}{eB_0} \frac{d \ln n_0}{dx} \mathbf{e}_y \quad (2.2)$$

The mechanism for development and propagation of drift waves in inhomogeneous plasmas is illustrated in Fig. 2.1. In the collisional regime the hypothesis of adiabatic response of the electrons is broken by dissipation, and the electron-ion collisions give rise to a phase difference of the order of $\omega \nu_e / k_z^2 v_e^2$ compared to unity [3]. Instead of Eq. (2.1), the parallel dynamics for the electrons gives the following relation between density and potential fluctuations [18]:

$$\tilde{n}_e = n_0 \frac{e\tilde{\phi}}{T_{e0}} \frac{1 - i\omega_{*e} m_e \nu_{ei} / k_z^2 T_{e0}}{1 - i\omega m_e \nu_{ei} / k_z^2 T_{e0}} \quad (2.3)$$

The dispersion relation is finally obtained [18]:

$$1 - \frac{\omega_{*e}}{\omega} + k_{\perp}^2 \rho_s^2 \left(1 - i \frac{\omega m_e \nu_{ei}}{k_z^2 T_{e0}} \right) = 0 \quad (2.4)$$

whose solution for positive imaginary ω describes the *drift resistive instability*. In the collisionless regime the phase difference between \tilde{n}_e and $\tilde{\phi}$ is produced by the interaction between the wave and resonant electrons, *i.e.* electrons with parallel velocity v_z close to the parallel phase velocity ω/k_z . The role of the wave-particle resonance in the destabilization of drift waves is shown in Fig. 2.2. For an overview of drift waves and the discussion of the stability in function of the various parameters, the interested reader is addressed to the review papers by Krall [29] and Mikhailovsky [18].

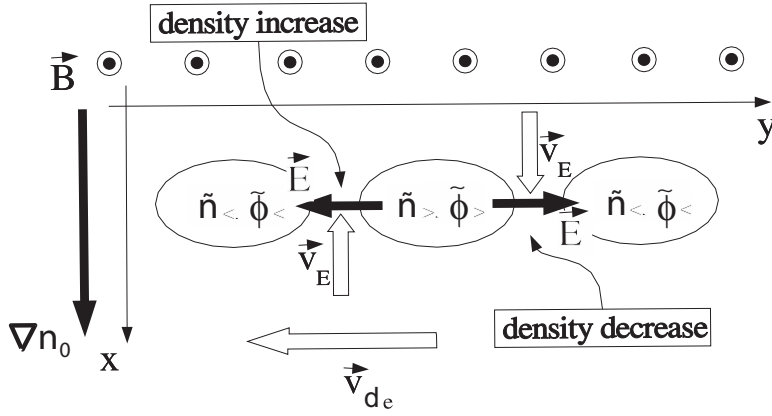


Figure 2.1: (*Courtesy of S. Brunner*). Basic mechanism for drift waves. Let's consider a perturbation quasi-perpendicular to \mathbf{B} that develops in a plasma with density gradient ∇n_0 along x at the equilibrium. If electrons can respond adiabatically, density (\tilde{n}) and electrostatic fluctuations ($\tilde{\phi}$) are in phase. The convection of the plasma is clockwise around a maximum of \tilde{n} and counter-clockwise around a minimum of \tilde{n} . This causes an increase of the density to the left of the maximum in \tilde{n} . The perturbation propagates in the direction of the electron diamagnetic current \mathbf{v}_{de} .

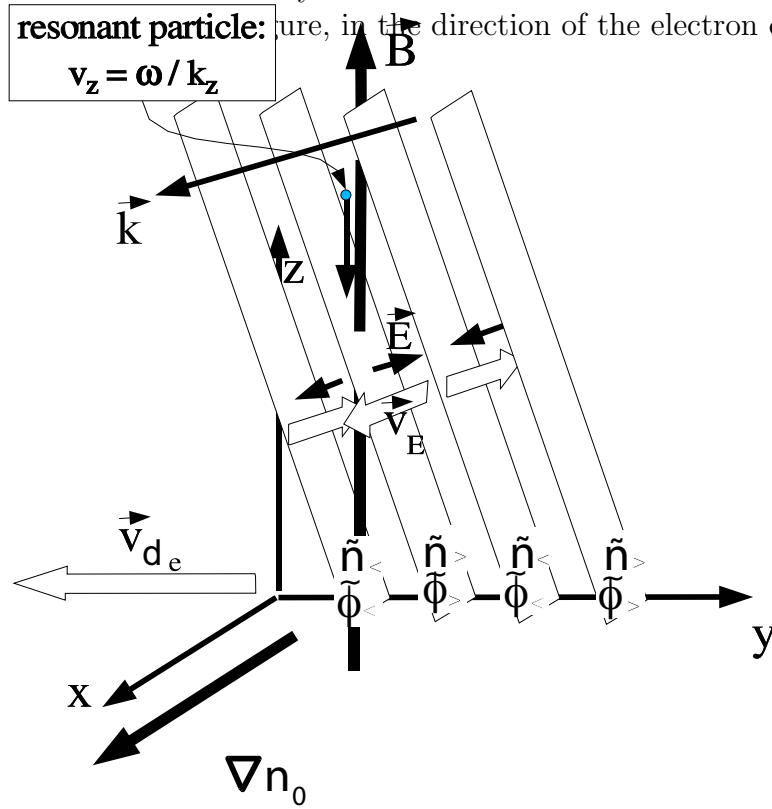


Figure 2.2: (*Courtesy of S. Brunner*). Mechanism for destabilization of drift waves via the resonant interaction along the magnetic field with particles having velocity v_z close to the phase velocity of the waves ω/k_z . The destabilizing effect arises from the fact that these particles undergo a constant \mathbf{v}_E drift that reinforces the density perturbation leading to instability.

2.2 The interchange mechanism

The interchange mechanism arises when a charge independent force opposes the density gradient of a plasma supported by a magnetic field. It is similar to the hydrodynamic instability occurring in a gravitational field when a heavy liquid is supported by a lighter liquid. In linear devices it is also called *centrifugal* instability, because it arises from the centrifugal effect due to the rotation of the plasma column induced by a background electric field. The interchange mechanism is illustrated in Fig. 2.3. Let's consider a plasma inhomogeneous along x and subject to an external force \mathbf{F} , charge sign independent and anti-parallel to the density gradient. The force \mathbf{F} will induce a drift with velocity:

$$\mathbf{v}_F = \frac{\mathbf{F} \times \mathbf{B}}{q_\alpha B^2} \quad (2.5)$$

The drifts are opposite for electrons and ions and cause a separation of charges. The resulting electric field induces a cross-field drift, $\mathbf{E} \times \mathbf{B}$, which amplifies density perturbations. Conversely, if the force is parallel to the density gradient, the effect is to damp out the perturbations.

Gradient and curvature of the magnetic field

In the presence of a gradient in the magnitude of the magnetic field ∇B , the magnetic moment $\mu = mv_\perp^2/2B$, related to the gyro-motion of the charged particle, gives rise to a force $\mathbf{F}_\mu = -\mu\nabla_\perp B$. In the presence of curvature of the magnetic field, the particle is submitted to the centrifugal force $F_c = -mv_\parallel^2 \mathbf{e}_\parallel \cdot \nabla \mathbf{e}_\parallel$. Here v_\perp and v_\parallel are the components of the velocity perpendicular and parallel to \mathbf{B} , and $\mathbf{e}_\parallel = \mathbf{B}/B$. One can show that, for a low- β plasma, $\mathbf{e}_\parallel \cdot \nabla \mathbf{e}_\parallel = \nabla_\perp \ln B$, and these two forces can be combined:

$$\mathbf{F}_B = F_\mu + F_c = -m \left(\frac{v_\perp^2}{2} + v_\parallel^2 \right) \nabla_\perp \ln B \quad (2.6)$$

This total force depends on the velocity of particles. However, for the simple purposes of calculating the drift induced by the curvature, we can consider the average of \mathbf{F}_B over the equilibrium particle distribution, which gives:

$$\mathbf{F}_B = -2 \frac{T}{R_c} \mathbf{e}_x \quad (2.7)$$

The sign is such that \mathbf{F}_B opposes the density gradient, necessary condition for the interchange instability. By comparing the curvature drift:

$$\mathbf{v}_B = \frac{m_\alpha}{q_\alpha} \left(\frac{v_\perp^2}{2} + v_\parallel^2 \right) \frac{\mathbf{R}_c \times \mathbf{B}}{R_c^2 B^2} \quad (2.8)$$

where $\nabla_\perp \mathbf{B} = -B \mathbf{R}_c / R_c^2$, with the gravitational drift

$$\mathbf{v}_g = \frac{m \mathbf{g} \times \mathbf{B}}{q_\alpha B^2} \quad (2.9)$$

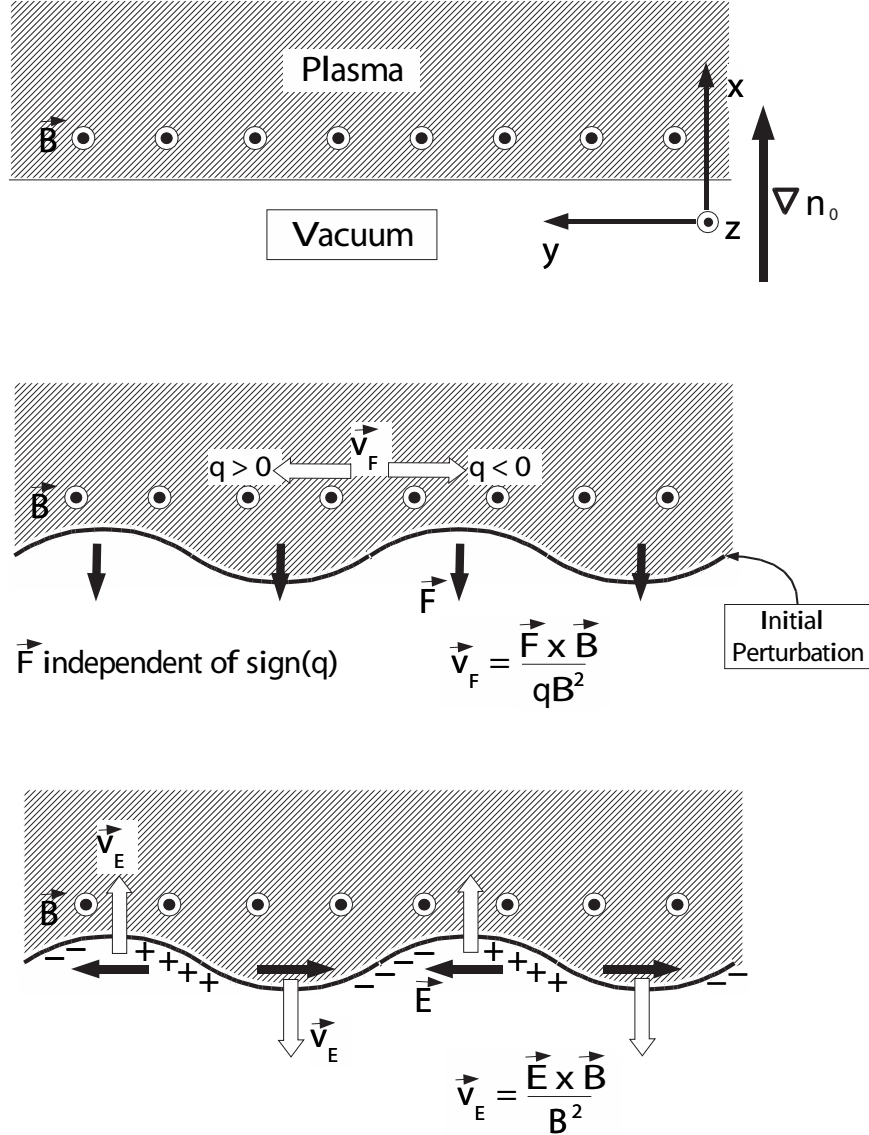


Figure 2.3: (Courtesy of S. Brunner). Basic mechanism for the interchange instability. (a) Initial state, with an inhomogeneous plasma with density gradient ∇n_0 along x , subject to an external force \mathbf{F} , independent of the charge sign and anti-parallel to ∇n_0 . (b) The force \mathbf{F} induces a drift \mathbf{v}_F with opposite directions for ions and electrons. The resulting electric field originates an $\mathbf{E} \times \mathbf{B}$ drift that reinforces the perturbation.

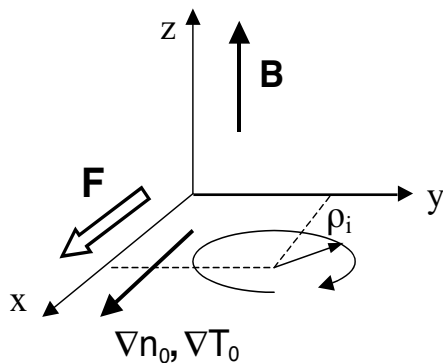


Figure 2.4: Slab geometry used for the calculation of the dispersion relation. Density and temperature gradients are along x , as well as the external force \mathbf{F} , the magnetic field is along z . The Larmor orbit, of radius ρ , is shown for a positive charge.

it can be seen that the gravitational drift provides a good model for the drifts in a curved magnetic field, provided the vectors \mathbf{g} and \mathbf{R}_c are in the same direction, and an effective gravity g is defined as:

$$g = \left(\frac{v_{\perp}^2}{2} + v_{\parallel}^2 \right) \frac{1}{R_c} = \frac{2T}{MR_c} \quad (2.10)$$

2.3 The dispersion relation for inhomogeneous plasmas

The evolution of the distribution function $f_{\alpha}(\mathbf{r}, \mathbf{v}, t)$ for the species α is governed by the Vlasov equation:

$$\frac{\partial f_{\alpha}}{\partial t} + \mathbf{v} \cdot \nabla f_{\alpha} + \frac{1}{m_{\alpha}} (q_{\alpha} \mathbf{v} \times \mathbf{B} + \mathbf{F}) \cdot \nabla_{\mathbf{v}} f_{\alpha} = 0 \quad (2.11)$$

where $q_{\alpha} \mathbf{v} \times \mathbf{B}$ is the Lorentz force and \mathbf{F} is an external force. We'll assume in the following that the plasma is subject to an electric field $\mathbf{E}_0 = \mathbf{F}_E/q_{\alpha}$ and to a curved magnetic field, so that $\mathbf{F} = \mathbf{F}_E + \mathbf{F}_B$. The evolution of the system in the electrostatic approximation¹ is entirely described by the Vlasov equation together with the Poisson equation:

$$\nabla \cdot \mathbf{E} = \frac{1}{\varepsilon_0} \sum_{\alpha} q_{\alpha} \int d\mathbf{v} f_{\alpha} \quad (2.12)$$

where the electric field derives from the potential ϕ , $\mathbf{E} = -\nabla\phi$. All physical quantities are assumed to be the superposition of an equilibrium and a fluctuating part, $f_{\alpha} =$

¹The experiments presented in this Thesis are run in plasmas with $\beta \sim 10^{-5}$, where $\beta = 2\mu_0 nT/B^2$ is the ratio of the plasma pressure nT to the magnetic field pressure $B^2/2\mu_0$. In the rest of this Thesis it is implied that $\mathbf{B} \equiv \mathbf{B}_0$, where \mathbf{B}_0 denotes the background magnetic field.

$f_{\alpha 0} + \tilde{f}_{\alpha}$ and $\phi = \phi_0 + \tilde{\phi}$. Figure 2.4 shows the slab geometry adopted, with the magnetic field along z and inhomogeneities and external forces along x . With the inhomogeneities along x , the perturbed quantities can be written as:

$$\begin{aligned}\tilde{\phi} &= \hat{\phi} e^{i(k_y y + k_z z - \omega t)} \\ \tilde{f}_{\alpha} &= \hat{f}_{\alpha} e^{i(k_y y + k_z z - \omega t)}\end{aligned}$$

with the amplitude of fluctuations, $\hat{\phi}$ and \hat{f}_{α} assumed to be small. The hypothesis that perturbations are independent of x , also called *local approximation*, is valid for wavelengths $k_{\perp} > d \ln n_0 / dx$. The dispersion relation is obtained from the Poisson equation written in Fourier space:

$$k^2 \tilde{\phi} = \frac{1}{\varepsilon_0} \sum_{\alpha} q_{\alpha} \tilde{n}_{\alpha}$$

where the perturbed density \tilde{n}_{α} is obtained by integrating the perturbed distribution function over velocities. The dispersion relation is given by the zeros of the dielectric function $\epsilon(\mathbf{k}, \omega)$:

$$\epsilon(\mathbf{k}, \omega) = 1 - \sum_{\alpha} \frac{q_{\alpha}}{\varepsilon_0 k^2} \frac{\hat{n}_{\alpha}}{\hat{\phi}} = 0. \quad (2.13)$$

2.3.1 The equilibrium distribution function

The equilibrium distribution function is a function of the constants of motion, the energy H and the momentum p_y and p_z :

$$p_y = mv_y + q \int dx B_0(x) \simeq mv_y + qx B_0 \quad (2.14a)$$

$$p_z = mv_z \quad (2.14b)$$

$$H = \frac{1}{2}mv^2 - Fx \quad (2.14c)$$

In writing Eq. (2.14a) we have assumed that the magnetic field is constant over the Larmor radius. It follows from Eq. (2.14a) that $X = x + v_y/\Omega$ is also a constant of motion, where $\Omega = q_{\alpha} B_0 / m_{\alpha}$ is the cyclotron frequency. The equilibrium distribution function can thus be chosen to be a function of X , $f_0(X, H_{\perp}, v_z)$. Assuming that the characteristic lengths $L = |d \ln n_0 / dx|^{-1}$, $|d \ln T_0 / dx|^{-1}$ of the inhomogeneities are large compared to the average Larmor radius ρ of the particles, one can expand to first order in ρ/L :

$$f_0(X, H_{\perp}, v_z) = f_0(x, H_{\perp}, v_z) + \frac{\partial f_0(x, H_{\perp}, v_z)}{\partial x} \frac{v_y}{\Omega} + \mathcal{O}(\epsilon^2) \quad (2.15)$$

The local distribution function $f_0(x, H_{\perp}, v_z)$ is defined as:

$$f_0 = \left(\frac{m}{2\pi T_0(x)} \right)^{3/2} n_0(x) e^{\frac{F}{T_0(x)} x} e^{-\frac{mv^2}{2T_0(x)}} \quad (2.16)$$

where $T_0(x)$ and $n_0(x)$ define the local temperature and density, respectively. The distribution function is thus a Maxwellian with the modified local density $n_0(x)e^{F_x/T_0(x)}$. With this choice, it results that:

$$\frac{\partial f_0}{\partial x} = \left[\frac{d \ln n_0(x)}{dx} + \frac{F}{T_0(x)} + \frac{d \ln T_0(x)}{dx} \left(\frac{H}{T_0(x)} - \frac{3}{2} \right) \right] f_0. \quad (2.17)$$

In the last equation we have identified $f_0 \equiv f_0(x, H_\perp, v_z)$. The term $F/T_0(x)$ represents the inverse scale length associated with the external force \mathbf{F} . It is easy to prove that the condition $\rho/L \ll 1$ implies:

$$\rho \frac{F}{T_0} = \frac{F}{q_\alpha B_0} \frac{1}{v_{th}} = \frac{|\mathbf{v}_F|}{v_{th}} \ll 1 \quad (2.18)$$

where $\mathbf{v}_F = (\mathbf{F} \times \mathbf{B})/(q_\alpha B^2)$ is the drift related to \mathbf{F} . The condition of weak inhomogeneities implies that the drifts associated to external forces must be small compared to thermal velocities.

Average drift velocities

The average velocity is obtained by integrating over velocities:

$$\begin{aligned} \mathbf{v}_d(x) &= \frac{\int d\mathbf{v} \mathbf{v} f_0(X, H_\perp, v_z)}{\int d\mathbf{v} f_0(X, H_\perp, v_z)} = \\ &= \frac{1}{n_0} \int d\mathbf{v} \mathbf{v} f_0(x, H_\perp, v_z) + \frac{1}{n_0} \int d\mathbf{v} \mathbf{v} \frac{\partial f_0}{\partial x} \frac{v_y}{\Omega} \end{aligned}$$

At $x = 0$ this gives:

$$\mathbf{v}_d(x = 0) = \frac{1}{q_\alpha B^2} \left(-\frac{\nabla p_0}{n_0} + \mathbf{F} \right) \times \mathbf{B}. \quad (2.19)$$

The first term is the diamagnetic drift $v_{d\alpha}$, which results from the interplay between spatial inhomogeneities and the finite Larmor radius. The second term is the drift induced by the presence of an external force $\mathbf{F} = F\hat{e}_x$, given by Eq. (2.5). In the presence of a background electric field \mathbf{E}_0 and of a gravity type force, \mathbf{F}_g , the resulting drift velocity is:

$$v_{\perp\alpha} = \frac{\nabla p_{0\alpha} \times \mathbf{B}}{q_\alpha n_0 B^2} - \frac{\mathbf{E}_0 \times \mathbf{B}}{B^2} - \frac{m_\alpha}{q_\alpha B^2} \mathbf{g} \times \mathbf{B} \quad (2.20)$$

where the second and third term on the right hand side are respectively the background $\mathbf{E}_0 \times \mathbf{B}$ velocity \mathbf{v}_E and the drift due to the gradient and the curvature of the magnetic field. The latter has been represented as a gravitational drift using Eq. (2.6) and Eq. (2.10). On TORPEX the electron diamagnetic drift velocities range typically between 200 and 1200 m/s, while v_E can reach 2.5×10^3 m/s and the curvature drift is approximately 100 m/s. On the low field side usually $|\mathbf{v}_{de}| \ll |\mathbf{v}_E|$ and the dominant drift is therefore the $\mathbf{E}_0 \times \mathbf{B}$ drift.

2.3.2 The perturbed distribution function

The perturbed distribution function \tilde{f}_α is solution of the linearized Vlasov equation:

$$\left. \frac{D}{Dt} \right|_{u.t.p.} \tilde{f}_\alpha = \left[\frac{\partial}{\partial t} + \mathbf{v} \cdot \frac{\partial}{\partial \mathbf{v}} + \frac{1}{m} (q_\alpha \mathbf{v} \times \mathbf{B} + \mathbf{F}_E + \mathbf{F}_B) \cdot \frac{\partial}{\partial \mathbf{v}} \right] \tilde{f}_\alpha = \frac{q_\alpha}{m_\alpha} \nabla \tilde{\phi} \cdot \frac{\partial f_{\alpha 0}}{\partial \mathbf{v}} \quad (2.21)$$

where $D/Dt|_{u.t.p.}$ stands for the total derivative along the unperturbed trajectories, $[\mathbf{r}'(t'), \mathbf{v}'(t')]$, defined by:

$$\frac{d\mathbf{r}'}{dt'} = \mathbf{v}' \quad (2.22a)$$

$$\frac{d\mathbf{v}'}{dt'} = \frac{1}{m} (q\mathbf{v}' \times \mathbf{B} + \mathbf{F}_E + \mathbf{F}_B) \quad (2.22b)$$

with the initial conditions $\mathbf{r}'(t' = t) = \mathbf{r}$, $\mathbf{v}'(t' = t) = \mathbf{v}$. The Eq. (2.21) can thus be solved for \tilde{f}_α by integrating along the unperturbed trajectories of the particles:

$$\tilde{f}_\alpha(\mathbf{r}, \mathbf{v}, t) = \frac{q_\alpha}{m_\alpha} \int_{-\infty}^t dt' \nabla \tilde{\phi} \cdot \frac{\partial f_{\alpha 0}}{\partial \mathbf{v}} \Big|_{\mathbf{r}'(t'), \mathbf{v}'(t'), t'} \quad (2.23)$$

having assumed $\Im(\omega) > 0$ to impose causality, so that $\tilde{f}_\alpha(t = -\infty) = 0$. After some algebra, the argument of the integral in Eq. (2.23) is written as:

$$\nabla \tilde{\phi} \cdot \frac{\partial f_{\alpha 0}}{\partial \mathbf{v}} = \imath(\omega_n + \omega'_T + \omega_E - \mathbf{k} \cdot \mathbf{v}) \frac{f_{\alpha 0}}{v_{th}^2} \hat{\phi} e^{\imath(\mathbf{k} \cdot \mathbf{r} - \omega t)} \quad (2.24)$$

where:

$$\omega_n = \frac{T_\alpha k_y}{q_\alpha B_0} \frac{d \ln n_\alpha}{dx} \quad (2.25a)$$

$$\omega'_T = \frac{T_\alpha k_y}{q_\alpha B_0} \frac{dT_\alpha}{dx} \frac{\partial}{\partial T_\alpha} \quad (2.25b)$$

$$\omega_E = -\frac{k_y E_0}{B_0} \quad (2.25c)$$

The term ω'_T is an operator acting on the distribution function through the partial derivative $\partial/\partial T_\alpha$. After integration along the unperturbed trajectories, the amplitude of \tilde{f}_α can be written as:

$$\hat{f}_\alpha = -\frac{q_\alpha \hat{\phi}}{T_\alpha} \left[1 - (\omega_n + \omega'_T + \omega_E - \omega) \sum_{N, N' = -\infty}^{+\infty} \frac{J_N \left(\frac{k_y v_\perp}{\Omega} \right) J_{N'} \left(\frac{k_y v_\perp}{\Omega} \right) e^{\imath(N - N')\theta}}{k_z v_z + N\Omega + \omega_E + \omega_B - \omega} \right] f_{\alpha 0} \quad (2.26)$$

where J_N are the Bessel functions and $\omega_B = k_y v_B$ with v_B given by Eq. (2.8). To obtain the density fluctuations amplitude \hat{n}_α and the dielectric function at the surface $x = 0$, one must therefore integrate \hat{f}_α over velocities:

$$\hat{n}_\alpha = -n_\alpha \frac{q_\alpha \hat{\phi}}{T_\alpha} \left[1 - (\omega_n + \omega'_T + \omega_E - \omega) \sum_{N = -\infty}^{+\infty} \int d\mathbf{v} \frac{f_{\alpha 0}}{n_\alpha} \frac{J_N^2 \left(\frac{k_y v_\perp}{\Omega} \right)}{k_z v_z + N\Omega + \omega_E + \omega_B - \omega} \right] \quad (2.27)$$

where the integral over θ leads to $N = N'$. The integral in (2.27) must be evaluated numerically over the perpendicular and parallel velocities, due to the dependence of ω_B on both v_\perp and v_\parallel .

2.4 Analytical solution for drift waves

The effect of a constant, background electric field on the dispersion relation is a Doppler shift in the real frequency of the instability. Equation (2.27) can therefore be written as a function of the Doppler-shifted frequency $\omega' = \omega - \omega_E$:

$$\hat{n}_\alpha = -n_\alpha \frac{q_\alpha \hat{\phi}}{T_\alpha} \left[1 - (\omega_n + \omega'_T - \omega') \sum_{N=-\infty}^{+\infty} \int d\mathbf{v} \frac{f_{\alpha 0}}{n_\alpha} \frac{J_N^2 \left(\frac{k_y v_\perp}{\Omega} \right)}{k_z v_z + N\Omega + \omega_F - \omega'} \right] \quad (2.28)$$

The term ω_F is now related to an external charge independent force $\mathbf{F} = F\mathbf{e}_x$. Under the hypothesis that F is independent of the velocity, the integral can be computed analytically. Replacing f_0 from Eq. (2.16) the integral over v_z gives:

$$\frac{1}{\sqrt{2\pi}} \int_{-\infty}^{+\infty} \frac{dv_z}{v_{th}} \frac{e^{-v_z^2/2v_{th}^2}}{k_z v_z + N\Omega + \omega_F - \omega'} = \frac{1}{\omega' - \omega_F - N\Omega} \left[W \left(\frac{\omega' - \omega_F - N\Omega}{|k_z|v_{th}} \right) - 1 \right]$$

where the plasma dispersion function $W(\cdot)$, defined as:

$$W(z) = \frac{1}{\sqrt{2\pi}} \int_{\Gamma} dx \frac{x}{x-z} e^{-x^2/2} \quad (2.29)$$

accounts for the resonant interactions along the magnetic field. The integral over v_\perp gives the scaled modified Bessel functions $\Lambda_N(\cdot)$:

$$\int_0^{+\infty} \frac{v_\perp dv_\perp}{v_{th}^2} e^{-v_\perp^2/2v_{th}^2} J_N^2 \left(\frac{k_y v_\perp}{\Omega} \right) = e^{-(k_y \rho)^2} I_N[(k_y \rho)^2] = \Lambda_N(\xi)$$

The terms $\Lambda_N(\xi)$, with $\xi = (k_y \rho)^2$, represent the finite Larmor radius effects. In the limit of low frequency fluctuations, with $\omega \ll \Omega_e, \Omega_i$, only terms with $N = 0$ need to be taken into account in Eq. (2.28). In the long wavelength limit, $k_y \rho \ll 1$, $\Lambda_0(\xi)$ can be expanded as $\Lambda_0(\xi) \simeq 1 - \xi$. For the electrons in particular, $\Lambda_0(\xi_e) \simeq 1$ because $\xi_e \ll 1$. The dispersion relation can finally be written as:

$$\epsilon(\mathbf{k}, \omega) = 1 + \sum_{\alpha} \frac{1}{(k\lambda_{D\alpha})^2} \left\{ 1 + \frac{\omega' - \omega_n - \omega'_T}{\omega' - \omega_F} \left[W \left(\frac{\omega' - \omega_F}{|k_z|v_{th}} \right) - 1 \right] \Lambda_0(\xi) \right\} = 0 \quad (2.30)$$

where $\lambda_{D\alpha} = (\epsilon_0 T_\alpha / n_0^2)^{1/2}$ is the Debye length. Under the hypothesis that $\nabla T_{e,i} = 0$, we'll calculate the analytic solution of the dispersion relation in two cases, namely in the limit of a straight magnetic field and in the interchange limit.

2.4.1 Drift waves in straight magnetic fields

In the simple case where only the density gradient is present, *i.e.* $\nabla T_{e,i} = 0$, and $F_{e,i} = 0$, the dispersion relation Eq. (2.30) reduces to:

$$\begin{aligned} \epsilon(\mathbf{k}, \omega) = & 1 + \frac{1}{(k\lambda_{De})^2} \left\{ 1 + \left(1 - \frac{\omega_{ne}}{\omega}\right) \left[W\left(\frac{\omega'}{|k_z|v_{the}}\right) - 1 \right] \right\} \\ & + \frac{1}{(k\lambda_{Di})^2} \left\{ 1 + \left(1 - \frac{\omega_{ni}}{\omega}\right) \left[W\left(\frac{\omega'}{|k_z|v_{thi}}\right) - 1 \right] \Lambda_0(\xi_i) \right\} = 0 \end{aligned}$$

For drift waves $k_z v_{thi} \ll \omega \ll k_z v_{the}$, *i.e.* the phase velocity along the magnetic field is sufficiently low that electrons can respond adiabatically. After expanding the plasma dispersion function using these limits for ions and electrons, the real frequency ω_R is calculated imposing $\epsilon(\mathbf{k}, \omega_R) = 0$, while the growth rate is given by $\gamma = \Im[\epsilon(\mathbf{k}, \omega_R)] \cdot (\partial \Re[\epsilon(\mathbf{k}, \omega_R)] / \partial \omega_R)^{-1}$ (resonant approximation).

After some algebra the real and the imaginary parts of the frequency can be expressed as:

$$\omega_R = \omega_{ne} \frac{\Lambda_0}{1 + \frac{T_e}{T_i} (1 - \Lambda_0) + (k\lambda_{De})^2} \quad (2.31a)$$

$$\gamma = \sqrt{\frac{\pi}{2}} \frac{\omega_{ne}^2}{|k_z|v_{the}} \frac{\Lambda_0 \left[\left(1 + \frac{T_e}{T_i}\right) (1 - \Lambda_0) + (k\lambda_{De})^2 \right]}{\left[1 + \frac{T_e}{T_i} (1 - \Lambda_0) + (k\lambda_{De})^2 \right]^3} \quad (2.31b)$$

where $\Lambda_0 \equiv \Lambda_0(\xi_i)$. In the limit of $\xi_i \ll 1$ and $\rho_i \gg \lambda_{De,i}$ Eq. (2.31) reduces to the fluid result:

$$\omega_R \simeq \frac{\omega_{ne}}{1 + (k_y \rho_s)^2} \quad (2.32a)$$

$$\gamma \simeq \sqrt{\frac{\pi}{2}} \frac{\omega_{ne}^2}{|k_z|v_{the}} \frac{1}{[1 + (k_y \rho_s)^2]^2} \quad (2.32b)$$

where $\rho_s = c_s / \Omega_i$ is the ion Larmor radius evaluated at the sound speed $c_s = \sqrt{T_e / m_i}$.

Numerical solution for typical TORPEX plasmas

We have run the dispersion relation in the limit of a straight magnetic field for Hydrogen and Argon plasmas, in a range of parameters typical for TORPEX (see Table 2.1). A gradient scale length $L_n = 4$ cm is taken for both gases, corresponding to the value measured at the location of maximum ∇n_0 . Electron and ion temperature are assumed to be constant, with $T_{e0} / T_{i0} = 40$, and no external forces are added in the dispersion relation. In the local approximation a constant background electric field E_0 causes a shift in the real frequency, equal to $\omega_E = k_y v_E$, without affecting the imaginary part and is not included in these examples.

Figure 2.5 shows the dependence of the numerical solution on k_z for fixed $k_y \rho_i = 0.1$, as well as the variation with k_y , for the value k_z corresponding to the maximum growth

	H₂	Ar
$\omega_{ci}/2\pi$ (Hz)	1.3×10^6	30×10^3
ρ_i	0.4×10^{-3}	2×10^{-3}
$(\rho_i/\lambda_{Di})^2$	500	10^5
L_n (cm)	5	5
T_e/T_i	40	40
m_i/m_e	1836	$1836 \cdot 40$
k_y (m ⁻¹)	(10, 250)	(5, 100)
k_z (m ⁻¹)	(10^{-3} , 0.4)	(10^{-3} , 0.4)
$k_y\rho_i$	0.01, 0.1	0.1

Table 2.1: Parameters used to calculate the numerical solution of the dispersion relation for Hydrogen and Argon plasmas.

rate. The behavior is similar for Hydrogen and Argon, with unstable drift waves predicted for $k_z\rho_i < 4 \times 10^{-3}$ in Hydrogen and $k_z\rho_i < 2 \times 10^{-2}$ in Argon, corresponding to $k_z \lesssim 10$ m⁻¹. The maximum growth rates are predicted around $k_z\rho_i \simeq 5 \times 10^{-5}$, which corresponds to $k_z \simeq 0.02$ m⁻¹ in Argon and $k_z \simeq 0.14$ m⁻¹ in Hydrogen plasmas.

Across the magnetic field, the most unstable drift mode has $k_y\rho_i = 0.1$, corresponding to $k_y = 50$ m⁻¹ in Argon and $k_y = 250$ m⁻¹ in Hydrogen plasmas. Negative frequencies indicate propagation along the electron diamagnetic drift direction, *i.e.* the negative y axis in Fig. 2.4. The most unstable solution has $\omega_{de}/2\pi \simeq 1$ kHz in Hydrogen and $\omega_{de}/2\pi \simeq 8$ kHz in Argon plasmas; to these values one should then add the $\mathbf{E}_0 \times \mathbf{B}$ drift frequency ω_E to compare with the value measured in the laboratory frame. As it will be discussed in the Sec. 8.5, in Argon plasmas these values are consistent with the parallel and perpendicular wavenumbers typically measured on TORPEX. Conversely, in Hydrogen plasmas, the perpendicular wavenumber is approximately a factor ten lower than the value of $k_y = 250$ m⁻¹, which corresponds to the most unstable drift wave.

In the case of Hydrogen plasmas the stability has been studied also for $k_y\rho_i = 0.01$, for three values of the density gradient scale length, $L_n = 2, 4$ and 10 cm. No solution has been calculated for Argon plasmas in this limit, which would correspond to wavenumbers of 5 m⁻¹, much lower than those commonly measured on TORPEX. Figure 2.6 shows the dependence of the numerical solution on the amplitude of k_y and k_z for the three values of L_n . For $L_n/\rho_i = 100$, drift waves are predicted to be unstable for $k_z\rho_i < 3 \times 10^{-6}$ with maximum growth rate at $k_z\rho_i \simeq 1.5 \times 10^{-6}$, corresponding to $k_z \simeq 4 \times 10^{-3}$ m⁻¹. The growth rate sharply decreases for larger values of the parallel wavenumber and no unstable solutions are predicted for drift waves for $k_z\rho_i \gtrsim 2.5 \times 10^{-6}$, *i.e.* for $k_z \gtrsim 6 \times 10^{-3}$ m⁻¹. This limit increases up to $k_z = 0.01$ m⁻¹ when L_n is decreased by a factor of two. As expected, the growth

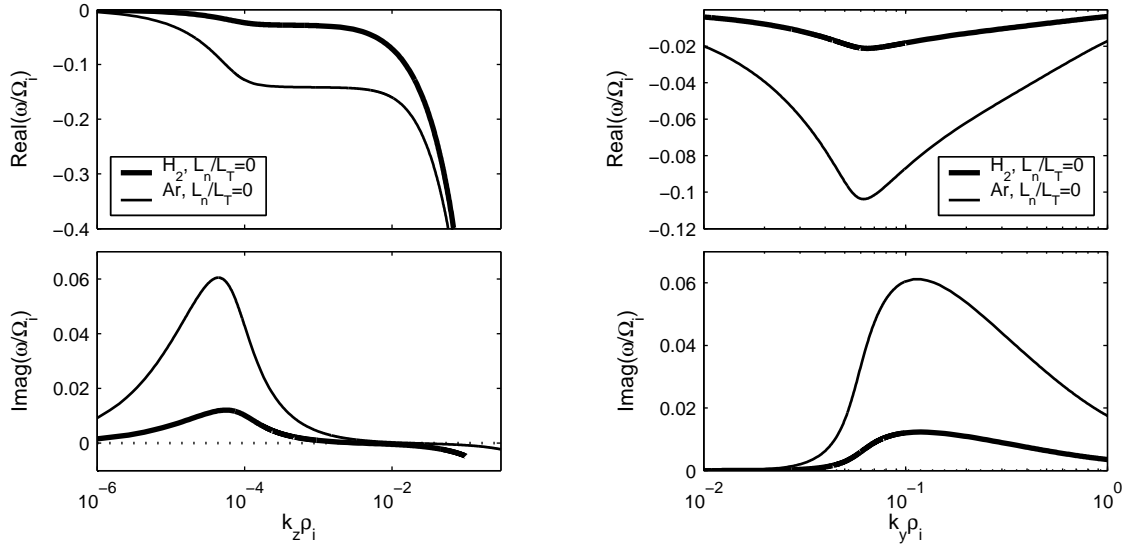


Figure 2.5: Numerical solution of the kinetic dispersion relation for drift waves, calculated for Hydrogen (thick curve) and for Argon (thin curve) plasmas, assuming $L_n = 4$ cm, $T_e/T_i = 40$, $L_n/L_T = 0$, $L_n/R = 0$ and $k_y\rho_i = 0.1$. For Hydrogen $L_n/\rho_i = 100$, $(\rho_i/\lambda_{Di})^2 = 500$ and $m_i/m_e = 1836$. For Argon $L_n/\rho_i = 20$, $(\rho_i/\lambda_{Di})^2 = 10^5$ and $m_i/m_e = 40 \times 1836$. Left: variation with $k_z\rho_i$ for fixed $k_y\rho_i = 0.1$. Right: variation with $k_y\rho_i$ for k_z corresponding to the maximum growth rate.

rate increases for smaller L_n , *i.e.* for larger density gradients. At the same time, the perpendicular wavenumber of the most unstable mode slowly increases with decreasing L_n . Note that, in the case of $L_n = 10$ cm, the limit above which the numerical solution is stable is shifted towards larger values of the parallel wavenumber, $k_z = 0.75$ m⁻¹. For the small values of $k_y\rho_i$ considered here, typical of Hydrogen plasmas on TORPEX, drift waves with parallel wavenumbers larger than 0.01 m⁻¹ are not expected to be unstable.

2.4.2 Drift waves in curved magnetic fields, interchange limit

In the limit of perturbations propagating exactly across the magnetic field, $k_z = 0$, the particles cannot interact resonantly with the waves. The plasma dispersion function $W(z)$ is zero for both species. As in the previous section, we neglect the temperature gradient and retain the density gradient. The external force, charge independent, is assumed independent of the velocity. From Eq. (2.30), at the lowest order in the Larmor radius, we find:

$$1 + \frac{1}{(k\lambda_{De})^2} \left[1 - \frac{\omega - \omega_{de}}{\omega - \omega_{Fe}} \right] + \frac{1}{(k\lambda_{Di})^2} \left[1 - \frac{\omega - \omega_{di}}{\omega - \omega_{Fi}} \Lambda_0 \right] = 0 \quad (2.33)$$

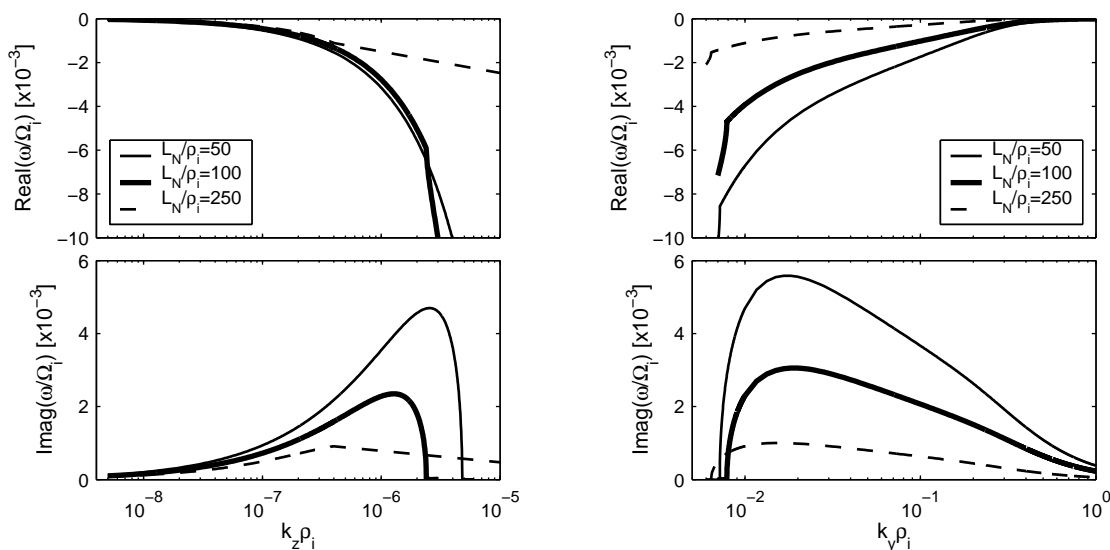


Figure 2.6: Numerical solution of the kinetic dispersion relation for drift waves, calculated for $m_i/m_e = 1836$, $T_e/T_i = 40$, $(\rho_i/\lambda_{Di})^2 = 500$, $L_n/R = 0$, $L_n/L_T = 0$ and for three values of L_n , corresponding to scale length of 2, 4 and 10 cm. Left: variation with $k_z \rho_i$ for fixed $k_y \rho_i = 10^{-2}$. Right: variation with $k_y \rho_i$ for k_z corresponding to the maximum growth rate.

where $\Lambda_0 \equiv \Lambda_0(\xi_i)$ and $\Lambda_0(\xi_e) \simeq 1$. After some algebra, the dispersion relation can be expressed in compact form as [30]:

$$\left(\frac{\omega - \omega_{Fe}}{\omega_{Fi}}\right)^2 - [\mu + \nu(1 - \Lambda_0)] \frac{\omega - \omega_{Fe}}{\omega_{Fi}} + \mu\nu = 0. \quad (2.34)$$

with

$$\mu = 1 - \frac{\omega_{Fe}}{\omega_{Fi}} \quad (2.35)$$

$$\nu = \frac{\omega_{ni}}{\omega_{Fi}} \frac{1}{(k\lambda_{Di})^2 + 1 - \Lambda_0} \quad (2.36)$$

The solutions of Eq. (2.34) are given by:

$$\frac{\omega - \omega_{Fe}}{\omega_{Fi}} = \frac{1}{2} \left\{ \mu + \nu(1 - \Lambda_0) \pm \sqrt{[\mu + \nu(1 - \Lambda_0)]^2 - 4\mu\nu} \right\} \quad (2.37)$$

By imposing the condition for instability, $[\mu + \nu(1 - \Lambda_0)]^2 - 4\mu\nu < 0$, one can calculate the growth rate:

$$\gamma = \frac{|\omega_{Fi}|}{2} \sqrt{4\mu\nu - [\mu + \nu(1 - \Lambda_0)]^2} \quad (2.38)$$

As $\mu > 0$, because the drifts are opposite, a necessary (but not sufficient) condition for instability is that $\nu > 0$. This implies:

$$F_i \frac{d \ln n_0}{dx} < 0 \quad (2.39)$$

i.e. the force must oppose the density gradient.

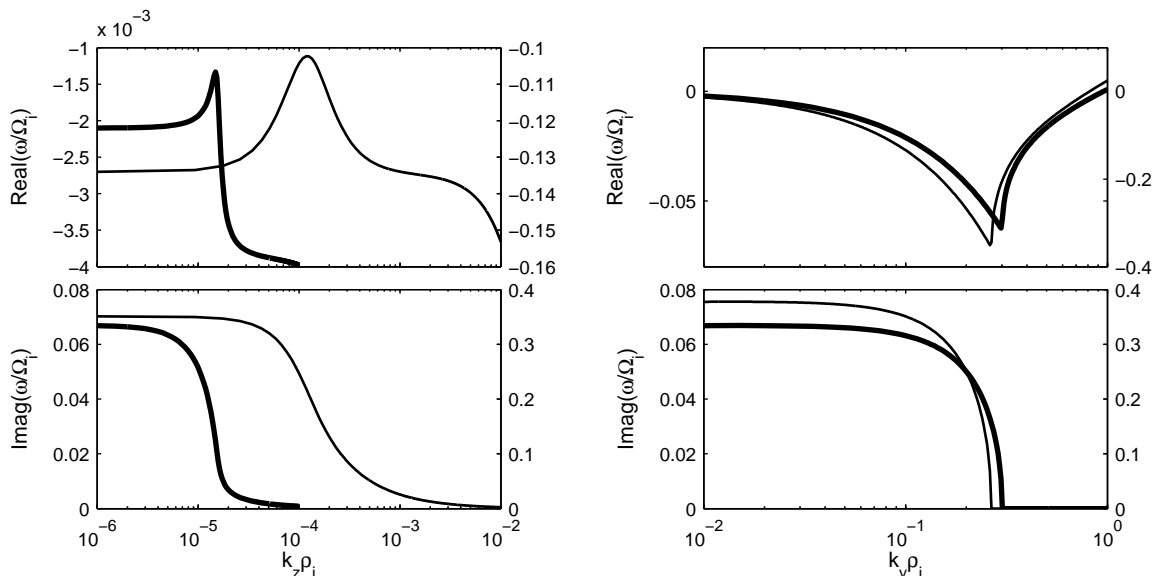


Figure 2.7: Numerical solution of the kinetic dispersion relation for interchange modes, calculated for Hydrogen (thick curve, left axis) and Argon (thin curve, right axis) plasmas, assuming $T_e/T_i = 40$, $L_n/L_T = 0$ and for $L_n = 4$ cm. For Hydrogen $L_n/\rho_i = 100$, $(\rho_i/\lambda_{Di})^2 = 500$ and $m_i/m_e = 1836$. For Argon $L_n/\rho_i = 20$, $(\rho_i/\lambda_{Di})^2 = 10^5$ and $m_i/m_e = 40 \times 1836$. Left: variation with $k_z\rho_i$ for fixed $k_y\rho_i = 0.1$. Right: variation with $k_y\rho_i$ for $k_z\rho_i = 10^{-6}$.

Numerical solution for typical TORPEX plasmas

The reference background values are the same as in the previous section, namely constant ion and electron temperatures, with $T_{e0}/T_{i0} = 40$ and $L_n = 4$ cm. The effect of the curvature is quantified by including an external, gravity type force in the dispersion relation, Eq. (2.30). Figure 2.7 shows the numerical solution calculated for Hydrogen and Argon plasmas, assuming $k_y\rho_i = 0.1$. The behavior is similar for the two gases, with growth rate large and approximately constant for perpendicular wavenumbers in the range of $k_y\rho_i \in [0.01, 0.1]$. For k_z approaching zero, the numerical solution tends to the analytical solution, Eq. (2.38), then the growth rate sharply goes to zero for $k_z\rho_i > 5 \times 10^{-6}$ in the case of Hydrogen and $k_z\rho_i > 5 \times 10^{-5}$ in the case of Argon. These values correspond to a parallel wavenumber of ~ 0.03 m $^{-1}$. The numerical solution for $k_y\rho_i = 10^{-2}$ does not need to be shown in this case, as it is very similar to that for $k_y\rho_i = 0.1$. The growth rate is in fact approximately constant in the range $k_y\rho_i \in [0.01, 0.1]$. The only differences are in the real frequency, related to the perpendicular wavenumber by $\omega = k_y v_B$.

2.5 Summary and discussion

We have presented in this Chapter the theoretical background for the analysis of electrostatic plasma instabilities on TORPEX, deriving a local, kinetic dispersion relation for non collisional drift waves in slab geometry (S. Brunner [30]). In the

Drift instabilities			
Properties	Pure drift	Drift-interchange	Interchange
phase velocity	$\mathbf{v}_{de} + \mathbf{v}_E$	$\mathbf{v}_{de} + \mathbf{v}_E$	\mathbf{v}_E
Frequency	$\omega_{de} + \omega_E$	$\omega_{de} + \omega_E$	ω_E
k_{\parallel}	$\neq 0$	$\neq 0$	0
k_{\parallel}/k_{\perp}	$\ll 1$	$\ll 1$	0
Driving mechanism	∇n_0	$\nabla n_0 + \text{curvature}$	$\nabla n_0 + \text{curvature}$

Table 2.2: Classification of instabilities adopted in this Thesis. Frequency and phase velocity are written in the laboratory frame.

original version, the effect of curvature was included as an external, constant, gravity type force, described by Eq. (2.7).

The numerical solution has been calculated for Hydrogen and Argon plasmas in the range of parameters routinely measured on TORPEX in the limit of straight magnetic field and in the interchange limit. For the typical wavenumbers measured on TORPEX perpendicular to the magnetic field, it is found that drift instabilities can develop in Argon plasmas in the presence of the density gradient alone. The effect of the curvature is to further destabilize the modes with small parallel wavenumbers.

Conversely, in the case of Hydrogen plasmas, for the measured perpendicular wavenumbers, only drift waves with very small parallel wavenumbers can be unstable in the presence of a density gradient alone. Modes with $k_{\parallel} \gtrsim 0.01 \text{ m}^{-1}$ are unstable only in the presence of the curvature, with a predicted growth rate decreasing rapidly to zero for $k_{\parallel} \gtrsim 0.2 \text{ m}^{-1}$. In this limit of marginally unstable solutions, the approximation of a constant gravity type force fails and Eq. (2.6) should be used instead of Eq. (2.7) to quantify the magnetic field contribution. The original dispersion relation has therefore been modified in order to treat correctly also these marginally unstable modes. The integral over velocities in Eq. (2.27) is calculated numerically over a step grid in the velocity space.

Although driven by the curvature of the magnetic field, instabilities with parallel wavenumbers in this range cannot be identified as pure interchange modes, because their parallel wavenumber is finite. We'll call them drift-interchange, because they satisfy a drift wave dispersion relation, but their destabilization requires the curvature of the magnetic field.

Note that, in deriving the dispersion relation, we have assumed that the distribution function is nearly Maxwellian. Plasmas are generated and sustained on TORPEX by microwaves with frequency in the electron cyclotron frequency range (see Sec. 3.4). At the location of the upper-hybrid resonance, a tail due to suprathermal electrons is measured in the electron energy distribution function [31]. The numerical solution of the dispersion relation, modified to allow a bi-maxwellian distribution function is nevertheless unaffected by the presence of the suprathermal electrons for the measured values of suprathermal temperature and density.

Chapter 3

The TORPEX device

The experiments presented in this Thesis are performed on the toroidal device TORPEX (TORoidal Plasma EXperiment, see Fig. 3.1) [27], operational at CRPP-EPFL, Lausanne, since March 2003. TORPEX is the primary experimental tool of the CRPP Basic Plasma Physics group, whose research interests include the study of plasma instabilities and turbulence and their implications on the cross-field particle and heat transport. The toroidal geometry (Sec. 3.1) was a natural choice to have the ingredients at the origin of plasma turbulence in tokamaks, *i.e.* pressure gradients combined to the curvature of the magnetic field lines. The design of TORPEX started during autumn 2001 with the goal of providing a device with maximum flexibility in terms of diagnostics access (Sec. 3.1) and magnetic field configuration (Sec. 3.2).

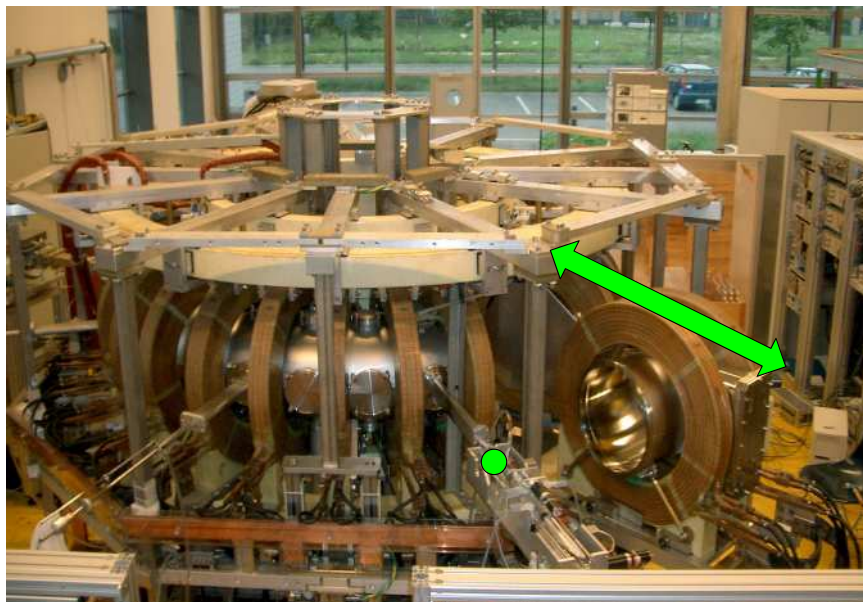


Figure 3.1: The TORPEX device, with view on one of the movable systems for the electrostatic Langmuir Probe arrays (green dot) and on the extractable sector on the right.

3.1 Geometrical parameters

The TORPEX toroidal vacuum vessel (major radius $R_0 = 1$ m) consists of 12 stainless steel sectors, 5 mm in thickness, spanning 30° each, with a circular cross-section of radius $a = 0.20$ m. The diameter of the vessel was constrained by the size of a set of coils, available from a previous experiment at CRPP, the LMP (Linear Magnetised Plasma) Device [32][33]. Four sectors are extractable and toroidally separated 90° from each other. They are provided with removable seals and spacer rings, specifically designed to enhance the ease and limit the duration of interventions, such as installation and modification of dedicated diagnostics. The remaining eight sectors are fixed, arranged into four pairs and electrically insulated to limit the induced eddy currents. Access for pumping and diagnostic instrumentation is provided by 48 port-holes in the *fixed* sectors. A visual overview of the diagnostics used for the experiments presented in this Thesis is given in Fig. 3.2, while the diagnostics setup is discussed more extensively in Chap. 4.

Four independent turbo-pumps provide a typical vacuum pressure of approximately 5×10^{-7} mbar. Two independent lines are available at present to inject neutral gas in the vessel, at one toroidal position. An upgrade of the gas injection system to double the number of injection lines is under way. The gas flow is controlled electronically by means of flow-meters that give the possibility to inject at the same time mixtures of different gases.

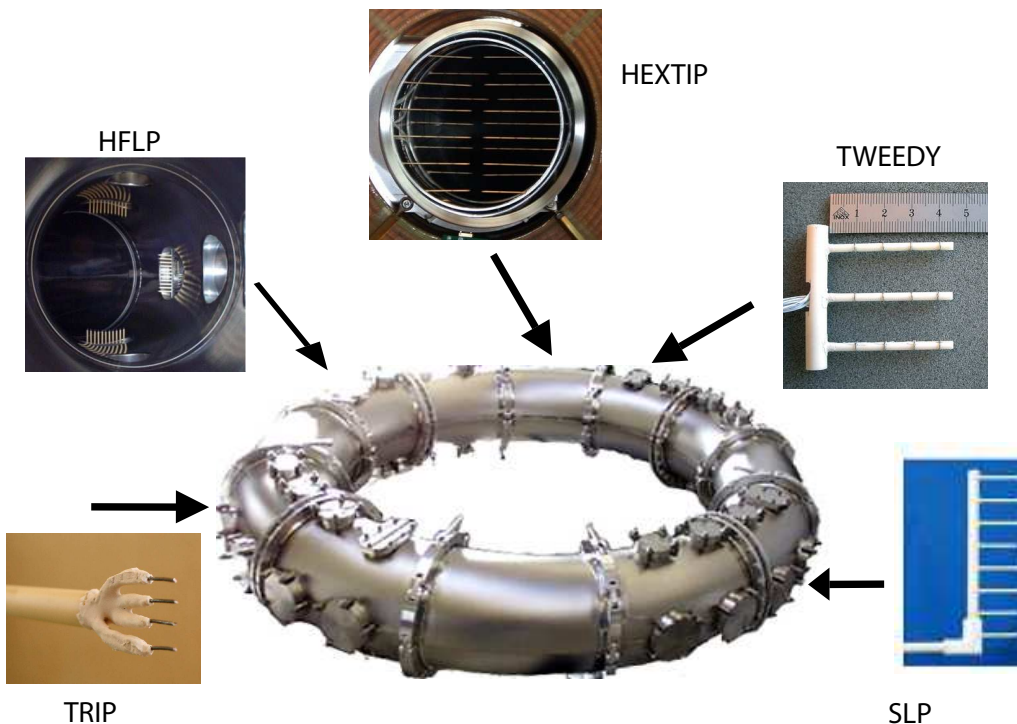


Figure 3.2: Overview of the TORPEX vacuum vessel with indicated the toroidal position of the electrostatic Langmuir probes used in this Thesis.

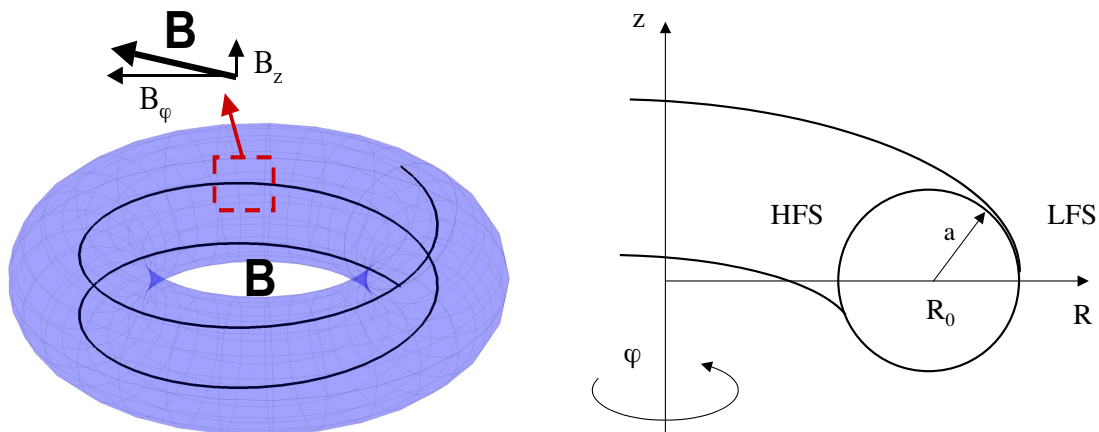


Figure 3.3: Left: Sketch of the magnetic field configuration for the simple magnetised torus, a dominant toroidal field B_φ and a small vertical field component B_z . Right: Cylindrical reference used in this Thesis: R is the radial position with respect to the torus axis, z the vertical position, φ the toroidal angle. R_0 and a are the major and minor radius of the TORPEX vessel.

3.2 Magnetic field configuration

The TORPEX magnetic field coil system allows a variety of configurations and encompasses a toroidal, a poloidal and an ohmic system. The 28 coils for the generation of the **toroidal magnetic field** originate from a former experiment at CRPP, the linear device LMP [32][33], while the other two coil systems have been designed and built *ex novo*. The feasibility study and the technical requirements of the magnetic field system are discussed in a previous Thesis work [34]. The toroidal field can be varied up to 200 mT on axis; the limit is imposed by the maximum current (400 A) that can flow into the coils without causing overheating. In this work, however, the useful range is limited to $B_\varphi \leq 100$ mT by the frequency of the available source for the injection of microwaves and the position of the EC resonance (see Sec. 3.4). All the experiments presented in this Thesis are run with the toroidal field $B_\varphi = 76.6$ mT on axis. A cylindrical coordinate system will be used in this Thesis, where R indicates the radial distance from the main axis of the torus, z is the vertical coordinate and φ denotes the toroidal direction (Fig. 3.3). In this coordinate system, the toroidal field will be therefore indicated as B_φ and the vertical field as B_z .

The **poloidal coil system**, which includes 10 different coils, is used at present to generate a uniform vertical field, with B_z up to 5 mT, corresponding to a maximum current of 300 A flowing into the coils (Fig. 3.4). The design and arrangement of the poloidal coils were optimized to provide also a cusp field up to 100 mT about 10 cm from the centre of the vessel, with a magnetic null (or X-point) at the centre of the cross-section [34] (Fig. 3.5). The cusp field configuration, planned to run experiments

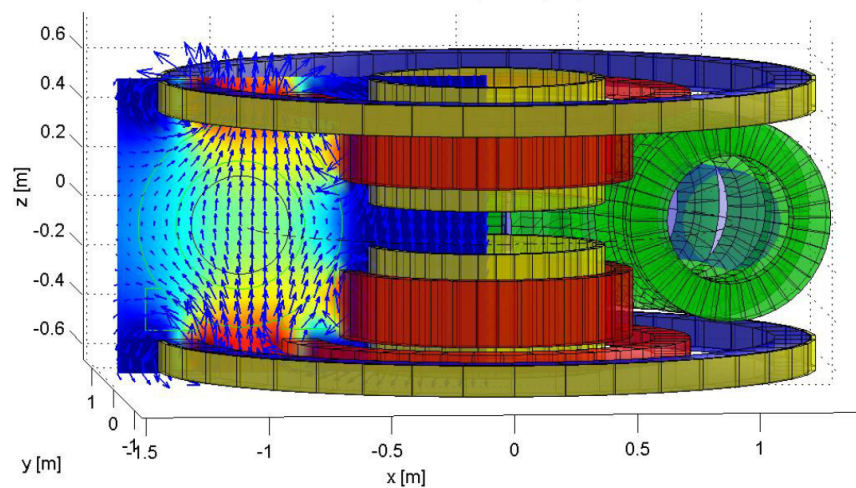


Figure 3.4: (Courtesy of S. H. Müller [34]). Representation of the magnetic field lines in the vertical field configuration.

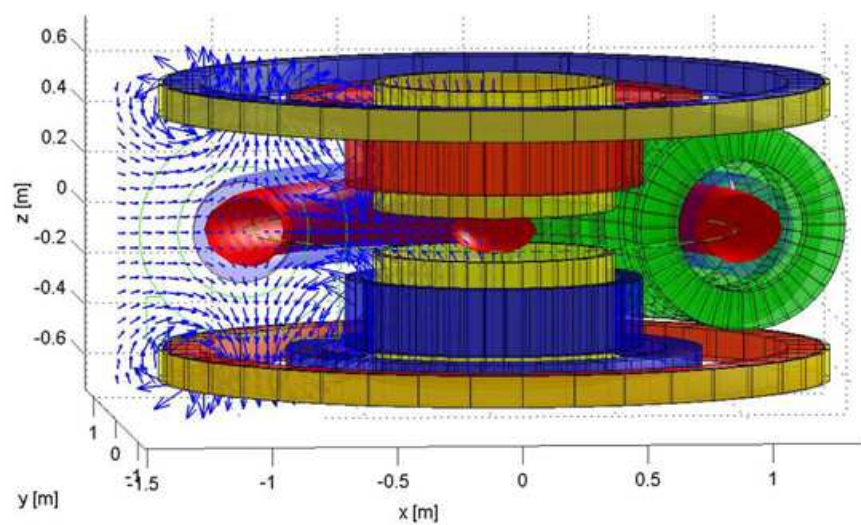


Figure 3.5: (Courtesy of S. H. Müller [34]). Representation of the magnetic field lines in the cusp field configuration.

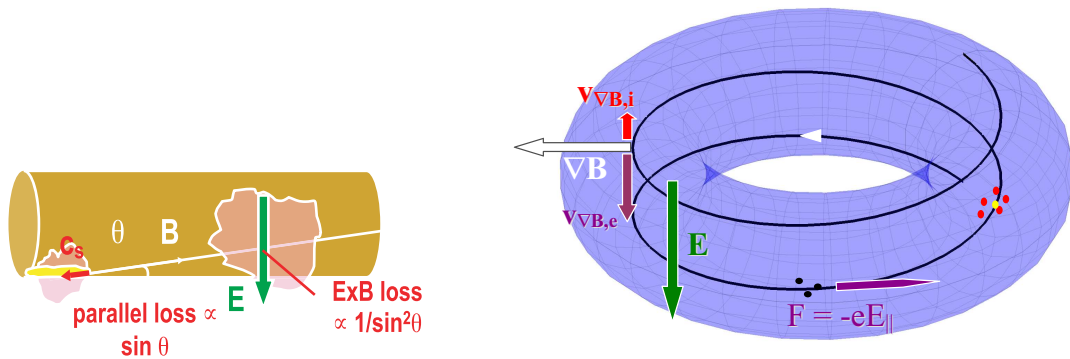


Figure 3.6: Scheme of the loss mechanisms taken into account in the model for the confinement time [34][37].

on magnetic reconnection, has not been explored so far. Experiments presented in this Thesis are conducted for values of B_z in the range of 0.2 to 2.5 mT.

A subset of the poloidal coils can be used to induce in the vessel a loop voltage of the order of 10 V for approximately 30 ms, to run operations in a tokamak-like configuration. A first proof of principle of these experiments in an **ohmic configuration** has been obtained [35]. The transition from open to closed field lines, not explored in this Thesis, is an interesting field of research for the physics of tokamak. The change in the topology of the magnetic field lines, occurring moving from the core to the edge region, results in a modification of the dispersion relation of electrostatic instabilities and of the properties of turbulence and transport [36].

3.3 Particle Confinement

Plasmas embedded in a purely toroidal magnetic field are not in magnetohydrodynamic equilibrium (see [38] and references therein). The ∇B and curvature drifts, as discussed in Sec. 2.2, induce a charge separation that is at the origin of a vertical electric field. The resulting cross-field drift causes an outward motion of the plasma. A vertical magnetic field B_z is commonly used to short-circuit the drifts induced by the toroidal field [39]. This configuration with open field lines, commonly referred to as *simple magnetized torus* provides poor confinement compared to fusion-oriented devices [38]. The mechanisms leading to a pseudo-equilibrium on TORPEX and the basic principles of particle confinement have been investigated in [34][37] and summarized in Fig. 3.6. In addition to the drift-induced particle losses, perpendicular to the magnetic field, the parallel dynamics of ions and electrons causes particles to be lost at the intersection of the magnetic field lines with the vessel. This mechanism is directly affected by the ratio of B_z to B_φ and is expected to be more efficient for large values of B_z . The competition between parallel and perpendicular losses has been studied on TORPEX. An optimal value of the vertical field leading to maximum confinement time has been found theoretically, then verified experimentally in a limited region of the plasma cross-section [34][37]. The main limitations of such a simplified model is

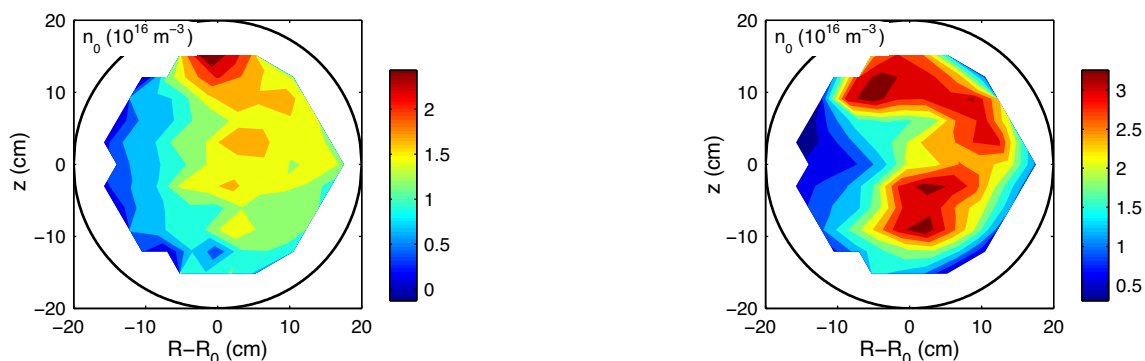


Figure 3.7: Profile of the average value of I_{sat} (units of 10^{16} m^{-3}), measured with the HEXTIP array (see Fig. 3.2 for the probe layout and Chap. 4 for a general description) in a plasma from Argon, with $p_0 = 2.5 \times 10^{-5}$ mbar, for $B_z = 0$ (left) and $B_z = 1$ mT (right).

that it assumes homogeneous plasma profiles. A possible reason for the discrepancies observed is that the global confinement time is finally determined by the background profiles and by the particle dynamics, including collisions [40].

Once the pseudo-equilibrium is formed, the time-averaged profiles and the particle dynamics are affected by the macroscopic fluid drifts that develop in the presence of inhomogeneities (Sec. 2.3.1). These drifts are the $\mathbf{E}_0 \times \mathbf{B}$ drift, due to a background electric field, $v_E = E_0/B_0^2$ and the \mathbf{v}_B drift due to the gradient and curvature of the magnetic field, $v_B = 2T/qB_0R_c$, Eqs. (2.8)-(2.10). The former is charge sign independent and causes a convection of the plasma along a direction that depends on the magnetic field orientation and on the background profile of the plasma potential ϕ_{p0} . The \mathbf{v}_B drift has opposite direction for ions and electrons and causes the ions to shift upward and the electrons to shift downward. Figure 3.7 reports two examples of density profiles measured in an Argon plasma, for $B_z = 0$ and for $B_z = 1$ mT, the estimated optimal value for maximum particle confinement in Argon plasmas. In the case of a purely toroidal magnetic field, the plasma tends to accumulate on the upper part of the plasma cross-section, where the maximum of density is measured. If a vertical component of the magnetic field is added to compensate for the effect of the fluid drifts, a better up-down symmetry is achieved, and the plasma appears more centered vertically.

3.4 Plasma production by microwaves

A magnetron, delivering up to 30 kW in pulsed mode during 100 ms or up to 5 kW in continuous mode, is used as a source of radio-frequency (hereafter RF) waves at frequency $f_{\text{RF}} = (2.45 \pm 0.02)$ GHz. The RF waves are injected perpendicularly to the toroidal magnetic field from the low field side with O-mode polarization, *i.e.* with their electric field parallel to the magnetic field (see Fig. 3.9). The choice of the polarization originates from the presence of a low-density cut-off for the X-mode

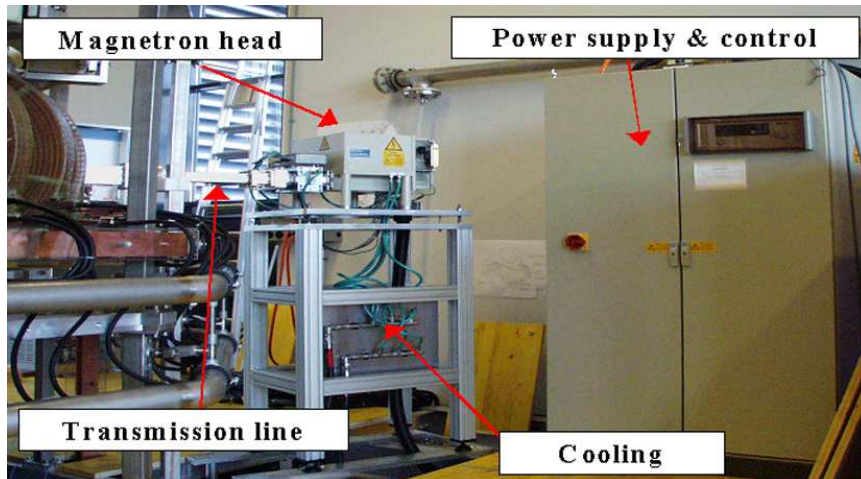


Figure 3.8: Layout of the system for the injection of microwaves.

close to the antenna. The RF waves propagate in the vacuum vessel, giving rise to a population of energetic electrons that ionise the neutrals, building up and sustaining plasmas with densities up to $n_0 \sim 10^{17} \text{ m}^{-3}$ and electron temperatures up to $T_e \lesssim 5 \text{ eV}$. A kinetic resonance exists with the electrons at their cyclotron frequency at the position where the magnetic field is $B_\varphi = 87.5 \text{ mT}$. For the imposed value of $B_\varphi = 76.6 \text{ mT}$ on axis, the position of the EC resonance is at $R - R_0 = -12.5 \text{ cm}$. Due to the transition from a rectangular to a circular waveguide at the entrance into the vessel, the waves penetrate into the vessel with a mixed polarization, combination of the ordinary and extraordinary mode. Due to the low value of $k_\perp \rho_e$, where ρ_e is the electron Larmor radius, only a fraction of the wave power is absorbed at the EC resonance layer [41], most of it being reflected back with mixed polarization from the HFS wall. The X-mode is partly absorbed at the UH resonance layer, at the location where the frequency is equal to $f_{\text{UH}} = (f_{\text{EC}}^2 + f_{\text{p}}^2)^{1/2}$, where $f_{\text{p}} = (e^2 n_e / \pi m_e)^{1/2}$ is the plasma frequency. The characterization of the ionization processes and the reconstruction of the plasma source on TORPEX are detailed in Refs. [42] [43] and were the subject of a previous Thesis work [40].

A sketch of the microwave propagation in the plasma, including the profiles of f_{UH} and f_{EC} and the expected resulting density profile, is given in Fig. 3.9. Figure 3.10 shows instead an example of the density profile measured on TORPEX in a plasma from Hydrogen gas, including the calculated position of the EC and of the UH resonances, where $f_{\text{RF}} = f_{\text{EC}}$ and $f_{\text{RF}} = f_{\text{UH}}$ respectively. Due to the finite bandwidth of the injected microwaves, the plasma source profile extends between the EC resonance, at $R - R_0 = -12.5 \text{ cm}$ and the outer boundary of the resonance layer, as shown in Fig. 3.10. The profile of the particle source is reconstructed with a simple code based on a Monte Carlo approach, which takes into account the finite bandwidth of the injected microwave, the effect of the curvature and of the ∇B drifts, as well as collisions [43].

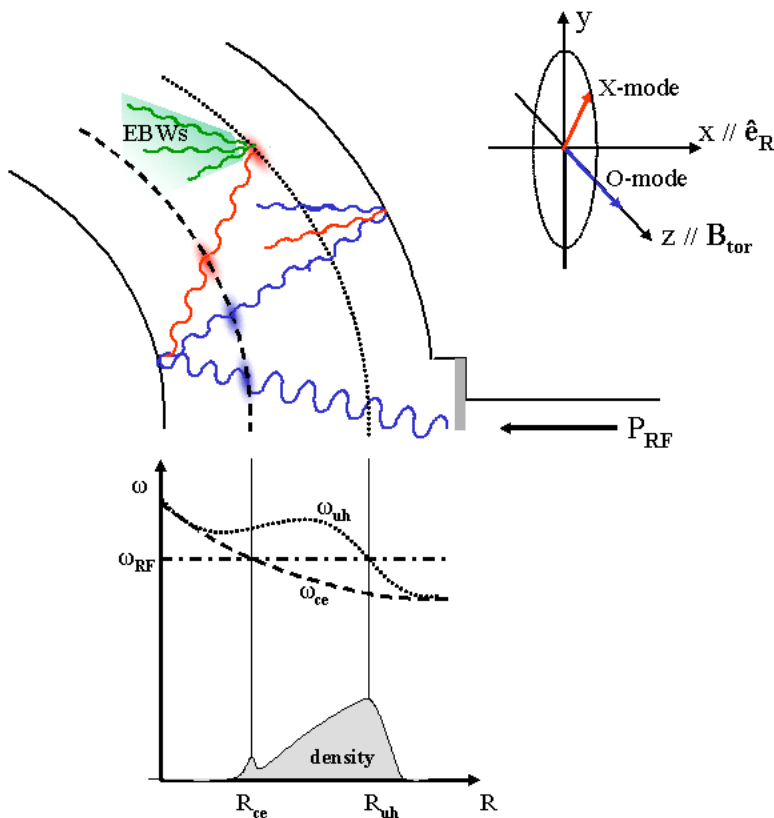


Figure 3.9: (Courtesy of M. Podestà [40]). Scheme of the propagation of microwaves inside the vacuum vessel, including the layer where mode conversion into Electron Bernstein waves (EBW) can occur. Also represented is a sketch of the profiles of the Electron Cyclotron and Upper Hybrid frequencies as well as position of the resonance layers, where $f_{\text{RF}} = f_{\text{EC}}$ and $f_{\text{RF}} = f_{\text{UH}}$.

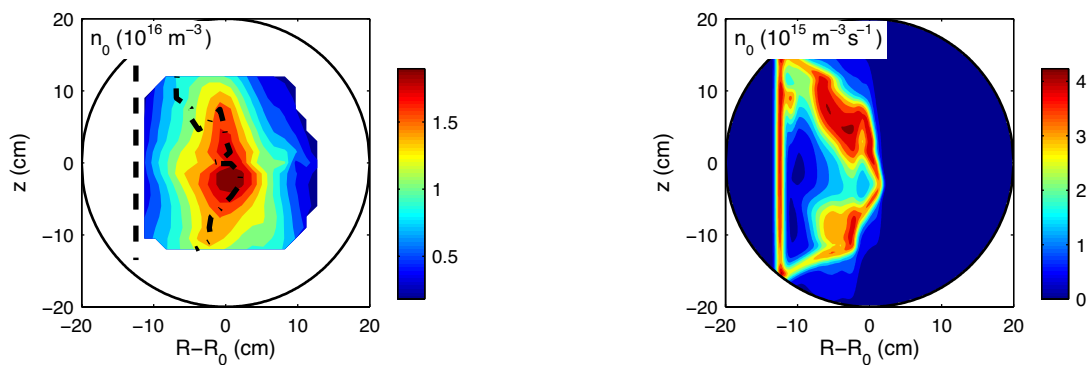


Figure 3.10: Left: density profile (units of 10^{16} m^{-3}) measured in a plasma from Hydrogen at $p_0 = 6 \times 10^{-5} \text{ mbar}$ and absorbed microwave power of 400 W. The toroidal and the vertical magnetic field are $B_\phi = 76.6 \text{ mT}$ on axis and $B_z = 0.6 \text{ mT}$. The dash and the dash-dot lines indicate respectively the position of the EC and of the UH resonances. Right: profile of the particle source for the same plasma (units of $10^{15} \text{ m}^{-3} \text{ s}^{-1}$) reconstructed from a code based on a Monte Carlo approach [43].

Chapter 4

Diagnostics

Plasmas in basic experiments are characterized by low values of density and temperature, comparable to those typically measured at the edge of tokamaks (on the TCV tokamak, *e.g.*, $T_{e0} < 50$ eV and $n_0 < 10^{19}$ m⁻³). Electrostatic probes can therefore be used to measure the background and the fluctuating values of density, temperature and electrostatic potential over the whole plasma cross-section. Almost 200 electrostatic Langmuir probes (hereafter LPs) [44][45] are installed on TORPEX, with different geometry and configuration. Some of these probes, installed before the first experimental campaign, were designed when the background profiles and the level and spectrum of fluctuations were still unknown. This set of *first generation* diagnostics includes two LPs, installed in front of the microwave source, and four LPs toroidally separated from the first two. These two groups of LPs were mainly used to monitor the plasma parameters close to the microwave source and to verify the toroidal symmetry of the plasma. In addition to these fixed LPs, an 8-tip LP array provided the measurement of the background parameters (**SLP**, Sec. 4.3) and three arrays of LPs monitored the density fluctuations along the azimuthal direction, at 4 cm from the vessel (referred to as **FLP**, Sec. 4.4). Both SLP and FLP are still operational. After initial experiments, in which plasma profiles were reconstructed, the set of *second generation* diagnostics were designed with specific requirements. It includes an 86-tip array for a direct monitoring of the space-time evolution of density and floating potential over the whole plasma cross-section (**HEXTIP**, Sec. 4.4) and a 4-tip LP array, specifically aimed at the measurement of the fluctuation driven particle flux and of the dispersion relation on the midplane (**TRIP**, Sec. 4.4). The other diagnostics presently operational on TORPEX include magnetic probes for the measurement of magnetic field fluctuations and two Rogowsky coils for the measurement of the plasma current during ohmic experiments. This Chapter focuses on electrostatic probes directly used during the experiments presented in this Thesis. After a brief review of the basic principles for the interpretation of the LP characteristic curve and of the different regimes of operation used in the experiments (Sec. 4.1), Sec. 4.3 and Sec. 4.4 provide a description of the probes used for the measurement of the background parameters and of the fluctuations, respectively. The Chapter is concluded with examples of the typical time-averaged profiles and of fluctuation spectra measured on TORPEX (Sec. 4.5).

4.1 Electrostatic Langmuir Probes

A typical Langmuir probe usually consists of a tip, made of a refractory material (*e.g.* platinum, tungsten or molybdenum), capable of sustaining large energy fluxes, surrounded by an insulating jacket (alumina and fused silica material are widely used) and a shield. When immersed in a plasma, a LP can carry a current I that depends on the value of the applied voltage V . Measurements with electrostatic probes are perturbing, the nature of the perturbation depending on the probe potential, on the current driven by the probe itself and, naturally, on the probe size. Under the hypothesis of quasi-neutrality, negligible ion temperature, and assuming that the electrons satisfy a Boltzmann distribution function, the $I - V$ characteristic is given by [44]:

$$I = \frac{1}{2} A e n \sqrt{\frac{T_e}{M}} \left[1 - \exp\left(-\frac{V - \phi_f}{T_e/e}\right) \right]. \quad (4.1)$$

Here e is the electron charge, n and T_e are respectively the plasma density and the electron temperature in the unperturbed plasma ¹, and A is the effective surface of the probe, *i.e.* the surface exposed to the particle flux. In a strongly magnetized plasma and for probes oriented perpendicularly to the magnetic field, A represents the projection of the surface perpendicularly to \mathbf{B} . Equation (4.1) is valid as far as the probe voltage is lower than the electrostatic plasma potential ϕ_p . The presence of suprathermal electrons results in a distorted curve, and can affect the measurement of the plasma parameters [40][31]. The hypotheses and methods to analyze the $I - V$ in the different TORPEX experimental configurations are discussed in [40]. An example of the measured time-averaged $I - V$ curve is given in Fig. 4.1. When the probe is at the plasma potential ϕ_p , the measured current is, ideally, the *electron saturation current*, as for applied voltages above this level, the electron current cannot further increase. If a triangular voltage, ranging between $\pm V_0$ is applied to the LP, then the time-average parameters n_0 , T_{e0} and ϕ_{p0} can be estimated from the mean $I - V$ curve, Eq. (4.1). Two regimes of operation can be selected, in particular: the *floating potential* configuration and the *ion saturation current* configuration, which are used in this Thesis for the measurement of the time trace of fluctuations in the plasma potential and in the density.

Floating potential - If the ion and electron fluxes on the probe are equal, the measured current is zero. In this condition, the measured voltage is defined as floating potential ϕ_f , as results from Eq. (4.1). In this configuration the probe is at a negative potential with respect to the plasma (see Fig. 4.1). In principle, the plasma potential can be extracted from the *knee* of the curve, where the electron current saturates, though in practice the saturation regime does not manifest as clearly. Following standard techniques [44], the time-averaged plasma potential can be estimated from the

¹Under the hypothesis that thermal equilibrium is satisfied for both ions and electrons, one expects, in general, the perturbing effect of a charge to be of the order of the Debye length λ_D . For the typical plasma parameters measured on TORPEX, density of 10^{17} m^{-3} and temperature of 5 eV, $\lambda_D \simeq 40 \text{ }\mu\text{m}$.

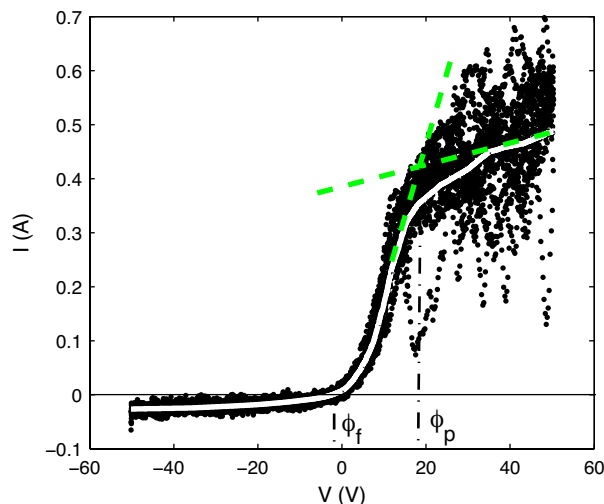


Figure 4.1: Experimental $I - V$ characteristics (black points), measured in a plasma from Hydrogen gas. The white curve is the result of a fitting procedure over the experimental points, using Eq. (4.1). The electrostatic plasma potential ϕ_p and the measured ϕ_f are indicated for comparison.

floating potential ϕ_{f0} and from the electron temperature T_{e0} as:

$$\phi_{p0} = \phi_{f0} + \mu \frac{T_{e0}}{e}. \quad (4.2)$$

The parameter μ is estimated experimentally for each probe, from a large number of complete $I - V$ characteristics, measured for different values of T_{e0} [42].

Ion saturation current - For sufficiently large and negative applied voltages, $|V| \gg \phi_f$, the response of the LP is independent of V and equal to

$$I_{\text{sat}} \simeq \frac{1}{2} A e n \sqrt{\frac{T_e}{M}} \quad (4.3)$$

For a given T_{e0} , the average value of I_{sat} is proportional to the background density n_0 . It results from Eq. (4.3) that, provided that the electron temperature fluctuations are negligible, the density fluctuations can be directly inferred from the fluctuating part of I_{sat} . Details on the measurement of fluctuations and on the effect of temperature fluctuations on the measurement of density fluctuations will be discussed in Chap. 5 and App. E.

4.2 Probe design and specifications

All the electrostatic probes installed on TORPEX have been designed and constructed by members of the TORPEX group, in collaboration with the CRPP technical staff. Both geometrical and mechanical design have been developed in order to

guarantee the highest flexibility in terms of operation, installation and modification of the probe setup. The use of standard components allows, for example, the same mechanical system to be adapted to a large variety of diagnostics, and individual parts to be interchangeable among different probes.

Ceramic materials are used for the probe holders. Although not as easy to machine as softer materials, like Teflon or PVC, ceramic provides a better resistance to the thermal stresses induced by electron fluxes, thus preventing the release of impurities. For similar motivations, liquid ceramic is preferred to glue to stick small pieces, and soldering of metallic parts is done with a tin containing silver rather than lead. Stainless steel has been chosen as material for the probe tips, because of its good thermal resistance and the high threshold against the emission of secondary electrons. Multi-pin, vacuum-tight electrical feed-throughs provide the transmission of signals from the probe to a dedicated electronics for the pre-treatment of signals. The connection between the probe tip and the feed-through is done using single shielded cables, passing inside the ceramic holders.

Besides these solutions, which are common to almost all the probes (with an exception represented by the FLP and TRIP arrays, for which special cables have been used, as discussed in Sec. 4.4), specific requirements have been considered each time according to needs, for example in terms of the size and the shape of the probe holder. On the one hand we want to maximize the number of tips in the same array to cover a plasma region as larger as possible. On the other hand we must limit the perturbations introduced by the probe itself, because of its size and because of the alteration of the charge balance induced by the large current it drives. A good compromise is the use of a movable support, which allows rotation and sliding of the probe on a shot to shot basis, with the advantage of an almost arbitrarily high spatial resolution. This choice, although time consuming for the reconstruction of a complete profile, because the probe must be moved between two shots, minimizes the amount of material inserted into the plasma. Most of the probes installed on TORPEX are mounted on a movable support, of ‘standard’ manufacture to fit in the same flange type and to ease the installation of probes at different toroidal positions. Three remotely-controlled positioning systems are at present available. The radial displacement and the rotation are provided by a stepping motor, controlled through a JAVA interface. The error in the positioning is ± 0.2 cm for the radial displacement and $\pm 3^\circ$ for the rotation.

The signals are sent to dedicated electronics, which provide amplification and filtering in a selected bandwidth. The amplification factor and the bandwidth are imposed by the technical specifications of the acquisition system, a set of two D-TACQ ACQ32CPCI digitizers², with sampling rate of 250 kHz. Low-pass filters at 125 kHz are used to avoid the aliasing of fluctuations with frequency larger than the Nyquist frequency. The 64 channels dedicated to the measurement of the saturation current with the FLP arrays (see Sec. 4.4 and App. C) have a band pass from 30 Hz to 250 kHz. Although this upper limit, above the Nyquist frequency, could be at the origin of aliasing effects in the measurement of fluctuation spectra, tests with an acquisition system at 10 MHz have confirmed the absence of spectral components at frequency

²Website: <http://www.d-tacq.com>

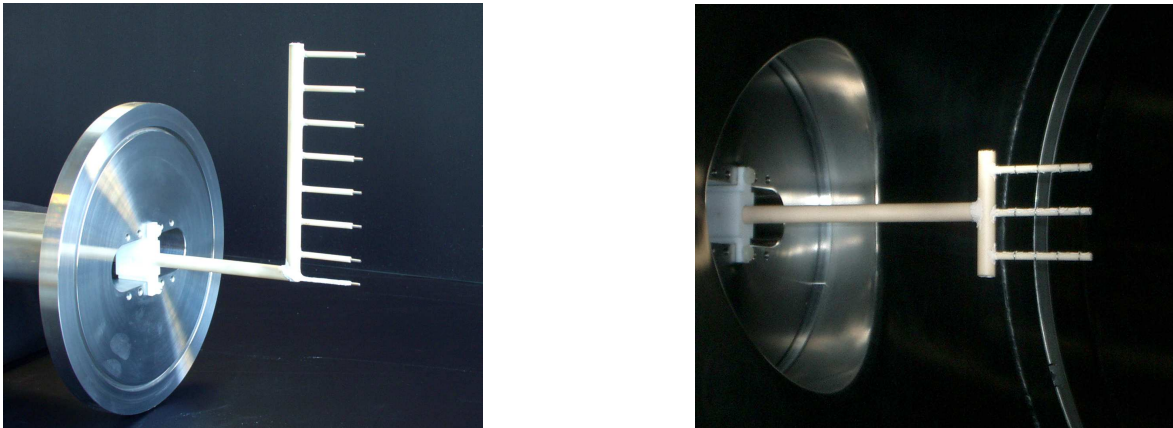


Figure 4.2: LPS for the measurement of background parameters: the 8-tip SLP array (left), and the 4×3 TWEEDY array (right).

larger than 100 kHz. A set of 24 identical modules, independent from each other, provide alternatively the measurement of the complete $I - V$ characteristics, of the floating potential or of the saturation (electron and ion) current. These modules were specifically designed for the measurement of the background parameters, paying thus attention to the DC part of the signal rather than to the high frequency response. Nevertheless, because of the low phase distortion and the constant amplitude response up to approximately 30 kHz (see App. C, Fig. C.6), which is identical for all the modules, they are also used to measure the density and potential fluctuations, as well as the dispersion relation for waves in the drift wave frequency range.

4.3 LPS for the measurement of the background parameters

The set of probes commonly used for the measurement of the background parameters includes an 8-tip and a 12-tip LP array, respectively named SLP (Slow LP) and TWEEDY (TWO Dimensional), shown in Fig. 4.2. These two arrays are mounted on a remotely-controlled positioning system, installed on the equatorial plane and separated from each other by $\pi/2$ in the toroidal direction. Technical details on the construction of these probe arrays and on the measurements of the background parameters are given in a previous Thesis work [40]. The time-averaged plasma parameters, n_0 , T_{e0} and ϕ_{p0} , are reconstructed from fits of the complete $I - V$ curves, obtained with a sweeping voltage of maximum amplitude 100 V and frequency 330 Hz during a stationary discharge ranging typically 200 to 300 ms.

The **SLP** array (Fig. 4.2) provides measurements of n_0 , T_{e0} and ϕ_{p0} in the region $|R - R_0| \leq 12$ cm and $|z| \leq 13$ cm. The separation between adjacent tips is approximately 1.8 cm, but the spatial resolution along z can be further increased by rotating the array.

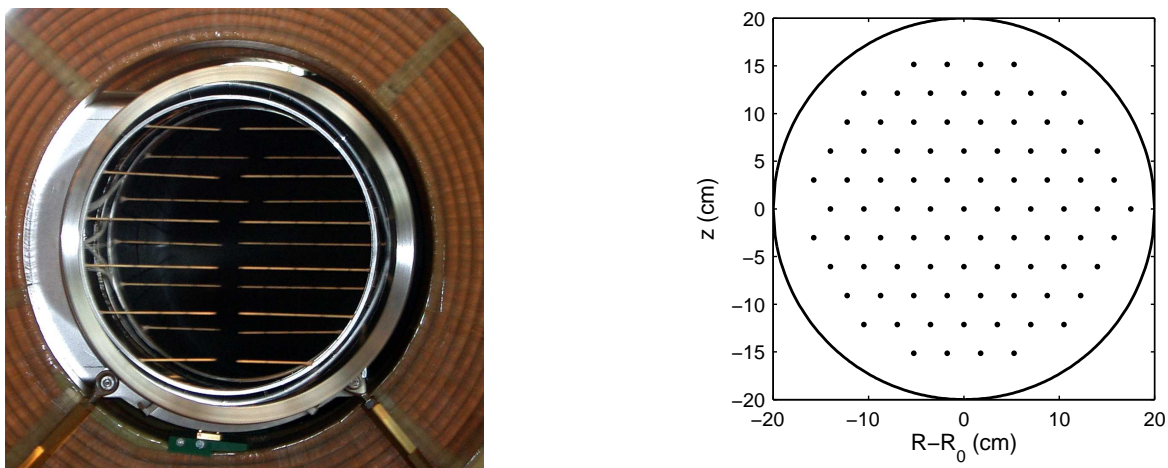


Figure 4.3: The HEXTIP array (left) and the position of the tips over the poloidal cross-section (right).

The **TWEEDY** array consists of 12 ring-shaped tips arranged in a 4×3 rectangular grid, with horizontal and vertical separation of 1 cm and 1.8 cm. TWEEDY is used to measure the background parameters between $R - R_0 = \pm 19$ cm, and the gradients of pressure and plasma potential at midplane along the radial and the vertical direction.

Both SLP and TWEEDY are usually connected to the standard LP modules. They can be therefore configured with tips to measure independently the floating potential or the ion saturation current. In the latter configuration they are routinely used to measure the wavenumber parallel to the magnetic field, as extensively described in Sec. 5.4.4.

4.4 LPs for the measurement of fluctuations

The set of probes commonly used for the measurement of fluctuations includes the HEXTIP array and three arrays of fixed LPs (hereafter FLP). A picture of the layout of these probes is given in Fig. 3.2. Contrary to the probes used for the measurement of the time-averaged parameters, this set of probes can only be used in floating potential configuration or biased at a constant voltage. This choice was dictated on one hand by the necessity of simplifying as possible the electronics for a large number of channels, 86 in the case of HEXTIP and 66 in the case of FLP. On the other hand, the current driven by 86 probes in sweeping configuration would have introduced a large perturbation of the charge equilibrium.

The **HEXTIP** (**HEX**agonal **TUR**bulence **IM**aging **PRO**be) array [34][46] consists of 86 ring-shaped tips, arranged in a hexagonal grid with a spatial resolution of 3.5 cm, maximizing the coverage of the poloidal cross-section (Fig. 4.3). HEXTIP can measure either the ion saturation current, I_{sat} , or the floating potential, ϕ_f . It is routinely used

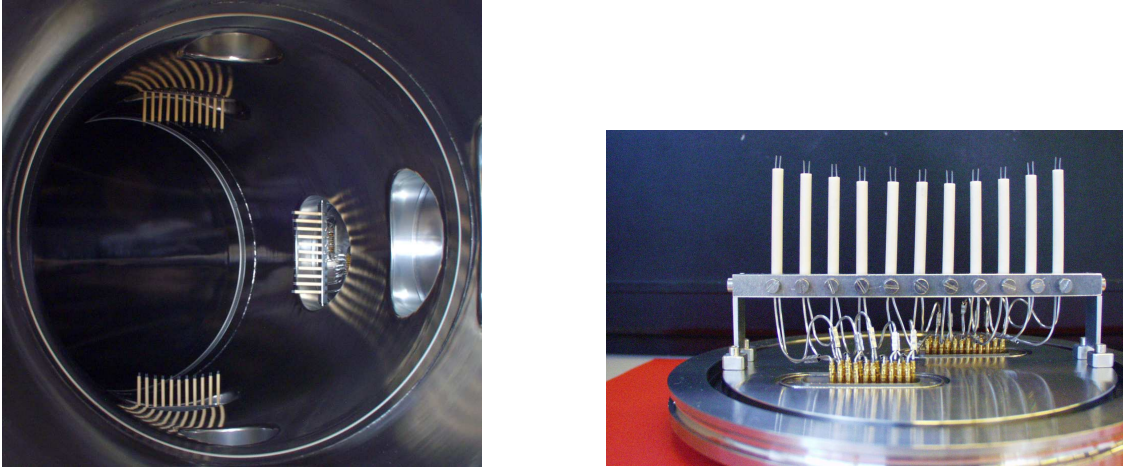


Figure 4.4: Left: the three FLP arrays installed in the vessel. Right: Particular of one of the arrays with the connections.

for a fast reconstruction of the density profiles from a single shot, *e.g.* during scans of the external control parameters. The main application of HEXTIP is for the statistical reconstruction of coherent structures in the density fluctuations [34][47]. In this Thesis it is used mainly to reconstruct the profile of the rms value of density and floating potential fluctuations in selected frequency ranges, as described in Sec. 5.3.

The three **FLP** arrays (see Fig. 4.4) measure the ion (or electron) saturation current (with bias at ± 50 V or ± 100 V) on the same poloidal cross-section. The geometry of these probes was planned before the first experimental campaign, when the background plasma profiles and the location of the maximum pressure gradient were still unknown. The existence of three ports on the same poloidal cross-section influenced the geometry of the probes (see App. C). The wavelength and the amplitude of fluctuations are measured along the azimuthal direction, at the same radial position, $r = (4.0 \pm 0.3)$ cm from the wall. Each array consists of eleven pairs of LPs, equally spaced by 1 cm. The separation between tips within the same pair is 0.13 cm, allowing the measurement of wavenumbers up to 24 cm^{-1} , corresponding to wavelengths longer than 0.3 cm.

THERMOCOAX[®] cables with external diameter of 1 mm have been employed to satisfy requirements of vacuum, thermal stress for the transmission of high frequency and low amplitude signals. The inner conductor (diameter of 0.4 mm) and the external jacket, both made of stainless-steel, are insulated with alumina. The drawback is that these cables are semi-rigid, with a large bending radius, and cannot easily be soldered. Specially designed connectors and feed-throughs are available on the market. Due to the large number of signals to be transmitted and to avoid technical complications due to the size and weight of the connectors, a low-cost solution was adopted, using the inner conductor as the probe tip and crimping the other head of the cable to a stainless-steel pin. Both the inner and the external conductor are then transmitted to the dedicated electronics, which provides the amplification of the probe signal, after the subtraction of the reference. Insulation and separation between adjacent probes is obtained by fitting

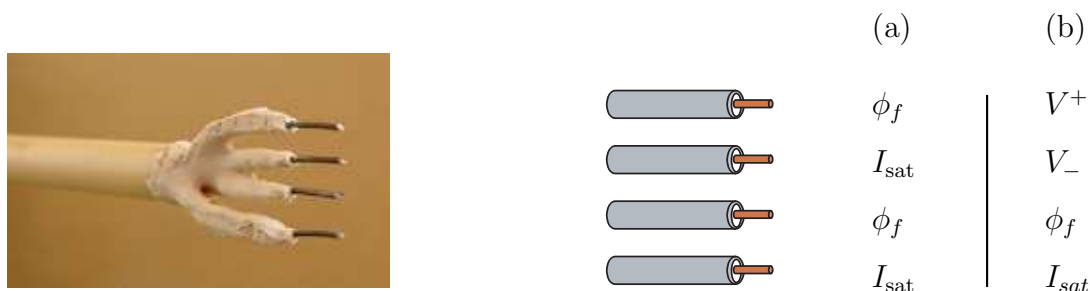


Figure 4.5: Left: Picture of the TRIP array. Right: Sketch of the configuration used for the measurement of the particle flux and of the dispersion relation (a) and for the measurement of temperature, density and plasma potential fluctuations (b).

the cables into ceramic tubes equipped with two 1 mm diameter holes. An electric circuit based on capacity coupling and low noise, low phase distortion amplification, has been designed to measure the fluctuating part of I_{sat} in the range [0.03,250] kHz. The frequency response in amplitude and phase for the different channels is reported in App. C.1.1.

The set of probes for the measurement of fluctuations is completed by a movable four-tip array (hereafter **TRIP**, **T**Ransport **P**robe) with vertical separation of approximately 0.25 cm, specifically designed for the measurement of the fluctuation-induced particle flux. As for the FLP arrays, each probe in the TRIP array is made of a THERMOCOAX[®] cable, one end of which is used as probe tip. Contrary to the FLP arrays, due to the limited number of channels for the TRIP array, special connectors and feed-throughs have been adopted.

The TRIP array can be used in two different configurations, both represented in Fig. 4.5. The configuration indicated as (a) is routinely used to measure the particle flux [48] and the dispersion relation associated with \tilde{n} and $\tilde{\phi}_f$. The configuration indicated as (b) allows the measurement of the electron temperature and of the electrostatic plasma potential fluctuations [49][50] (see App. E). The TRIP array is mounted on the third remotely-controlled positioning system. A prototype of a more sophisticated 2D positioning system has recently been installed on TORPEX and used to positioning a Rogowski coil [51]. The probe shaft is mounted on a sphere, capable to rotate around a horizontal axis passing through the center. Combining the sliding of the probe and the rotation of the joint, almost the whole plasma cross-section can be covered. A safety margin of approximately 4 cm, to prevent the probe hitting the wall, is provided by a mechanical control system, external to the vessel. The importance of a complete coverage of the poloidal cross-section is illustrated in the following section, where some examples of time-average profiles measured on TORPEX are given.

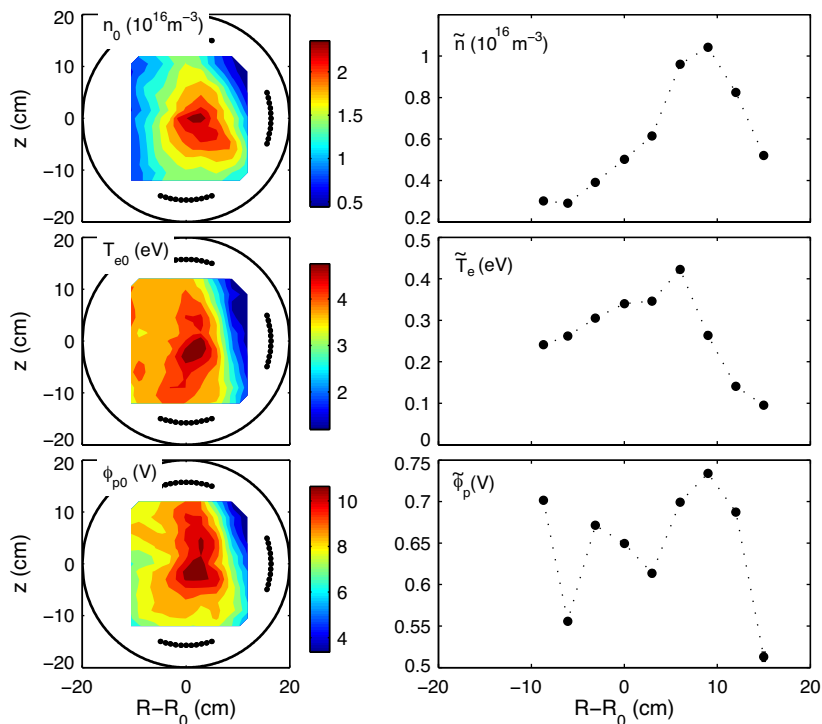


Figure 4.6: Left: time-averaged profiles of density, temperature and plasma potential, measured in a Hydrogen plasma from the $I - V$ curve of SLP, during a stationary discharge of 300 ms, with constant absorbed microwave power of 400 W. The neutral gas pressure is $p_0 = 6 \times 10^{-5}$ mbar, the toroidal and vertical magnetic field are respectively $B_\varphi = 76.6$ mT on axis and $B_z = 0.6$ mT. Right: radial profile at the midplane of density, temperature and electrostatic potential fluctuations, measured with the TRIP array configured as in Fig. 4.5b.

4.5 Typical parameters of TORPEX plasmas.

Experiments on plasmas produced from Hydrogen, Helium and Argon gases have been conducted on TORPEX, for different values of neutral gas pressure, injected microwave power, and vertical magnetic field. Typical values for density, electron and ion temperatures, and plasma potential are $n_{i0} \simeq n_{e0} = n_0 \simeq 10^{16} - 10^{17} \text{ m}^{-3}$, $T_{e0} \lesssim 5 \text{ eV}$, $T_{i0} \lesssim 0.1 \text{ eV}$, $\phi_{p0} \simeq 10 - 20 \text{ V}$. The upper limit to T_{i0} was obtained from spectroscopic measurements in Argon and Hydrogen plasmas.

While we can talk about typical values of the plasma parameters on TORPEX, we cannot define a *typical profile*. The profile of the bulk plasma over the poloidal cross-section depends in fact on the external control parameters, in particular the absorbed microwave power and the magnetic field configuration. Their effect on the time-averaged profiles and on the spectral properties of fluctuations will be discussed in detail in Chap. 7. The examples presented in this Section are intended to show what information can be extracted from the various diagnostics. Figure 4.6 shows the time-averaged profiles of density, temperature and plasma potential, measured with the

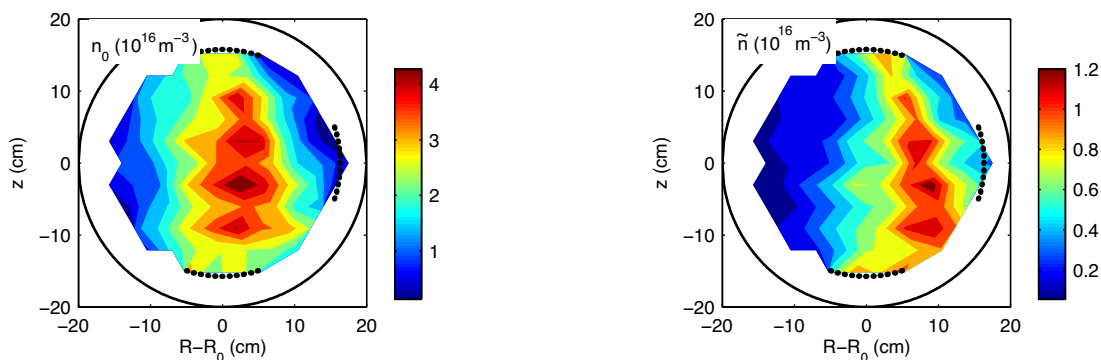


Figure 4.7: Profile of the time-averaged value (left) and the standard deviation (right) of I_{sat} , measured with HEXTIP in a plasma with the same magnetic field and neutral gas pressure as in Fig. 4.6. The black dots indicate the position of the FLP arrays.

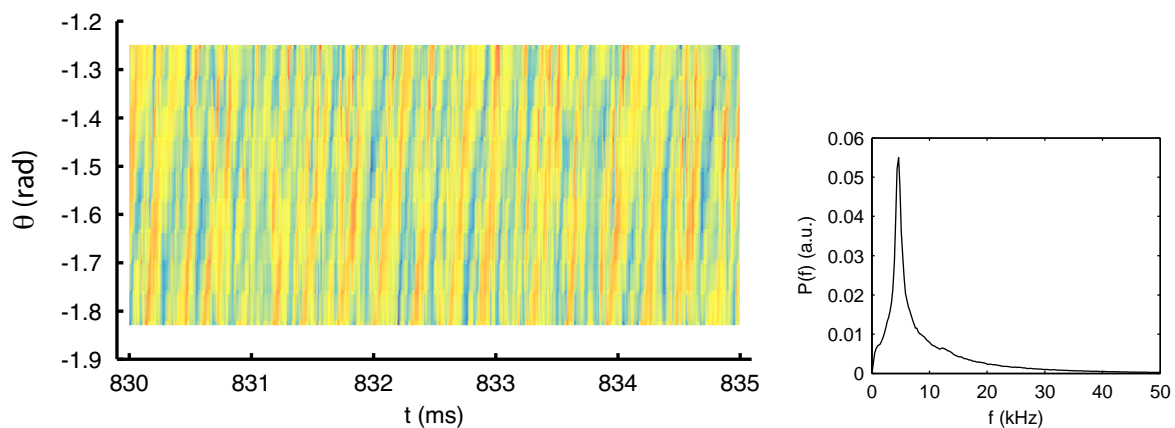


Figure 4.8: Left: Space-time evolution of the fluctuating part of I_{sat} , measured at the bottom of the plasma cross-section with one of the FLP arrays. Right: power spectrum of density fluctuations, measured from the time trace of I_{sat} at $\theta = -1.3$ rad (see figure on the left).

SLP array in a Hydrogen plasma, at neutral gas pressure $p_0 = 6 \times 10^{-5}$ mbar and with a constant absorbed microwave power of 400 W. The toroidal field is $B_\phi = 76.6$ mT on axis, and the vertical field $B_z = 0.6$ mT. It is worth noting that this is a particular case, chosen for the symmetry of the profiles; it will be analyzed in detail in Chap. 8 for a complete characterization of drift-interchange instabilities in Hydrogen plasmas.

The time-averaged profiles are centered with respect to the poloidal cross-section and density fluctuations peak on the low field side with respect to the maximum of n_0 . Temperature fluctuations are below 10% of maximum T_{e0} , while density fluctuations can reach 80% of the background density level. The profile of the background and the fluctuating part of the density, measured from HEXTIP in the same plasma, is shown in Fig. 4.7. The density profile is estimated from the average value of the time trace of I_{sat} , calculated over the whole discharge duration, assuming a uniform electron temperature

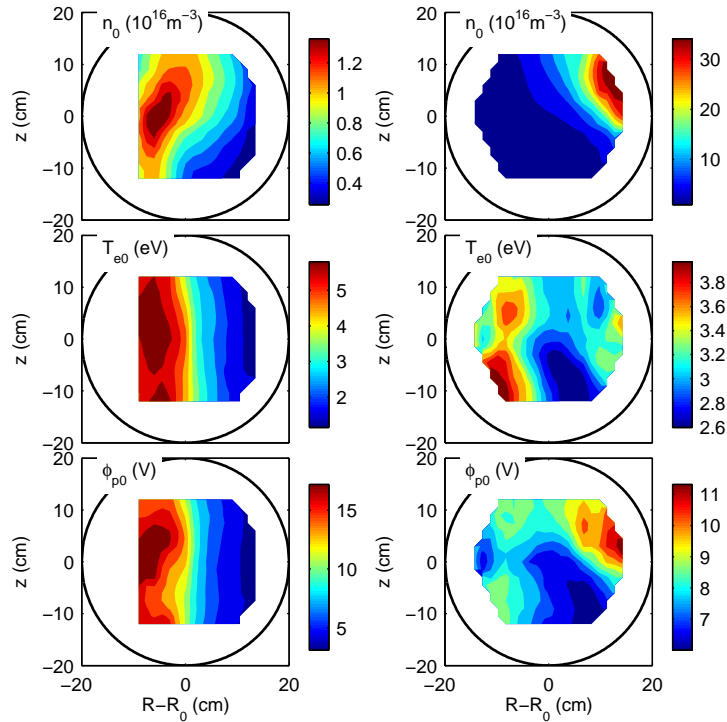


Figure 4.9: Left: time-averaged profiles of density, temperature and plasma potential, measured in a Hydrogen plasma with $p_0 = 3.5 \times 10^{-5}$ mbar, 400 W of absorbed microwave power, $B_\varphi = 76.6$ mT and $B_z = 2.3$ mT. Right: time-averaged profiles of density, temperature and plasma potential, measured in an Argon plasma with $p_0 = 2.5 \times 10^{-5}$ mbar, $B_z = 0.2$ mT and 6 kW of absorbed microwave power.

of 5 eV. The profiles are qualitatively similar, with differences in the density amplitude that can vary between 15% on the high field side, where the temperature is constant, and 70% on the low field side, where the temperature gradient is large. The profile of density fluctuations is estimated from the standard deviation of I_{sat} , neglecting the contribution of temperature fluctuations. The error done in neglecting temperature fluctuations is discussed more in detail in App. E.

Figure 4.8 shows the time traces of the fluctuations of I_{sat} , measured at the bottom of the plasma cross-section with one of the FLP arrays. The oblique stripes indicate the presence of coherent density fluctuations propagating along the azimuthal direction. A frequency of approximately 3.3 kHz can be estimated from the time separation between adjacent stripes, and an average propagation velocity of approximately 800 m/s from the ratio of the poloidal displacement to the time delay for a single stripe. The power spectrum of density fluctuations is peaked at 4 kHz, consistently with what observed in the space-time domain.

We conclude this Chapter presenting two cases of plasma parameter profiles that do not satisfy the symmetry properties, shown in Fig. 4.9. The first example refers to a slab-like Hydrogen plasma, with the same injected power and the same value of B_φ as in Fig. 4.6, but with $B_z = 2.3$ mT. No azimuthal propagation can be predicted in this

case from the time-average profiles and the FLP arrays provide only information about the plasma edge condition, but cannot be used to infer information on the fluctuation dispersion relation. In this case, the pressure gradient is mainly along R , therefore the TRIP array can be used to measure the radial profile of the dispersion relation $k_z(\omega)$ at midplane.

The second example refers to a plasma from Argon and it has been chosen to emphasize the importance of an extended coverage of the poloidal cross-section. The injected power is in this case approximately 6 kW, thus the maximum of the density is shifted toward the low field side because of the dependence of the position of the upper hybrid resonance on the density [42]. The upward shift is due to the value of the vertical magnetic field, $B_z = 0.2$ mT, a factor five lower than the optimal value for the confinement time estimated for Argon [37]. It is clear from the figure that in this case neither the FLP nor the TRIP array can be used to infer the dispersion relation, because no measurements are available at the location where the pressure gradient is maximum. The power spectra of density and potential fluctuations can be measured with the HEXTIP array, but the large separation between tips and the phase distortion for frequency larger than 10 kHz, prevent the measurement of the wavenumber. The use of a mechanical system with large spatial coverage is in this case the most appropriate solution.

Chapter 5

Measurement of the linear properties of fluctuations

The analysis of plasma fluctuations is traditionally based on Fourier spectral analysis [48], which considers fluctuating quantities as the superposition of statistically independent modes. In a stationary, infinite, homogeneous and isotropic medium, they can be described as simple plane waves, $Ae^{i(\mathbf{k}\cdot\mathbf{r}-\omega t)}$, oscillating at frequency ω , with constant amplitude A and wavenumber $k = N\omega/c$, where N is the index of refraction of the medium along the direction of propagation. In a weakly inhomogeneous plasma, fluctuations - *e.g.* in the density - can still be represented as superposition of plane waves with a slowly varying amplitude $|n(\mathbf{k}, \omega)|$, where the coefficients $n(\mathbf{k}, \omega)$ are defined by the **Fourier transform**:¹

$$n(\mathbf{k}, \omega) = \iiint \tilde{n}(\mathbf{r}, t) e^{-i(\mathbf{k}\cdot\mathbf{r}-\omega t)} d\mathbf{r} dt \quad (5.1)$$

Space-frequency representation

As time and space are decoupled, it is possible to consider separately fluctuations in frequency or in wavenumber. Representation in the \mathbf{k} -space only is commonly used in theoretical models, but is impractical in experiments, because the estimate of the Fourier coefficients $n(\mathbf{k}, t)$ requires measurements at a large number of grid points. As time sequences are easier to obtain, the frequency representation is more practical and

¹ The notation used in MATLAB[®] routines is consistent with the notation most common among engineers:

$$f(\mathbf{r}, t) = \iiint F(\mathbf{k}, \omega) e^{i(\mathbf{k}\cdot\mathbf{r}+\omega t)} \frac{d\mathbf{k}}{(2\pi)^3} \frac{d\omega}{2\pi}$$
$$F(\mathbf{k}, \omega) = \iiint f(\mathbf{r}, t) e^{-i(\mathbf{k}\cdot\mathbf{r}+\omega t)} d\mathbf{r} dt$$

where the complex term $e^{\pm i(\mathbf{k}\cdot\mathbf{r}+\omega t)}$ represents a wave travelling in the negative \mathbf{k} direction. The difference with the notation adopted in this Thesis, dominant among physicists, is a complex conjugate $e^{i\omega t}$. The output of the MATLAB[®] FFT (Fast Fourier Transform) algorithms in the time domain should be transformed accordingly.

widely used. A frequency representation will be adopted in the rest of this Thesis:

$$\tilde{n}(\mathbf{r}, t) = \sum_{\omega} n_{\omega}(\mathbf{r}) e^{-i\omega t} \quad (5.2a)$$

$$n_{\omega}(\mathbf{r}) = |n_{\omega}(\mathbf{r})| e^{i\theta_{\omega}(\mathbf{r})} \quad (5.2b)$$

where $n_{\omega}(\mathbf{r})$ are the discrete Fourier coefficients of the time series measured at position \mathbf{r} , with amplitude $|n_{\omega}(\mathbf{r})|$ and phase $e^{i\theta_{\omega}(\mathbf{r})}$. The sum is over discrete frequencies $\omega \equiv \omega_m$ defined as $\omega_m = m\pi(N\delta t)^{-1}$, where $m = \{1, \dots, N\}$ and δt is the time resolution. If all spectral components of interest have frequency below the Nyquist frequency ω_N , then the discrete, finite representation, Eq. (5.2), is a good approximation of the continuous spectrum of fluctuations.

5.1 Stationary and homogeneous processes

Fluctuations in a plasma depend on space and time. Let $n(\mathbf{r}, t)$ and $n(\mathbf{r}', t')$ denote the density measured at different positions \mathbf{r}, \mathbf{r}' and times t, t' . A random process is said to be **stationary** if time-averaged quantities, such as the average value or the correlation function, are invariant to translations in time, but depend only on the time separation, *i.e.*:

$$n_0(\mathbf{r}) = \lim_{T \rightarrow \infty} \frac{1}{T} \int_{T_0}^{T_0+T} n(\mathbf{r}, t) dt \quad (5.3a)$$

$$R(\mathbf{r}, \mathbf{r}', \tau) = \lim_{T \rightarrow \infty} \frac{1}{T} \int_{T_0}^{T_0+T} n^*(\mathbf{r}, t) n(\mathbf{r}', t + \tau) dt \quad (5.3b)$$

are independent of T_0 . Note that these averages still depend on the position.

Similarly, a random process is said to be **homogeneous** if the space averaged value and the correlation function in space do not depend on position, but only on the spatial separation $\xi = \mathbf{r} - \mathbf{r}'$:

$$n_0(t) = \lim_{V \rightarrow \infty} \frac{1}{V} \int_V n(\mathbf{r}, t) d\mathbf{r} \quad (5.4a)$$

$$\mathcal{R}(\xi, t, t') = \lim_{V \rightarrow \infty} \frac{1}{V} \int_V n^*(\mathbf{r}, t) n(\mathbf{r} + \xi, t') d\mathbf{r} \quad (5.4b)$$

5.2 Measurement of fluctuations rms

Stationarity is satisfied in all the experiments presented in this Thesis. Physical quantities will therefore be represented as the superposition of a time invariant and a fluctuating component, $n(\mathbf{r}, t) = n_0(\mathbf{r}) + \tilde{n}(\mathbf{r}, t)$. The former corresponds to an average value:

$$n_0(\mathbf{r}) = \lim_{T \rightarrow \infty} \frac{1}{T} \int_0^T n(\mathbf{r}, t) dt,$$

while the significance of the fluctuating part can be described by the variance:

$$\langle |\tilde{n}(\mathbf{r}, t)|^2 \rangle = \lim_{T \rightarrow \infty} \frac{1}{T} \int_0^T [n(\mathbf{r}, t) - n_0(\mathbf{r})]^2 dt$$

Using the Parseval theorem, the rms value of fluctuations can be estimated from the power spectrum, after removal of the time-averaged value: ²

$$\langle |\tilde{n}(\mathbf{r}, t)|^2 \rangle = \frac{1}{2\pi} \int_{-\infty}^{+\infty} P(\mathbf{r}, \omega) d\omega \quad (5.5)$$

where

$$P(\mathbf{r}, \omega) = \lim_{T \rightarrow \infty} \frac{1}{T} n^*(\mathbf{r}, \omega) n(\mathbf{r}, \omega) \quad (5.6)$$

is the power spectrum. For discrete signals and for a large number M of identical realizations of the same physical quantity, the power spectrum is calculated as the ensemble averaging:

$$P(\omega) = \langle n_\omega(\mathbf{r}) n_\omega^*(\mathbf{r}) \rangle = \frac{1}{M} \sum_{j=1}^M n_\omega^{(j)}(\mathbf{r}) n_\omega^{*(j)}(\mathbf{r}) \quad (5.7)$$

where we have dropped the explicit dependence on \mathbf{r} . It follows from Eq. (5.5), that, if one or more modes at frequencies ω_m are present in the power spectrum, the rms value of fluctuations associated with individual modes can be calculated from the area under the peak as [48]:

$$\langle |n_{\omega_m}|^2 \rangle = P(\omega_m) \Delta\omega_m \quad (5.8)$$

If the peak is fitted by a gaussian curve of width σ_ω centered at ω_m , $P(\omega_m)$ is the height of the curve at ω_m and $\Delta\omega_m = \sigma_\omega$.

5.2.1 Measurement of density fluctuations

Density fluctuations are estimated from the fluctuating part of the ion saturation current, Eq. (4.3), assuming constant electron temperature:

$$\tilde{n} \approx \frac{2}{eA} \sqrt{\frac{T_{e0}}{M}} \tilde{I}_{\text{sat}} = n_0 \frac{\tilde{I}_{\text{sat}}}{I_0} \quad (5.9)$$

² The power spectrum of a stationary signal of mean value $n_0(\mathbf{r})$ is given by a delta function of strength $2\pi|n_0(\mathbf{r})|^2$ positioned at $\omega = 0$ superposed to the power spectrum of the fluctuating part. This can be easily proved [52] calculating the correlation function of $n(\mathbf{r}, t) = n_0(\mathbf{r}) + \tilde{n}(\mathbf{r}, t)$:

$$R_n(\mathbf{r}, \tau) = \lim_{T \rightarrow \infty} \frac{1}{T} \int_{-T/2}^{T/2} [n_0(\mathbf{r}) + \tilde{n}(\mathbf{r}, t)] [n_0(\mathbf{r})^* + \tilde{n}(\mathbf{r}, t + \tau)^*] dt = n_0^2(\mathbf{r}) + R_{\tilde{n}}(\mathbf{r}, \tau)$$

The Fourier transform gives then:

$$P_n(\mathbf{r}, \omega) = 2\pi n_0(\mathbf{r})^2 \delta(\omega) + P_{\tilde{n}}(\mathbf{r}, \omega)$$

The contribution of the time-independent component is a constant value and can be recovered at any time. The symbol ‘ \sim ’ will be therefore dropped in the following when referring to fluctuations represented in the Fourier domain.

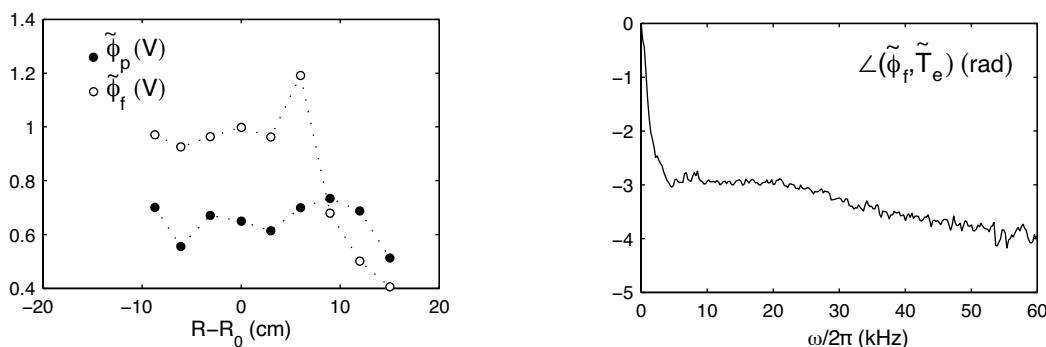


Figure 5.1: Left: Radial profile of $\tilde{\phi}_f$ and $\tilde{\phi}_p$ measured at midplane. Right: Phase shift between $\tilde{\phi}_f$ and \tilde{T}_e measured at midplane, at $R - R_0 = 6$ cm. The time-averaged profiles of n_0 , T_{e0} and ϕ_{p0} are shown in Fig. 4.6.

The corrections to the power spectrum of \tilde{n} due to \tilde{T}_e are negligible, as discussed in App. E.2. The power spectrum of density fluctuations is therefore approximated with the power spectrum of \tilde{I}_{sat} .

5.2.2 Measurement of electrostatic potential fluctuations

Plasma potential fluctuations are measured from temperature and floating potential fluctuations as:

$$\tilde{\phi}_p = \tilde{\phi}_f + \mu \frac{\tilde{T}_e}{e} \quad (5.10)$$

where $\tilde{\phi}_f$ and $\tilde{\phi}_p$ indicate respectively the fluctuating part of the floating and of the plasma potential. The power spectrum of $\tilde{\phi}_p$ is related to that of \tilde{T}_e and $\tilde{\phi}_f$ by:

$$P_{\phi_p} = P_{\phi_f} + \frac{\mu^2}{e^2} P_{T_e} + 2 \frac{\mu}{e} \Re [\langle \phi_{f,\omega}^* T_{e,\omega} \rangle]. \quad (5.11)$$

The amplitude of P_{ϕ_p} depends not only on the amplitude of P_{T_e} and P_{ϕ_f} , but also on the sign of the phase between $\tilde{\phi}_f$ and \tilde{T}_e . To illustrate this, Fig. 5.1 shows the radial profile of potential fluctuations measured at midplane, in a plasma from Hydrogen, with $B_\varphi = 76.6$ mT and $B_z = 0.6$ mT (see Fig. 4.6). In this example the difference between $\tilde{\phi}_f$ and $\tilde{\phi}_p$ is approximately a factor two, with $\tilde{\phi}_p < \tilde{\phi}_f$ because of the negative value of the phase shift $\angle(\tilde{\phi}_f, \tilde{T}_e)$.

5.2.3 Measurement of the phase between \tilde{n} and $\tilde{\phi}_p$

The measurement of the phase shift between density and potential fluctuations is important for the estimate of the fluctuation induced particle flux. Moreover it is commonly used as a parameter for the identification of the nature of the instabilities. Under the hypothesis that electrons are adiabatic, the phase should be zero for collisionless plasmas, as results from Eq. (2.1) written in the Fourier space. Non-adiabatic

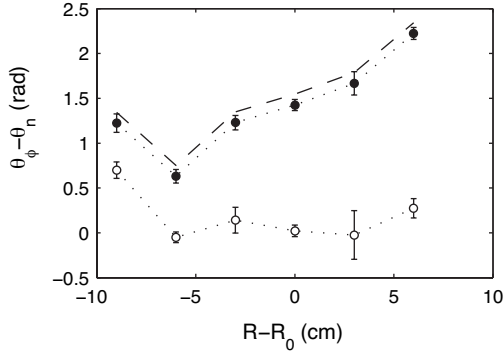


Figure 5.2: Phase shift between density and potential fluctuations, calculated between \tilde{n} and $\tilde{\phi}_f$ (open circles) and between \tilde{n} and $\tilde{\phi}_p$ (black circles). The dashed line represents the additional correction to $\theta_{\phi_p} - \theta_n$ given by the tip separation, assumed to be constant over R . Plasma parameters are the same as in Fig. 5.1.

electrons, as well as the presence of collisions, alter this value, cfr Eq. (2.3). The phase shift between density and potential fluctuations is calculated from the argument of the cross spectrum between \tilde{n} and $\tilde{\phi}_p$:

$$P_{n\phi_p} = P_{n\phi_f} + \frac{\mu}{e} [\langle n_{\omega}^* T_{e,\omega} \rangle] \quad (5.12)$$

where we have used Eq. (5.10). If $\tilde{T}_e = 0$, the phase shift can be measured from the floating potential fluctuations, but in general temperature fluctuations should be taken into account. Beside the error done by neglecting the effect of \tilde{T}_e , another source of error is represented by the finite separation between tips that measure \tilde{I}_{sat} and $\tilde{\phi}_p$ (or $\tilde{\phi}_f$). Both of these effects, discussed in App. E, are taken into account whenever the measurements of \tilde{T}_e are available. Figure 5.2 shows an example of the effect of temperature fluctuations on the measurement of the phase shift between density and plasma potential for the same case as in Fig. 5.1.

5.3 Reconstruction of the 2D profile of fluctuations rms

As it will be discussed in Chap. 7, instabilities are generated in TORPEX at specific locations over the plasma cross-section, depending on the local value of the background profiles of plasma pressure and electric field. As discussed in Sec. 2, drift waves are associated with gradients in the background pressure profile. We expect to measure the maximum amplitude of fluctuations at the location of maximum $\nabla(n_0 T_{e0})$, corresponding to the location of the maximum linear drive. Interchange modes are driven where the pressure gradient is co-linear with the magnetic field gradient. Their amplitude will therefore be maximum in the region of unfavourable curvature, where they are most (linearly) unstable.

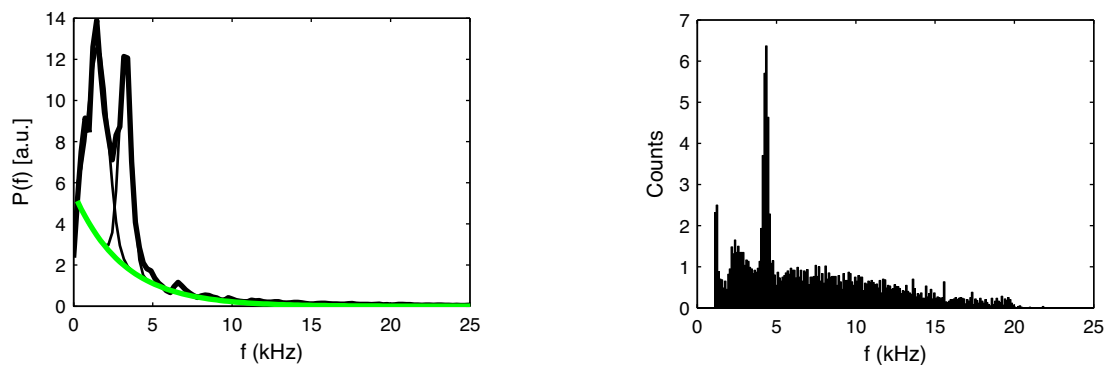


Figure 5.3: Left: Measured power spectrum (thick black) for an Hydrogen plasma, with the fitted exponential background (thick green) and the gaussian fit of the two dominant peaks (thin black). Right: Histogram of the central frequency of each fitted peak, independently on the amplitude and width of the peaks.

The identification of the location where individual modes are generated is therefore the first step to identify the mechanism that has driven the instabilities. The distribution of mode amplitudes over the plasma cross-section is reconstructed from the HEXTIP array on a statistical basis, using a semi-automatic method. First, the power spectrum of density and floating potential fluctuations is estimated from \tilde{I}_{sat} and $\tilde{\phi}_f$, at each position $(R - R_0, z)$ covered by the array. The power spectrum is then decomposed into a monotonic background and a discrete series of coherent components at frequencies f_j . After the subtraction of the background, which is generally well fitted by an exponentially decreasing function of frequency, coherent components of the residual spectrum appear. These are recursively fitted with a gaussian function to determine frequency, height and width of each peak, starting from the mode with the largest amplitude and retaining only those modes whose amplitude is larger than a chosen fraction of the background level ³.

An example of the fitting procedure is shown in Fig. 5.3 for an experimental situation with a low degree of turbulence. The exercise is repeated over a number of identical discharges to increase statistics. For sufficiently long discharges, because of the stationarity, more sub-samples can be extracted from the same discharge. After fitting the power spectrum measured over the whole poloidal cross-section, the histogram of the central frequency of each peak can be used to separate frequency ranges, as shown in Fig. 5.3. The histogram is normalized to the number of shots used for the estimate, thus it represents the average number of counts per shot, *i.e.* it indicates how many times a peak with frequency in the range $f \pm \Delta f/2$ (Δf is the bin length) is measured, on average, in one shot.

The histogram contains global information for all positions, independently on the amplitude and on the width of peaks in the power spectrum. Nevertheless, it contains useful information on the measured power spectrum. For example, in Fig. 5.3

³The choice of the threshold depends on the number of modes present in the power spectrum and on the degree of turbulence. A level of 10% to 30% is in most cases chosen to discard most of spurious contributions coming from the higher frequencies.

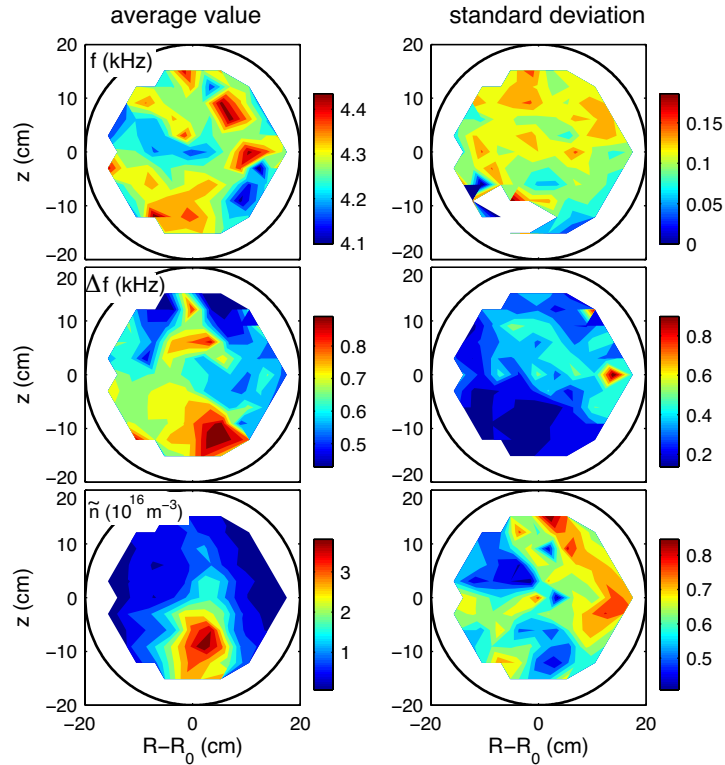


Figure 5.4: Left: Example of the reconstruction of the profile of the average frequency, spectral width and amplitude of peaks measured in the power spectrum. Profiles refer to density fluctuations with frequency in the range [4.5,5.5] kHz. Right: standard deviation from the average value, same units.

the maximum number of counts is measured around 5 kHz, with a low dispersion in frequency, indicating that a mode at this frequency dominates the power spectrum of \tilde{n} . After selecting the range of frequency from the histogram, the average value of the fluctuations rms in that frequency range, measured at each position, is calculated from all the shots.

Figure 5.4 shows the reconstruction of fluctuations with frequency in the range [4.5, 5.5] kHz. The region of the plasma cross-section where the mode has its maximum amplitude is quite localized and is referred to as ‘source’. A comparison with the background profiles at the same location provides then an indication of the driving mechanism. The plasma parameters at this location should be used as inputs for numerical codes with which to compare the measured dispersion relation.

As shown in Fig. 5.4(c), the region where the mode has its maximum amplitude has a spatial extension between 7 and 10 cm, where the uncertainty is given by the spatial resolution of HEX TIP, 3.5 cm. Over this region the deviation around the mean value of amplitude is minimum ($\simeq 40\%$), while the width of the peak is 0.9 kHz. The apparent decreasing of the peak width, measured away from the source region, is mainly an artifact of the automatic fitting procedure. Broad peaks with low amplitude are in fact detected as sharp peaks with close frequencies.

5.4 Measurement of the dispersion relation

The dispersion relation is a way for characterizing the space-time nature of a wave. Let's assume, for the time being, that nonlinear interactions are negligible, and that the background pressure profiles have a gradient along R ; the resulting drifts are therefore along z ⁴. Using the polar representation, Eq. (5.2b), the space variation of $n_\omega(\mathbf{r})$ along z is given by the derivative:

$$\frac{\partial n_\omega(z)}{\partial z} = \left[\frac{1}{|n_\omega(z)|} \frac{\partial |n_\omega(z)|}{\partial z} + i \frac{\partial \theta_\omega(z)}{\partial z} \right] n_\omega(z). \quad (5.13)$$

The first term, which represents the relative amplitude variation, is related to the growth (damping) of the wave, while the second, which represents the phase variation, is related to its dispersion:

$$k_z(\omega) \equiv \frac{\partial}{\partial z} \theta_\omega(z)$$

If the medium is homogeneous along z , the wavenumber is constant in space and the measured phase shift depends only on the probe separation d_{tip} , $k_\omega = \Delta\theta_\omega/d_{\text{tip}}$. If $n_{1,\omega}$ and $n_{2,\omega}$ denote the Fourier components of density fluctuations measured at position z_1 and $z_2 = z_1 + d_{\text{tip}}$, the dispersion relation along z , $k_z(\omega)$, can then be estimated from the argument of their cross-spectrum $\langle n_{2,\omega} n_{1,\omega}^* \rangle$:

$$k_z(\omega) = \frac{1}{d_{\text{tip}}} \arg \langle n_{2,\omega} n_{1,\omega}^* \rangle \quad (5.14)$$

where

$$\arg \langle n_{2,\omega} n_{1,\omega}^* \rangle = \arctan \left(\frac{\Im \langle n_{2,\omega} n_{1,\omega}^* \rangle}{\Re \langle n_{2,\omega} n_{1,\omega}^* \rangle} \right).$$

Here \Re and \Im denote the real and imaginary part of the cross-spectrum. If d_{tip} is sufficiently small that the variation of the amplitude and the phase is negligible over the probe separation, the medium can be considered homogeneous and Eq. (5.14) be used to calculate the dispersion relation. In general d_{tip} should be kept smaller than the correlation length. Another condition, which will be discussed more in detail in Sec. 6.4 is that the variation of the amplitude and phase due to nonlinear interactions is negligible over d_{tip} . These conditions are cast in the so-called *wave packet* assumptions [53]:

$$\left| \frac{1}{|n_\omega(z)|} \frac{\partial^m |n_\omega(z)|}{\partial z^m} \right| \ll |k_z^m(\omega)|, \quad (5.15a)$$

$$\left| \frac{1}{k_z(\omega)} \frac{\partial^m k_z(\omega)}{\partial z^m} \right| \ll |k_z^m(\omega)|. \quad (5.15b)$$

⁴This hypothesis is valid in general. In most experimental situations and in all the cases analyzed in this Thesis, the pressure gradient and the electric field are at midplane along R . The dispersion relation $k_z(\omega)$ is therefore routinely measured at midplane using two probes separated along z (usually the TRIP array). Without loss of generality, z is the direction of propagation. In some cases the dispersion relation is measured with the FLP arrays along the azimuthal direction. When this is the case, the direction of measurement will be specified.

The dispersion relation, calculated in this way, does not account for the broadening of the power spectrum $P(k, \omega)$ in the wavenumber space. If a coherent mode is present in the plasma, the power spectrum is peaked at the frequency and at the wavenumber of the mode and the power spectrum can be easily recovered from the frequency spectrum as ⁵:

$$P(k_z, \omega) = P(\omega)\delta[k_z - k_z(\omega)] \quad (5.16)$$

In a weakly turbulent medium, the power spectrum can be peaked in ω , but broad in k_z . In this case, corresponding to most experimental scenarios investigated in this Thesis work, the power spectrum $P(k_z, \omega)$ can be statistically reconstructed from two-point measurements [53] as described in the following section.

5.4.1 Estimate of $P(k_z, \omega)$

If a large number of independent realizations of the same physical process are available, the power spectrum $P(k_z, \omega)$ can be reconstructed using the discrete representation of Eq. (5.16):

$$P(k_z, \omega) = \frac{1}{M} \sum_{j=1}^M I_{\Delta k_z}[k_z - k_z^{(j)}(\omega)] \frac{1}{2} [P_1^{(j)}(\omega) + P_2^{(j)}(\omega)], \quad (5.17)$$

where $P(\omega)$ in Eq. (5.16) is replaced by the mean of the power spectra measured at z_1 and z_2 , and the wavenumber $k_z^{(j)}(\omega)$ is calculated for each sample from the argument of the cross-spectrum, Eq. (5.14).

$$k_z^{(j)}(\omega) = \frac{1}{d_{\text{tip}}} \arg [n_{2,\omega}^{(j)} n_{1,\omega}^{(j)*}] \quad (5.18)$$

The indicator function $I_{\Delta k_z}$, the discrete equivalent of the delta function, is defined as:

$$I_{\Delta k_z}[k_z - k_z^{(j)}(\omega)] = \begin{cases} 1 & k_z \leq k_z^{(j)}(\omega) < k_z + \Delta k_z \\ 0 & \text{elsewhere.} \end{cases} \quad (5.19)$$

$P(k_z, \omega)$ is estimated from two probes with mutual separation d_{tip} , using the method described in Ref. [53]. The bin width Δk_z is chosen to minimize the variance of the estimate. The tip separation must be small enough that $k_{z,\text{max}} = \pi/d_{\text{tip}}$ is larger than the maximum wavenumber associated with spectral components of interest, to avoid aliasing in the measured wavenumbers.

The time sequences from each probe are divided into M samples of length $T = N\delta t$, with a 50% overlapping, where δt is the sampling time and N the number of points in each sample. The sample length T is chosen such that the frequency resolution

⁵ As the wavenumber k_ω is measured with two probes aligned along a particular direction, $P(k, \omega)$ defined in this way is one-dimensional. This definition is consistent with the linearity of the Fourier Transform operator:

$$P(k_z, \omega) = \int dk_x dk_y P(k_x, k_y, k_z, \omega)$$

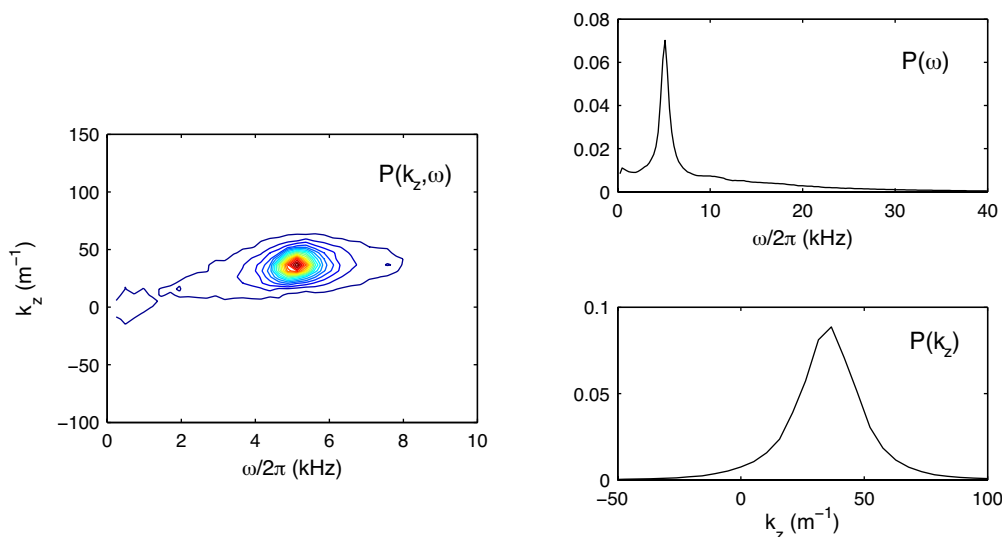


Figure 5.5: Wavenumber and frequency power spectrum $P(k_z, \omega)$, frequency spectrum $P(\omega)$ and wavenumber spectrum $P(k_z)$, calculated from $P(k_z, \omega)$ by summing respectively over k_z or over ω .

$\delta\omega = \pi/T$ is small enough to resolve the spectral components of interest. For each sample j the Fourier coefficients $n_{1,\omega}^{(j)}$ and $n_{2,\omega}^{(j)}$ are estimated using the Fast Fourier Transform (FFT) algorithm.

For a fixed frequency ω , the final power spectrum $P(k_z, \omega)$ is peaked at the most probable wavenumber k_0 . An example of the reconstruction of $P(k_z, \omega)$ is shown in Fig. 5.5 for an experimental situation where a coherent mode at 5 kHz is measured in the power spectrum. The wavenumber spectrum $P(k_z)$ is calculated from $P(k_z, \omega)$ by summing over frequencies. The value of k_z and its spectral width σ_{k_z} are estimated from a fit of $P(k_z)$ with a gaussian function, respectively as the central value and the FWHM. The inverse of the spectral width, $\sigma_{k_z}^{-1}$, provides an estimate of the correlation length along z . It is common to indicate as *weakly turbulent* those spectra with $\sigma_{k_z} \lesssim k_z$ and as *strongly turbulent* those with $\sigma_{k_z} > k_z$.

5.4.2 Statistical dispersion relation

A statistical estimate of the dispersion relation, which takes into account the broadening of the spectrum in the wavenumber space, was proposed by Iwama and Tsukishima [54]. They introduced the concept of conditional wavenumber-frequency spectrum $p(k_z|\omega)$ whose discrete representation is [53][55]:⁶

$$p(k_z|\omega) = \frac{P(k_z, \omega)}{\sum_{k_z} P(k_z, \omega)}. \quad (5.20)$$

⁶ The exact definition of the conditional spectrum is in terms of the normalized power spectrum $p(k, \omega)$:

$$p(k|\omega) = \frac{p(k, \omega)}{\int dk p(k, \omega)} \quad \text{with} \quad p(k, \omega) = \frac{P(k, \omega)}{\iint dk d\omega P(k, \omega)}$$

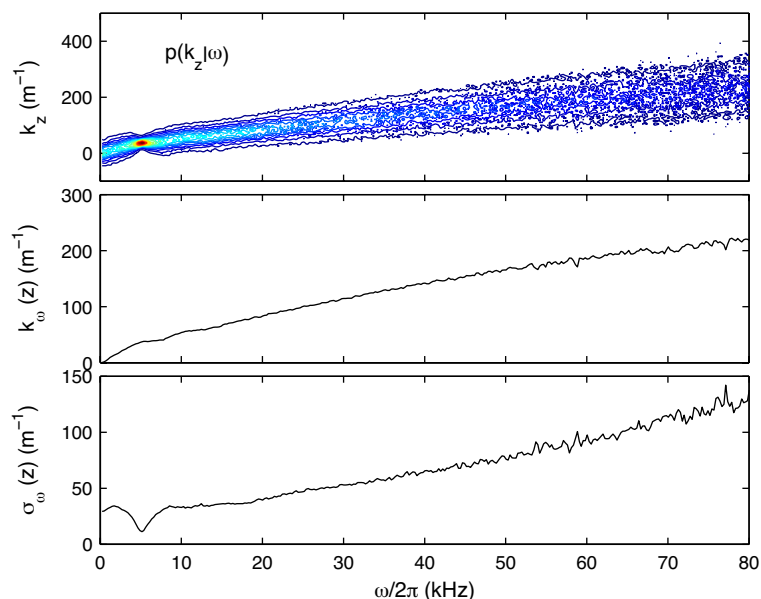


Figure 5.6: Statistical dispersion relation reconstructed in a H plasma in a case of weak turbulence. The power spectrum $P(k_z, \omega)$ is shown in Fig. 5.5

The conditional spectrum $p(k_z|\omega)$ gives the normalised power spectrum of k_z for fixed ω . The quantity $p(k_z|\omega)dk_z$ represents the fraction of spectral power at frequency ω due to fluctuations with wavenumbers in the range k_z to $k_z + dk_z$. Taking advantage of the analogy between the conditional spectrum and a probability density function, the value of $\bar{k}_z(\omega)$ and $\bar{\sigma}_{k_z}(\omega)$ - respectively the mean wavenumber and the mean wavenumber spectral width - can be estimated from the first and second moment of the spectral density in wavenumber space using fixed probe pairs [56][53]:

$$\bar{k}_z(\omega) = \sum_{m=1}^{N_c} k_z^m p(k_z^m|\omega), \quad (5.21a)$$

$$\bar{\sigma}_{k_z}^2(\omega) = \sum_{m=1}^{N_c} [k_z^m - \bar{k}_z(\omega)]^2 p(k_z^m|\omega), \quad (5.21b)$$

where $N_c = 2\pi/(d_{\text{tip}}\Delta k_z)$ is the number of grid points in k_z -space.

Figure 5.6 shows the statistical dispersion relation reconstructed from $P(k_z, \omega)$ for the same case shown in Fig. 5.5. Fluctuations with frequency larger than 5 kHz propagate with the same group velocity, as indicated by the linear dependence of $\bar{k}_z(\omega)$

As the total spectral power $\iint dk d\omega P(k, \omega)$ is a constant, the two definitions are equivalent. Note that $p(k, \omega)$ defined in this way has the mathematical properties of a probability function, *i.e.*:

$$p(k, \omega) \geq 0 \quad \forall k, \omega$$

$$\sum_{k, \omega} p(k, \omega) = 1$$

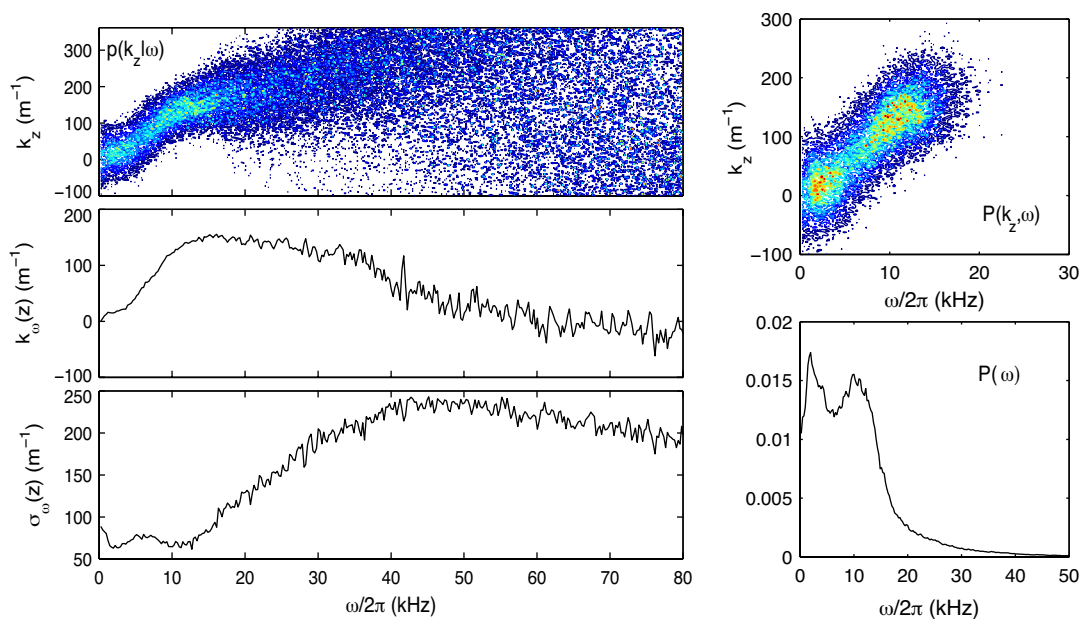


Figure 5.7: Same as Fig. 5.6, but for larger degree of turbulence.

on the frequency. The wavenumber dispersion $\bar{\sigma}_{k_z}(\omega)$ has a drop at the frequency of the dominant mode, then increases with ω , indicating broadening for larger frequencies, *i.e.* a decreasing of the correlation length associated with fluctuations with large frequencies.

Figure 5.7 shows, for comparison, the reconstruction of the dispersion relation in an experimental situation with more developed turbulence, with a broad feature measured around 10 kHz. The broadening of the wavenumber spectrum is larger in this case, with $\bar{\sigma}_{k_z}(\omega) > \bar{k}_z(\omega)$ already for frequencies above 20 kHz and it is not possible to define a group velocity. It should be underlined that the estimate of the statistical dispersion relation from Eq. (5.21) is valid in those frequency ranges where $\bar{\sigma}_{k_z}(\omega) < \bar{k}_z(\omega)$. The weak turbulence approximation, which is at the basis of the analysis, fails when $\bar{\sigma}_k(\omega) > \bar{k}(\omega)$.

5.4.3 Phase velocity

The phase velocity along z is estimated as the average value of the ratio ω/k_z , weighted over the power spectrum $P(k_z, \omega)$:⁷

$$v_{\text{ph}} = \frac{\sum_{k_z, \omega} \frac{\omega}{k_z} P(k_z, \omega)}{\sum_{k_z, \omega} P(k_z, \omega)} \quad (5.22)$$

The phase velocity estimated in this way accounts for the spectral broadening, because each component (k_z, ω) contributes proportionally to its spectral amplitude. For given (k_z, ω) , the power spectrum is fitted with a bi-dimensional gaussian function centered

⁷ The exact definition of the phase velocity is in term of the normalized power spectrum, $p(k_z, \omega)$.

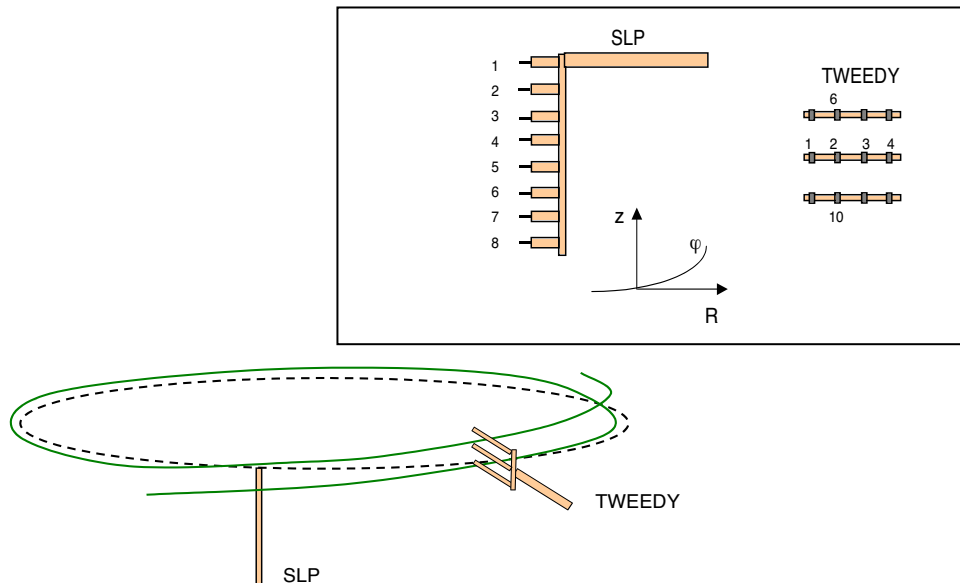


Figure 5.8: Geometrical setup of the SLP and TWEEDY arrays for the measurements of the parallel wavenumber. The arrays are positioned at the midplane (black dashed line) and are separated by $\pi/2$ along the toroidal direction. Numbers indicate which tips are connected. The green line indicates the field line that intersects TWEEDY tip#2.

at ω and k_z . The sum in Eq. (5.22) is then calculated over a range of frequencies and wavenumbers $\omega \pm \sigma_\omega$, $k_z \pm \sigma_{k_z}$ defined by the peak width in the ω - and k_z -space. For the two cases shown in Figs. 5.6-5.7, for example, the phase velocity calculated from Eq. (5.22) is $v_{\text{ph}} = (1.0 \pm 0.2)$ km/s in the case where a coherent mode is detected and $v_{\text{ph}} = (0.5 \pm 0.2)$ km/s in the case of turbulent spectrum.

5.4.4 Measurement of the parallel wavenumber

The value of the component of the wavenumber parallel to the magnetic field is very important not only for wave identification, but also as it is a key parameter for wave-particle interaction, in particular for the energy exchange. As discussed in Chap. 2, interchange modes propagate purely across \mathbf{B} , and have $k_{\parallel} \simeq 0$, while drift waves (including drift-interchange) propagate obliquely to \mathbf{B} and have $k_{\parallel} \neq 0$, with $k_{\parallel} \ll k_{\perp}$.

Parallel wavenumbers are routinely measured on TORPEX from the phase shift between the SLP and the TWEEDY arrays, using the setup shown in Fig. 5.8. This measurement is very delicate, as many factors can introduce errors in the measurement of k_{\parallel} , especially when the ratio of k_{\parallel} to k_{\perp} is low. In this case the measurement is strongly affected by the projection of k_{\perp} along the direction of measurement (see App. D).

Figure 5.10 shows an example of the effect of k_{\perp} on the measurement of k_{\parallel} , for two cases where a coherent mode can be identified in the power spectrum, *i.e.* $P(k_{\perp}, \omega)$ is peaked at a specific frequency and wavenumber. The two examples refer respectively

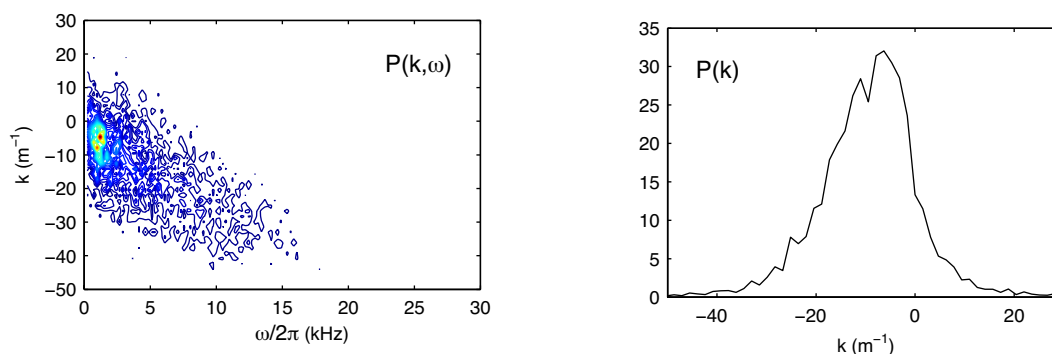


Figure 5.9: Power spectrum (left) and wavenumber spectrum (right) measured with the TWEEDY array, using two tips with separation of 1.8 cm.

to a mode with $k_{\parallel} \approx 0$ and a mode with $k_{\parallel} \neq 0$. For each combination of pairs SLP-TWEEDY, we have measured the wavenumber and frequency power spectrum $P(k, \omega)$. The error bars in the figure represent the width of the wavenumber spectrum. In both cases the measured wavenumbers increase linearly with the vertical separation between tips, the slope being a function of k_{\perp} (see App. D). It results from the figure that measurements done with probes not exactly aligned along the same field line result in an overestimate of $|k_{\parallel}|$. For given B_{φ} and B_z , a field line that intersects a reference tip of the TWEEDY array, will intersect the SLP array at the coordinate z_0 :

$$z_0 = R\Delta\varphi \frac{B_z}{B_{\varphi}}, \quad (5.23)$$

where R is the radial position of the probes and $\Delta\varphi$ their toroidal separation, measured on the midplane. The alignment of the probes with the field line is verified by looking at the value of the coherence spectrum γ^2 at the frequency of the mode. As shown in Fig. 5.10, in both cases the maximum of the coherence is measured at those coordinates that are closest to the calculated z_0 .

The toroidal separation between the probes that measure k_{\parallel} must be sufficiently large that tips can be considered point-like. An example of this is shown in Fig. 5.9, which reports the spectrum reconstructed with the TWEEDY array, rotated by 90° to have tips aligned along the toroidal direction. The distance between tips is 1.8 cm and the diameter of the ring-shaped tips is 3 mm; the value of z_0 calculated for this distance is 0.16 mm, much smaller than the diameter of the probes.

Two problems arise. First, the alignment of the tips along the field line is practically impossible. Second, due to the finite probe size, the measured phase shift will be the result of an integral over the tip surface, giving an overestimate of the parallel wavenumber [56]. The separation between SLP and TWEEDY was chosen on the basis of these considerations to minimize the errors introduced in the measurements by the finite probe size, yet maintaining high the level of coherence. Measurements performed with a third array, positioned at 120° from SLP, revealed in some cases a reduction of the coherence of a factor 3.

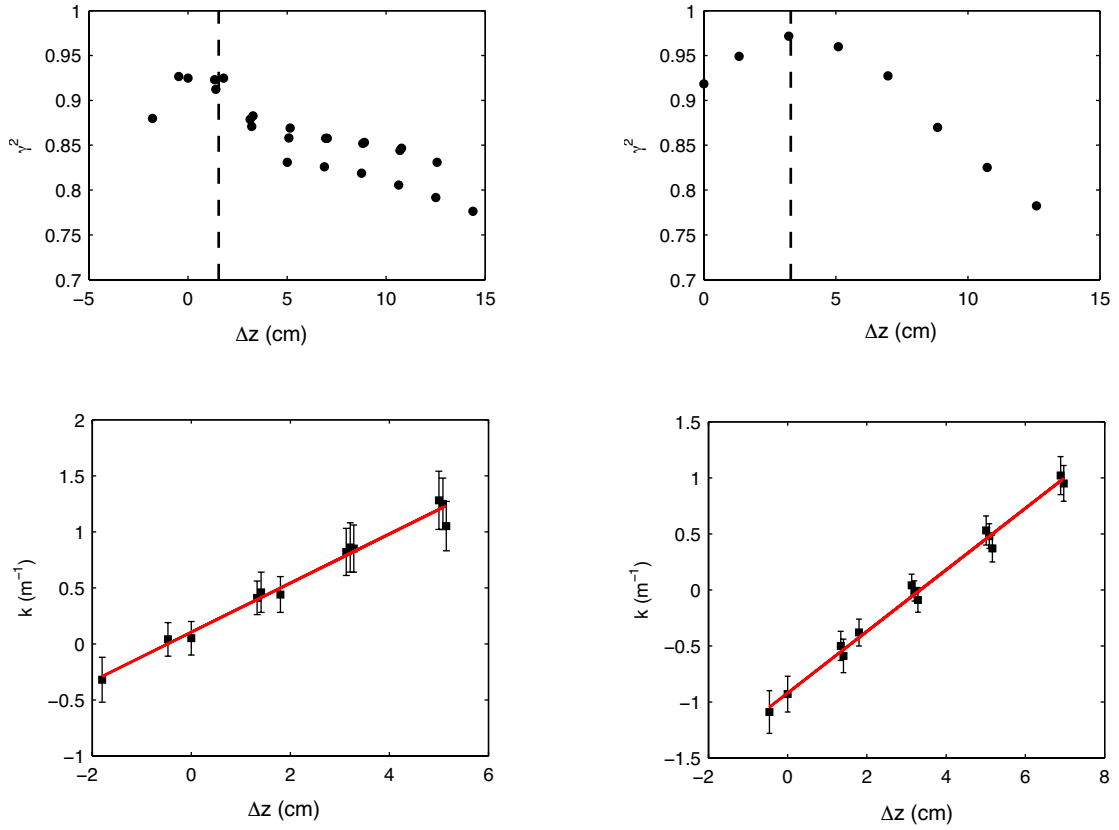


Figure 5.10: Examples of the effect of k_{\perp} on the measurement of k_{\parallel} , for a case of a mode with $k_{\parallel} \neq 0$ (left), and a mode with $k_{\parallel} \simeq 0$ (right). Top: value of the coherence spectrum measured at the frequency of the mode. The dashed line indicates the coordinate z_0 of the field line, calculated from Eq. (5.23).

Chapter 6

Measurement of the nonlinear properties of fluctuations

The spectral analysis discussed in the previous Chapter is suitable to the study of the amplitude distribution of fluctuations in frequency and wavenumber, and of the linear dispersion relation. When nonlinear processes are at play, Fourier analysis is of limited use, as no information on the phase coupling among different modes can be inferred from the power spectrum or the cross-spectrum. When the departure from linearity is weak, the standard Fourier analysis can be generalized to include information on the nonlinear phase coherence among different modes.

In this Chapter, we describe a spectral method to reconstruct the coefficients of nonlinear interactions. The basic assumption made is that nonlinear interactions are sufficiently weak that fluctuations can still be represented as the superposition of independent Fourier modes. A Volterra model, introduced in Sec. 6.1, is used to write the equations for the nonlinear dynamics of fluctuations. These equations are then used to derive an expression for the transfer of spectral energy in terms of the linear growth rate and of the nonlinear coupling coefficients (see Sec. 6.2). The latter are reconstructed by means of a multivariate regression analysis, described in Sec. 6.3, where the convergence of the solution with respect to the number of samples and to the level of noise is discussed. The Chapter is concluded with the quantification of the effect of nonlinear interactions on the measurement of the wavenumber from two probes (Sec. 6.4).

6.1 Spectral evolution of fluctuations due to nonlinear interactions

Under the hypothesis of small amplitude fluctuations and weak departure from linearity, and assuming a convective propagation along z , the dynamics of $\tilde{n}(z, t)$ can be modeled with a series expansion [57]:

$$\frac{\partial \tilde{n}(z, t)}{\partial z} = \sum_{m=1}^{\infty} f_m(\tilde{n}) \quad (6.1)$$

where $f_m(\tilde{n})$ are convolution integrals of increasing order:

$$f_1(\tilde{n}) = \int g(\tau_1) \tilde{n}(z, t - \tau_1) d\tau_1 \quad (6.2a)$$

$$f_2(\tilde{n}) = \iint g(\tau_1, \tau_2) \tilde{n}(z, t - \tau_1) \tilde{n}(z, t - \tau_2) d\tau_1 d\tau_2 \quad (6.2b)$$

...

The Volterra kernels $g(\tau_1, \dots, \tau_m)$ describe the dynamics of the system at order m . By taking the Fourier transform in time of the series $\tilde{n}(z, t)$ and for discrete values of the frequency, Eq. (6.1) can be written as:

$$\frac{dn_\omega}{dz} = \Gamma_\omega n_\omega + \sum_{\substack{\omega_l \geq \omega_m \\ \omega = \omega_l + \omega_m}} \Gamma_\omega^{l,m} n_l n_m + \sum_{\substack{\omega_l \geq \omega_m, \omega_p \\ \omega = \omega_l + \omega_m + \omega_p}} \Gamma_\omega^{l,m,p} n_l n_m n_p + \dots \quad (6.3)$$

where n_l , n_m , n_p denote the spectral components of \tilde{n} at frequency respectively ω_l , ω_m and ω_p . The linear term Γ_ω is related to the growth rate and the wave dispersion, as it can be easily seen by taking $\Gamma_\omega^{l,m} = \Gamma_\omega^{l,m,p} = 0$ and comparing this equation with Eq. (5.13). We'll write this term as $\Gamma_\omega = \gamma_\omega + ik_\omega$. The quadratic coupling coefficients $\Gamma_\omega^{l,m}$ describe nonlinear interactions involving three waves that satisfy the resonance condition $\omega_l + \omega_m = \omega$. Similarly, the cubic coupling coefficients $\Gamma_\omega^{l,m,p}$ describe nonlinear interactions involving four waves that satisfy the resonance condition $\omega_l + \omega_m + \omega_p = \omega$.

6.1.1 Nonlinear dynamics in the laboratory frame

Frequencies are measured in the laboratory frame, where they are Doppler shifted by a flow velocity \mathbf{v}_p , which, on TORPEX, corresponds to the $\mathbf{E}_0 \times \mathbf{B}$ drift velocity \mathbf{v}_E :

$$\omega_{\text{lab}} = \omega_{\text{pl}} + \mathbf{k} \cdot \mathbf{v}_E \quad (6.4)$$

where ω_{pl} is the frequency measured in the plasma frame. For drift waves, the measured frequency will be the sum of the electron diamagnetic frequency $\mathbf{k} \cdot \mathbf{v}_{\text{de}}$ and the $\mathbf{E}_0 \times \mathbf{B}$ frequency $\mathbf{k} \cdot \mathbf{v}_E$:

$$\omega_{\text{lab}} = \mathbf{k} \cdot (\mathbf{v}_{\text{de}} + \mathbf{v}_E) \quad (6.5)$$

For interchange modes, the measured frequency will be essentially ω_E , because in TORPEX plasmas $\mathbf{v}_B \ll \mathbf{v}_E$:

$$\omega_{\text{lab}} = \mathbf{k} \cdot (\mathbf{v}_B + \mathbf{v}_E) \simeq \mathbf{k} \cdot \mathbf{v}_E \quad (6.6)$$

In most of the experimental situations verified on TORPEX, the background profiles of pressure and plasma potential are similar in shape, with maximum at the same $R - R_0$ and parallel gradients. At midplane, in particular, where the gradients are along R and the corresponding drifts are along z , one can write:

$$\omega_{\text{lab}} = \omega_{\text{pl}} + k_z v_E. \quad (6.7)$$

Making the Galileian transform $n(z, t) \rightarrow n(z, t' = t - z/v_E)$ and using the shifting properties of Fourier transforms, the Fourier coefficients in the laboratory frame are written as:

$$\exp\left(i\frac{\omega}{v_E}z\right) n_\omega. \quad (6.8)$$

Equation (6.3) assumes in the laboratory frame the form:

$$\frac{d}{dz} \left(e^{i\omega z/v_E} n_\omega \right) = \Gamma_\omega e^{i\omega z/v_E} n_\omega + \sum_{\substack{\omega_l \geq \omega_m \\ \omega = \omega_l + \omega_m}} \Gamma_\omega^{l,m} e^{i(\omega_l + \omega_m)z/v_E} n_l n_m + \dots, \quad (6.9)$$

where the explicit dependence on z in the Fourier components $n_\omega(z)$ has been dropped. Expanding the space derivative on the left hand side and using the resonance condition $\omega_l + \omega_m = \omega$, we obtain:

$$\frac{dn_\omega}{dz} = \left(\Gamma_\omega - i\frac{\omega}{v_E} \right) n_\omega + \sum_{\substack{\omega_l \geq \omega_m \\ \omega = \omega_l + \omega_m}} \Gamma_\omega^{l,m} n_l n_m + \dots \quad (6.10)$$

As expected, the $\mathbf{E}_0 \times \mathbf{B}$ velocity affects the imaginary part of the linear term, related to the dispersion relation, without affecting the growth rate and the quadratic coupling coefficients.

6.1.2 Spatial versus temporal representation

Equation (6.3) is a particular case of a general model that describes both spatial and temporal dynamics. In the general case, the resonance condition must be interpreted as a conservation both in energy and in momentum:

$$\omega_l + \omega_m = \omega \quad (6.11a)$$

$$\mathbf{k}_l + \mathbf{k}_m = \mathbf{k} \quad (6.11b)$$

The frequency measured in the laboratory frame, as discussed in the previous section, can be written as:

$$\omega_{\text{lab}} = \mathbf{k} \cdot \mathbf{v}_p \simeq k_z v_p \quad (6.12)$$

where v_p is the phase velocity measured in the laboratory frame and we have assumed that the dynamics is one-dimensional along z . It follows from Eq. (6.12) that, in those

cases where a linear phase velocity is measured in a frequency range $\Delta\omega$, the time dynamics can be extracted from the space dynamics using the relation: ¹

$$\frac{\partial}{\partial t} = v_p \frac{\partial}{\partial z}$$

where $v_p = \Delta\omega/\Delta k_z$. In this case the resonance among frequencies $\omega_l + \omega_m = \omega$ implies a resonance among wavenumbers conjugate to z , $k_z(\omega_l) + k_z(\omega_m) = k_z(\omega)$. It should be underlined that this extension is valid as far as the degree of turbulence is low. In case of strong turbulence, in fact, the wavenumber and frequency spectrum $P(k_z, \omega)$ is broad in k_z and a resonance between specific frequencies does not necessarily imply that the associated wavenumbers are also resonant.

6.2 Spectral power transfer

In a plasma, instabilities generally evolve from a fluctuation spectrum that covers a limited range of frequency. This spectral energy is then redistributed through nonlinear wave-wave interaction over the wider regions of the spectrum. An equation for the evolution of the spectral power in a weakly turbulent plasma is obtained multiplying Eq. (6.3) by n_ω^* and averaging over a large number of samples: ²

$$\begin{aligned} \frac{1}{2} \frac{d}{dz} \langle n_\omega n_\omega^* \rangle &= \Re(\Gamma_\omega) \langle n_\omega n_\omega^* \rangle + \sum_{\substack{\omega_l \geq \omega_m \\ \omega = \omega_l + \omega_m}} \Re[\Gamma_\omega^{l,m} \langle n_l n_m n_\omega^* \rangle] \\ &+ \sum_{\substack{\omega_l \geq \omega_m, \omega_p \\ \omega = \omega_l + \omega_m + \omega_p}} \Re[\Gamma_\omega^{l,m,p} \langle n_l n_m n_p n_\omega^* \rangle] + \dots \end{aligned} \quad (6.14)$$

where the relation:

$$\frac{dn_\omega}{dz} n_\omega^* = \frac{1}{2} \frac{d}{dz} (n_\omega n_\omega^*)$$

has been used. The variation of spectral power $\langle n_\omega n_\omega^* \rangle$ moving along the distance dz is due to the linear term through the average linear growth rate $\Re(\Gamma_\omega)$ and to nonlinear interactions through the terms:

$$T_\omega^{l,m} = \Re[\Gamma_\omega^{l,m} \langle n_l n_m n_\omega^* \rangle] \quad (6.15a)$$

$$T_\omega^{l,m,p} = \Re[\Gamma_\omega^{l,m,p} \langle n_l n_m n_p n_\omega^* \rangle] \quad (6.15b)$$

¹ Space and time derivative can be switched in Eq. (6.1), and an expression equivalent to Eq. (6.3) can be written for the space dynamics [58]:

$$\frac{dn_k}{dt} = \mathcal{L}_k n_k + \sum_{\substack{k_l, k_m \\ k = k_l + k_m}} \mathcal{Q}_k^{l,m} n_l n_m \quad (6.13)$$

where the fluctuating field is written in terms of the Fourier components in wavenumber, $n_k(t)$. The Hasegawa-Mima equation for collisionless plasmas or the Hasegawa-Wakatani equations, for example, can be reconduced to a model represented by Eq. (6.13).

² As the energy is invariant for Galileian transforms of coordinate, the equation representing the transfer of energy assumes the same form also in the laboratory frame, as can be easily proven by multiplying Eq. (6.10) by $e^{-i\omega z/v_E} n_\omega^*$.

The terms $T_\omega^{l,m}$ represent the amount of spectral power transfer due to three-wave interactions. This transfer depends on the coupling coefficients $\Gamma_\omega^{l,m}$ and on the strength of three-wave coupling, quantified by the *bispectrum* $\langle n_l n_m n_\omega^* \rangle$. Positive values of $T_\omega^{l,m}$ correspond to three-wave interactions in which spectral components with angular frequencies $\omega_{l,m}$ transfer energy to the component $\omega = \omega_l + \omega_m$. Conversely, negative values correspond to decay processes $\omega \rightarrow \omega_l + \omega_m$. The amplitude of individual coefficients $T_\omega^{l,m}$ is usually small, although the contribution of all triplets of waves $(\omega_l, \omega_m, \omega)$ to the power spectrum at ω can be significant.

The terms $T_\omega^{l,m,p}$ represent the amount of spectral transfer due to four-wave interaction processes. They depend on the cubic interaction coefficients $\Gamma_\omega^{l,m,p}$ and on the *trispectrum* $\langle n_l n_m n_p n_\omega^* \rangle$. In most experimental situations the cubic coupling coefficients are vanishing and Eq. (6.14) can be truncated to the second order. It is worth noting that, in any case, the validity of this assumption must be verified by comparing, for example, the relative amplitudes of the bispectrum and of the trispectrum.

Estimate of the bispectrum

An estimate of the bispectrum is given by the ensemble average [59]:

$$B(\omega_l, \omega_m) = \frac{1}{M} \sum_{j=1}^M n_l^{(j)} n_m^{(j)} n_{l+m}^{*(j)} \quad (6.16)$$

If waves at frequency ω_l, ω_m and $\omega_l + \omega_m$ are independent, each wave may be characterized by statistically independent random phases. The phase $(\theta_l + \theta_m - \theta_{l+m})$, calculated for each realization $j = 1, \dots, M$, is randomly distributed over $[-\pi, \pi]$. In this case a statistical averaging over a large number of samples leads to a vanishing bispectrum. On the other hand, if the three spectral components are nonlinearly coupled, the total phase, averaged over the ensemble, converges to a finite value. From Eq. (6.16), using the relation $n_{-\omega} = n_\omega^*$, it can be shown that the bispectrum satisfies the following symmetry relations:

$$B(\omega_l, \omega_m) = B(\omega_m, \omega_l) = B^*(-\omega_l, -\omega_m) \quad (6.17a)$$

$$B(\omega_l, \omega_m) = B(-\omega_l - \omega_m, \omega_m) = B(\omega_l, -\omega_l - \omega_m) \quad (6.17b)$$

These symmetries are such that the frequency range for the calculation of the bispectrum can be reduced to the area enclosed between dotted lines in Fig. 6.1. The number of samples M over which to calculate the average in Eq. (6.16) must be chosen to have convergence of the bispectrum. An example is shown in Fig. 6.1, where the absolute value of the bispectrum corresponding to a fixed triplet of frequencies $(\omega_l, \omega_m, \omega)$ is plotted as a function of the number of samples. It is found that the value of the bispectrum strongly oscillates for $M < 2000$, then reaches saturation for larger M .

An estimate of the phase coupling independent of the power spectral amplitude, the so-called *bicoherence* [59], is obtained normalizing the bispectrum:

$$b^2(\omega_l, \omega_m) = \frac{|\langle n_l n_m n_{l+m}^* \rangle|^2}{\langle |n_l n_m|^2 \rangle \langle |n_{l+m}|^2 \rangle} \quad (6.18)$$

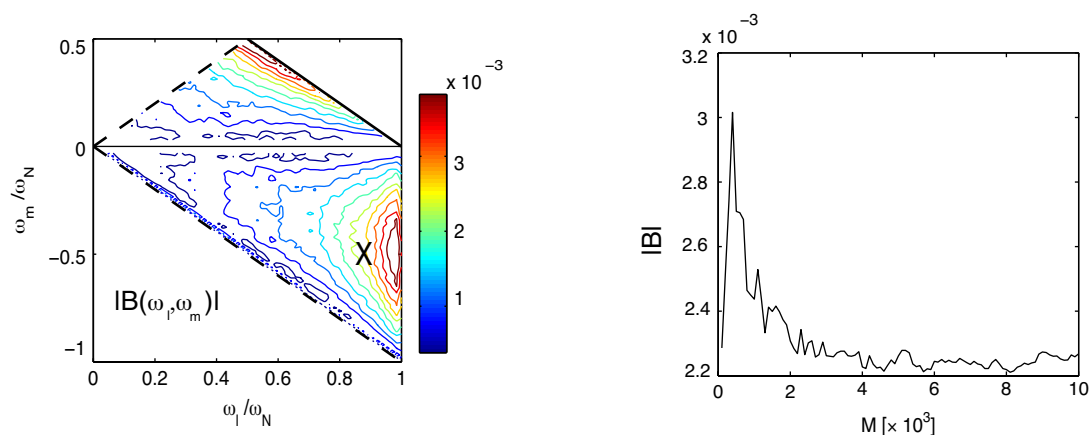


Figure 6.1: Left: Absolute value of the bispectrum, $|B(\omega_l, \omega_m)|$, calculated from a synthetic signal (see Sec. 6.3.1). Frequencies are in units of the Nyquist frequency ω_N . Right: Convergence of the value of the bispectrum on the number of samples; the curve refers to the value of $|B(\omega_l, \omega_m)|$ calculated at the frequencies (ω_l, ω_m) indicated by a cross in the left figure.

As a natural extension of the definition of the bispectrum, four-wave interactions can be estimated by the ensemble average:

$$B(\omega_l, \omega_m, \omega_p) = \frac{1}{M} \sum_{j=1}^M n_l^{(j)} n_m^{(j)} n_p^{(j)} n_{l+m+p}^{*(j)} \quad (6.19)$$

and the corresponding *tricoherence* as:

$$b^2(\omega_l, \omega_m, \omega_p) = \frac{|\langle n_l n_m n_p n_{l+m+p}^* \rangle|^2}{\langle |n_l n_m n_p|^2 \rangle \langle |n_{l+m+p}|^2 \rangle} \quad (6.20)$$

The resonance condition $\omega_l + \omega_m + \omega_p = \omega$ defines a tetrahedron in the frequency domain. One should therefore fix a frequency component, for example ω_p , and use Eq. (6.16) to calculate the equivalent bispectrum associated with the resonance condition $\omega_l + \omega_m = \omega - \omega_p$. The calculation of the trispectrum is time consuming because this operation should be repeated over all spectral components of interest.

6.3 Estimate of the quadratic coupling coefficients

The coupling coefficients can be estimated from two-point measurements by a difference approach [58]. If $n_{1,\omega}$ and $n_{2,\omega}$ denote the spectral components of density fluctuations at frequency ω measured respectively at positions z_1 and $z_2 = z_1 + d_{\text{tip}}$, the derivative Eq. (5.13) can be approximated by:

$$\frac{dn_\omega(z)}{dz} \approx \frac{1}{d_{\text{tip}}} \lim_{d_{\text{tip}} \rightarrow 0} \left[\frac{|n_{2,\omega}| - |n_{1,\omega}|}{|n_{1,\omega}|} + i\Delta\theta_\omega \right] n_{1,\omega}. \quad (6.21)$$

Here $\Delta\theta_\omega = \theta_{2,\omega} - \theta_{1,\omega}$ is the phase shift measured between $n_{1,\omega}$ and $n_{2,\omega}$, and the z axis is oriented such that the measured phase shift $\Delta\theta_\omega$ is positive. In practice one should measure the phase shift between two probes and attribute an *upstream* and a *downstream* position according to the measured phase shift.

Replacing Eq. (6.21) into Eq. (6.10) and solving for $n_{2,\omega}$ with d_{tip} small, the fluctuations measured at z_1 and z_2 can be written as part of an input-output system:

$$n_{2,\omega} = \left(L_\omega - i \frac{\omega}{v_E} d_{\text{tip}} \right) n_{1,\omega} + \sum_{\substack{\omega_l \geq \omega_m \\ \omega = \omega_l + \omega_m}} Q_\omega^{l,m} n_{1,l} n_{1,m} + \sum_{\substack{\omega_l \geq \omega_m, \omega_p \\ \omega = \omega_l + \omega_m + \omega_p}} C_\omega^{l,m,p} n_{1,l} n_{1,m} n_{1,p} + \dots \quad (6.22)$$

where

$$L_\omega = (1 + \Gamma_\omega d_{\text{tip}} - i\Delta\theta_\omega) e^{i\Delta\theta_\omega} \quad (6.23a)$$

$$Q_\omega^{l,m} = \Gamma_\omega^{l,m} d_{\text{tip}} e^{i\Delta\theta_\omega} \quad (6.23b)$$

$$C_\omega^{l,m,p} = \Gamma_\omega^{l,m,p} d_{\text{tip}} e^{i\Delta\theta_\omega} \quad (6.23c)$$

Equation (6.22) can be solved by iteration [58] or by means of multivariate linear regression techniques [57]. We choose the latter approach because it can be most easily extended to include cubic interaction terms.

The time series from two probes separated by a distance d_{tip} are divided into M samples of length $T = N\delta t$, with 50% overlapping, where δt is the sampling time. As discussed in Sec. 5.4.1, the number of points N in each sample must be large enough that the frequency resolution $\delta\omega = \pi\delta t/N$ is sufficient to resolve spectral components of interest. After subtraction of the mean value and evaluation of the Fourier coefficients for each sample, we build for each value ω of the frequency the system of M linear equations:

$$Y_\omega = X_\omega A_\omega \quad (6.24)$$

where the output Y_ω contains the Fourier components of the *downstream* probe:

$$Y_\omega = [n_{2,\omega}^{(1)}, n_{2,\omega}^{(2)}, \dots, n_{2,\omega}^{(M)}]^T. \quad (6.25)$$

A_ω is the array of unknown coefficients, defined as:

$$A_\omega = [L_\omega, Q_\omega^{\omega_1, \omega - \omega_1}, \dots, Q_\omega^{\omega_N, \omega - \omega_N}]^T. \quad (6.26)$$

The input array X_ω contains the terms involving linear and quadratic interactions between Fourier components of the *upstream* probe, with:

$$X_\omega = \begin{bmatrix} n_{1,\omega}^{(1)} & n_{1,\omega_1}^{(1)} n_{1,\omega-\omega_1}^{(1)} & \dots & n_{1,\omega_N}^{(1)} n_{1,\omega-\omega_N}^{(1)} \\ \vdots & \vdots & & \vdots \\ n_{1,\omega}^{(M)} & n_{1,\omega_1}^{(M)} n_{1,\omega-\omega_1}^{(M)} & \dots & n_{1,\omega_N}^{(M)} n_{1,\omega-\omega_N}^{(M)} \end{bmatrix} \quad (6.27)$$

The number of unknown coefficients depends on the value of the frequency ω and on the number of possible combinations $\omega_l \pm |\omega_m| = \omega$ given by the resonance conditions. The solution of this system is given by the model that minimizes the squared residual errors ϵ_ω between the measured Y_ω and the predicted output \hat{Y}_ω

$$\epsilon_\omega = |Y_\omega - \hat{Y}_\omega|^2 \quad (6.28)$$

In order for the solution of Eq. (6.24) to be numerically stable and physically relevant, the matrix X_ω must be non singular and the number of equations much larger than the number of unknown coefficients. A compromise is thus needed between the number of samples M and the number of Fourier modes N , which must be large enough to yield sufficient frequency resolution. Secondly, the frequency range should be truncated at a frequency above which the power spectral content becomes negligible. A further reduction of the frequency range can be done when the nonlinear interactions are very localised in frequency space.

6.3.1 Test of convergence

We have built an exact quadratic model, with L_ω and $Q_\omega^{l,m}$ defined as in [60]:

$$L_\omega = 1.0 - 0.4 \frac{\omega^2}{\omega_N^2} + i0.8 \frac{\omega}{\omega_N} \quad (6.29a)$$

$$Q_\omega^{l,m} = \frac{i}{5\omega_N^4} \frac{\omega_l \omega_m (\omega_m^2 - \omega_l^2)}{1 + \frac{\omega^2}{\omega_N^2}} \quad (6.29b)$$

where frequencies are normalized to the Nyquist frequency ω_N and $\omega = \omega_l + \omega_m$. Three regions can be identified in Fig. 6.2, indicated as I, II, III. The triangular region (I) gives the quadratic transfer function at the highest frequency ω involved in the interactions, $\omega > \omega_l, \omega_m$. Region (II) gives the strength of the coupling at the intermediate frequency ω due to wave-wave coupling with a spectral component of larger frequency ω_l and one with a smaller frequency ω_m , $\omega_l > \omega > |\omega_m|$. The triangular region (III) shows $|Q_\omega^{l,m}|$ at the lowest frequency component ω due to coupling with the two others, $\omega < \omega_l, |\omega_m|$.

We have constructed $M = 10000$ realizations of a gaussian signal, with $N = 128$ points. This represents the first input signal, which is passed through a *black box* consisting of L_ω and $Q_\omega^{l,m}$ as defined above. The output is then used as input for an identical black box. The process is iterated 10 times, using each time the output of the $n^{th} - 1$ box as input for the n^{th} box. The iteration is necessary to ensure that the final input and output signals are non gaussian [60]. Figure 6.2 shows the power spectra of the final input and output signals, X_ω and Y_ω .

In a second step, we estimate the linear and quadratic coefficients using the method described above and in Ref. [57]. Half of the total number of samples are used to solve the system, while the other half are kept for cross-validation. The error on the estimate is given by the cross-coherence between the output signal Y_ω and the prediction of the

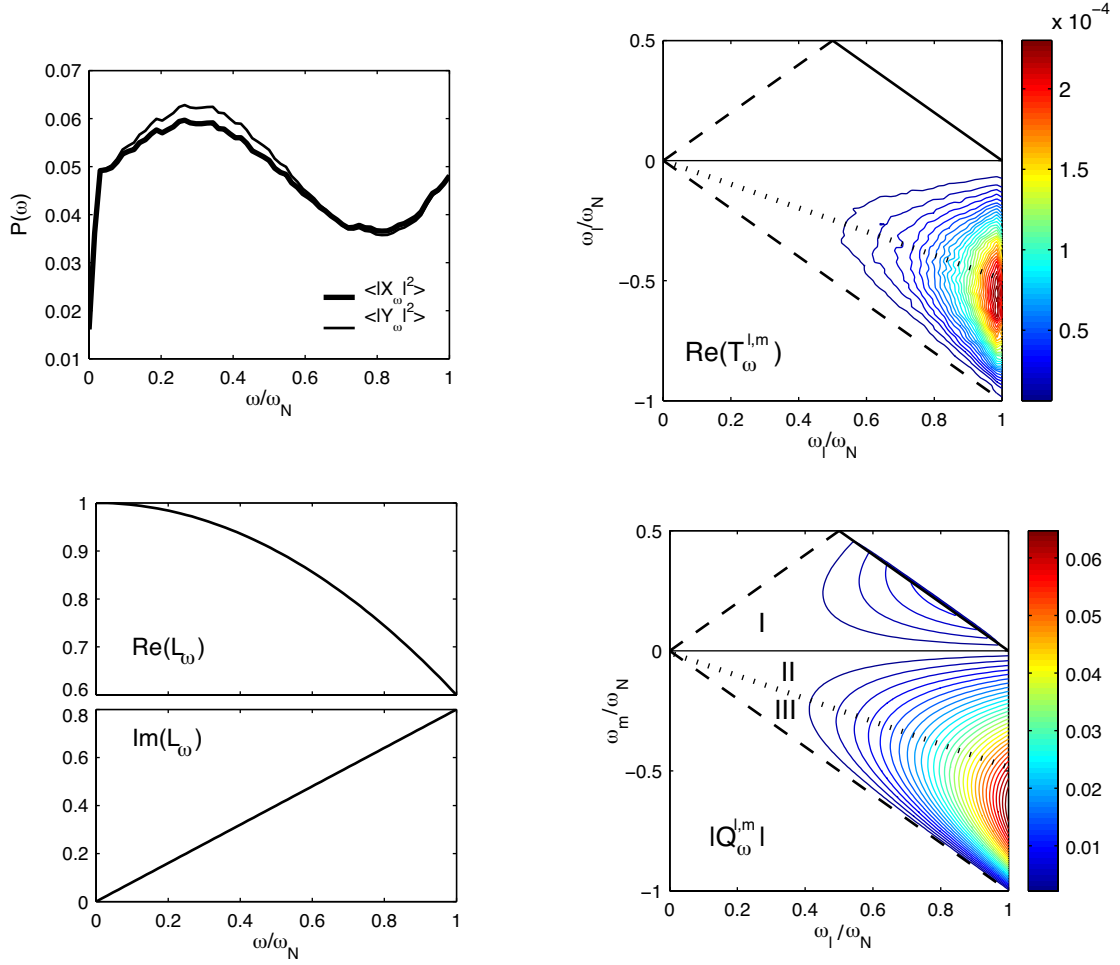


Figure 6.2: Top left: Power spectra of the input and output signals, X_ω and Y_ω . Top right: Quadratic coefficients for the transfer of energy associated with three-wave interaction, Eq. (6.15a). Bottom: Synthetic linear and quadratic term, defined from Eq. (6.29).

model, \widehat{Y}_ω , [57]:

$$\gamma_\omega^2 = \frac{|\langle Y_\omega \widehat{Y}_\omega^* \rangle|^2}{\langle |Y_\omega|^2 \rangle \langle |\widehat{Y}_\omega|^2 \rangle} \quad (6.30)$$

Figure 6.3 shows the results of the reconstruction of L_ω and $Q_\omega^{l,m}$ from $M = 20$ and $M = 100$ samples. Perfect correspondence is found for $M = 100$, as indicated by the unity value of the cross-coherence. Conversely, the reconstruction of the quadratic coefficients is poor for an insufficient number of equations. For comparison, we also show in the figure the value of the coherence calculated assuming a linear system:

$$\widehat{Y}_\omega = L_\omega X_\omega \quad (6.31)$$

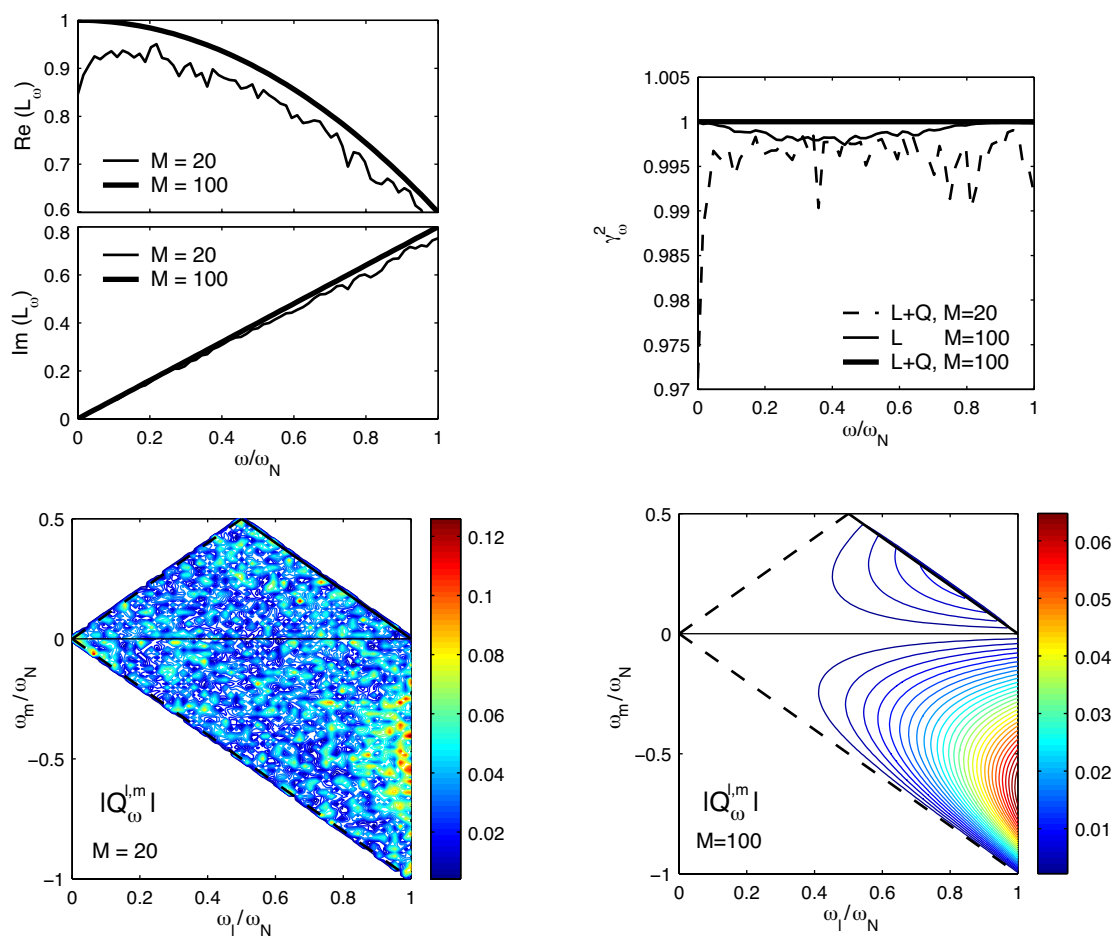


Figure 6.3: Top left: Linear term L_ω reconstructed with 20 and 100 samples. Top right: coherence between the measured output and the estimate of the model for $M = 20$ (dashed line) and $M = 100$ (thick line) samples. The thin line represents the coherence calculated assuming a linear model. Bottom: Absolute value of quadratic coefficients $|Q_\omega^{l,m}|$ reconstructed from $M = 20$ (left) and $M = 100$ (right) samples.

where L_ω is calculated as:

$$L_\omega = \frac{\langle Y_\omega X_\omega^* \rangle}{\langle X_\omega X_\omega^* \rangle}. \quad (6.32)$$

As shown in Fig. 6.3, the error done in neglecting the quadratic contributions is small, resulting in a variation of γ_ω^2 smaller than 0.3%.

The number of samples needed to reconstruct the linear and quadratic coefficients increase in the presence of noise. This effect has been quantified adding to each sample $X_\omega^{(j)}$ and $Y_\omega^{(j)}$ the Fourier Transform of a gaussian noise signal of amplitude $\sqrt{\langle X_\omega X_\omega^* \rangle} (S/N)^{-1}$ (resp. $\sqrt{\langle Y_\omega Y_\omega^* \rangle} (S/N)^{-1}$), where S/N is the signal-to-noise ratio.

Figure 6.4 shows the results of the reconstruction in the case of $S/N = 30$ and $S/N = 100$. The presence of noise results in an offset in the estimate of the real part of L_ω , related to the growth rate, and in an underestimate of the slope of the imaginary part of L_ω , related to the wave dispersion, cfr Eq. (6.23a). The offset increases and the

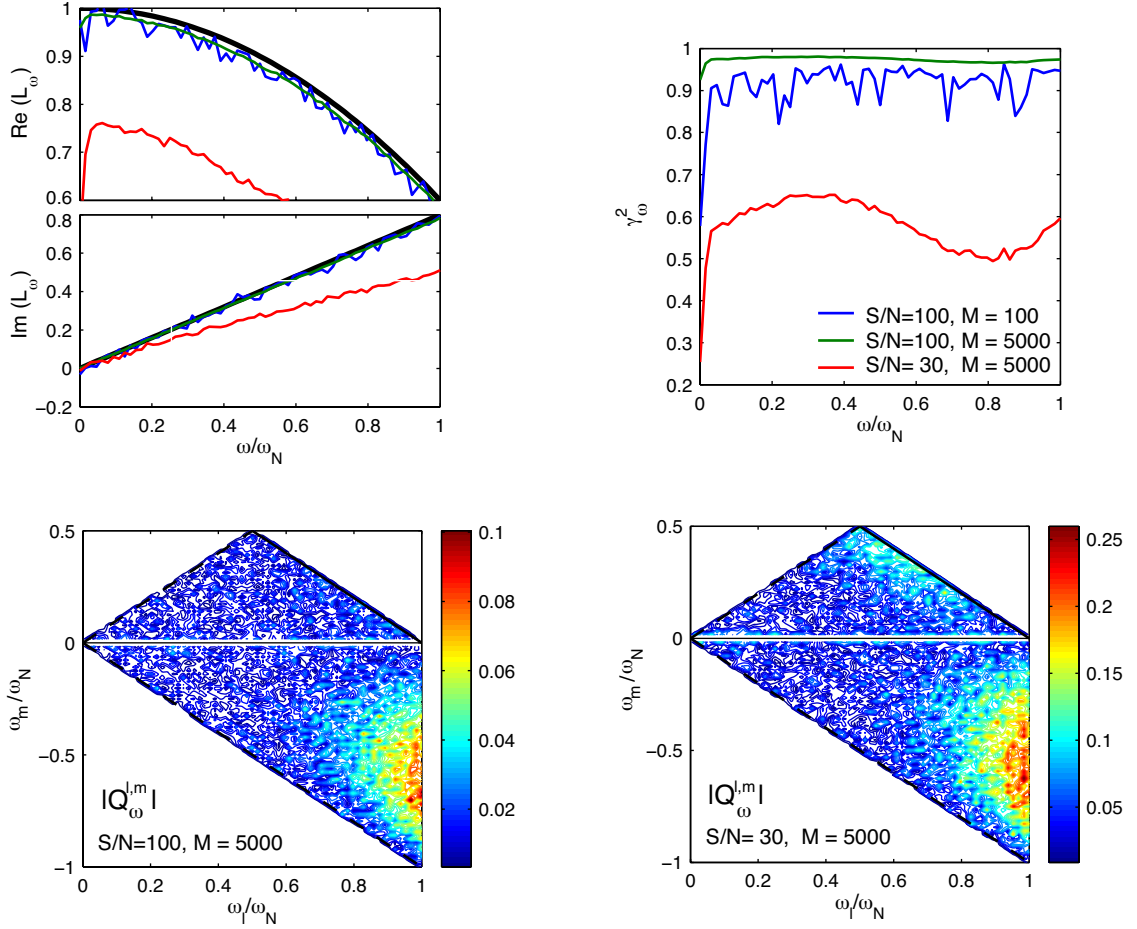


Figure 6.4: Reconstruction of the linear and quadratic terms in the presence of gaussian noise, for signal to noise ratio $S/N = 30$ and $S/N = 100$ for $M = 5000$ samples. Top left: Linear term L_ω ; the black line is the reference linear term. The reconstruction for the case of $S/N = 100$ and $M = 100$ is shown for comparison. Top right: coherence between the measured output and the estimate of the model, same cases. Bottom: Absolute value of quadratic coefficients, $|Q_\omega^{l,m}|$, reconstructed from $M = 5000$ samples, in the case of $S/N = 100$ (left) and $S/N = 30$ (right).

slope decreases with increasing noise levels. Increasing the number of samples does not remove the offset, as shown in Fig. 6.4 for the case of $S/N = 100$ and for $M = 100$ and $M = 5000$. The value of γ_ω^2 is on average 5% lower if less samples are used, but the average value of L_ω at fixed frequency ω is comparable in the two cases. Increasing the number of samples in the presence of noise reduces the statistical noise in the estimate of the coefficients, but does not eliminate the effect of gaussian noise in the signals. The underestimate of $\Re(L_\omega)$ is reflected in an overestimate of the quadratic terms $|Q_\omega^{l,m}|$, although the qualitative features are preserved. A direct consequence is that the power spectral transfer due to quadratic interactions is overestimated and that associated to the linear term is underestimated, as shown in Fig. 6.5.

Figure 6.6 shows the offset level and the variation of the slope of the real and

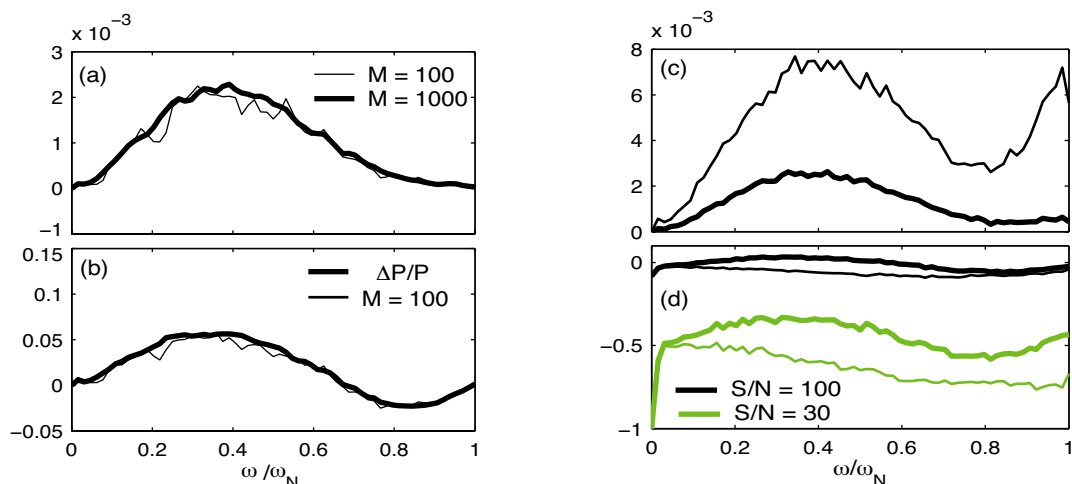


Figure 6.5: Left: Spectral power transfer calculated in the case of noise-free signals. The quadratic coefficients are calculated using $M = 100$ samples (see Fig. 6.3), while the bispectrum is calculated with $M = 100$ and $M = 1000$ samples. (a) Total contribution of the quadratic coefficients $T_{\omega}^{l,m}$, Eq. (6.15a). (b) Relative power transfer, $\Delta P/P = 2(P_2 - P_1)/(P_1 + P_2)$ and relative power transfer associated with nonlinear interactions $2\Sigma T_{\omega}^{l,m}/P$. Right: Same as left figure, but for two levels of noise and for $M = 5000$ samples. (c) Total contribution of the quadratic coefficients $T_{\omega}^{l,m}$, for $S/N = 100$ (thick curve) and $S/N = 30$ (thin curve). (d) Relative spectral power transfer $2\gamma_{\omega} + 2\Sigma T_{\omega}^{l,m}/P$ (thick curves). The thin lines represent the contribution to the spectral power transfer due to the linear term.

imaginary part of the linear term L_{ω} for signal to noise ratio between 2 and 1000. Plotted quantities are referred to the reference values from Eq. (6.29). The linear and quadratic term have been calculated using $M = 5000$ samples to reduce the statistical noise in the analysis. For $S/N > 100$ the deviation from the reference value tends to zero, the reconstruction of the linear and quadratic coefficients is almost unaffected by noise. Conversely, the results are strongly affected by the noise level for decreasing signal to noise ratio down to $S/N < 20$. Below this limit the reconstruction of the coefficients becomes unreliable.

6.4 Measurement of the wavenumber from two probes

The wavenumber related to a fluctuating quantity is routinely measured from the argument of the cross-spectrum between two probes with finite separation d_{tip} , using Eq. (5.14). By multiplying Eq. (6.22) times $n_{1,\omega}^*$ and averaging over many samples, we obtain:

$$\langle n_{2,\omega} n_{1,\omega}^* \rangle = L_{\omega} \langle n_{1,\omega} n_{1,\omega}^* \rangle + \sum_{\substack{\omega_l \geq \omega_m \\ \omega = \omega_l + \omega_m}} Q_{\omega}^{l,m} \langle n_{1,l} n_{1,m} n_{1,\omega}^* \rangle + \langle \epsilon n_{1,\omega}^* \rangle. \quad (6.33)$$

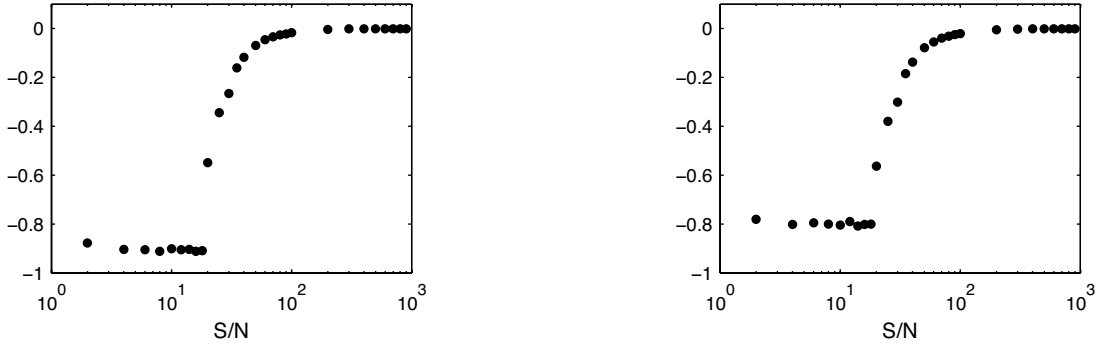


Figure 6.6: Left: Variation of the offset in the estimate of the real part of L_ω with the value of the signal to noise ratio. Right: Variation of the slope of the imaginary part of L_ω with respect to the reference slope, as a function of the signal to noise ratio.

Using Eq. (6.23a), which relates $\Gamma_\omega = \gamma_\omega + ik_\omega$ and L_ω , the real and the imaginary part of Γ_ω can be written respectively as:

$$\gamma_\omega = \frac{1}{d_{\text{tip}}} [\Re(L_\omega e^{-i\Delta\theta_\omega}) - 1] \quad (6.34a)$$

$$k_\omega = \frac{1}{d_{\text{tip}}} [\Delta\theta_\omega + \Im(L_\omega e^{-i\Delta\theta_\omega})] \quad (6.34b)$$

where $\Delta\theta_\omega$ is the measured phase shift over distance d_{tip} . If nonlinear contributions are negligible, the system reduces to a linear input-output system:

$$\langle n_{2,\omega} n_{1,\omega}^* \rangle = L_\omega \langle n_{1,\omega} n_{1,\omega}^* \rangle$$

and the phase variation is given by:

$$\tan \Delta\theta_\omega = \frac{\Im[\langle n_{2,\omega} n_{1,\omega}^* \rangle]}{\Re[\langle n_{2,\omega} n_{1,\omega}^* \rangle]} = \frac{L_\omega^I}{L_\omega^R} \quad (6.35)$$

where L_ω^I and L_ω^R denote, respectively, the real and imaginary part of L_ω . Using the relation:

$$e^{i\Delta\theta_\omega} = \frac{\langle n_{2,\omega} n_{1,\omega}^* \rangle}{|\langle n_{2,\omega} n_{1,\omega}^* \rangle|}$$

and replacing it in Eq. (6.34b), the imaginary term inside the parentheses cancels out and the wavenumber is given by the ratio of the phase shift to the distance. In the general case, however, the expression for the total phase variation $\Delta\theta_\omega$ includes also nonlinear terms:

$$\tan \Delta\theta_\omega = \frac{L_\omega^I + \frac{Y_Q^I}{P_X} + \frac{P_\epsilon^I}{P_X}}{L_\omega^R + \frac{Y_Q^R}{P_X} + \frac{P_\epsilon^R}{P_X}} \quad (6.36)$$

where $P_X = \langle n_{1,\omega} n_{1,\omega}^* \rangle$ and $P_\epsilon = P_\epsilon^R + iP_\epsilon^I = \langle \epsilon n_{1,\omega}^* \rangle$. Y_Q^R and Y_Q^I denote the real and the imaginary part of the total contribution of quadratic interactions:

$$\sum_{\substack{\omega_l \geq \omega_m \\ \omega = \omega_l + \omega_m}} Q_\omega^{l,m} \langle n_{1,l} n_{1,m} n_{1,l+m}^* \rangle = Y_Q^R + iY_Q^I = Y_Q \quad (6.37)$$

In this case, the imaginary part in Eq. (6.34b) reduces to:

$$\frac{L_\omega^I}{L_\omega^R} \left(1 - \frac{P_X + \frac{Y_Q^I}{L_\omega^I}}{P_X + \frac{Y_Q^R}{L_\omega^R}} \right)$$

This term represents the correction to the measured k_ω due to quadratic interactions. It can be neglected if the real and imaginary part of the total quadratic contribution are much smaller than the corresponding linear terms. The condition $Y_Q^R/L_\omega^R \ll 1$ implies that the variation of the amplitude due to quadratic interactions is negligible with respect to the growth rate. The condition Y_Q^I/L_ω^I implies that the phase variation due to quadratic interactions is negligible with respect to the linear wave dispersion. Using Eq. (6.23b), which relates $Q_\omega^{l,m}$ to $\Gamma_\omega^{l,m}$, Y_Q can be written as:

$$Y_Q = d_{\text{tip}} e^{i\Delta\theta_\omega} \sum_{\substack{\omega_l \geq \omega_m \\ \omega = \omega_l + \omega_m}} \Gamma_\omega^{l,m} \langle n_{1,l} n_{1,m} n_{1,l+m}^* \rangle$$

The measured coefficients $Q_\omega^{l,m}$ increase in amplitude with increasing d_{tip} , simply because fluctuations have more time to interact non linearly. For the measurement of the wavenumber the probe separation should be kept as small as possible to minimize the corrections on the phase shift due to nonlinear interactions. Conversely, if one is interested in the reconstruction of the coupling coefficients, the probe separation should be not too small. How large d_{tip} can be, depends on the degree of plasma inhomogeneity and on the limits of validity of the Fourier representation, Eq. (5.15).

Chapter 7

General properties of the instabilities observed on TORPEX

The instabilities observed on TORPEX have general features that are common to different experimental scenarios. The largest level of density fluctuations is measured where the pressure gradient is maximum and co-linear with the gradient of the magnetic field. Large-scale bipolar structures are usually detected in the density fluctuations. These structures form in the region of high fluctuation level, typically at the lower part of the plasma cross-section and on the low-field side of the maximum of the background density, then are observed to propagate (in the laboratory frame) along the $\mathbf{E}_0 \times \mathbf{B}$ direction. There are indications that their size is related to the wavelength and to the degree of turbulence in the spectrum [28].

Experiments in Hydrogen, Helium and Argon plasmas have been conducted on TORPEX, for different values of neutral gas pressure, injected microwave power, and vertical magnetic field. Typical values for density, electron and ion temperatures, and plasma potential are respectively $n_0 \simeq 10^{16} - 10^{17} \text{ m}^{-3}$, $T_{e0} \lesssim 5 \text{ eV}$, $T_{i0} \lesssim 0.1 \text{ eV}$, $\phi_{p0} \simeq 10 - 20 \text{ V}$. The background profiles are affected by external control parameters. This Chapter gives an overview of the dominant effects of selected control parameters on the time-average profiles and on the spectra of density fluctuations. Most of the examples are selected from Hydrogen plasmas, in which we have constructed the widest and most complete database for the identification and the characterization of the observed instabilities. The motivations leading to this choice are discussed in Sec. 7.1, where examples of plasmas from both Argon and Hydrogen are presented and the effect of the ion mass on the profiles and on the spectra is shortly discussed. In general, the value of the toroidal magnetic field is kept fixed at $B_\varphi = 76.6 \text{ mT}$ on axis and the vertical field is set at the value calculated for the optimization of the confinement time, namely $B_z = 0.6 \text{ mT}$ for Hydrogen and $B_z = 1.0 \text{ mT}$ for Argon [37], as discussed in Sec. 3.3. The effect of the variation of the magnetic field on the background profiles and on the fluctuation spectra is discussed in Sec. 7.3 for the toroidal component and in Sec. 7.4 for the vertical component. A neutral gas pressure of $p_0 = 6.0 \times 10^{-5} \text{ mbar}$ is taken as a reference, noting that this parameter has minor effects on the profiles and on the fluctuation spectra, as discussed in Sec. 7.5. When a control parameter is varied, the others are kept fixed at the relevant reference value, indicated in Table 7.1.

	B_φ (mT)	B_z (mT)	p_0 (10^{-5} mbar)	P_{RF} (kW)
reference	76.6	0.6 (Hydrogen)	6	0.4
value		1.0 (Argon)	2	
range	(71,89)	(0.2,1.8)	(2.5,14)	0.4, 1.0

Table 7.1: List of control parameters used for the scan and range of variation of each parameter. When one parameter is varied in a scan, the others are kept fixed at the reference values reported in the first line.

	Argon		Hydrogen	
Neutral pressure (mbar)	2×10^{-5}		3.5×10^{-5}	
B_z (mT)	1		0.6	
Connection length (m)	42		58	
Collision type	$\sigma[10^{-20} \text{ m}^2]$	λ_{mfp} (m)	$\sigma[10^{-20} \text{ m}^2]$	λ_{mfp} (m)
Coulomb	8.2	76	8.2	76
e/n scattering	10.7	5.8	1.87	20
Ionization	2.6	23	0.61	60

Table 7.2: Collision cross-sections and corresponding mean-free paths for Coulomb collisions, scattering of electrons on neutrals and ionisation for Argon and Hydrogen plasmas. Values refer to a test electron with parallel energy equal to 5 eV. A representative value of 50 eV is assumed for the perpendicular energy of the suprathermal electrons responsible for ionisation [40]. The length of a field line connecting the bottom to the top of the vacuum vessel at the center is also reported.

7.1 Ion mass

The ratio of the ion to electron mass can affect the drift wave dispersion relation, introducing electromagnetic corrections. As mentioned in Sec. 2.4, the phase velocity of drift waves along the magnetic field is in the range $v_{\text{thi}} < \omega/k_{\parallel} < v_{\text{the}}$. When ω/k_{\parallel} approaches the Alfvén speed, $v_A = (B_0^2/\mu_0\rho_0)^{1/2}$, the magnetic field lines are expected to be distorted by the perturbation. Using the definition of β , the ratio of the plasma pressure n_0T_{e0} to the magnetic pressure, $B_0^2/2\mu_0$, the condition $v_A < v_{\text{the}}$ implies $\beta > m/M$. Although on TORPEX β is typically $10^{-4} - 10^{-5}$, it can be larger than m/M if ions are sufficiently heavy. For fixed temperature and magnetic field there is then a ‘critical’ density value above which the electrostatic approximation is expected to fail. For $B_0 \simeq B_{\varphi} = 76.6$ mT and $T_{e0} = 3$ eV, this value is approximately $7 \times 10^{16} \text{ m}^{-3}$ for Argon plasmas, a limit often reached even in case of low absorbed power, as shown in Fig. 7.1. Conversely, in Hydrogen plasmas the measured densities are well below the corresponding ‘critical’ value of $2 \times 10^{18} \text{ m}^{-3}$. This Thesis focuses on electrostatic instabilities and preference is given to plasmas from Hydrogen, for which β can be assumed to be zero.

Figure 7.1 shows examples of time-averaged profiles measured in Hydrogen and Argon plasmas for the reference values of magnetic field and pressure. The density is

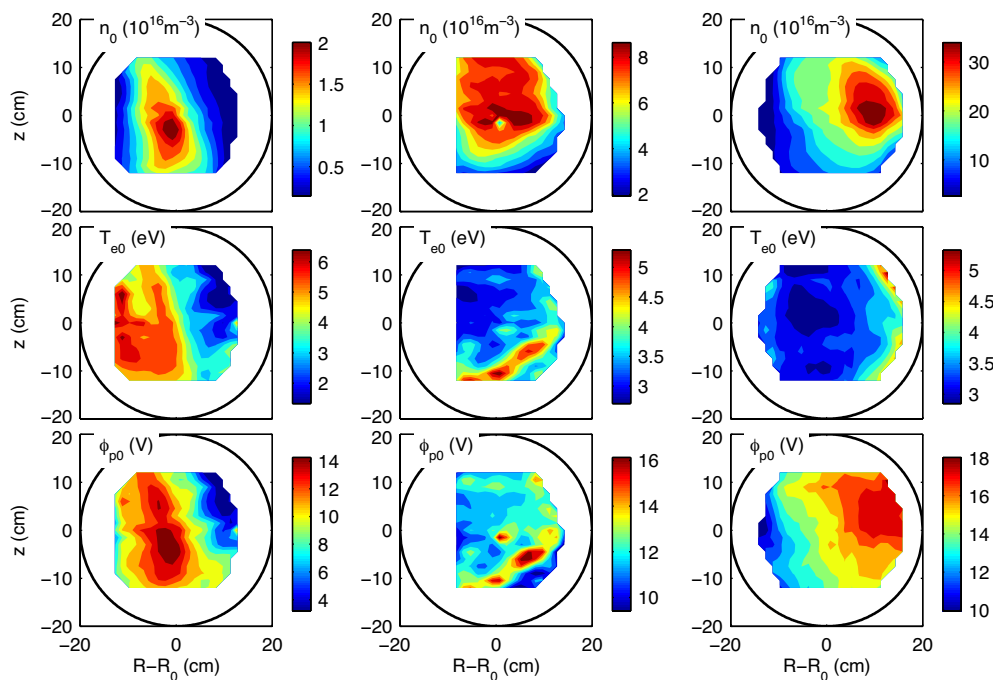


Figure 7.1: Left: time-averaged profiles of density, temperature and plasma potential for an Hydrogen plasma at $p_0 = 2.5 \times 10^{-5}$ mbar, with 0.3 kW of absorbed power, and $B_z = 0.6$ mT. Center: same as left column, but for an Ar plasma at $p_0 = 2.5 \times 10^{-5}$ mbar, with 0.6 kW of absorbed power, and $B_z = 1.0$ mT. Right: same as center column, but for 2 kW of absorbed power.

higher in Argon than in Hydrogen plasmas, because of the larger ion inertia and the higher cross section for the ionization [42]. Typical values for the collision cross-sections and the corresponding mean free paths, calculated for the two gases, are reported in Tab. 7.2 and in [42]. The electron temperature is similar for the two gases, although slightly larger values are measured in Hydrogen plasmas. In the latter case the density profiles are also generally more symmetric along the vertical direction and less extended along R . This symmetry is usually maintained for injected power up to 10 kW, while Argon plasmas assume in some cases a bean-like shape. The database available for plasmas from Helium is still incomplete, and limited to the measurement of the ion saturation current from the HEXTIP array. Density profiles appear to be qualitatively similar to Hydrogen plasmas. The profiles of temperature and plasma potential are not available, but - on the basis of the comparison between Hydrogen and Argon plasmas - there are reasons to believe that the maximum temperature is similar to that measured in the other two gases. The effect of control parameters, as the vertical field and the neutral gas pressure, on the profile of the total density and on the statistical properties of coherent structures in Helium plasmas is discussed in a previous Thesis work [34].

7.1.1 Spectral features

The ion mass M has a direct effect on the value of the ion cyclotron frequency, $\omega_{ci} = ZeB/M$. For the reference value of the toroidal field, the ion cyclotron frequency is approximately 30 kHz for Argon and 1.2 MHz for Hydrogen plasmas. Figure 7.2 shows two examples of the power spectrum of \tilde{n} measured in Argon plasmas. The absorbed microwave power is respectively 2 and 10 kW. The power spectrum of \tilde{n} is peaked at frequencies close to the ion cyclotron frequency, thus the approximation of $\omega \ll \omega_{ci}$ fails. In this Thesis we focus on low frequency electrostatic fluctuations, with $\omega \ll \omega_{ci}$. The general properties of plasma profiles and fluctuations spectra and their dependence on the various control parameters will therefore be discussed in the rest of this Chapter only for Hydrogen plasmas.

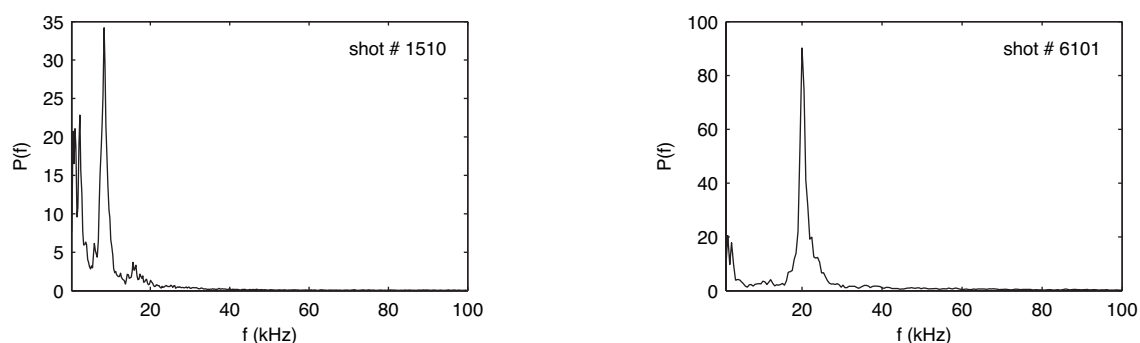


Figure 7.2: Power spectrum of density fluctuations, measured in an Argon plasma, with $B_z = 1.0$ mT, $p_0 = 2 \times 10^{-5}$ mbar, and absorbed power approximately 2 kW (left) and 10 kW (right).

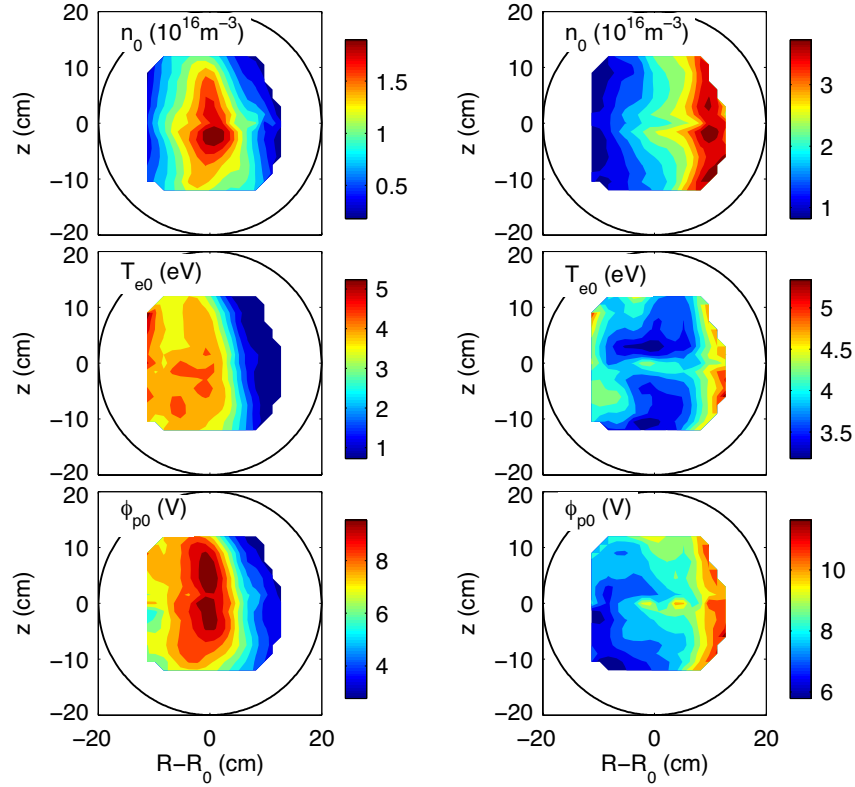


Figure 7.3: Time averaged profiles of density, temperature and plasma potential for a Hydrogen plasma at $p_0 = 6 \times 10^{-5}$ mbar, with 0.3 kW (left) and 1 kW (right) of absorbed power.

7.2 Microwave power

Plasmas on TORPEX are generated and sustained by microwaves. As discussed in Sec. 3.4, the main absorption and ionization occur at the Upper Hybrid resonance layer [40][42]. Due to the dependence of the UH resonance frequency on the plasma frequency, $\omega_{pe} = (4\pi e^2 n_e / m_e)^{1/2}$, the position of the UH layer depends on the value of the plasma density. If the background density profiles are known from the experiments, the position of the UH layer can be found from the equation [42]:

$$n_{\text{UH}} [10^{17} \text{ m}^{-3}] = \frac{f_{\text{RF}}^2 [\text{GHz}]}{8} \left[1 - \left(\frac{R_{\text{EC}}}{R} \right)^2 \right] \quad (7.1)$$

where n_{UH} denotes the value of the density at the position where $f_{\text{UH}} = f_{\text{RF}}$. Figure 7.3 shows an example of the time-averaged profiles measured in a Hydrogen plasma, for two values of absorbed power, $P_{\text{RF}} \sim 0.3$ kW and $P_{\text{RF}} \sim 1$ kW. Working at a low level of absorbed power offers two practical advantages.

First, the position of the maximum of n_0 , T_{e0} and ϕ_{p0} is centered with respect to the plasma cross section. This allows one to measure the background gradients and the fluctuations over an extended region around the maximum of the peak density, and

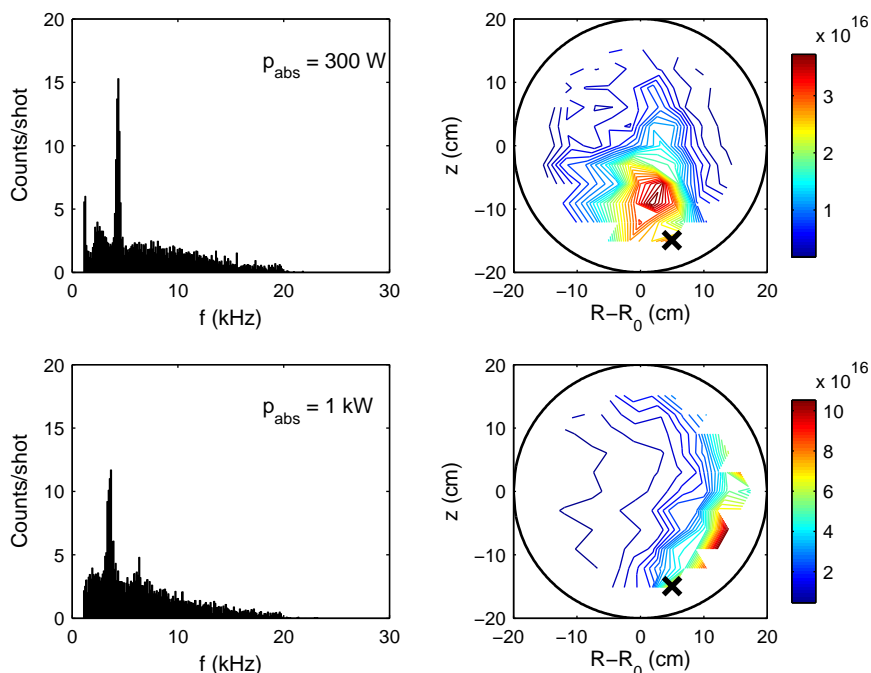


Figure 7.4: Left: number of counts related to the frequency of peaks detected in the power spectrum of \tilde{n} measured over the whole plasma cross-section, for two levels of absorbed power. Right: profile of the amplitude of \tilde{n} associated with the mode at 4 kHz for $P_{\text{RF}} = 0.3$ kW (top) and $P_{\text{RF}} = 1.0$ kW (bottom). The black crosses indicate the position where the spectra in Fig. 7.5 are measured.

to compare the destabilizing role of the pressure gradient and of the curvature of the magnetic field lines.

Second, the fluctuation level is lower than with larger absorbed power. Fluctuations can be treated as small perturbations on top of a constant background, identified with the time-averaged value (Sec. 5.2). A univocal dispersion relation can be defined and measurements can be compared to linear models for the drift-wave dispersion relation. For all the experiments presented herein, the injected power is kept constant at 0.4 kW, with an absorbed power of approximately 80%.

7.2.1 Spectral features

The general characteristics of density fluctuations do not show appreciable variations when the absorbed power is increased by a factor of three. A mode at low frequency, with $f_0 \sim 4$ kHz is measured in the power spectrum of \tilde{n} both for low and high absorbed power, as shown in Fig. 7.4. Here we represent the histogram of the frequencies of peaks detected in the power spectrum of \tilde{n} , reconstructed using the method described in Sec. 5.3. The maximum amplitude for this mode is measured in both cases on the low field side of the maximum of n_0 and at the lower part of the plasma cross-section. The wavenumber and frequency spectrum $P(k_\theta, \omega)$ measured at the lower part of the poloidal cross-section with one of the FLP arrays is shown in

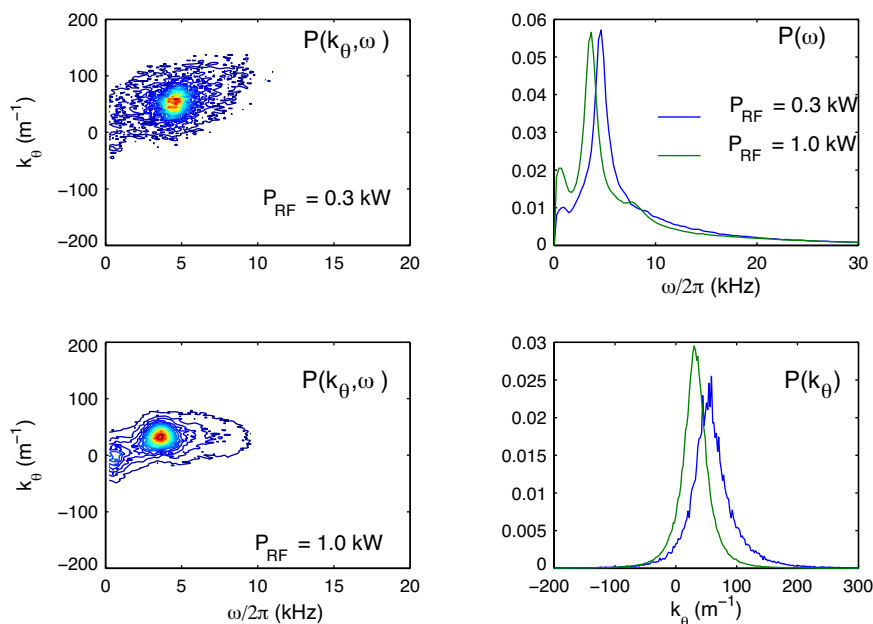


Figure 7.5: Left: Wavenumber and frequency spectrum measured at the lower part of the poloidal cross-section with one of the FLP arrays, at the positions indicated in Fig. 7.4. Right: Frequency spectrum (top) and wavenumber spectrum (bottom) calculated from $P(k_\theta, \omega)$, for the two levels of absorbed power.

Fig. 7.5. The mode is fairly localized both in ω - and k_θ -spaces, indicating a low degree of turbulence. Increasing the microwave power from 0.3 to 1 kW results in a decrease of the frequency and the wavenumber of the mode of 0.7 kHz and 30 m^{-1} , respectively. This variation is consistent with the local values of the background parameters, under the hypothesis that the velocity in the laboratory frame is the electron diamagnetic drift velocity corrected for the $\mathbf{E}_0 \times \mathbf{B}$ drift.

7.3 Toroidal magnetic field

As discussed in Sec. 3.2, an upper limit of 100 mT to the amplitude of the toroidal field is imposed by the frequency of the microwave source. For $B_\varphi = 76.6 \text{ mT}$ on axis, the position of the EC resonance layer is at $R - R_0 = -12.5 \text{ cm}$. If B_φ is increased, the position of the EC resonance layer shifts towards larger R . This causes also the position of the UH resonance, thus that of the maximum density, to move towards the low field side, as indicated by Eq. (7.1).

Figure 7.6 shows the profiles of n_0 and \tilde{n} measured for different values of B_φ in the range $[72, 85] \text{ mT}$. In this range the position of the EC resonance layer moves from -19 to 1.4 cm . The profiles of n_0 and \tilde{n} are calculated respectively from the average value and from the standard deviation of I_{sat} , measured with HEX TIP, assuming a uniform electron temperature of 5 eV . For each value of B_φ the injected microwave power is ramped up from 0 to 10 kW during 100 ms. The profiles shown in the figure

are measured during the first 30 ms of discharge, where the level of absorbed power is constant and approximately equal to 0.3 kW.

7.3.1 Spectral features

The power spectrum of density fluctuations is peaked at 4 kHz for toroidal field values in the range between 73 mT and 85 mT, as shown in Fig. 7.7. The case at 77 mT is the same as described in the previous section, and the wavenumber and frequency spectrum $P(k_\theta, \omega)$ measured at the lower part of the plasma cross-section is shown in Fig. 7.5.

The amplitude of the mode is maximum at the lower part of the plasma cross-section, and always on the low field side with respect to the maximum n_0 . When B_φ is increases from 73 mT up to 85 mT, the frequency of the mode decreases by approximately 10%. However, we cannot conclude that this effect is merely due to a variation of B_φ , because it cannot be excluded that the background pressure and the electric field vary as well.

7.4 Vertical magnetic field

As discussed in Sec. 3.3, particle losses along the magnetic field lines are directly affected by the pitch angle, *i.e.* the ratio B_z/B_φ . For given B_φ , the larger B_z , the shorter the connection length. We expect therefore the direct particle losses to dominate with increasing vertical magnetic field. On the other hand, owing to a more efficient compensation of the particle drifts associated with the curvature and the gradient of the magnetic field, a better up-down symmetry can be achieved. Figure 7.8 shows the time-averaged profiles of density, temperature and plasma potential, reconstructed from the $I - V$ characteristics of the SLP array, during 300 ms of stationary plasma discharge, with absorbed power of approximately 0.4 kW. The vertical magnetic field is increased from 0.2 to 1.8 mT. The case with a purely toroidal magnetic field is not considered here, neither are vertical fields larger than 3 mT, because of the loss of toroidal symmetry. For 3 mT the vertical displacement of a magnetic field line after a complete turn, calculated on axis, is 36 cm, comparable to the diameter of the vessel.

The connection length¹, calculated as the length of the field line connecting the bottom to the top of the vessel at R_0 , varies from 147 m for $B_z = 0.2$ mT down to approximately 16 m for $B_z = 1.8$ mT. With reference to Fig. 7.8, the density profile is centered with respect to the cross-section and symmetric along R , at least in the range of B_z considered here. A variation of the maximum n_0 below 20% is measured when the vertical field is increased by a factor of three, while the temperature and the

¹For a toroidal magnetic field the connection length depends on the distance from the torus main axis:

$$L_c = 2 \frac{B_\varphi}{B_z} \sqrt{a^2 - (R - R_0)^2} \quad (7.2)$$

where $a = 0.2$ m and $R_0 = 1$ m are respectively the minor and major radius. The toroidal field B_φ is defined as $B_\varphi = B_0 R_0 / R$, where $B_0 = 76.6$ mT is the value at R_0 .

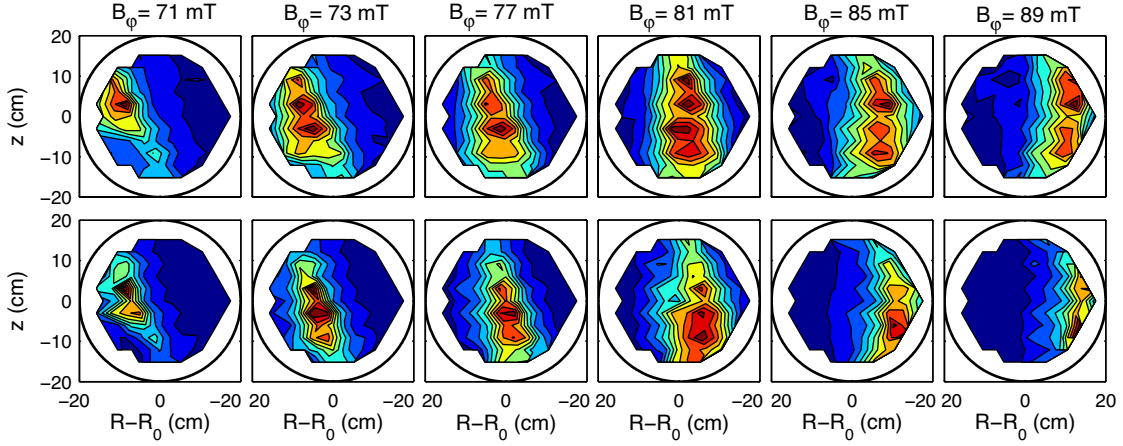


Figure 7.6: Profile of the time-averaged density (top) and of the fluctuating density (bottom) for different values of the toroidal magnetic field. The values on the top refer to B_ϕ on axis.

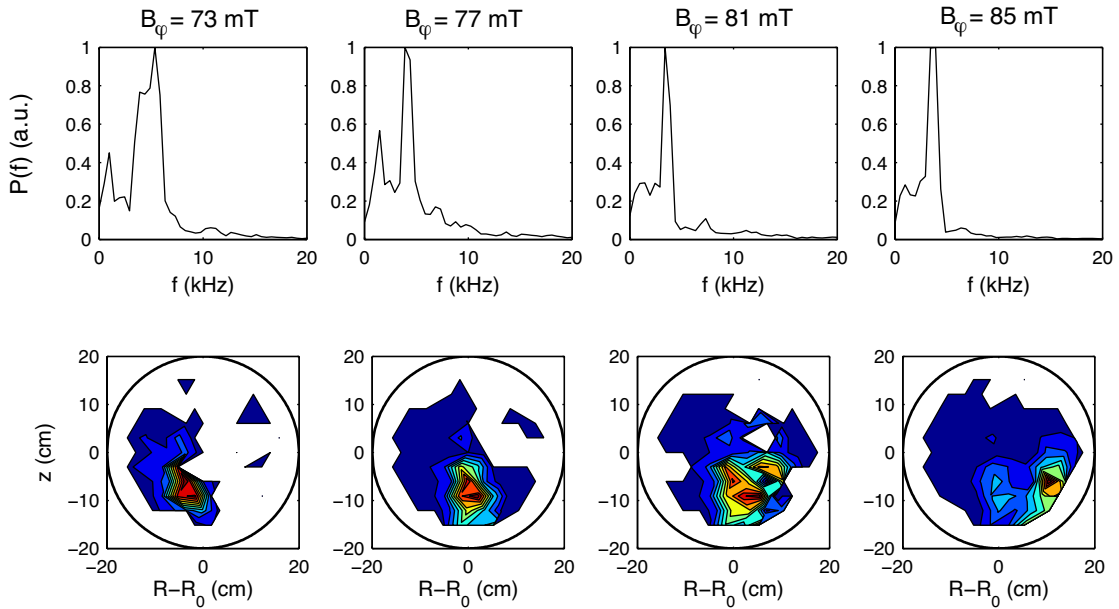


Figure 7.7: Top: Power spectrum of density fluctuations, measured with the HEX TIP array at the lower part of the plasma cross-section, $(R - R_0, z) = (0, -10)$ cm. Bottom: Profile of the rms value of fluctuations associated with the dominant mode in the power spectrum.

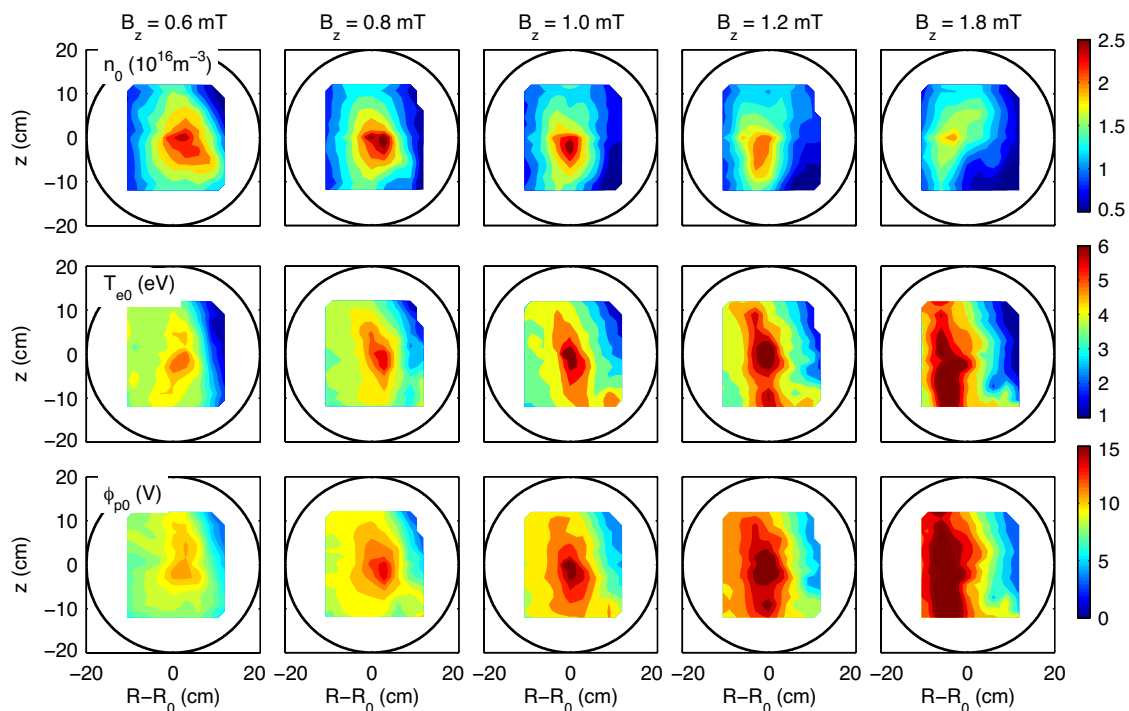


Figure 7.8: time average profiles of density (top), temperature (middle) and plasma potential (bottom) for different values of the vertical field

electrostatic potential increase approximately by 40%. The profiles of T_{e0} and ϕ_{p0} are generally more elongated along z than density profiles.

7.4.1 Spectral features

Figure 7.9 shows the radial profile of the normalized density fluctuations, \tilde{n}/n_0 , for $B_z \in [0.4, 1.8]$ mT, measured at the midplane with the TRIP array. With an exception represented by the lowest value of B_z , for which the normalized fluctuations are comparable for all the radial positions, for $B_z > 0.4$ mT the largest values of \tilde{n} are measured on the low field side of the maximum n_0 . The power spectra of \tilde{n} , measured at $R - R_0 = -9$ cm and at $R - R_0 = 6$ cm, exhibit distinct features. A mode with frequency $f_0 \simeq 4$ kHz is measured for $B_z \geq 0.6$ mT on both the high and the low field side, with spectral power larger on the low field side. The frequency and the spectral width of the mode are barely affected by the value of B_z . A second mode with frequency larger than f_0 , indicated in the following as f_1 , is measured only on the low field side. Contrary to the mode at f_0 , the frequency, amplitude and width of this mode are strongly affected by the value of the vertical field.

Differences in the radial localization and in the dependence on B_z indicate that the two modes are related to two distinct instabilities. Their spectral properties will therefore be analyzed separately. The dispersion relation of the mode at frequency f_0 will be analyzed for $B_z = 0.6$ mT and discussed more in detail in Chap. 8. For this value of the vertical field, in fact, the instability at frequency f_1 does not develop and

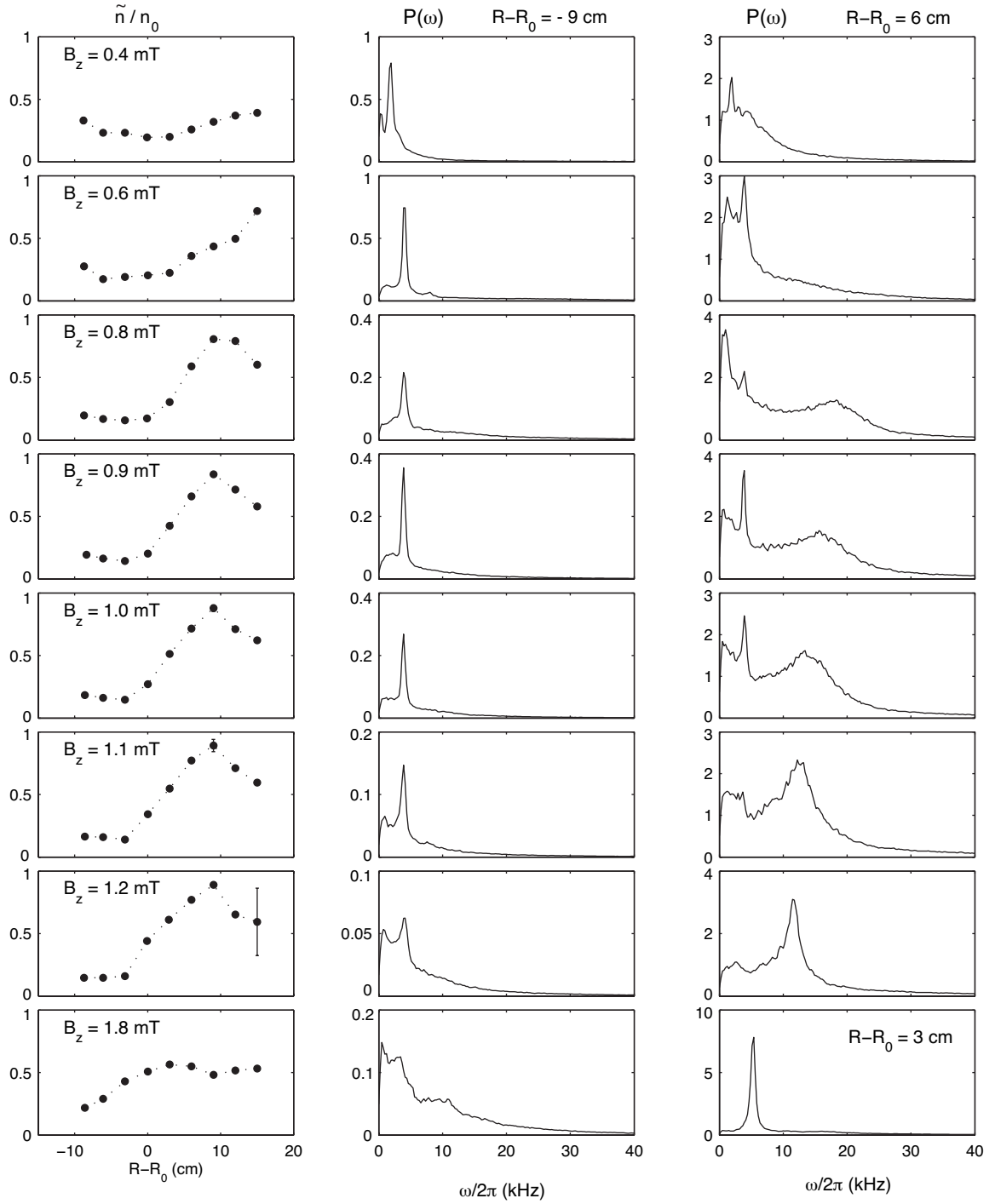


Figure 7.9: Radial profile of \tilde{n}/n_0 (left) for $B_z \in [0.4, 1.8]$ mT, with the value of B_z increasing from top to bottom. Power spectrum of \tilde{n} (a.u.), measured for the same values of B_z on the high (center) and on the low (right) field side.

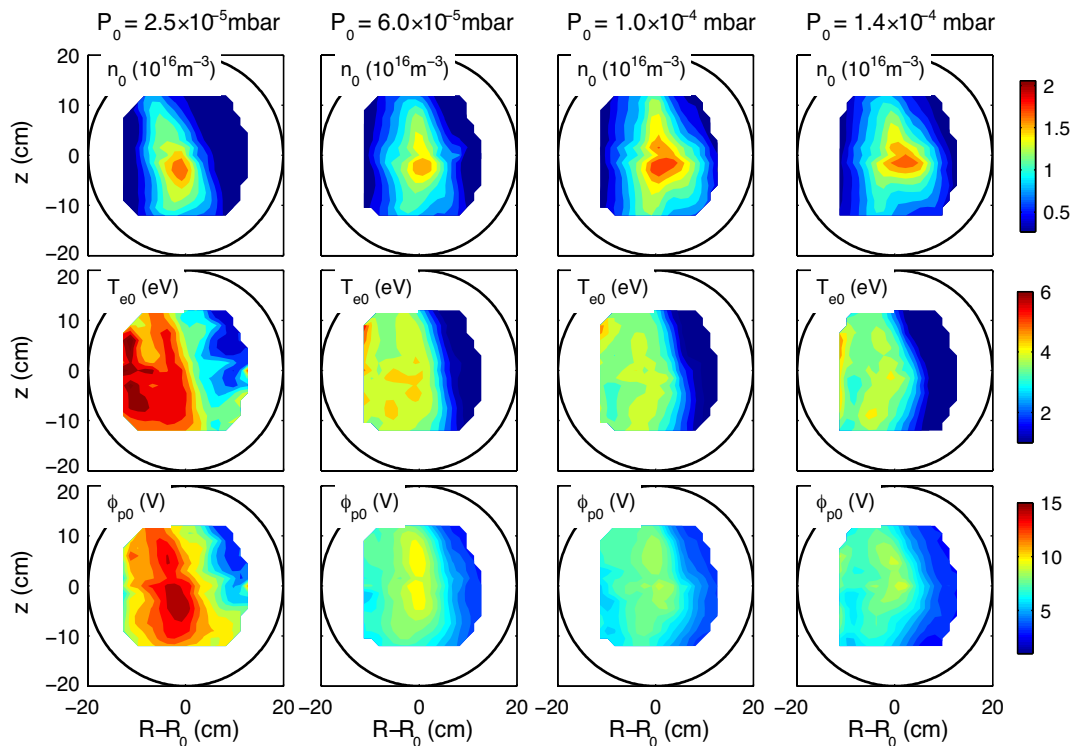


Figure 7.10: Time-averaged profiles of n_0 , T_{e0} and ϕ_{p0} , for $p_0 \in [2.5, 14] \times 10^{-5}$ mbar.

the power spectrum is peaked at frequency f_0 . The spectral properties and the linear dispersion relation of the mode at frequency f_1 will instead be discussed in Chap. 9.

7.5 Neutral gas pressure

The neutral gas pressure affects the plasma production mechanisms [43] and the rate of collisions of plasma particles with neutrals. For the values of p_0 considered here, $[2.5, 14] \times 10^{-5}$ mbar, the electron-neutral collision frequency varies in the range $[2, 20] \times 10^4 \text{ s}^{-1}$. Density profiles are barely affected by the value of the neutral gas pressure, as shown in Fig. 7.10. The maximum value of n_0 does not show appreciable variations with increasing p_0 , while the temperature and the electrostatic plasma potential decrease by approximately 30% when p_0 increases from 2.5×10^{-5} mbar to 6×10^{-5} mbar. No appreciable variations are measured for further increases of the neutral gas pressure.

7.5.1 Spectral features

No major variations of the main spectral features are observed with increasing p_0 from 2.5×10^{-5} to 1.4×10^{-4} mbar. The global, statistical spectral features for each value of the pressure are summarized by the histogram of the central frequency of peaks detected in the power spectrum of \tilde{n} , shown in Fig. 7.12. The histogram is obtained from the measurement of I_{sat} from HEX TIP, over the whole plasma cross-section, using

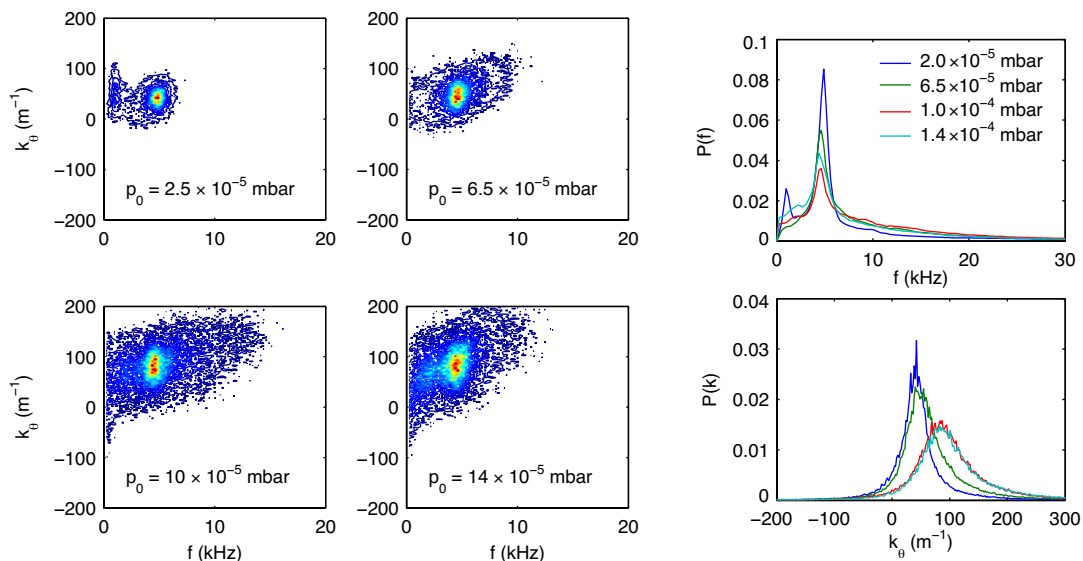


Figure 7.11: Wavenumber and frequency spectrum for density fluctuations, measured with the FLP array at the lower part of the plasma cross-section, at $(R - R_0, z) = (3, -15.5)$ cm.

the method described in Sec. 5.3. Results for floating potential fluctuations are very similar and are not shown here. As the number of shots used for the statistical estimate of the histogram is not the same for the different configurations, the number of counts in each frequency range has been normalized to the number of shots used for the analysis. The values indicated on the vertical axis represent therefore the average number of counts per shot.

Increasing the gas pressure from 2.5×10^{-5} to 6.0×10^{-5} mbar results in a decrease of the frequency of approximately 0.5 kHz, as results from the position of the maximum of the ‘most probable’ frequency in the histogram. This frequency shift seems to be related to differences in the pressure profile and in the background electric field. No variations of the central frequency of the mode are in fact observed for a further increase of the pressure, where the time-averaged profiles of pressure and plasma potential do not vary. For all values of p_0 , the fluctuations associated with the dominant mode have their maximum amplitude at the lower part of the plasma cross-section and in the unfavourable curvature region (Fig. 7.12).

Figure 7.11 shows the power spectrum $P(k_\theta, \omega)$ measured at the lower part of the plasma cross-section with one of the FLP arrays. The power spectrum is peaked in frequency and wavenumber for all the values of p_0 . The amplitude of the dominant mode decreases, possibly because of a larger degree of turbulence. The development of turbulence is indicated in particular by a broadening of the wavenumber spectrum, whose width is representative of the correlation length. The decrease of the correlation length is accompanied by a decrease of the wavelength of the dominant mode when p_0 increases from 6×10^{-5} mbar up to 10^{-4} mbar [28].

The main effect of the neutral gas pressure is therefore on the degree of turbulence, rather than on the nature of the instabilities or in their linear dispersion relation, the

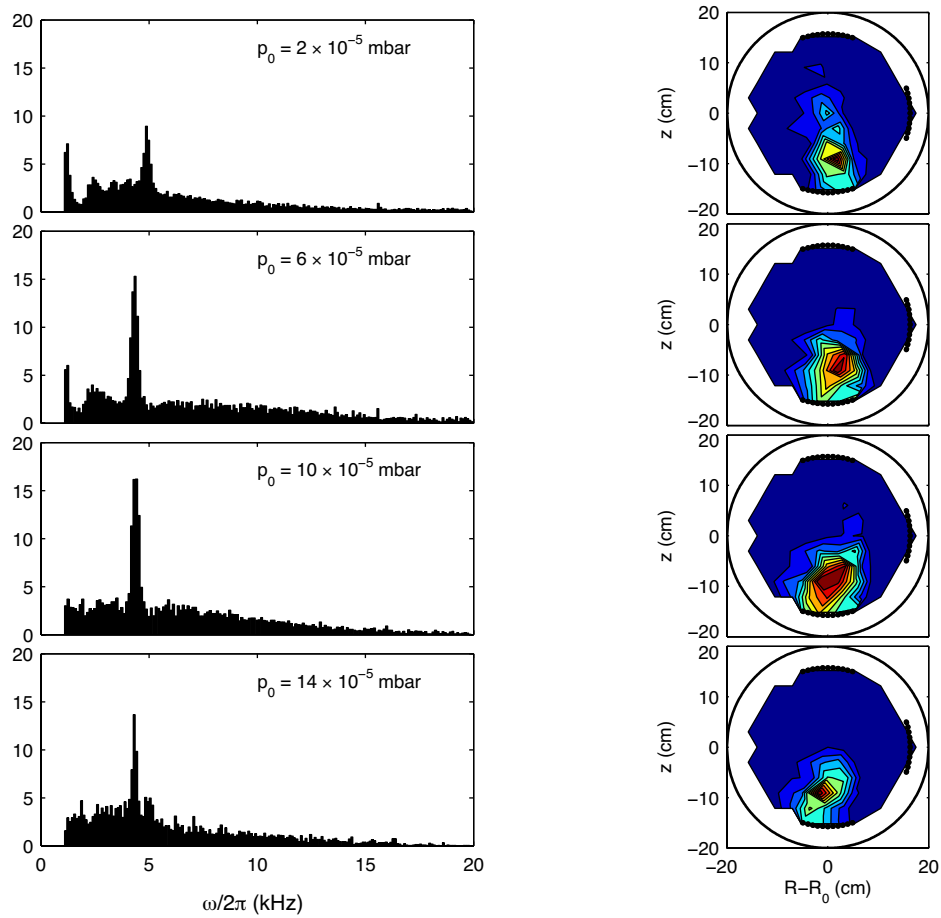


Figure 7.12: Left: Average number of counts per frequency per shot, reconstructed from the power spectrum of density fluctuations measured from the I_{sat} of the HEXTIP array. The plots refer to different values of the neutral gas pressure between 2.5×10^{-5} mbar and 14×10^{-5} mbar (from top to bottom). Right: reconstructed profile of the amplitude of density fluctuations with frequency approximately equal to 4 kHz.

effect being more evident for larger injected powers [28].

7.6 Summary and discussion

We have shortly presented in this Chapter an overview of the main features of plasmas on TORPEX and their dependence on external control parameters. We have discussed in particular the effect of the gas type and neutral gas pressure, of the level of microwave power and of the amplitude of the magnetic field on the time-averaged profiles and on the power spectra. We concentrate primarily on Hydrogen plasmas, because of the high ion cyclotron frequency, much larger than the frequency of the observed fluctuations. Moreover, time-averaged plasma profiles maintain their symmetry along R and z when the external control parameters are varied.

The time-averaged profiles are mostly influenced by the microwave power level through the mechanisms of absorption and ionization at the Upper Hybrid resonance layer. The maximum of the density shifts towards larger R with increasing power, as discussed in detail in [40][42]. A configuration with $P_{\text{RF}} \simeq 0.3$ kW will be taken in the rest of this Thesis for the analysis of the linear properties of electrostatic instabilities on TORPEX. At low power the time-averaged pressure profile is centered with respect to the poloidal cross-section and the fluctuation level is below 40%.

The maximum of n_0 is barely affected by the other control parameters and the density profiles maintain horizontal and vertical symmetry when the magnetic field or the neutral gas pressure are changed. Conversely, the temperature and plasma potential profiles are affected by the value of p_0 up to 6×10^{-5} mbar and become more elongated along z with increasing vertical field.

Among the control parameters, the vertical magnetic field has the strongest influence on the character of the instabilities. Two modes with distinct features are detected in the power spectrum of density fluctuations for different B_z values, most probably related to instabilities of different nature. These instabilities will be discussed more in detail in the next Chapters. At low vertical field, $B_z = 0.6$ mT, one of the two modes dominates the power spectrum of density fluctuations. Its frequency is barely affected by the other control parameters, the only variations being related to modifications in the background profiles.

Chapter 8

Identification and characterization of drift-interchange instabilities

Two distinct types of instabilities can be identified in Hydrogen plasmas, as discussed in the previous Chapter. The first is detected both on the high and on the low field side with respect to the maximum of the density profiles. The characterization of its linear dispersion relation is the subject of this Chapter.

The analysis is conducted in an experimental configuration characterized by a low degree of turbulence, where the power spectrum peaks at a definite frequency and wavenumber. The relatively low level of fluctuations makes it possible to define a background profile, distinct from a small, fluctuating component superimposed onto it. The microwave power level is fixed at $P_{\text{RF}} = 0.3$ kW to maintain pressure profiles centered on the poloidal cross-section. This simplifies the analysis of the properties of fluctuations and the effect of the curvature of the magnetic field lines over an extended region around the maximum of the density profile. Other parameters are set to standard values (see Table 7.1).

After a brief introduction on the background and fluctuation profiles (Sec. 8.1), we discuss the spectral properties of density and potential fluctuations (Sec. 8.2). The source region, *i.e.* the geometrical location where an instability is generated, is identified from measurements of the power spectra of \tilde{n} and $\tilde{\phi}_f$ over the whole plasma cross-section (Sec. 8.2). The linear dispersion relation is measured at different locations, starting from the source region and following the convection path. It will be shown in Sec. 8.3 that the power spectrum of \tilde{n} is narrow at the frequency and the wavenumber of the mode close to the location of generation, then broadens during convection away from the source region. The dispersion relation, measured across and along the magnetic field, is consistent with the drift-wave dispersion relation and the perpendicular phase velocity, corrected for the $\mathbf{E}_0 \times \mathbf{B}$ Doppler shift, is comparable to the electron diamagnetic drift velocity. A comparison with the numerical solution of the kinetic dispersion relation derived in Chap. 2 demonstrates that the curvature is essential for the destabilization of these modes, which are identified as drift-interchange.

8.1 Background and fluctuation profiles

Figure 8.1 shows the background profiles of n_0 , T_{e0} , and ϕ_{p0} , reconstructed from the time-averaged value of the corresponding parameters, calculated from the $I - V$ characteristics of the SLP array during 200 ms of discharge with constant absorbed power of 0.3 kW. The profiles of pressure and plasma potential are vertically elongated and have their maximum at $R \simeq R_0$, where $n_0 \simeq 1.8 \times 10^{16} \text{ m}^{-3}$ and $\phi_{p0} \simeq 9 \text{ V}$. The electron temperature is approximately constant to 4 eV for $R < R_0$ and decreases for $R > R_0$. The inverse temperature gradient scale length, $L_T^{-1} = |\nabla T_{e0}/T_{e0}|$, is maximum at $r_s = R - R_0 \simeq 5 \text{ cm}$. At this position L_T is comparable with $L_n = |\nabla n_0/n_0|^{-1} \simeq 5 \text{ cm}$. The profile of ϕ_{p0} is reconstructed from the floating potential ϕ_{f0} and from the electron temperature as $\phi_{p0} = \phi_{f0} + \mu T_{e0}/e$ [44][45], with $\mu = 3.15$ [42], as described in Sec. 4.1. The strong gradient of ϕ_{p0} on the low field side gives rise to a inhomogeneous electric field whose maximum value is reached at r_s . This results in a non-uniform $\mathbf{E}_0 \times \mathbf{B}$ drift:

$$\mathbf{v}_E = \frac{\mathbf{E}_0 \times \mathbf{B}}{B^2} = \frac{\mathbf{B} \times \nabla \phi_{p0}}{B^2}. \quad (8.1)$$

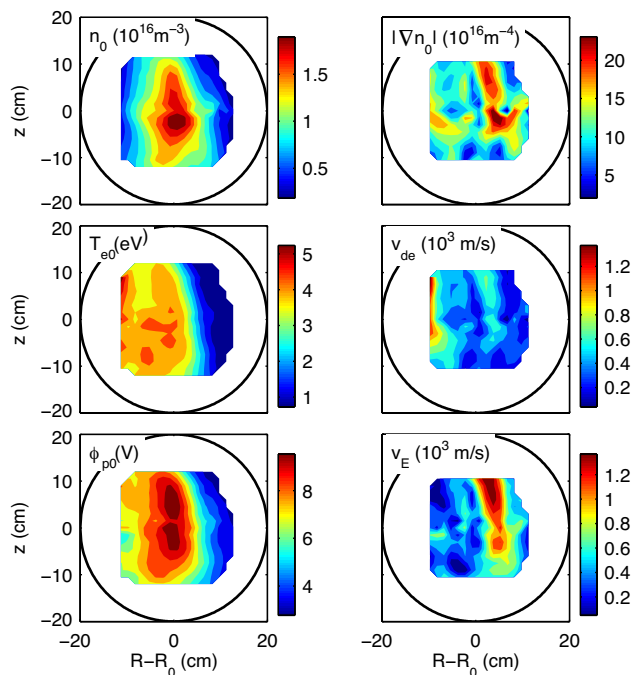


Figure 8.1: Left: Background profiles of n_0 , T_0 and ϕ_{p0} estimated from the $I - V$ characteristics of the SLP array. Profile of $|\nabla n_0|$, $|\mathbf{v}_{de}| = T_{e0}/(eBL_n)$ and $|\mathbf{v}_E|$. The toroidal field B_φ is directed into the plane of the figure, the electron diamagnetic velocity \mathbf{v}_{de} is clockwise and \mathbf{v}_E is counter-clockwise. The extension of the plasma source for this plasma is shown in Fig. 3.10.

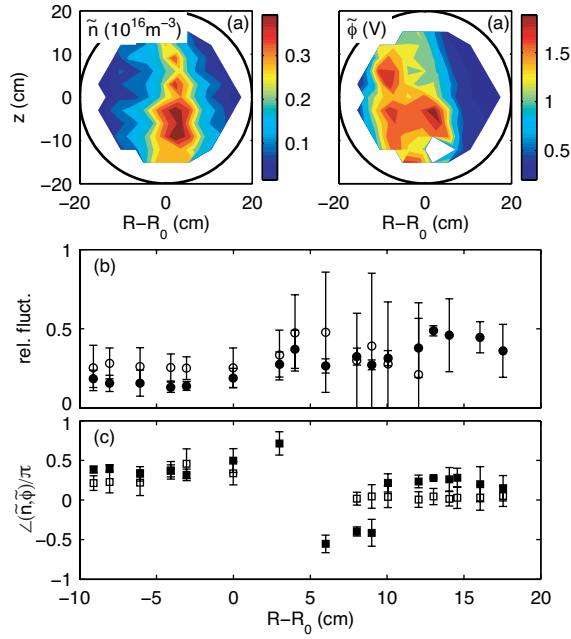


Figure 8.2: (a): Poloidal profiles of the rms value of \tilde{n} and $\tilde{\phi}_f$ estimated from the power spectrum, integrated over the frequency range (0, 125) kHz. (b): Profile of \tilde{n}/n_0 (full circles) and $e\tilde{\phi}_f/T_{e0}$ (open circles) at the midplane, measured with the TRIP array. (c): Average phase shift between \tilde{n} and $\tilde{\phi}_f$ at midplane, in the frequency ranges [0.7, 1.4] kHz (open squares) and [3.7, 5] kHz (full squares).

The electron diamagnetic drift \mathbf{v}_{de} , in general directed in the opposite direction, is calculated from the background profiles as:

$$\mathbf{v}_{\text{de}} = \frac{1}{eB^2} \frac{\nabla(n_0 T)}{n_0} \times \mathbf{B} \quad (8.2)$$

The rms values of density and potential fluctuations, \tilde{n} and $\tilde{\phi}_f$, are estimated as the square root of their power spectra, integrated over the frequency range covered by the measurements, (0, 125) kHz. Normalized temperature fluctuations, T_e/T_{e0} , are much lower in amplitude than density and potential fluctuations and are neglected in these measurements. Plasma potential fluctuations are therefore approximated by floating potential fluctuations, $\tilde{\phi}_p \approx \tilde{\phi}_f$.

Figure 8.2 shows the 2D profile of the rms values of \tilde{n} and $\tilde{\phi}_f$, measured with the HEX TIP array. Density fluctuations have their maximum for $R > R_0$, where ∇n_0 and ∇B are co-linear. This is a general feature on TORPEX, verified experimentally for a large variety of scenarios in Argon and Hydrogen plasmas, with microwave power in the range [0.1, 30] kW and neutral gas pressure in the range $[1, 20] \times 10^{-5}$ mbar. The normalized density and potential fluctuations, \tilde{n}/n_0 and $e\tilde{\phi}_f/T_{e0}$, are comparable in amplitude and vary at midplane between 20% and 50%, as shown in Fig. 8.2b.

Figure 8.2c shows the phase difference between \tilde{n} and $\tilde{\phi}_f$, $\angle(\tilde{n}, \tilde{\phi}_f)$, measured at the frequency of the dominant modes in the spectrum (see Fig. 8.3). The phase difference is below $\pi/2$ and constant over a wide range of positions over the midplane, with

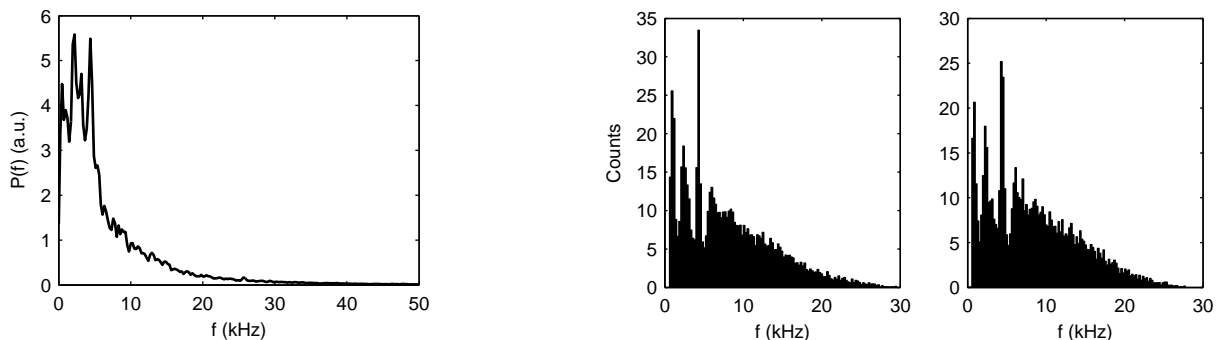


Figure 8.3: Left: Power spectral density of \tilde{n} , measured at $R - R_0 = 1.75$ cm, $z = -3$ cm, in the region of largest level of fluctuations. Right: Histogram of the central frequency of the peaks resulting from a recursive fit of the power spectrum of \tilde{n} (left) and $\tilde{\phi}_f$ (right), evaluated over a set of 24 discharges with HEXTIP in I_{sat} and 22 discharges with HEXTIP in floating potential configuration.

$\angle(\tilde{n}, \tilde{\phi}_f) \simeq 0$ for $R - R_0 > r_s$ for fluctuations with frequency in the range $[0.7, 1.4]$ kHz. Deviations from these values are measured at r_s for fluctuations with frequency in the range $[3.7, 5]$ kHz, probably due to the combined effect of the strong electric field and the large temperature gradient.

8.2 Spectral properties

The main contributions to the spectral power, measured at different locations over the cross-section, come from fluctuations below 30 kHz. Figure 8.3 shows the power spectrum of \tilde{n} , measured at $R - R_0 = 1.75$ cm, and $z = -3$ cm, *i.e.* in the region of large fluctuation level (see Fig. 8.2). Three modes dominate the power spectrum measured at this location, with frequency approximately 1, 2 and 4 kHz. Peaks at the same frequency are observed in the spectra measured over most of the poloidal cross-section, with deviations from the central value of less than 0.5 kHz. Nevertheless, depending on the location of measurement, the amplitude of the peaks can vary by more than one order of magnitude.

8.2.1 Reconstruction of the profile of spectral amplitude

The profile of the amplitude of fluctuations for the individual modes is reconstructed using the statistical method described in Sec. 5.3. From the HEXTIP array we measure at each position $(R - R_0, z)$ the power spectral density of \tilde{n} and $\tilde{\phi}_f$ over a set of discharges with the same parameters and background profiles.

The histogram of the central frequency of all peaks resulting from the fit of the power spectra of \tilde{n} and $\tilde{\phi}_f$, shown in Fig. 8.3, contains several pieces of information.

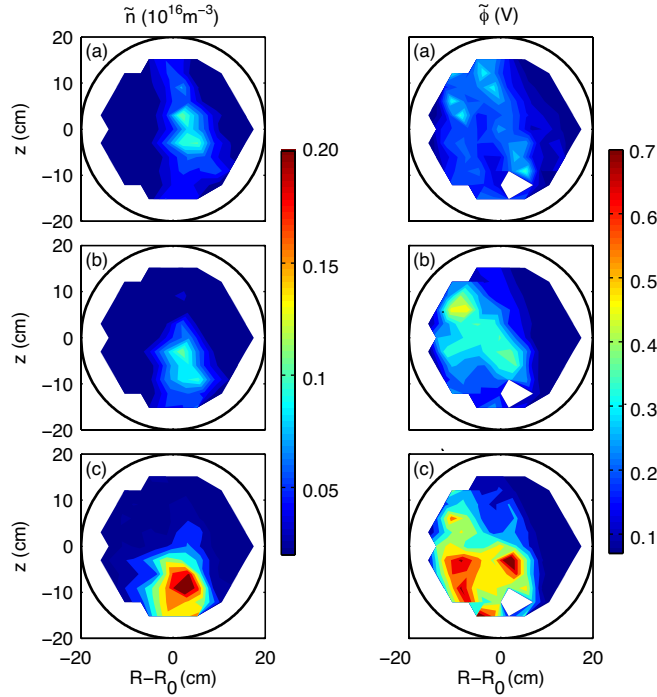


Figure 8.4: Profile of rms value of \tilde{n} (left) and $\tilde{\phi}_f$ (right) estimated in the frequency ranges [0.7,1.4] kHz (a), [1.4,3.7] kHz (b), and [3.7,5.0] kHz (c). The average frequency of the modes in each frequency range is, respectively, 1.0 kHz, 2.5 kHz and 4.3 kHz.

First, the histograms for \tilde{n} and $\tilde{\phi}_f$ are very similar and modes with the same frequency are measured in the power spectrum of both quantities, indicating that density and potential fluctuations are coupled. Second, the largest number of counts corresponds to frequencies below 5 kHz. The power spectrum shown in Fig. 8.3 is therefore representative of the frequencies detected in most of the poloidal cross section. Finally, the modes are distinct, with a statistical deviation from the central value of the frequency among different discharges smaller than the separation between adjacent peaks. This is also an indirect indication of good reproducibility of the plasma discharges.

Three non-overlapping frequency ranges are identified from the local minima in the histogram, namely [0.7,1.4] kHz, [1.5,3.5] kHz, and [3.6,5.0] kHz. Provided a frequency peak is measured at a given position over the poloidal cross-section, the rms value of \tilde{n} and $\tilde{\phi}_f$ is estimated, for each range, as the square root of the amplitude of the peak times its width, Eq. (5.8). The results of this operation for \tilde{n} and $\tilde{\phi}_f$ in each of the three frequency ranges are displayed in Fig. 8.4.

The regions of maximum amplitude of \tilde{n} for the peaks at 1 and 4 kHz are separated, indicating that these modes are generated at different locations. The region where the mode at 2 kHz is generated is at an intermediate position between the other two and partially overlaps with them. The profiles of \tilde{n} and $\tilde{\phi}_f$ appear quite different. However, the values of \tilde{n}/n_0 and $e\tilde{\phi}_f/T_{e0}$ associated with each mode are comparable in amplitude at the location where the modes are generated. They increase from approximately 6% for the modes at 1 and 2 kHz up to approximately 15% for the mode at 4kHz. The

linearized Boltzmann relation, $\tilde{n}/n_0 \cong e\tilde{\phi}/T_{e0}$, is therefore verified separately for the amplitude of each mode. One cannot conclude that in general electrons behave adiabatically as, for example, along the radial profile at the midplane, the phase $\angle(\tilde{n}, \tilde{\phi}_f)$ varies between 0 and $\pi/2$. After generation waves are subject to convection. Depending on the background profiles and the level of turbulence, a loss of the correlation between \tilde{n} and $\tilde{\phi}_f$ is observed.

The measurement of the phase shift between density and potential fluctuations is commonly used as a parameter for the identification of the nature of the instabilities. Under the hypothesis that electrons are adiabatic, the phase shift should be zero for non collisional drift waves, as results from Eq. (2.1) written in the Fourier space. The presence of collisions alters this value, cfr Eq. (2.3). A phase shift in the range of $[0, \pi/4]$ is usually attributed to collisional drift waves, while a phase shift close to $\pi/2$ is attributed to interchange modes [26][12][61].

The value of the phase is nevertheless affected by many factors, usually not taken into account in simplified linear theories. The presence of a temperature gradient, or the nonlinear coupling between \tilde{n} , \tilde{T}_e and $\tilde{\phi}_p$ introduce corrections in the expression relating density and electrostatic potential. Apart from these physical factors, measurements are in practice affected by \tilde{T}_e , neglected in most cases, and by the finite distance between tips, both effects quantified in App. E.3. As shown in Fig. 8.2, no clear conclusion on the nature of the instability can be drawn from the measurement of the phase shift between density and potential fluctuations.

The value of the phase shift has direct implications on the estimate of the fluctuation-induced particle flux. If the phase is independent of the nature of the instabilities, one cannot define ‘typical’ particle fluxes associated with instabilities of different nature. Experiments on TORPEX have demonstrated in fact that interchange and drift instabilities give comparable values of the particle flux related to fluctuations [40].

8.3 Measurement of the dispersion relation

In addition to the determination of the region where unstable modes are generated, a reconstruction of the dispersion relation both perpendicular and parallel to \mathbf{B} is necessary to determine the nature of the instabilities. We measure the wavenumber and frequency spectrum $P(k, \omega)$ by applying the two-point correlation technique [53] to the \tilde{I}_{sat} signals from two probes with small separation with respect to the correlation length (Sec. 5.4.1):

$$P(k, \omega) = \frac{1}{M} \sum_{j=1}^M I_{\Delta k}[k - k^{(j)}(\omega)] \frac{1}{2} [P_1^j(\omega) + P_2^j(\omega)]. \quad (8.3)$$

Here M is the number of independent realizations extracted from the time traces of the probes and the function $I_{\Delta k}[k - k^j(\omega)]$ is defined in Sec. 5.4.1. In Eq. (8.3) $P_1^j(\omega)$ and $P_2^j(\omega)$ are the power spectra of the two probe signals measured for each sample j , while $k^j(\omega)$ represents the local wavenumber estimated from their cross-spectrum. The width of the bins in k -space, Δk , is chosen to minimize the variance of $P(k, \omega)$ at the values of k and ω associated with the observed peaks.

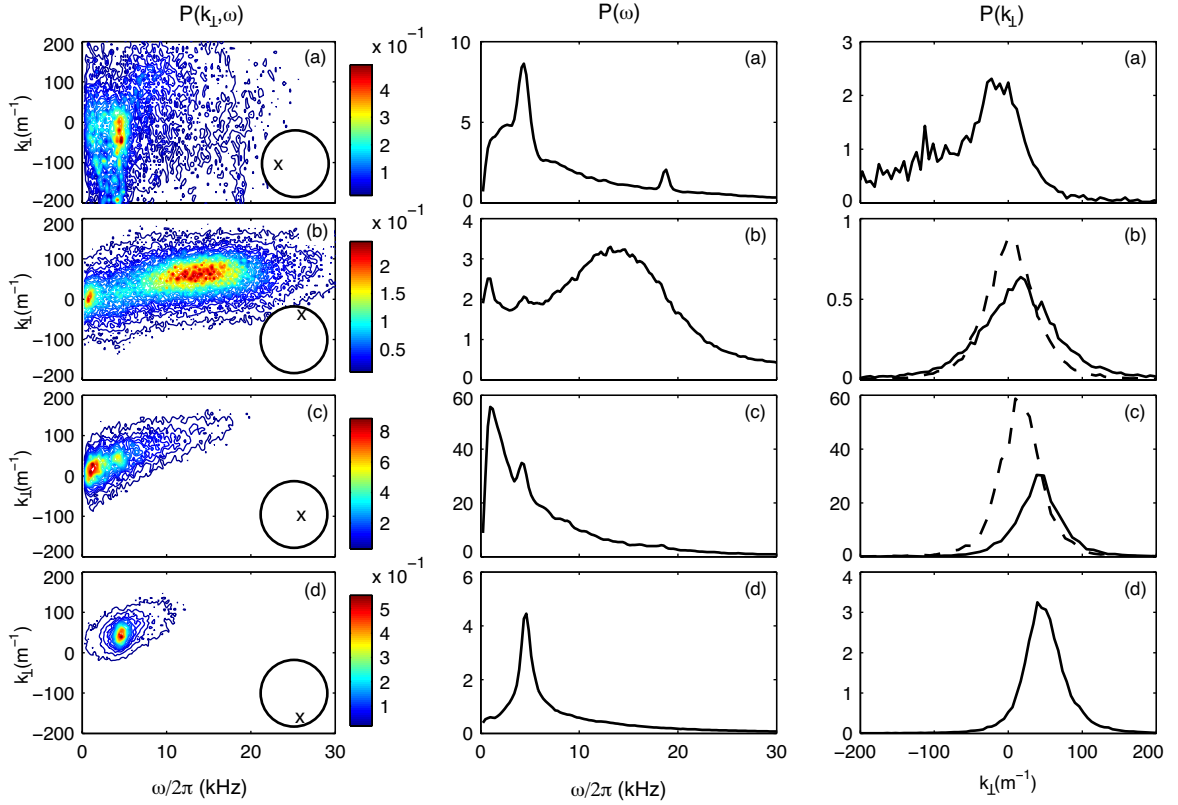


Figure 8.5: Left: Wavenumber and frequency spectrum $P(k_{\perp}, \omega)$; the insets show the position of measurements on the poloidal cross-section, namely $(R-R_0, z) = (-9, 0)$ cm (a), $(R-R_0, z) = (0.5, 16)$ cm (b), $(R-R_0, z) = (6, 0)$ cm (c), $(R-R_0, z) = (3.5, -15.3)$ cm (d). Plot (c) should be compared with Fig. 8.4a-b, plot (d) should be compared to Fig. 8.4c. Center: Frequency spectrum $P(\omega)$, calculated as integral of $P(k_{\perp}, \omega)$ over all wavenumbers k_{\perp} . Right: Wavenumber spectrum $P(k_{\perp})$ calculated from the integral of $P(k_{\perp}, \omega)$ over $\omega \pm \sigma_{\omega}$, where ω and σ_{ω} are defined by a fit over $P(k_{\perp}, \omega)$ with a gaussian function. The dashed lines refer to $P(k_{\perp})$ relative to the mode at 1 kHz, continuous lines to the mode at 4 kHz. The peak at 18 kHz in the power spectrum measured on the high field side (a) is not related to any mode.

8.3.1 Perpendicular wavenumbers

The power spectrum in terms of the wavenumber perpendicular to the magnetic field is measured at midplane, at different values of $R-R_0$, with the TRIP probe array and along the azimuthal direction with the FLP arrays. In the first case we can estimate the statistical dispersion relation along z , in the second case that along θ . In this Section we'll indicate case by case the power spectrum for the different components, $P(k_z, \omega)$ or $P(k_{\theta}, \omega)$, as $P(k_{\perp}, \omega)$. Figure 8.5 shows the measurements taken at four positions over the poloidal cross-section, azimuthally separated by approximately 90° . The frames have been arranged from bottom to top in Fig. 8.5 according to the (counter-clockwise) direction of the $\mathbf{E}_0 \times \mathbf{B}$ drift, starting from the bottom of the poloidal cross-section, where the amplitude of the mode at 4 kHz is the largest. Positive values of k_{\perp} in

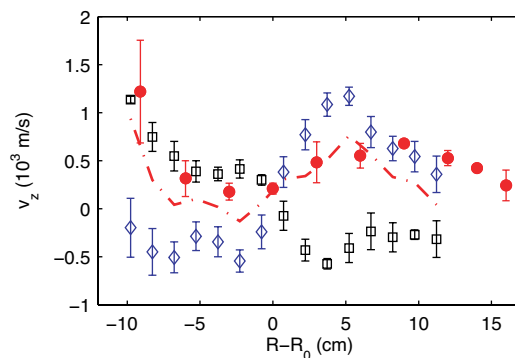


Figure 8.6: Radial profile of the phase velocity v_{ph} of the mode at 4 kHz (full circles) measured at midplane, z component of \mathbf{v}_{de} (squares) and of \mathbf{v}_E (diamonds). The difference $|\mathbf{v}_{de} \cdot \hat{\mathbf{Z}}| - |\mathbf{v}_E \cdot \hat{\mathbf{Z}}|$ is reported for comparison (dash-dot line).

Fig. 8.5 indicate propagation along the direction of \mathbf{v}_E .

Frames (a) and (c) in the figure refer to measurements performed with the TRIP probe array at two midplane positions, respectively in the region of good and bad curvature, $R - R_0 = -9$ cm and $R - R_0 = 6$ cm. At these positions the scale lengths of the density gradient are comparable and approximately equal to 5 cm, but on the LFS the amplitude of \tilde{n} is one order of magnitude larger. This is also the location where ∇n_0 , ∇T_{e0} and E_0 have their maximum amplitude, and is identified in Sec. 8.2 as ‘source’ region for the mode at 1 kHz. It is worth noting that at midplane the density gradient is directed along R , as can be seen from the profiles in Fig. 8.1, thus $k_{\perp} \equiv k_z$ at $R - R_0 = -9$ cm and $R - R_0 = 6$ cm. Frame (d) shows measurements in the region identified as ‘source’ for the mode at 4 kHz, while frame (b) shows measurements in the upper portion of the poloidal cross-section. The background profiles are not available at these locations.

The power spectral density is localized both in ω and k_{\perp} at the location where the mode at 4 kHz has its maximum amplitude, as can be seen comparing Fig. 8.5d and Fig. 8.4. The frequency and the wavenumber of the mode, as well as the spectral width in ω and k_{\perp} , are estimated from a two-dimensional gaussian fit. We find $\omega/2\pi = 4.6$ kHz and $\sigma_{\omega}/2\pi = 1.2$ kHz, consistently with the mean value and the spread of frequencies in the range [3.7, 5.0] kHz calculated over the whole plasma cross-section. The fit over the wavenumbers gives $k_{\perp} = 48$ m $^{-1}$, which corresponds to a perpendicular wavelength of 12 cm. The inverse width of the wavenumber spectrum $\sigma_{k_{\perp}}^{-1} \approx 13$ cm, gives a local estimate of the correlation length on the plane perpendicular to the magnetic field.

At the upper part of the cross-section (Fig. 8.5b), the power spectrum $P(k_{\perp}, \omega)$ broadens. The value of $\sigma_{k_{\perp}}$ increases, indicating a reduction of the correlation length, *i.e.* an increase in the degree of turbulence. At the same time, the maximum of $P(k_{\perp})$ shifts towards lower values of k_{\perp} for both the modes, although a secondary peak at 40 m $^{-1}$, possibly associated with the mode at 4 kHz, can still be detected in $P(k_{\perp})$. The broad band feature observed in the range [8,25] kHz corresponds to a coherent spectrum in k_{\perp} , with maximum at 55 m $^{-1}$. As it will be discussed in next Chapter, the

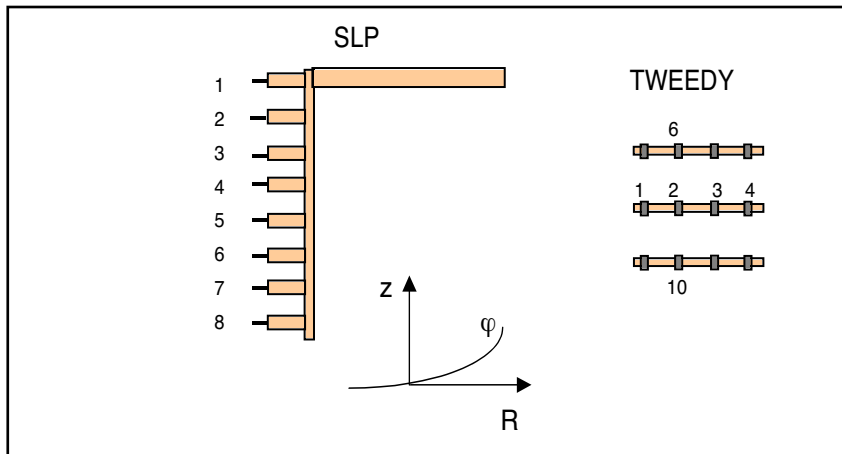


Figure 8.7: Convention adopted in the numeration of tips in the TWEEDY and SLP arrays.

dispersion properties of this mode are consistent with a pure interchange instability, as observed for $B_z > 0.6$ mT.

8.3.2 Phase velocity

The profile of the phase velocity of the mode at 4 kHz is estimated at midplane as the average value of the ratio ω/k_z weighted on $P(k_z, \omega)$, using Eq. (5.22). The power spectrum $P(k_z, \omega)$ is fitted with a bi-dimensional gaussian function centered on the frequency and wavenumber of the mode. The sum is then calculated over a range of frequencies and wavenumbers $\omega \pm \sigma_\omega$, $k_z \pm \sigma_{k_z}$ defined by the spectral width of the peak in ω - and in k_z -space. Figure 8.6 shows the radial profile of the phase velocity, as well as the projection along z of \mathbf{v}_{de} and \mathbf{v}_E , calculated from the time-averaged profiles. As results from the profiles of n_0 and ϕ_{p0} in Fig. 8.1, \mathbf{v}_{de} and \mathbf{v}_E have opposite directions. The density and the plasma potential gradients are directed radially at midplane and the corresponding drifts are vertical. The phase velocity measured in the laboratory frame is in good agreement with the difference of their amplitudes, $|\mathbf{v}_{de} \cdot \hat{\mathbf{z}}| - |\mathbf{v}_E \cdot \hat{\mathbf{z}}|$. Deviations from the exact value are within the errors due to the estimate of E_0 from ϕ_{p0} .

8.3.3 Parallel wavenumber

The parallel wavenumber is measured at midplane from the phase shift between the SLP and the TWEEDY arrays, with the geometrical arrangement shown in Fig. 5.8. Figure 8.7 reproduces a sketch of the two arrays along with the convention used to numerate the tips. The SLP tip#1 and the TWEEDY tip#2 are located on the equatorial plane and toroidally separated by $\pi/2$. During measurements over the radial position, they are kept at the same R . The wavenumber and frequency spectrum $P(k, \omega)$ is calculated for each combination of pairs SLP-TWEEDY.

Figure 8.8 shows measurements done with respect to TWEEDY tip#2 at different

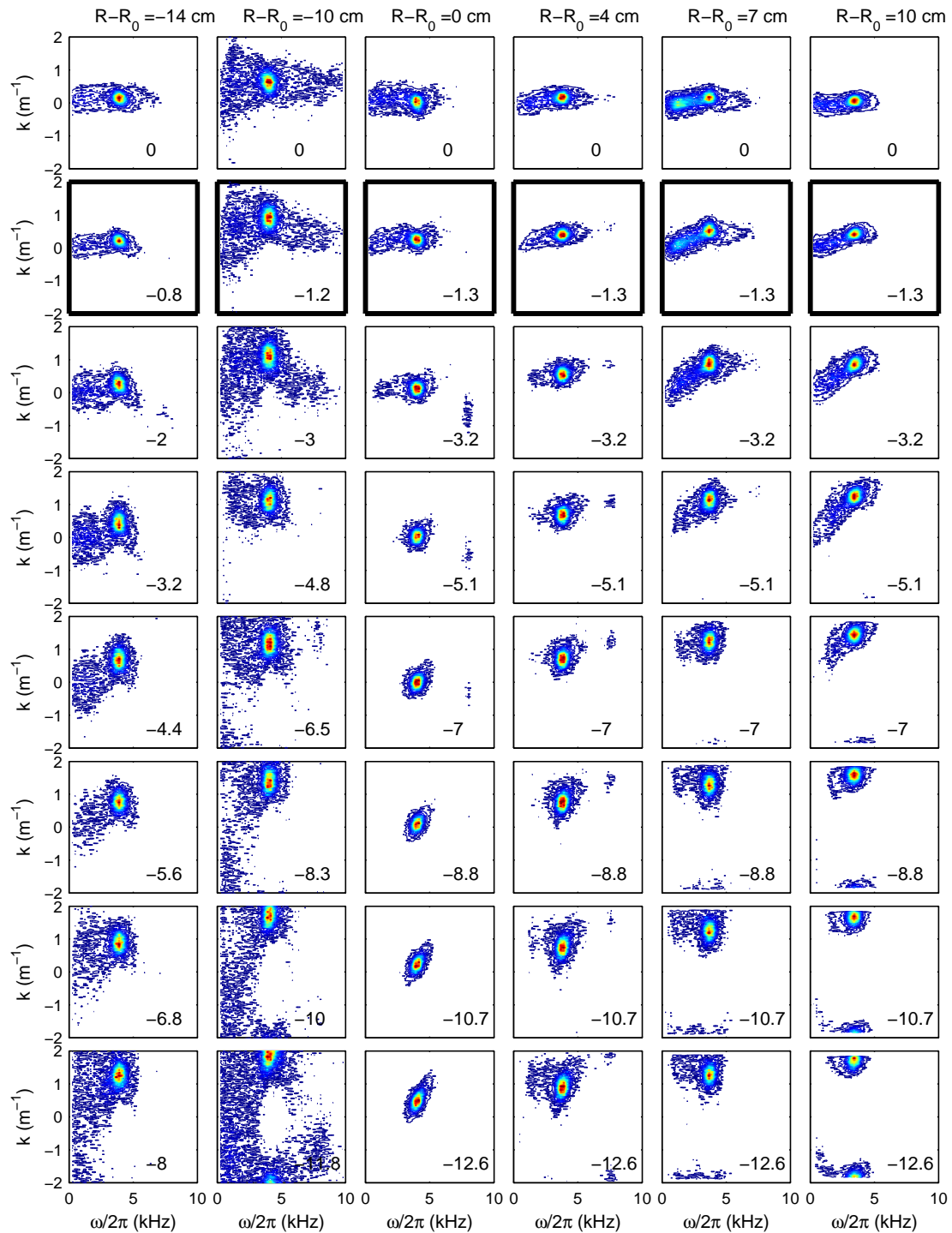


Figure 8.8: $P(k, \omega)$ measured between each tip in the SLP array and the TWEEDY tip#2 at different radial positions. The value of $R - R_0$ increases from left to right in the figure. SLP tip#1 is on top, SLP tip#8 is on bottom of the figure, the vertical coordinate of each tip (units of cm) is reported in the plot. The thick axes indicate measurements corresponding to the best alignment with the magnetic field line.

radial positions. The coordinate z_0 that corresponds to the vertical displacement of the field line that intersects TWEEDY tip#2 and the SLP array increases from 0.9 to 1.5 cm in the range $-14 \leq R - R_0 \leq 4$ cm. As shown in the figure, for a fixed position R , the measured wavenumber increases in absolute value with the vertical distance from the field line, because of the contribution of the projection of k_\perp along the direction of measurement (see Sec. 5.4.4 and App. D). The aliasing effect in k in the reconstruction of $P(k, \omega)$ is visible for measurements taken at $R - R_0 = -10$ cm and $R - R_0 \geq 7$ cm, when Δz approaches 10 cm. Differences in the value of k measured at the same vertical position, but at different R , are most probably due to the effect of k_\perp , which is not constant along R (see Fig. 8.6).

Figure 8.9 shows the value of the coherence spectrum measured at 4 kHz, at $R - R_0 = -14$ cm and at $R - R_0 = 4$ cm. At both positions the maximum value of the coherence is measured with the SLP tip closest to z_0 , then it decreases with increasing the distance from the field line. At $R - R_0 = -14$ cm, in particular, a second maximum is measured in the coherence, at a distance of approximately 4.5 cm from the first. This position corresponds to the intersection of a field line that passes through the position occupied by TWEEDY after a complete turn:

$$z_1 = \frac{B_z}{B_\varphi} R (\Delta\varphi + 2\pi)$$

The measured wavenumber as a function of the vertical separation between tips is shown in Fig. 8.9. For the sake of completeness and to increase the statistical significance of the linear fit, we have added in the figure also the wavenumbers measured using TWEEDY tip#6 and tip#10. At $R - R_0 = -14$ cm $k_\parallel = 0.21 \text{ m}^{-1}$ at the position where the coherence is maximum; this value corresponds to a parallel wavelength of 30 m, shorter than the connection length at this location, $L_c = 41$ m. For comparison, the wavenumber measured at the second maximum of coherence, correcting for the total length of the field line, is 0.16 m^{-1} , comparable with the measurement taken at the absolute maximum of coherence. On the low field side $k_\parallel = 0.39 \text{ m}^{-1}$, almost twice than the value measured on the high field side.

8.4 Comparison with linear theory

The measured dispersion relation is compared with the numerical solution of the theoretical dispersion relation derived in Chap. 2. The ion temperature is assumed to be uniform, while a gradient is allowed in the temperature profile. The effect of the $\mathbf{E}_0 \times \mathbf{B}$ drift and of the gradient and curvature of the magnetic field are included as ‘external’ forces \mathbf{F} perpendicular to \mathbf{B} in the dispersion relation, Eq. (2.13) and Eq. (2.27), which we report here below for simplicity:

$$\epsilon(\mathbf{k}, \omega) = 1 + \sum_\alpha \frac{1}{(k\lambda_D)^2} \left[1 - \int d\mathbf{v} \frac{f_{0\alpha}}{n_\alpha} \frac{\omega - (\omega_n + \omega'_T + \omega_E)}{\omega - (\omega_E + \omega_B + k_\parallel v_\parallel)} J_0^2 \left(\frac{k_z v_\perp}{\Omega} \right) \right]. \quad (8.4)$$

The cartesian reference used in Chap. 2 to derive the slab dispersion relation is replaced here by the cylindrical coordinates adopted in Chap. 3. The x and y directions,

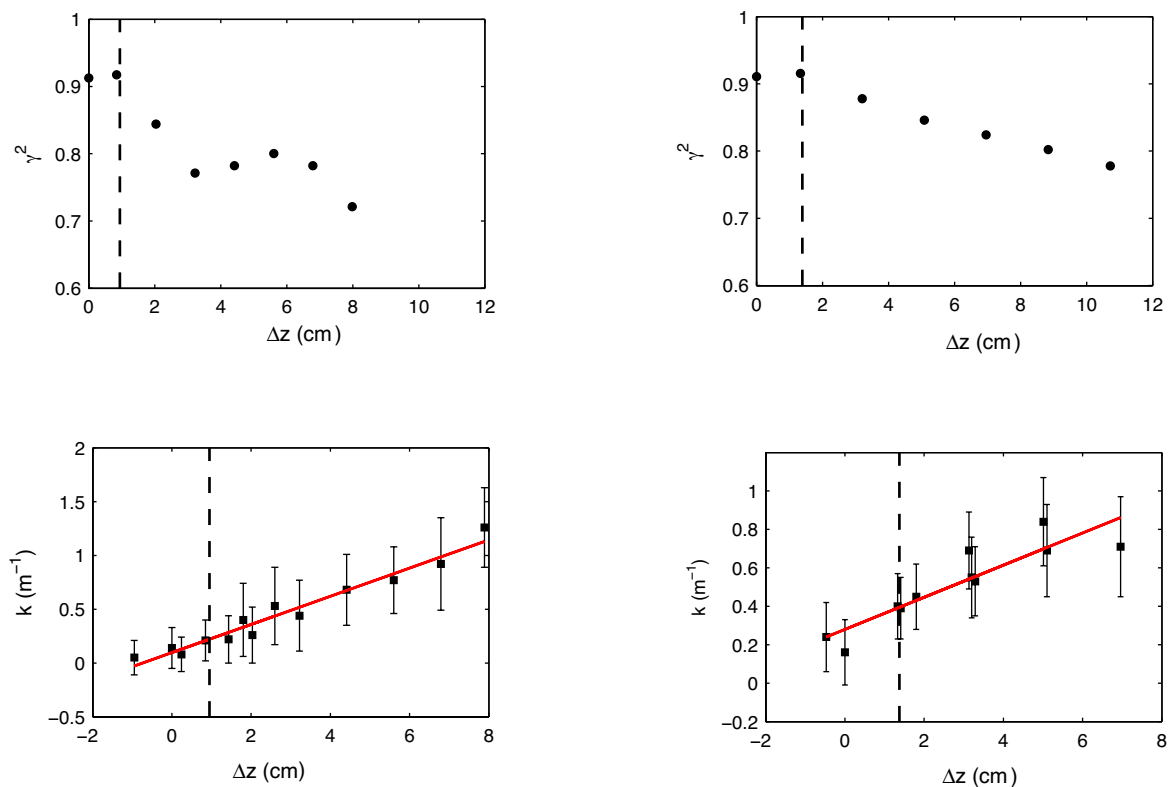


Figure 8.9: Top: Value of the coherence spectrum associated with the unstable mode at 4 kHz, measured between the 8 tips in the SLP probe array and the TWEEDY tip#2. Bottom: wavenumber measured with respect to TWEEDY tips#2, 6, 10. Plots refer to measurements done at $R - R_0 = -14$ cm (left) and $R - R_0 = 4$ cm (right).

respectively associated with the background gradients and with the drifts, are replaced by R and z , while the magnetic field direction is indicated with ‘ \parallel ’. The various drift terms are defined in Chap.2, Eq. (2.25). The dependence on the velocity in the term ω_B is maintained and the integral over the perpendicular and parallel velocities is evaluated numerically to correctly represent the resonant denominator, which is essential to study marginal stability.

Figure 8.10 shows the solution of the dispersion relation calculated at midplane, on the high and on the low field side, for the local values of the background parameters. Equation (8.4) has been solved first assuming the pressure gradient as the only driving mechanism, then adding the curvature term. The solution has been calculated on the high field side for $k_z = 20$ m^{-1} and $k_{\parallel} = 0.2$ m^{-1} and on the low field side for $k_z = 40$ m^{-1} and $k_{\parallel} = 0.4$ m^{-1} . After having calculated the solution for these values, the dependence of the real frequency and of the the growth rate on k_{\parallel} has been studied keeping fixed k_z . On the high field side the measured frequency is in fairly good agreement with the real frequency in the range of the measured k_{\parallel} . For the local values of L_n , L_T and E_0 , unstable solutions are found for $k_{\parallel} < 0.4$ m^{-1} , although the most unstable solution has a value of k_{\parallel} almost ten times smaller than the measured values.

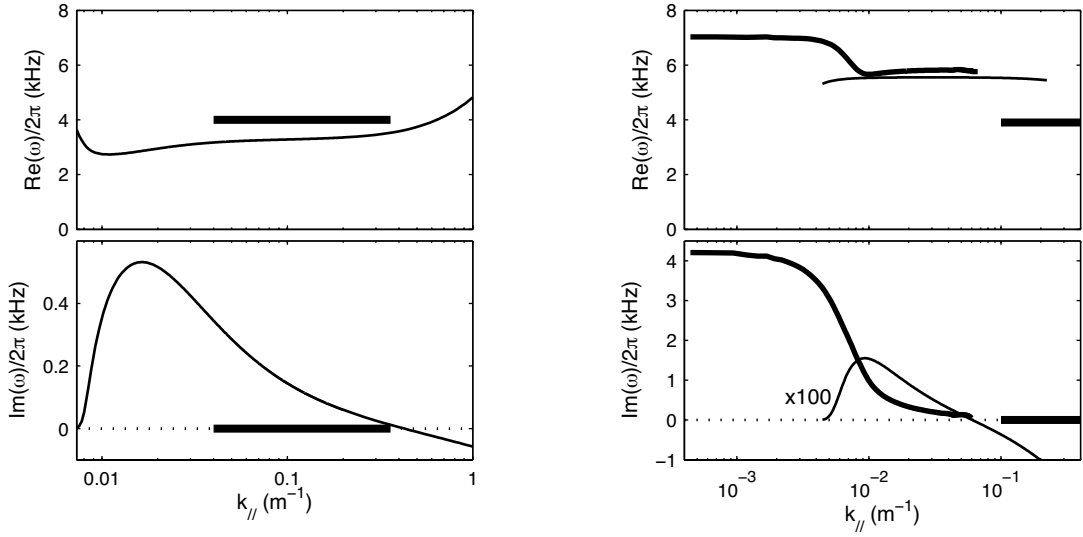


Figure 8.10: Left: Solution of the dispersion relation calculated on the high field side without the curvature term, for $L_n = 5$ cm, $L_n/L_T = 0$, $E_0 = 20$ V/m. The thick horizontal bar represents the measured k_{\parallel} , including the error bar. In the top figure k_{\parallel} is plot at the vertical coordinate corresponding to the measured frequency, in the bottom plot it is plotted on the horizontal axis. Right: Solution of the dispersion relation calculated on the low field side, for $k_z = 40$ m⁻¹, $L_n = L_T = 5$ cm, $E_0 = 90$ V/m. The thick horizontal lines refer to the result with the curvature term, the thin lines refer to the result without the curvature. In the latter case the growth rate is multiplied times 100 for graphical representation.

On the low field side the pressure gradient alone is not sufficient to destabilize the modes in the measured k_{\parallel} range. The solution of the dispersion relation is unstable only if the curvature is taken into account. In the latter case the growth rate increases with decreasing k_{\parallel} , as expected for interchange drive, and decreases with increasing k_{\parallel} down to approximately 10^{-3} times the real frequency for the experimental k_{\parallel} values. The dispersion relation has been solved including the curvature also for $R < R_0$, where the pressure gradient opposes the magnetic field gradient. Here the curvature has a stabilizing effect on drift waves [18][29] and no unstable solutions are found. These results confirm the hypothesis that the unstable mode is driven in the bad curvature region, therefore it can be referred to as drift-interchange.

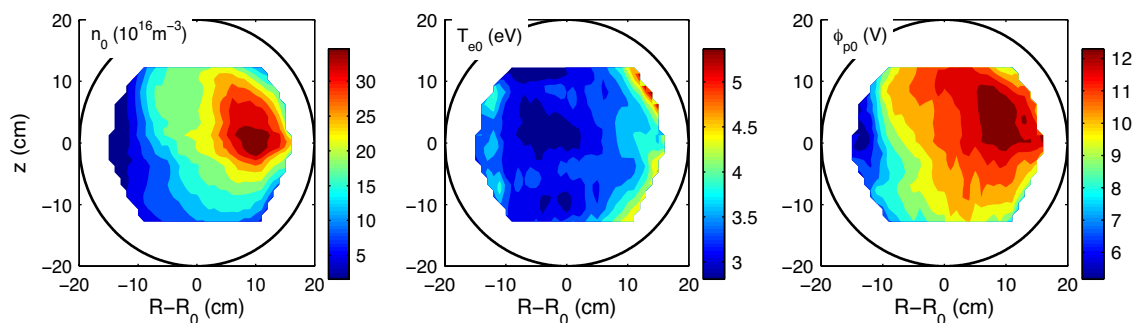


Figure 8.11: Time-averaged profiles of density, temperature and plasma potential, measured in Argon plasmas, with $B_\varphi = 76.6$ mT, $B_z = 1.0$ mT, $p_0 = 2.5 \times 10^{-5}$ mbar, with 2 kW of absorbed power.

8.5 Drift instabilities in Argon plasmas

We conclude this Chapter illustrating an example of drift instabilities measured in Argon plasmas. Figure 8.11 shows the time-averaged profiles of n_0 , T_{e0} and ϕ_0 , measured during 80 ms of a stationary phase of plasma discharge, with 2 kW of absorbed power. The density profile is shifted toward the low field side [42] and the maximum n_0 is almost 20 times larger than the value measured in Hydrogen plasmas. The temperature is fairly constant across the section and slightly increases at the plasma edge, on the low field side. The plasma potential profile is similar to the density profile. Even in this plasma the electron diamagnetic drift velocity and the $\mathbf{E}_0 \times \mathbf{B}$ velocity have opposite directions.

The power spectrum of density fluctuations, measured at midplane exhibits a pronounced peak at 8.5 kHz (Fig. 8.12). The same peak is detected also on the upper part of the plasma cross-section, but not on the bottom and on the high field side with respect to the maximum of n_0 . The wavenumber and frequency spectrum is peaked at 54 m^{-1} , a value comparable to that measured in Hydrogen plasmas and corresponding to a wavelength of approximately 12 cm. The turbulence is weakly developed, as indicated by the low value of the wavenumber spectral width $\sigma_{k_\theta} = 18 \text{ m}^{-1} < k_\theta$. The average phase velocity associated with the mode is $v_{\text{ph}} = (1.0 \pm 0.09) \text{ km/s}$ along the poloidal direction.

The poloidal counter-clockwise propagation is also confirmed by the phase delay at 8.5 kHz measured between all the tips in the FLP-HOR array with respect to one tip located upstream with respect to the direction of propagation, shown in Fig. 8.13 (see Fig. C.1 for the numeration of tips). The phase velocity is estimated from a linear fit of the curve as:

$$v_{\text{ph}} = 2\pi f \frac{r}{m} \quad (8.5)$$

where f is the frequency of the mode, m is the poloidal wavenumber, which is equal to the coefficient of the linear term and $r = 16.5$ cm is the distance of the FLP array with respect to the center of the vessel poloidal cross-section. We obtain $v_{\text{ph}} = 944$ m/s, comparable with the value measured locally from $P(k_\theta, \omega)$. The measured phase

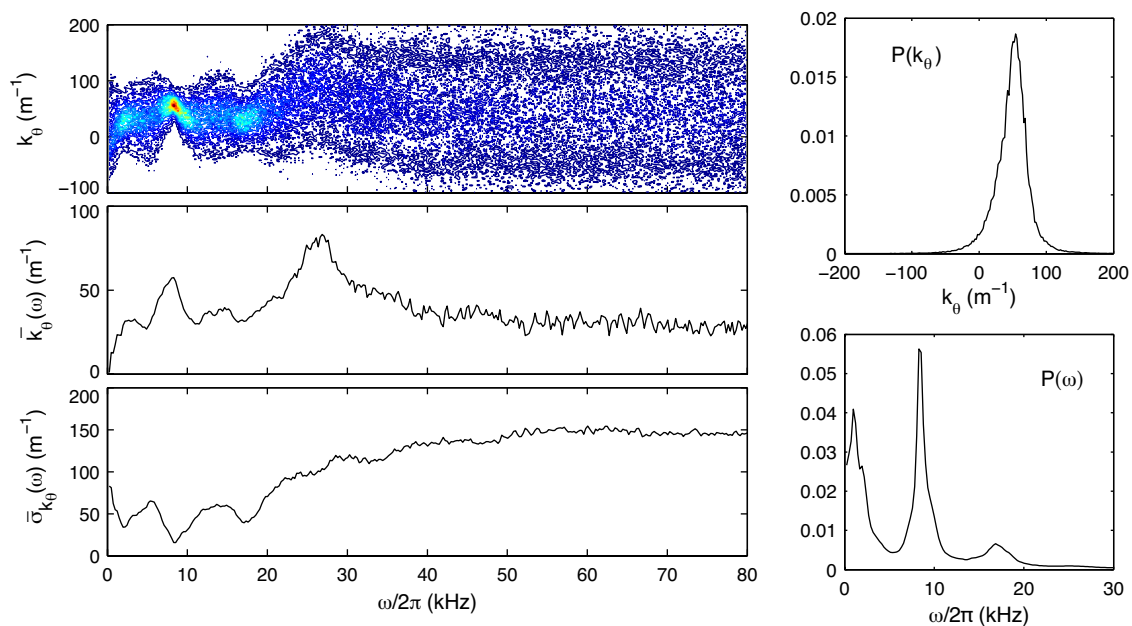


Figure 8.12: *Left*: conditional spectrum $p(k_\theta|\omega)$ (top), and statistical dispersion relation measured at midplane, at $R - R_0 = 16.3$ cm. *Right*: Frequency and wavenumber spectra, calculated integrating $P(k_\theta, \omega)$ respectively over k_θ and over ω .

velocity should be compared to the $\mathbf{E}_0 \times \mathbf{B}$ drift velocity, $v_E = (1.3 \pm 0.1)$ km/s and the electron diamagnetic drift velocity, $v_{de} = (0.3 \pm 0.1)$ km/s, calculated from the background profiles. The difference between the two is consistent with the measured phase velocity.

The parallel wavenumber was measured with two probes toroidally separated by 0.9 m and fixed on the equatorial plane, at 4 cm from the vessel edge. An upper estimate to the parallel wavenumber, is 2 m^{-1} , much larger than the value measured in Hydrogen plasmas.

Figure 8.14 shows the numerical solution of the dispersion relation calculated for the local background parameters at the same location where the dispersion relation has been measured and for $k_\perp = 50 \text{ m}^{-1}$. The curvature term is not included in these calculations. As shown in the figure, the measured dispersion relation is consistent with the existence of an unstable solution for drift waves, even in the case where the curvature of the magnetic field is not taken into account. Fairly good agreement is found between the measured frequency and the real frequency for drift waves in a wide range of k_\parallel .

Note that for Argon plasmas the term $k_\perp \rho_s \simeq 0.5$ should be taken into account in the estimate of the electron diamagnetic drift frequency from the background parameters from Eq. (2.32a) and Eq. (8.2). We obtain 2.5 kHz that, subtracted to the $\mathbf{E}_0 \times \mathbf{B}$ frequency of 11.5 kHz, gives 9 kHz, consistent with the measurements.

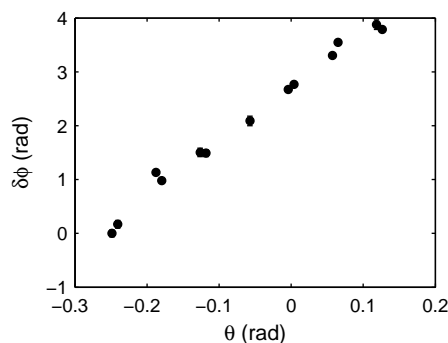


Figure 8.13: Phase shift measured between each tip in the FLP-HOR array and the first tip of the series, at the bottom edge of the array, below the equatorial plane.

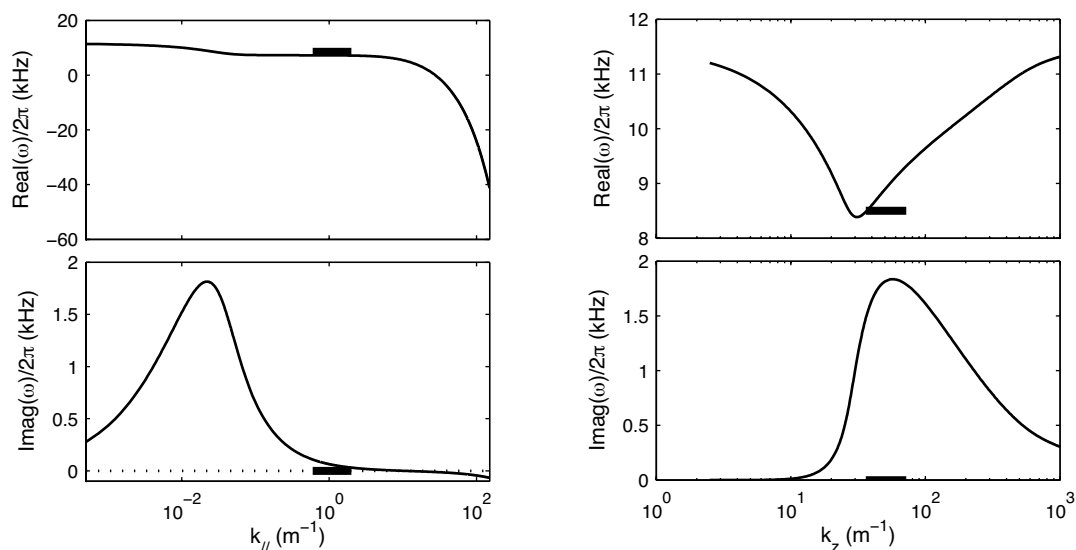


Figure 8.14: Numerical solution of the kinetic dispersion relation for drift waves, calculated for $L_n = 4$ cm, $T_e/T_i = 40$, $L_n/L_T = 0$, $(\rho_i/\lambda_{Di})^2 = 10^5$, $m_i/m_e = 40 \times 1836$, no curvature and $k_y = 50$ m $^{-1}$. Left: variation with $k_{||}$ for fixed k_z . Right: variation with k_z for $k_{||}$ corresponding to the maximum growth rate.

8.6 Summary and discussion

We have presented in this Chapter the characterization of the linear properties of electrostatic drift instabilities in Hydrogen and Argon plasmas. In both cases density fluctuations peak on the low field side of the maximum of n_0 and at the location of maximum density gradient.

In Hydrogen plasmas a mode at approximately 4 kHz is measured both on the high and on the low field sides, with amplitude much larger on the low field side. The density fluctuations associated with this mode have their maximum amplitude in a delimited region at the bottom of the plasma cross-section. The power spectrum is narrow in frequency and wavenumber at this location, then it broadens during the convection

path.

The phase velocity of the unstable mode, measured at midplane, is consistent with the electron diamagnetic velocity for drift waves, corrected for the Doppler shift induced by the $\mathbf{E}_0 \times \mathbf{B}$ drift. The parallel wavenumber is larger than zero both on the high and the low field side, with a ratio of k_{\parallel} to k_z of the order of 10^{-3} .

The measured dispersion relation has been compared with the numerical solution of the kinetic dispersion relation derived in Chap. 2. It is found that the curvature of the magnetic field is essential to drive the observed modes unstable.

Note that a mode at 4 kHz is detected also on the high field side, as shown in Fig. 8.5 and Fig. 7.9. It is narrow in frequency and wavenumber for $R - R_0 \lesssim -10$ cm and it is broad between -10 cm and the maximum of n_0 . This region corresponds to the location of the EC resonance layer, where density profiles have a secondary maximum and background gradients are steep, as discussed in [40][42]. Because of the presence of this local minimum in the density profiles, a region of unfavourable curvature exists also on the high field side, between the EC resonance layer, at -12.5 cm, and approximately -9 cm. With the data available at present we cannot conclude whether the mode detected on the high field side is a remnant of the drift-interchange instability generated at the bottom of the plasma cross-section and convected from the source region to the high field side, or it is a seed of the drift-interchange instability observed later on the low field side.

Further investigations are foreseen. Experimentally, measurements of the dispersion relation with higher spatial resolution are needed around the EC resonance layer and, possibly, in an extended vertical region, to highlight asymmetries in the wavenumber spectra above and below the equatorial plane. On the theory side, insight could be gained by nonlinear models of electrostatic turbulence in toroidal geometry, which take into account the effect of the plasma source at the EC and at the UH resonance layers [40].

In Argon plasmas the measured dispersion relation is also consistent with the dispersion relation for drift waves and the measured frequency comparable to the difference between the $\mathbf{E}_0 \times \mathbf{B}$ and the electron diamagnetic drift frequency. Contrary to Hydrogen plasmas, according to the kinetic linear model, curvature does not need to be invoked to justify the detection of unstable drift waves on the low field side of the maximum of n_0 . In Argon, the drift mode is not detected on the high field side. This excludes the hypothesis that it is generated as a drift wave on the high field side, is convected to the low field side by the $\mathbf{E}_0 \times \mathbf{B}$ drift and is saturated here by the interchange mechanism. Further investigations are required in this direction, possibly choosing configurations with background profiles centered over the vessel cross-section, in order to separate the contribution of the curvature and of the pressure gradients.

Chapter 9

Identification and characterization of interchange instabilities

As discussed in Chap. 7, two low frequency modes with different properties are detected in the power spectrum of density fluctuations. One of the modes has frequency ≈ 4 kHz, is measured both on the high and the low field side, and is identified as a drift-interchange instability. The other mode is measured only on the low field side. Its frequency is larger and is strongly affected by the value of the vertical field. This Chapter focuses on the characterization of the nature and spectral features of this second mode. After a short summary of the experimental setup and the background profiles, the power spectra of density and plasma potential fluctuations are compared in Sec. 9.2. Section 9.3 illustrates the measured dispersion relation across and along the magnetic field and the comparison of the measured phase velocities with the drift velocities calculated from the background profiles. The experimentally reconstructed dispersion relation is then compared with the numerical solution of the kinetic dispersion relation derived in Chap. 2. The observed instability is demonstrated to be an interchange mode, with a wavelength across the magnetic field that is consistent with the vertical displacement of the magnetic field lines after a complete toroidal turn.

9.1 Time-averaged profiles

The main properties of the background profiles and the variation of n_0 , T_{e0} and ϕ_{p0} with the vertical field have been discussed in Sec. 7.4. We nonetheless report in Fig. 9.1 the time-averaged profiles for four selected values of B_z in the range (0.8, 1.8) mT. The density profile is centered with respect to the vessel cross-section, and has good symmetry along R and z . Temperature and plasma potential profiles are more elongated in the z direction and approach a slab-like configuration with increasing vertical field magnitude. The maximum density stays approximately constant, with relative variations below 20% across the full range of the vertical field variations. On the other hand, the relative increase in temperature and plasma potential is twice as large.

Figure 9.2 shows the variations of the density and temperature gradient scale lengths

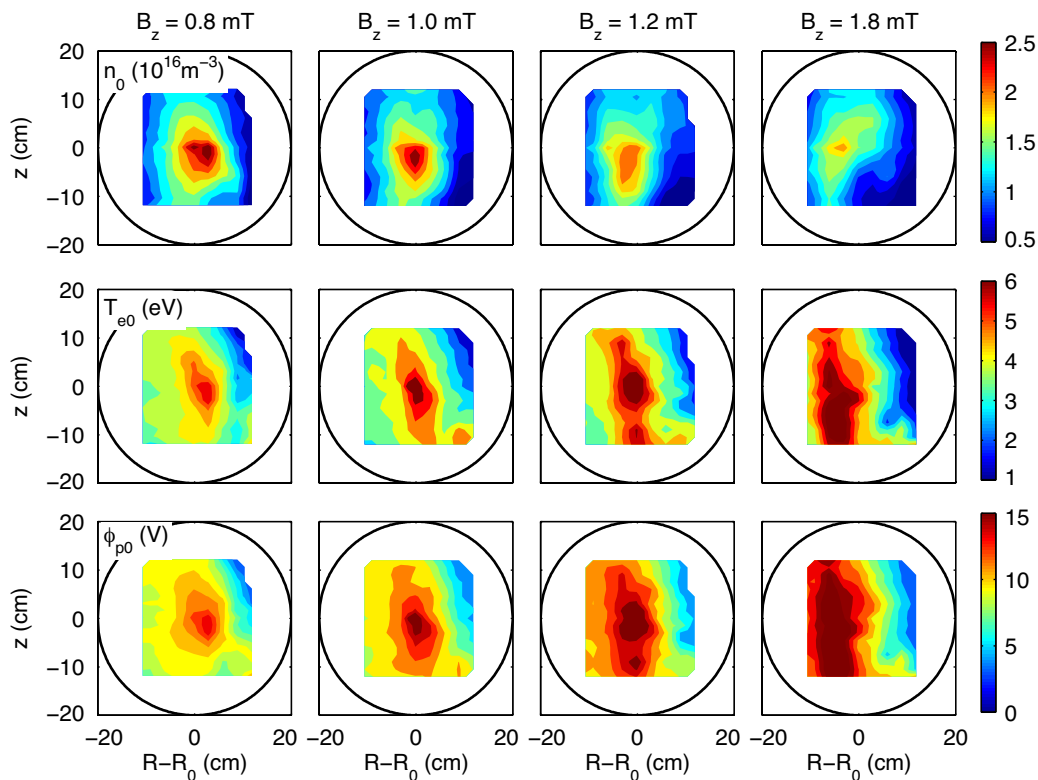


Figure 9.1: time averaged profiles of density (*top*), temperature (*middle*) and plasma potential (*bottom*) for different values of the vertical field, increasing from left to right.

and of the background electric field as a function of the vertical field. The plotted values correspond to measurements on the low field side, at the position of the maximum gradient of n_0 , T_{e0} and ϕ_{p0} . As shown in Fig. 9.1, for a fixed value of B_z , the radial position where ∇n_0 , ∇T_{e0} and E_0 peak is the same and approximately equal to $R - R_0 = 6$ cm. The density gradient scale length stays approximately constant up to $B_z = 1.2$ mT and is comparable to the temperature gradient scale length for all values of vertical field. Although the maximum value of electrostatic potential monotonically increases, the electric field varies between 80 and 150 V/m, without a clear trend with B_z . The variations are anyhow within the large error bars in the measured electric field.

9.2 Power spectrum of fluctuations

Figure 9.3 shows the power spectrum of \tilde{n} and $\tilde{\phi}_p$, measured at midplane, for $B_z \in [0.4, 1.8]$ mT. The power spectrum of \tilde{n} is normalized to the local value of n_0^2 , while the power spectrum of $\tilde{\phi}_p$ is normalized to T_{e0}^2/e^2 . The square root of the area under a peak represents therefore the normalized rms value of fluctuations, \tilde{n}/n_0 and $e\tilde{\phi}_p/T_{e0}$, associated with the mode, Eq. (5.8). The power spectra shown in the figure refer to measurements taken on the high field side, at $R - R_0 = -9$ cm and on the low field side, at the position of maximum level of density fluctuations.

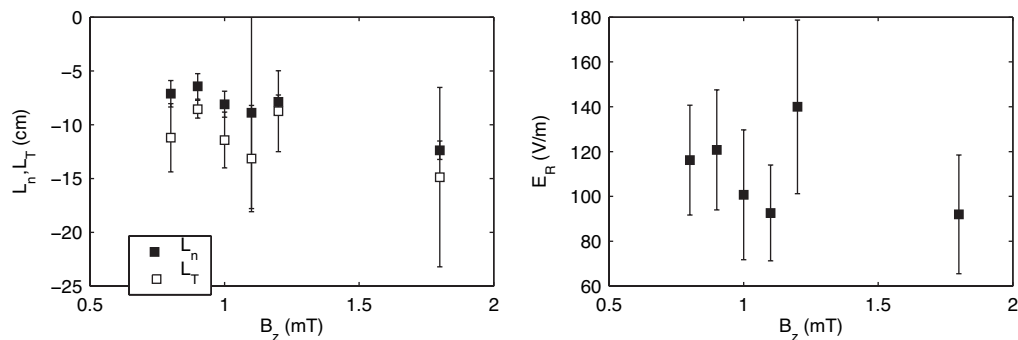


Figure 9.2: Left: Variation of the density gradient scale length L_n (black squares) and of the temperature gradient scale length L_T (open squares) with the amplitude of the vertical field. Negative values of L_n and L_T indicate that the relative gradients decrease with R . Right: variation of the radial electric field with B_z .

A mode with frequency f_1 larger than that of the drift-interchange mode, is measured on the low field side, in a layer with radial extension between 5 and 8 cm. Its spectral features are strongly affected by the value of the vertical field, as shown in the figure. The peak associated with the mode is broad for low values of B_z and its amplitude is smaller than that of the drift-interchange mode for $B_z < 1.0$ mT. With increasing vertical field amplitude the peak becomes more and more narrow and its amplitude increases. The variation of the frequency and of the spectral width for $B_z \in [0.8, 1.8]$ mT is shown in Fig. 9.5. The frequency decreases from 15 kHz to 5 kHz and the spectral width from 8 kHz to 0.8 kHz. The ratio of the spectral width of a peak to its central value can be taken as a measure of the degree of coherence of the associated mode in the time domain. The corresponding correlation time increases from 0.125 to 1.25 ms in the range of B_z considered.

As shown in Fig. 9.3, the normalized values of density and potential fluctuations, integrated over the whole range of frequencies, are comparable on the high field side for all values of B_z . Conversely, on the low field side, $\tilde{n}/n_0 > e\tilde{\phi}_p/T_{e0}$ for $B_z > 0.6$ mT. These differences are mostly due to the unstable mode detected on the low field side. They are in fact negligible for $B_z < 0.8$ mT, where the mode does not develop, but are large for $B_z \geq 0.8$ mT, where the area of the peak in the power spectrum of \tilde{n} is much larger than the area in the power spectrum of $\tilde{\phi}_p$. From the square root of the area of the peaks, Eq. (5.8), it follows that $\tilde{n}/n_0 \gg e\tilde{\phi}_p/T_{e0}$ for the unstable mode.

The asymmetry between the high and the low field side appears evident from the power spectrum $P(k_\theta, \omega)$ measured with the FLP arrays, shown in Fig. 9.4. Contrary to the mode at frequency f_0 , which is measured both on the high and the low field side, the mode at frequency f_1 is measured only on the low field side.

At the upper part of the plasma cross-section the two modes are also separated, but the drift-interchange mode is not detected on the low field side. Figure 9.4 shows the profile of the rms value of fluctuations associated with the drift-interchange instability and with the instability at $f_1 = 12$ kHz, reconstructed from the power spectrum of \tilde{n} measured with the HEXTIP array (see Sec. 5.3) for $B_z = 1.2$ mT. The drift-interchange

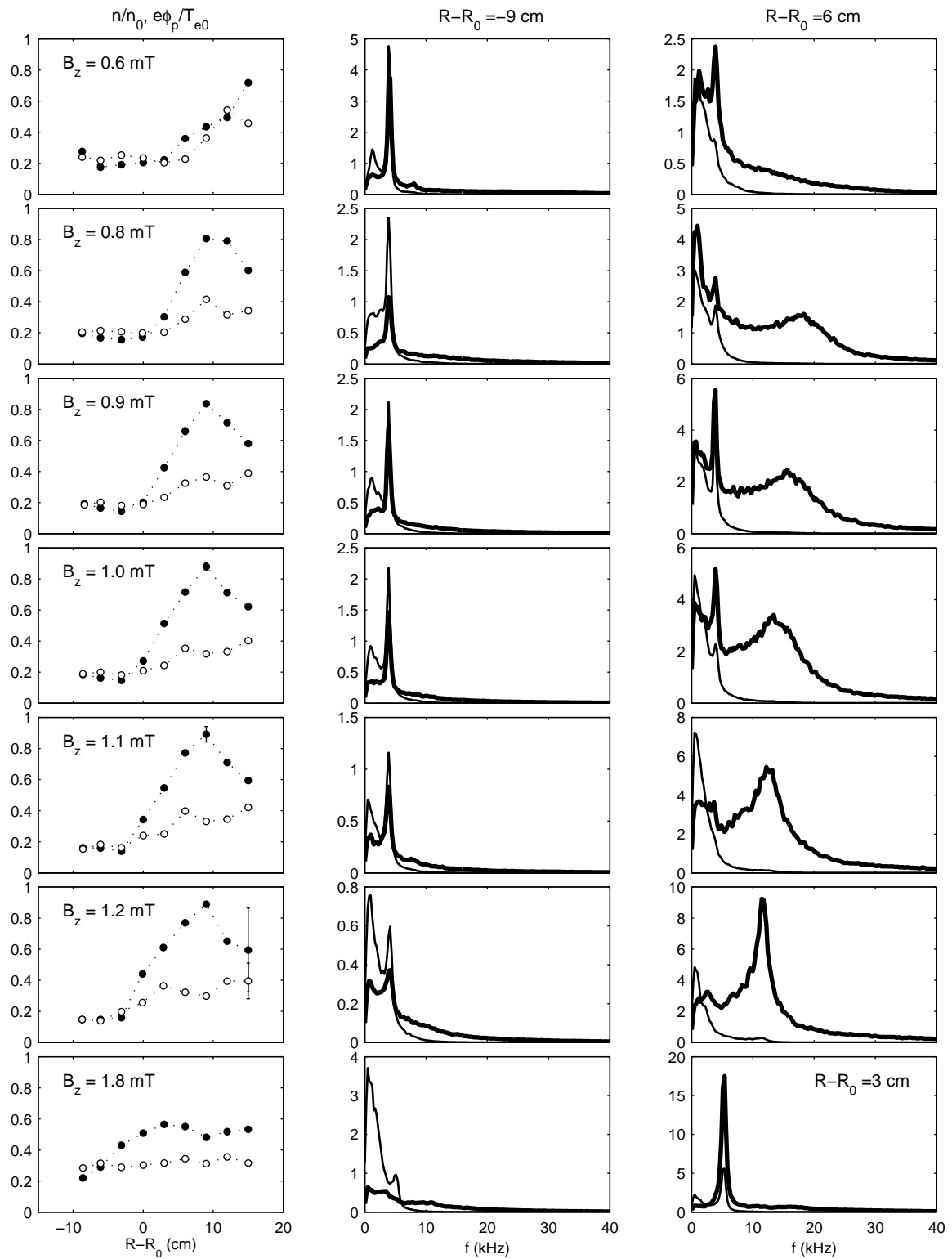


Figure 9.3: Left: Radial profile of \tilde{n}/n_0 (black circles) and $\tilde{\phi}_p/T_{e0}$ (open circles), for different values of B_z , increasing from top to bottom. Center: power spectrum of \tilde{n} and $\tilde{\phi}_p$ measured at the high field side. Right: power spectrum of \tilde{n} and $\tilde{\phi}_p$ measured at the low field side.

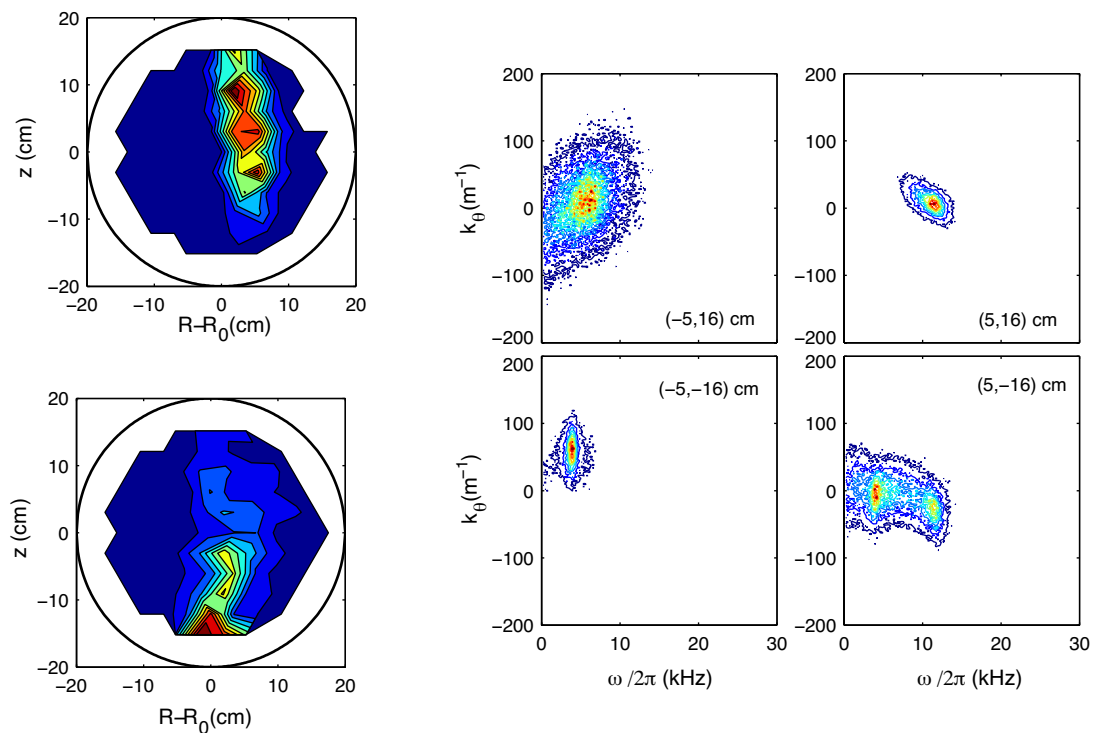


Figure 9.4: Left: Profile of the rms value of density fluctuations associated with the instability at 12 kHz (top) and to the drift-interchange instability at f_0 (bottom), for $B_z = 1.2$ mT. Right: wavenumber and frequency spectrum of \tilde{n} , measured from the FLP array at the upper part top) and the lower part (bottom) of the plasma cross-section, for $B_z = 1.2$ mT.

mode has its maximum amplitude at the lower part of the plasma cross-section, as already remarked in Sec. 8.2.1 for the case at lower B_z , while the other mode has its maximum amplitude in a region extended along the z direction. In order to identify the nature of this mode we need to measure its dispersion relation along and perpendicularly to the magnetic field.

9.3 Dispersion relation

We proceed as in Sec. 8.3 and measure the wavenumber and frequency spectrum across and along the magnetic field, at different locations over the plasma cross-section.

9.3.1 Dispersion relation across B

Figure 9.6 shows the wavenumber and frequency spectra of density and floating potential fluctuations, respectively indicated as $P_n(k_z, \omega)$ and $P_\phi(k_z, \omega)$, measured at midplane using the TRIP array. The configuration for these measurements is shown in Fig. 4.5(a). The power spectra shown in the figure are taken on the low field side and,

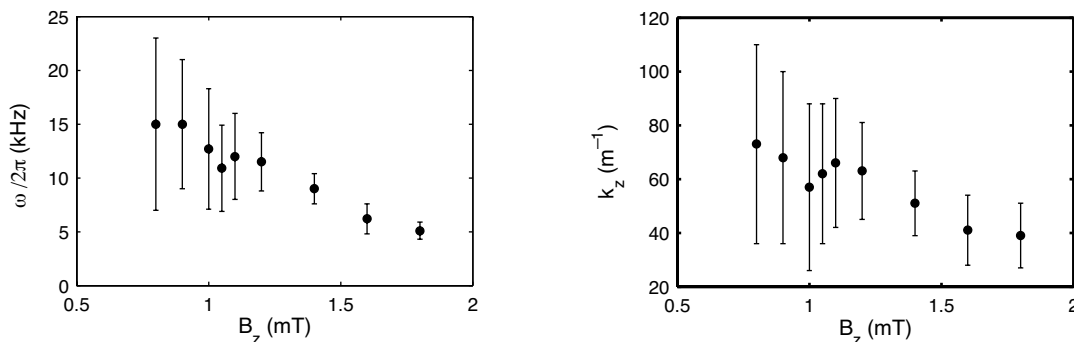


Figure 9.5: Variation of the measured frequency (left) and of the perpendicular wavenumber (right) of the mode with the amplitude of the vertical field. The vertical bars represent the spectral width in the frequency and in the wavenumber space, respectively.

for each value of B_z , at the position of the maximum level of density fluctuations.

Even for low values of B_z , where the frequency spectrum is broad, can a wavenumber k_z be identified. With increasing vertical field amplitude the spectrum becomes narrower both in the ω - and in the k_z -space and peaks at lower values of frequency and wavenumber, as shown in Fig. 9.5. The plotted values are the central ω and k_z resulting from a fit of $P_n(k_z, \omega)$ with a bi-dimensional gaussian function; the error bars represent the wavenumber spectral width σ_{k_z} .

For all values of B_z is $\sigma_{k_z} < k_z$, indicating that turbulence is weakly developed even for the lowest vertical fields. The correlation length, estimated as the inverse of the spectral width in k_z , increases from 17 to 48 cm when B_z is increased from 0.8 to 1.8 mT.

The power spectrum $P_\phi(k_z, \omega)$ is peaked at wavenumbers larger than $P_n(k_z, \omega)$ for all values of B_z . This difference is most likely due to temperature fluctuations, not taken into account in the measurement of $P_\phi(k_z, \omega)$, as discussed in App. E.4.

9.3.2 Radial profile of the phase velocity

Figure 9.7 shows the radial profile of ω/k_z , measured at midplane, for $B_z = 0.9$, 1.0 and 1.8 mT. For each B_z value, the measured phase velocity is compared with the radial profile of the electron diamagnetic drift \mathbf{v}_{de} and of the $\mathbf{E}_0 \times \mathbf{B}$ drift velocity, \mathbf{v}_E . As the background density gradient ∇n_0 and the electric field \mathbf{E}_0 are at midplane along R , the component along z of \mathbf{v}_{de} and \mathbf{v}_E is represented in the figure. As \mathbf{v}_E and \mathbf{v}_{de} are in opposite directions, the resulting velocity at midplane is the difference between their absolute values. Over most of the radial profile $|\mathbf{v}_{de}| < |\mathbf{v}_E|$ for all the values of B_z and the difference between the two is close to v_E . As the instability is measured only on the low field side, the comparison between the phase velocity and the drift velocities is possible only in a limited region of the equatorial plane. The measured phase velocity is in good agreement with \mathbf{v}_E for $B_z = 0.9$ mT and $B_z = 1.0$ mT. For $B_z = 1.8$ mT the amplitude of \mathbf{v}_{de} is much lower than that of \mathbf{v}_E and it is difficult to conclude whether

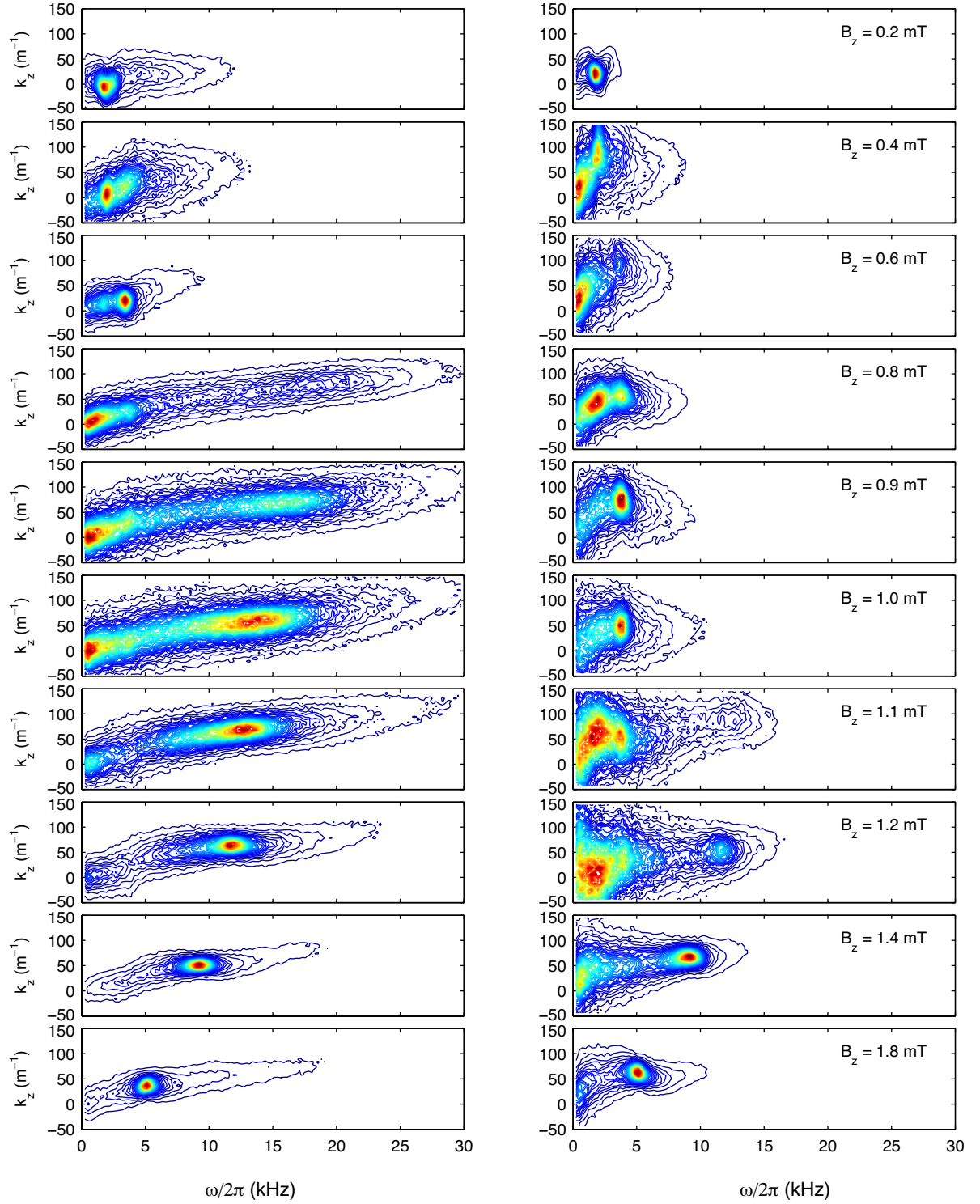


Figure 9.6: Wavenumber and frequency spectrum of \tilde{n} (left) and $\tilde{\phi}_f$ (right), measured at midplane from two LPs with vertical separation $\Delta z = 0.6$ cm, as a function of the vertical field. Measurements have been done for each value of B_z at the radial position of the maximum level of fluctuations. The value of $P(k_z, \omega)$ is normalized to the total power, $\sum_{k_z, \omega} P(k_z, \omega)$.

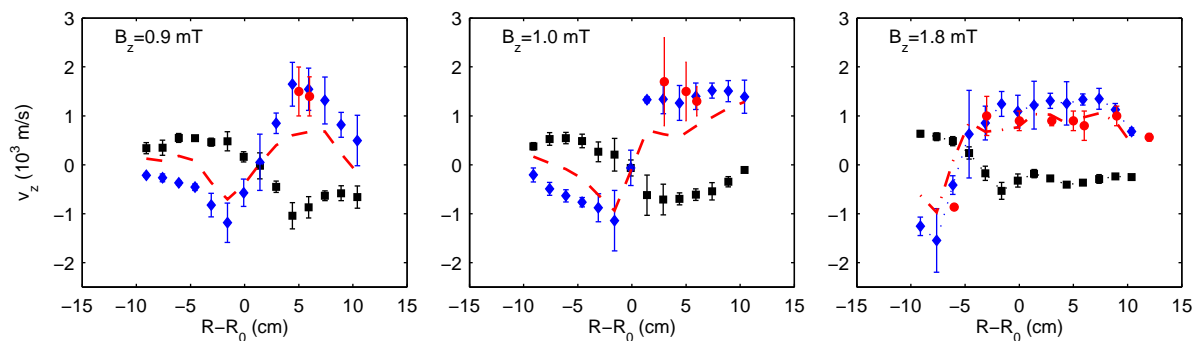


Figure 9.7: Radial profile of the phase velocity (red circles), ω/k_z , measured at the midplane, for different values of the vertical field. Black squares indicate the vertical component of the electron diamagnetic drift velocity, $\mathbf{v}_{de} \cdot \hat{\mathbf{z}}$, while blue diamonds indicate the $\mathbf{E} \times \mathbf{B}$ drift velocity, $\mathbf{v}_E \cdot \hat{\mathbf{z}}$. The component along $\hat{\mathbf{z}}$ of the difference $|\mathbf{v}_E \cdot \hat{\mathbf{z}}| - |\mathbf{v}_{de} \cdot \hat{\mathbf{z}}|$ is indicated with a dashed line.

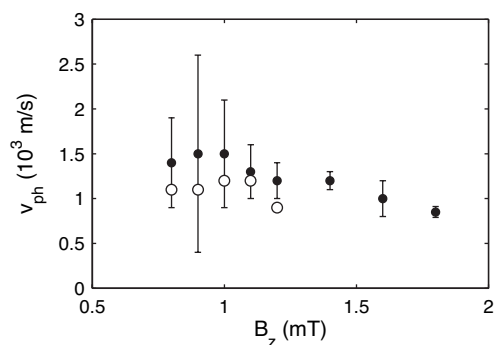


Figure 9.8: Phase velocity of the interchange mode (black circles) and phase velocity of the drift-interchange mode (empty circles) measured for different values of B_z .

the measured phase velocity is consistent with \mathbf{v}_E or with $|\mathbf{v}_E| - |\mathbf{v}_{de}|$.

For those values of B_z where both instabilities are observed on the low field side, the phase velocity of the drift-interchange mode is, on average, 300 m/s lower than that of the other mode, as shown in Fig. 9.8. Such difference suggests that the mode observed on the low field side is related to an instability of different nature, with pure interchange nature. Nevertheless, a reconstruction of the dispersion relation in terms of the parallel wavenumber and a comparison with theory are needed for an unambiguous identification.

9.3.3 Dispersion relation along \mathbf{B}

The parallel wavenumber has been measured with the SLP and the TWEEDY arrays using the method described in Sec. 5.4. Figure 9.9 shows the results of the measurements for $B_z = 1.6$ mT. The value of the coherence spectrum measured at the frequency of the mode, $\omega/2\pi \simeq 9$ kHz, is maximum at a coordinate z close to the

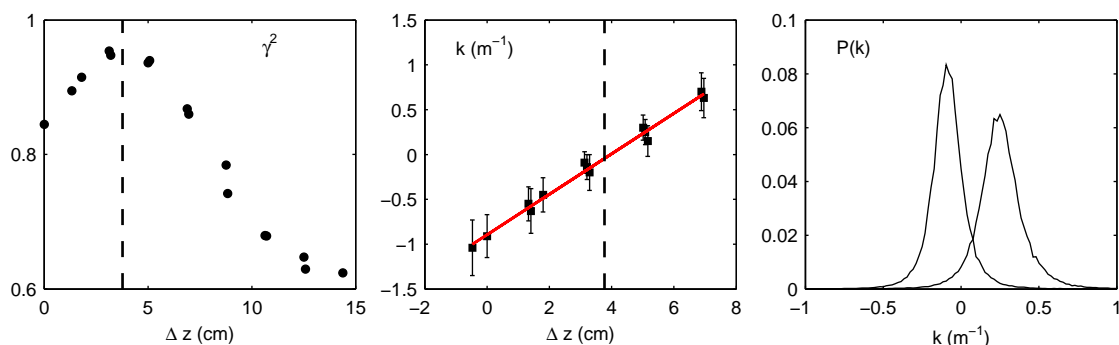


Figure 9.9: Wavenumber measured at $R - R_0 = 5$ cm, for $B_z = 1.6$ mT with the SLP and the TWEEDY arrays. Left: Variation of the amplitude of the coherence spectrum, calculated at the frequency of the mode, with the vertical separation between tips. Δz is calculated with respect to the TWEEDY tip. The dashed line indicates the vertical coordinate z_0 where the magnetic field line that passes through the reference tip at the location of TWEEDY intersects the SLP array. Center: Measured wavenumber with respect to the vertical separation between tips. The plotted value of k_m is the center of the gaussian curve that fits the wavenumber spectrum $P(k_m)$, the error bar is its spectral width. Right: Wavenumber spectrum measured around z_0 , at $\Delta z \simeq 3$ cm ($k = -0.1 \text{ m}^{-1}$) and $\Delta z = 5$ cm ($k = -0.22 \text{ m}^{-1}$).

ideal position of the magnetic field line, z_0 , indicated in the figure with a dashed line. The measured wavenumber changes its sign across z_0 , suggesting that k_{\parallel} is close to zero and only an upper estimate of k_{\parallel} can be given (see App. D). The wavenumber estimated from the spectrum $P(k)$ at the coordinate where the coherence is maximum is $k_{\parallel} = 0.1 \text{ m}^{-1}$, with a width $\sigma_{k_{\parallel}} = 0.1 \text{ m}^{-1}$, see Fig. 9.9. An interpolation of k at the coordinate z_0 , using the parameters of a linear fit, gives $k_{\parallel} \simeq 0.06 \text{ m}^{-1}$. The same sign inversion in the measured k is observed for all values of B_z , suggesting that the instability detected at the low field side has interchange characteristics.

9.4 Comparison with theory

The measured dispersion relation has been compared with the numerical solution of the kinetic dispersion relation described in Chap. 2. We have assumed as background values $L_n = 5$ cm, $T_{e0} = 4$ eV, $E_0 = 100 \text{ Vm}^{-1}$. The solution has been calculated for $k_z = 39 \text{ m}^{-1}$ and $k_{\parallel} = 10^{-3} \text{ m}^{-1}$, the wavenumbers measured at $B_z = 1.8$ mT. The stability with respect to the value of k_z or k_{\parallel} has been studied by varying one of the two at a time.

As discussed in Sec. 2.4.1, for the experimental parameters typical on TORPEX, unstable solutions for drift waves exist in the limit of $k_{\parallel} < 5 \times 10^{-3} \text{ m}^{-1}$. Figure 9.10 shows the solution of Eq. (2.30), for $L_n = 5, 10$ cm and in the limit of straight magnetic field.

Unstable solutions for pure drift waves exist for small values of k_{\parallel} with the most unstable solution calculated for $k_{\perp} \simeq 40 \text{ m}^{-1}$ and $k_{\parallel} \simeq 4 \times 10^{-3} \text{ m}^{-1}$. Nevertheless,

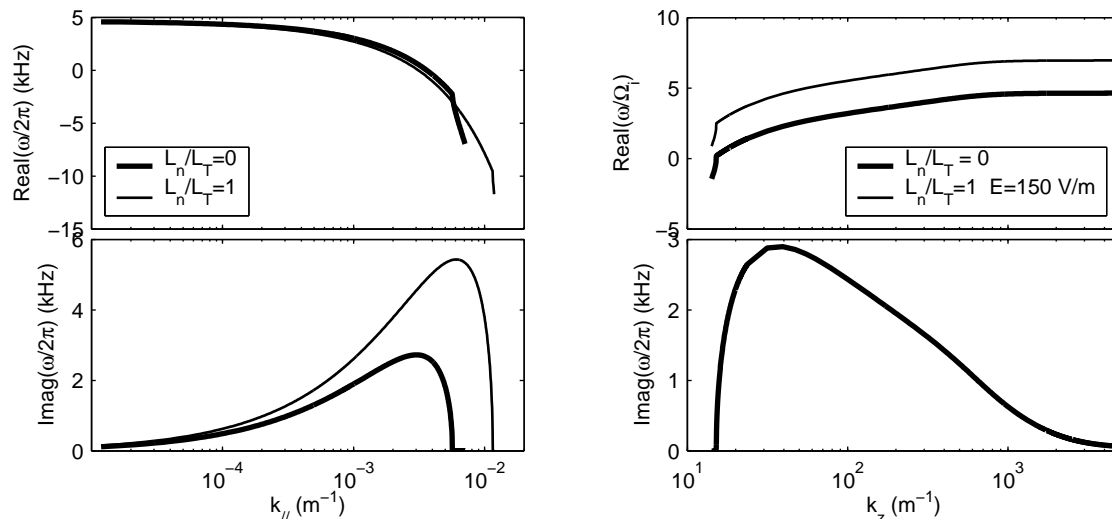


Figure 9.10: Results of the kinetic dispersion relation for drift waves, calculated using Eq. (2.30) in the limit of straight magnetic field, assuming $L_n = 5$ cm, $T_{e0} = 4$ eV, $T_{e0}/T_{i0} = 40$, a constant background electric field $E_0 = 100$ V/m. Left: dispersion relation as a function of the parallel wavenumber, for $k_z = 25$ m $^{-1}$ and $L_n/L_T = 0$ (thick curve) and $L_n/L_T = 1$. Right: dispersion relation as a function of the perpendicular wavenumber k_z , for $k_{||} = 10^{-3}$ m $^{-1}$ and $L_n/L_T = 0$ (thick curve) and for $L_n/L_T = 1$ and $E_0 = 150$ V/m, $k_{||} = 3 \times 10^{-3}$ m $^{-1}$ (thin curve).

the growth rate falls rapidly to zero for $k_{||} \simeq 5 \times 10^{-3}$ m $^{-1}$ and the real frequency is not consistent with the measured frequency for large k_z . The frequency measured at large k_z cannot be justified neither including a temperature gradient, nor assuming a larger background electric field.

Figure 9.11 shows the solution of the dispersion relation calculated in the interchange limit. The curvature and the gradient of the magnetic field are represented as an external gravity-type force, Eq. (2.7). For fixed $k_z = 25$ m $^{-1}$, the growth rate saturates to a constant value for $k_{||} \rightarrow 0$ and the real frequency is approximately constant for $k_{||} < 10^{-2}$ m $^{-1}$. This is the limit of the analytical solution for interchange instabilities, Eq. (2.38). The value of the real frequency is in this limit the $\mathbf{E}_0 \times \mathbf{B}$ drift frequency, $\omega_E = k_z v_E$.

For fixed $k_{||} = 10^{-3}$ m $^{-1}$ the growth rate is approximately constant for $k_z \in (4, 100)$ m $^{-1}$, while the real frequency is predicted to decrease with increasing k_z . This is inconsistent with the dispersion relation measured perpendicularly to \mathbf{B} , as shown in Fig. 9.5, which reveals an increase of both the frequency and the wavenumber. The measured frequency is thus inconsistent with the numerical solution of the dispersion relation both in the drift and in the interchange limits. In the latter case, however, the predicted growth rate is constant for a wide range of values of k_z and $k_{||}$, indicating that modes with parallel and perpendicular wavenumbers in a wide range of values are unstable.

The monotonic variation of k_z with B_z is most likely related to the value of the connection length, L_c . Larger values of the vertical field correspond to shorter connec-

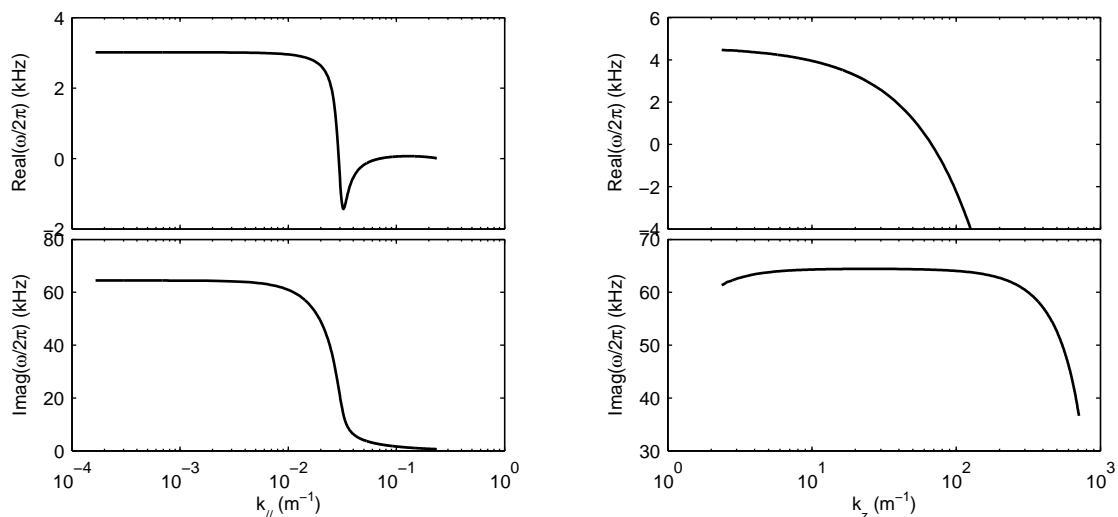


Figure 9.11: Results of the kinetic dispersion relation for interchange modes, calculated using Eq. (2.30), assuming $\nabla T_{e0} = \nabla T_{i0} = 0$, $T_{e0} = 4$ eV, $T_{e0}/T_{i0} = 40$, $E_0 = 100$ V/m and $L_n = 5$ cm. Left: dispersion relation as a function of the parallel wavenumber, for $k_z = 39$ m $^{-1}$. Right: dispersion relation as a function of the perpendicular wavenumber k_z , for $k_{\parallel} = 10^{-3}$ m $^{-1}$.

tion lengths; when B_z increases from 0.6 to 1.8 mT, L_c , calculated at $R - R_0 = 5$ cm, decreases from 45 to 14 m.

According to the numerical solution shown in Fig. 9.11, an interchange instability, with $k_{\parallel} \simeq 0$, can ‘choose’ its perpendicular wavenumber in a wide range of allowed values, from 2 up to 200 m $^{-1}$. All these modes correspond in fact to equally probable unstable solutions of the dispersion relation. It is most likely that the perpendicular wavelength is selected to satisfy periodicity along the magnetic field line. The optimal wavelength would coincide with the vertical displacement of the magnetic field line after a complete turn, $z_{2\pi} = 2\pi R B_z / B_{\varphi}$. Larger values of B_z correspond to longer ‘optimal’ perpendicular wavelengths. The measured k_z is consistent with this hypothesis, as shown in Fig. 9.12, where k_z is compared with $2\pi/z_{2\pi}$.

Once the value of the wavenumber is fixed, the real frequency is imposed by the value of v_E as $\omega_E = k_z v_E$. The real frequency for interchange instabilities is in fact much lower than ω_E and the frequency measured in the laboratory frame is essentially the $\mathbf{E}_0 \times \mathbf{B}$ drift frequency.

According to this picture, for lower values of B_z , associated with longer connection lengths, we expect to observe interchange instabilities with shorter perpendicular wavelengths. This is indeed consistent with the measurements. The broadening of the wavenumber for low values of the vertical field can be interpreted as a decrease of the correlation length associated with shorter perpendicular wavelengths.

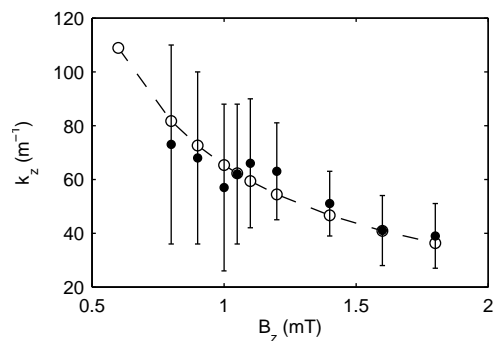


Figure 9.12: Variation of the perpendicular wavenumber (black circles) of the mode with the amplitude of the vertical field. The vertical bar represent the spectral width in the wavenumber space. The open circles represent the wavenumber calculated from the vertical displacement of a field line after a complete turn.

9.5 Drift-interchange vs interchange instabilities

Measurements from the same plasma scenarios described above show that interchange and drift-interchange instabilities coexist on the low field side of the maximum of n_0 for $B_z \leq 1.0$ mT (see Fig. 9.3 and Fig. 9.6). The amplitude of the interchange mode is much larger than that of the drift-interchange mode, which, for $B_z > 1.0$ mT, can no longer be detected at midplane.

It was also shown that the drift-interchange mode is detected both on the high and on the low field side. This is the case not only for measurements taken at midplane, as shown in Fig. 9.3, but also for measurements taken at the upper and at the lower part of the plasma cross-section, as shown in Fig. 9.4 for the case at $B_z = 1.2$ mT. Figures 9.13-9.15 show the wavenumber and frequency spectrum $P(k_\theta, \omega)$ measured at a number of positions along the azimuthal direction using the FLP arrays, at the lower and at the upper part of the plasma cross-section, for $B_z = 1.0, 1.4$ and 1.6 mT.

For $B_z = 1.4$ mT the two modes are separated in frequency and detected at distinct locations. At the lower part of the plasma cross-section, moving from the high to the low field side along the θ direction, the spectra change from being dominated by the drift-interchange mode to being dominated by the interchange mode. At intermediate positions both modes are visible, although the amplitude of the drift-interchange decreases during convection and the amplitude of the interchange increases and becomes dominant. At the upper part of the plasma cross-section, moving from the low to the high field side, the opposite process is observed: the interchange mode decreases in amplitude and eventually disappears, until the drift-interchange mode is again visible on the high field side.

The same behavior is observed for lower values of the vertical field, with the two modes separated in frequency and detected at distinct locations at the upper part of the plasma cross-section. Note that for $B_z \leq 1.0$ mT, the interchange mode is not detected at the lower part of the plasma cross-section. For $B_z = 1.6$ mT the frequencies of the two modes become comparable. At the lower part of the plasma cross-section the situation is similar to that observed for lower B_z , but at the upper part of the plasma

cross-section only the interchange mode is detected.

These measurements suggest that, because of the different value of the parallel wavenumber, the two instabilities maintain their individual properties, both being convected by the $\mathbf{E}_0 \times \mathbf{B}$. A discussion of their weak nonlinear interactions (much weaker than for the drift-interchange and its harmonics, for example) will be undertaken in Sec. 10.4.

9.6 Summary and discussion

We have identified in this Chapter interchange instabilities in Hydrogen plasmas and characterized their linear properties. This instability is observed only on the low field side, as confirmed by the measurement of the power spectrum over the whole plasma cross-section. The parallel wavenumber is close to zero and it does not show apparent dependence on the vertical field. The perpendicular wavenumber and the frequency of the mode decrease with increasing the amplitude of the vertical field and the peak associated with the mode becomes narrower. The phase velocity of the mode stays almost constant with increasing the amplitude of B_z and is comparable to the $\mathbf{E}_0 \times \mathbf{B}$ drift velocity.

The vertical field has a direct effect on the wavelength perpendicularly to the magnetic field. Measurements are consistent with the hypothesis that the instability, essentially elongated along the magnetic field, ‘selects’ its perpendicular wavelength in order to satisfy periodicity conditions. This hypothesis is consistent with the measurement of structures in the spatio temporal domain, extremely elongated along the magnetic field line and periodic along the z direction [62].

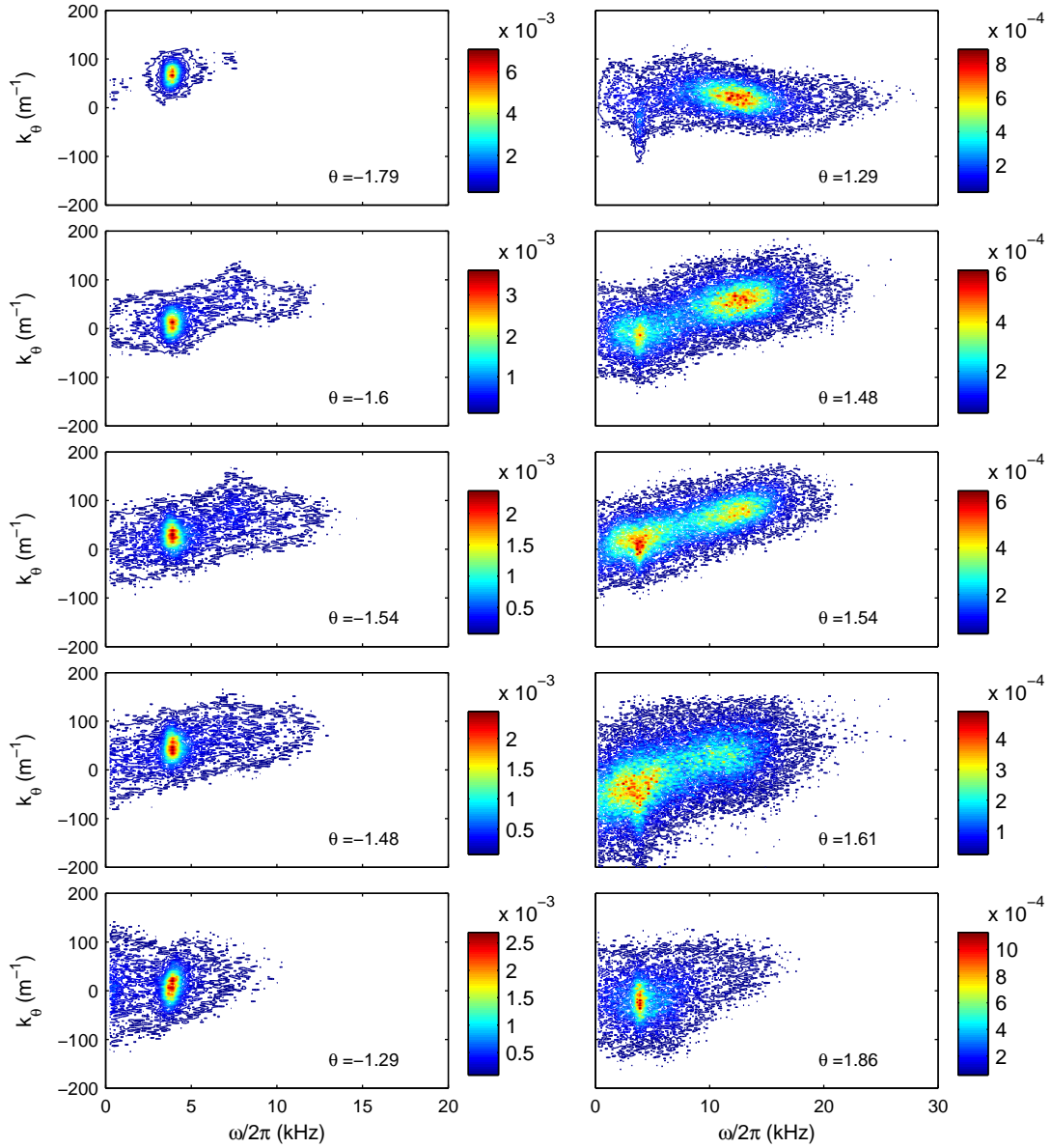


Figure 9.13: Wavenumber and frequency spectrum $P(k_\theta, \omega)$, measured at the bottom (left) and at the top (right) of the plasma cross-section for $B_z = 1.0$ mT. The plots are arranged from top to bottom according to the direction of the $\mathbf{E}_0 \times \mathbf{B}$ convection. Measurements are done at the azimuthal positions (radians units) indicated in the plots.

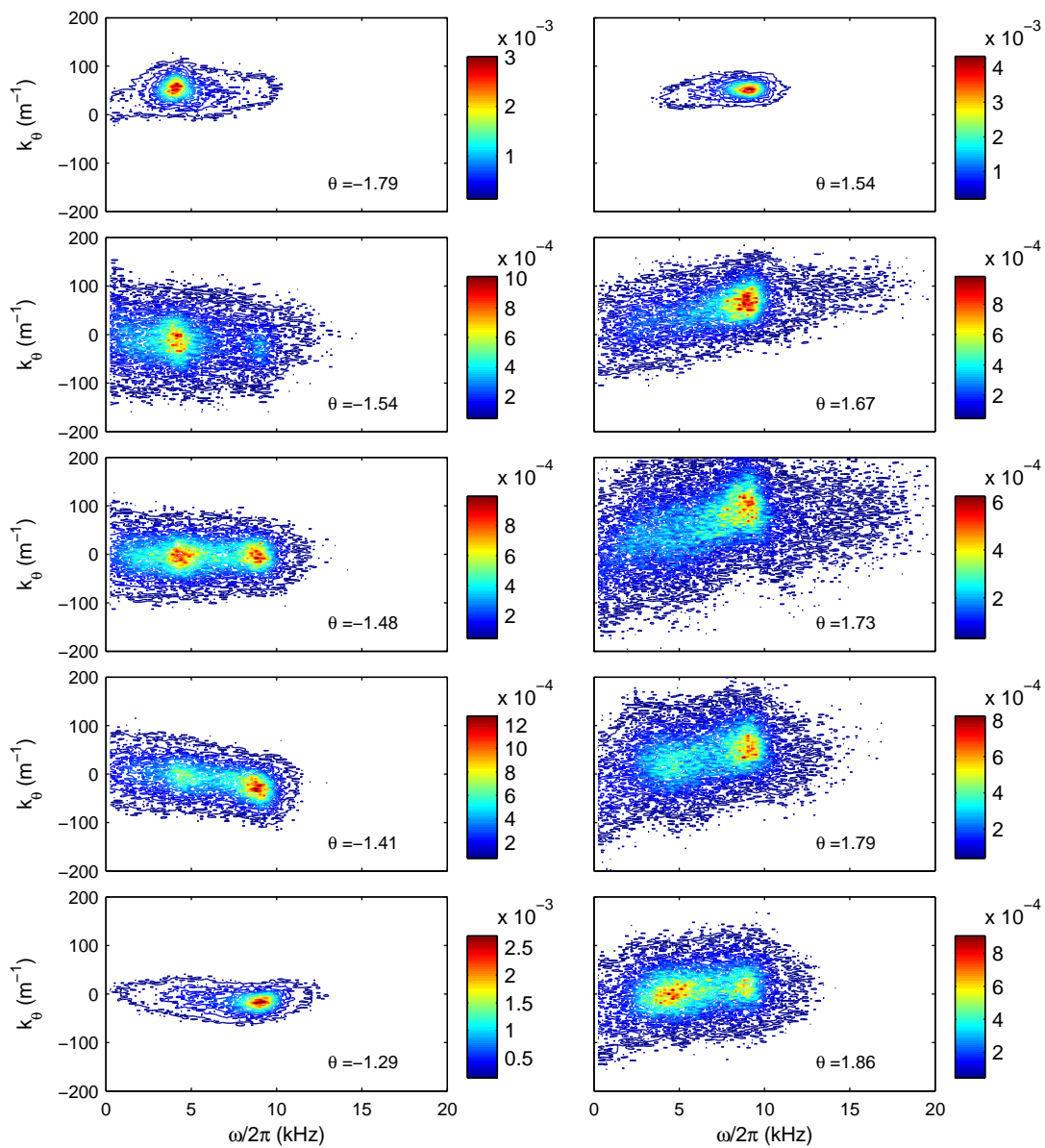


Figure 9.14: Same as Fig. 9.13, but for $B_z = 1.4$ mT.

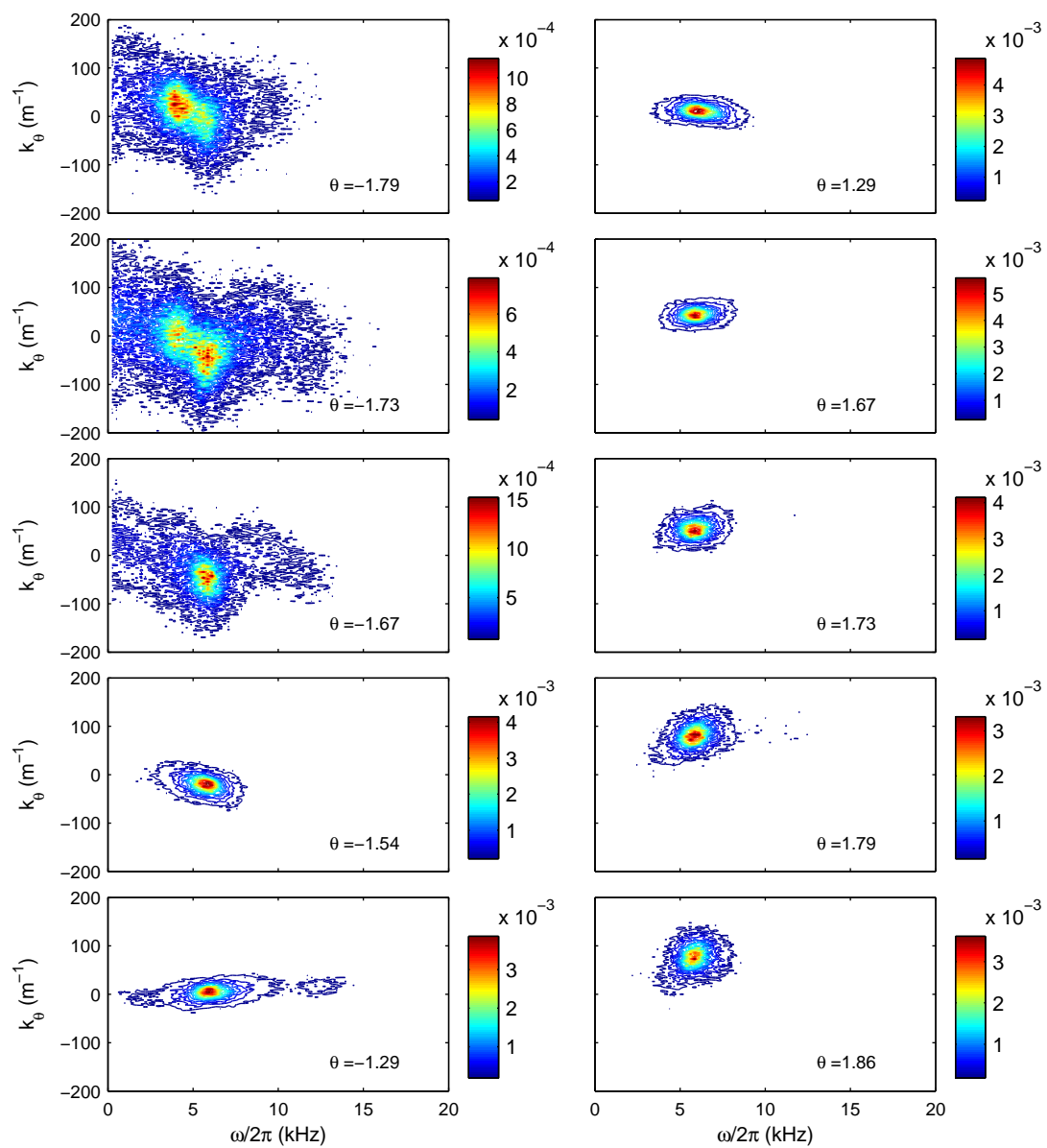


Figure 9.15: Same as Fig. 9.13, but for $B_z = 1.6$ mT.

Chapter 10

Development of turbulence from drift-interchange instabilities

The previous Chapters have addressed the linear properties of fluctuations and drift instabilities on TORPEX, including a comparison of the measured dispersion relation with that calculated using a kinetic linear dispersion relation for electrostatic waves. We have found that both interchange and drift-interchange instabilities can develop. We have shown in Chap. 8 that drift-interchange instabilities have a coherent character at the location where they are generated and that the power spectrum broadens in frequency and wavenumber along the direction of convection.

The present Chapter is aimed at characterizing the evolution of the nonlinear properties of fluctuations at the various stages of development of turbulence. This is done by comparing the amplitude of the bispectrum measured at different locations over the plasma cross-section, starting from the region where the drift-interchange instability is generated and following the direction of convection. We show that the broadening of the spectrum is mainly due to three-wave interactions (Sec. 10.1), in which the linearly unstable mode loses its energy to the partner components (Sec. 10.2.3). Based on the measurement of a linear dispersion relation along the direction of convection, the cascade in frequency can be interpreted as a cascade in wavenumber, indicating an energy transfer from large to small scales (Sec. 10.3). We discuss in Sec. 10.4 the nonlinear properties of interchange instabilities and possible interactions with the drift-interchange instabilities at the location where both are present, namely on the low field side. Section 10.5 summarizes some properties of the coherent structures commonly detected on TORPEX, and attempts a comparison of their spatio-temporal properties with the locally measured spectral features.

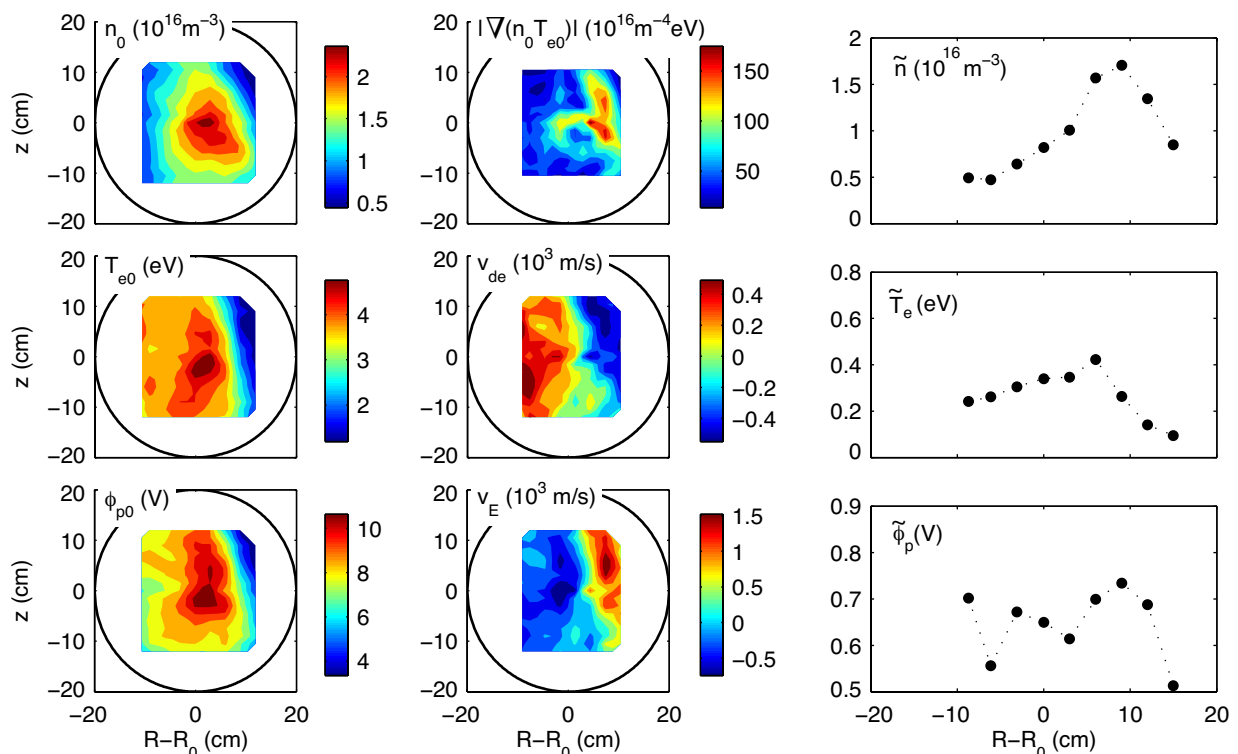


Figure 10.1: (Same as Fig. 4.6). Left: Time-averaged background profiles, reconstructed during 300 ms of stationary discharge, with 0.4 kW of absorbed power. Center: profile of the amplitude of the background pressure gradient, of the electron diamagnetic drift velocity \mathbf{v}_{de} and of the $\mathbf{E}_0 \times \mathbf{B}$ drift velocity, \mathbf{v}_E . The toroidal magnetic field is directed into the plane of the figure, \mathbf{v}_{de} is clockwise and \mathbf{v}_E is counter-clockwise. Right: Radial profile of the rms value of \tilde{n} , \tilde{T}_e and $\tilde{\phi}_p$ measured at midplane from the power spectra, measured over 1.5 s of stationary discharge.

The experimental configuration used in this Chapter is the same as in Chap. 8, namely an Hydrogen plasma at standard values of p_0 , B_φ and B_z , except the absorbed microwave power, which is 10% larger. This causes the maximum of n_0 to shift towards the low field side [42], without affecting the typical pressure gradient scale length and the spectral properties of fluctuations. The characteristics of the time-averaged profiles of density, temperature, and plasma potential, as well as the corresponding fluctuating quantities have already been discussed in Sec. 8.1. For the sake of completeness, these profiles are reported in Fig. 10.1. Density fluctuations have their maximum amplitude on the low field side, at the position of maximum pressure gradient, where they reach $\tilde{n}/n_e \approx 60\%$. Normalized fluctuations, \tilde{n}/n_e and $e\tilde{\phi}_p/T_e$ are comparable in amplitude, although electrons are strongly non adiabatic.

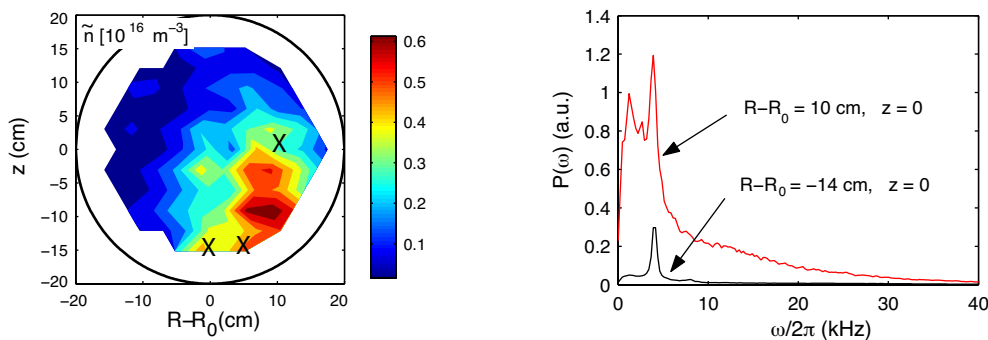


Figure 10.2: Left: rms value of fluctuations of \tilde{n} associated with the mode at frequency $f_0 \sim 4$ kHz. The crosses indicate the positions where the bispectra in Fig. 10.3 have been measured. Right: power spectrum of \tilde{n} , measured at midplane, on the high and on the low field side.

10.1 Nonlinear coupling

Figure 10.2 shows the profile of the rms fluctuations associated with the drift-interchange instability, reconstructed using the method described in Sec. 5.3. The mode amplitude is maximum on the low field side, where the pressure gradient and the magnetic field gradient are co-linear. On the midplane the mode amplitude increases by a factor of four moving from the high to the low field side, as indicated by Fig. 10.2. This increase in amplitude is accompanied by an increase in the level of fluctuations at frequencies larger than f_0 , from 10% to 40%, suggesting a development of turbulence during convection. Under the hypothesis of a weak departure from linearity, the development of turbulence can be described in terms of the energy cascade from an unstable mode to other spectral components via three-wave interactions [8]. A measure of the statistical dependence between three waves is provided by the *bispectrum*, whose estimate is given, *e.g.* for density fluctuations, by the ensemble average [59], Eq. (6.16):

$$B(l, m) = \frac{1}{M} \sum_{j=1}^M n_l^{(j)} n_m^{(j)} n_{l+m}^{*(j)}.$$

Here M is the number of independent realizations and n_l , n_m and n_{l+m} denote the spectral components of density fluctuations at frequency ω_l , ω_m and $\omega_l + \omega_m$, respectively. If the modes are independent, the bispectrum vanishes due to random phase mixing effects. Only if the three spectral components are coupled to each other, can the total phase, averaged over a large number of samples, converge to a nonzero value. A measure of the phase coupling, independent of the amplitude of fluctuations, is given by the *bicoherence*, a normalized bispectrum [59]. Figure 10.3 shows the bispectrum and the bicoherence measured at two locations: at the lower part of the plasma cross-section, where the instability at frequency f_0 is generated, and at the midplane, at $R - R_0 = 10$ cm, where the magnitude of \tilde{n} is maximum. Due to the symmetry $B(l, m) \equiv B(m, l) \equiv B(-l, -m)^*$, the bispectrum needs to be estimated only in a restricted region of the frequency plane (ω_l, ω_m) , delimited in the figure by thick

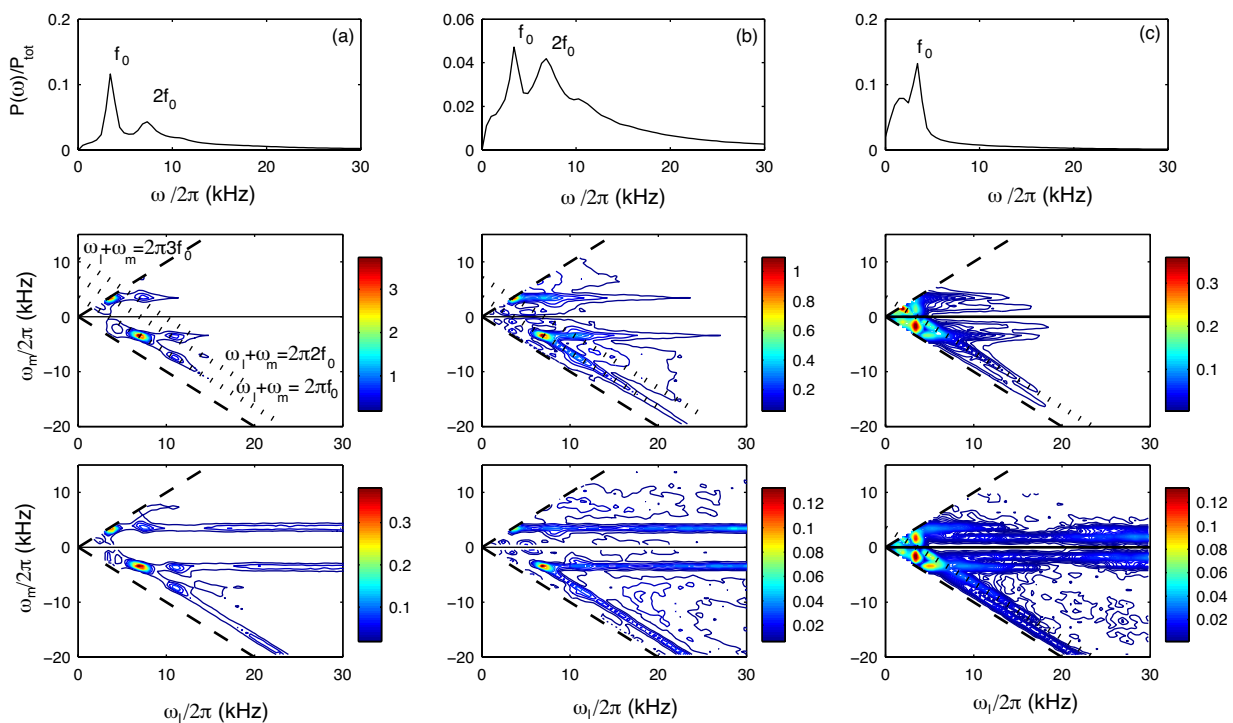


Figure 10.3: Top: Power spectrum of \tilde{n} , normalized to the total power, measured at (a) $R - R_0 = 0$ cm, $z = -16$ cm, (b) $R - R_0 = 5$ cm, $z = -15$ cm. (c) $R - R_0 = 10$ cm, $z = 0$. Middle: Bispectrum of \tilde{n} , measured at the same positions, estimated from more than 15000 samples, with a frequency resolution of 0.25 kHz. Bottom: Bicoherence of \tilde{n} , measured at the same positions.

dashed lines. Note that both sum and difference combinations between frequencies are allowed by the resonance condition $\omega_l \pm \omega_m = \omega$, with $|\omega_l| > |\omega_m|$. For purposes of representation, all quadratic interactions are indicated by a sum where $\omega_l > 0$ and ω_m can assume both positive and negative values. Interactions among components with $\omega_l, \omega_m > 0$, referred to as “sum” interactions, are represented in the upper triangle in Fig. 10.3, while interactions among components with $\omega_l > 0$ and $\omega_m < 0$, referred to as “difference” interactions, are represented in the lower triangle. The interactions occurring among triplets with comparable frequencies, $\omega_l \sim \omega_m \sim \omega$, will be indicated in the following as “local”, and those where one frequency is much smaller than the others as “nonlocal”.

The dominant nonlinear coupling close to the location where the drift-interchange instability is generated [Fig. 10.3(a)] is between the fundamental f_0 and the second harmonic $2f_0$, with $f_0 = \omega_0/2\pi$, indicated by the value of $|B(l, m)|$ at (ω_0, ω_0) and $(2\omega_0, -\omega_0)$. To facilitate the interpretation of the bispectrum, parallel dotted lines are added to Fig. 10.3. Spectral components (ω_l, ω_m) lying on the same line are quadratically coupled to the same frequency ω , indicated by the value at the intersection with the positive vertical axis. For example, the peak at $2f_0$ in the power spectrum is the result of the interactions $f_0 + f_0$ and $3f_0 - f_0$, both represented by the same dotted line.

The same considerations apply to the dominant peak, f_0 , which is quadratically coupled to all spectral components with frequency $2f_0 \leq \omega_l/2\pi \leq 3f_0$, and $|\omega_m|/2\pi \leq 2f_0$. The power spectral density of fluctuations with frequency $f > 2f_0$ increases moving toward the LFS [Fig. 10.3(b)], while the fundamental harmonic decreases in amplitude (see Fig. 10.2), becoming comparable to the second harmonic. Interactions become more nonlocal in character along the $\mathbf{E}_0 \times \mathbf{B}$ convection path, with coherent phase coupling among f_0 and fluctuations with significantly larger frequency. Spectral regions between harmonics are rapidly filled in, and the value of $|B(l, m)|$ is comparable for interactions between f_0 and fluctuations with frequency in the range $[2f_0, 3f_0]$. It will be shown in Sec. 10.2.3 that in these interactions the unstable mode at f_0 loses its energy to the partner components, causing the filling of the spectrum.

In addition to the mode at f_0 , a mode at lower frequency is detected at midplane [63], with $f_1 \simeq 1.5$ kHz. The amplitude of the bispectrum indicates phase coupling between the two modes and among all spectral components with frequency in between [see Fig. 10.3(c)]. Proceeding along the direction of convection, the harmonics of f_0 are not detectable in the power spectrum of \tilde{n} , and quadratic coupling is measured between f_0 and fluctuations with frequency $f \geq f_0$. The ridges corresponding to interactions $(\omega_l/2\pi, \pm|f_1|)$ and $(\omega_l/2\pi, \pm|f_0|)$ indicate that the modes at f_1 and f_0 are phase coupled to spectral components with larger frequency.

10.2 From nonlinear coupling to energy cascade

The bispectrum can be used to identify the frequency range over which quadratic coupling occurs, but does not provide direct information on the energy transfer. The measured phase coupling could be, in fact, the signature of nonlinear interactions occurred upstream with respect to the location of measurement and then convected at that location. To discriminate between these processes and nonlinear interactions active at the location of measurement, two-point techniques are needed [60][64]. Let $n_{1,\omega}$ and $n_{2,\omega}$ denote the Fourier coefficients of density fluctuations at frequency ω , measured respectively at positions z_1 and $z_2 = z_1 + \Delta z$. Considering the plasma as a causal input-output system with unknown response function, $n_{2,\omega}$ can be written as a function of $n_{1,\omega}$ using a network representation [60] (see Sec. 6.3):

$$n_{2,\omega} = \left(L_\omega - i \frac{\omega}{v_E} d_{\text{tip}} \right) n_{1,\omega} + \sum_{\substack{\omega_l \geq \omega_m \\ \omega = \omega_l + \omega_m}} Q_\omega^{l,m} n_{1,l} n_{1,m} + \epsilon_\omega. \quad (10.1)$$

Here the sum is evaluated over all frequencies such that $\omega_l + \omega_m = \omega$. As discussed in Sec. 6.3, the complex linear term L_ω contains information about the ‘‘amplification’’ and phase variation, and is related to the linear growth (damping) rate and dispersion. The coupling coefficients $Q_\omega^{l,m}$ describe quadratic interactions among triplets of waves satisfying the resonance condition $\omega_l \pm |\omega_m| = \omega$. Contributions not directly included in the model, such as nonlinear interactions of order larger than second and dissipation, are cast into the error term ϵ_ω . Cubic interaction terms, not introduced in Eq. (10.1), are related to processes involving four waves, which can be quantified by the ensemble

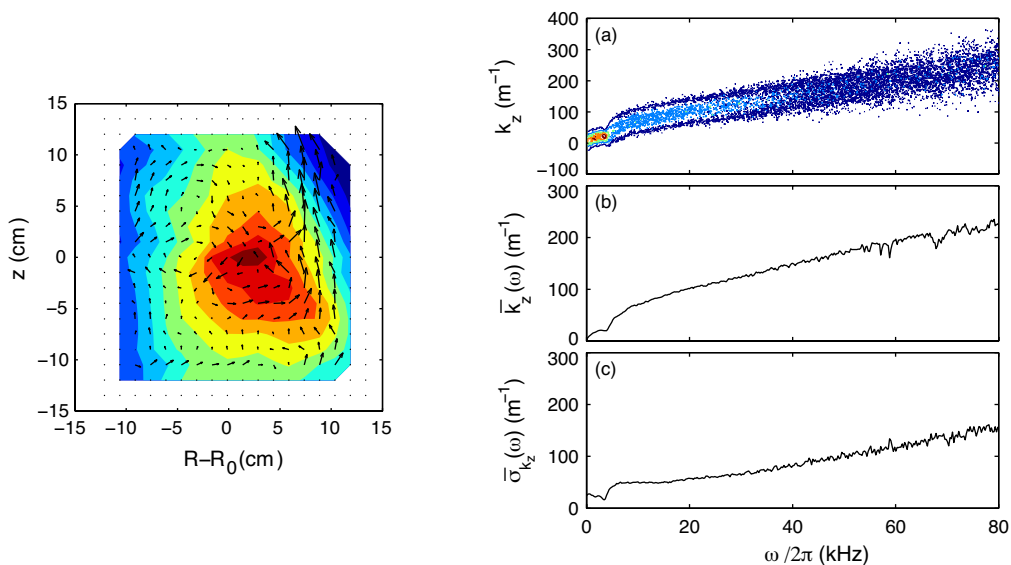


Figure 10.4: Left: Density profile (same as Fig. 10.1). Arrows indicate the direction of propagation of instabilities in the laboratory frame, resulting from the vector sum of the electron diamagnetic and the $\mathbf{E}_0 \times \mathbf{B}$ drift velocities. The arrow length is proportional to the velocity strength. Right: (a) Conditional spectrum of density fluctuations, $p(k_z|\omega)$, measured at the midplane, $R - R_0 = 10$ cm, from the ion saturation current signal of two probes with vertical separation $\Delta z = 0.6$ cm. Statistical dispersion relation (b) and spectral width (c), calculated from Eq. (5.21).

average $\langle n_l n_m n_p n_{l+m+p}^* \rangle$, Eq. (6.19). The measured four-wave phase coherence is very localized in frequency and is significant only for combinations of modes involving f_0 . Nevertheless, the amplitude of the trispectrum corresponding to these interactions is two orders of magnitude smaller than the amplitude of the bispectrum, thus justifying truncation to second order.

10.2.1 Hypotheses and limits of the model

Equation (10.1) is derived from a Volterra model, assuming that fluctuations are stationary and the spatial evolution is one dimensional, with the z axis taken along the direction of propagation and oriented to have the measured phase shift positive [65] (see Sec. 6.1). In the laboratory frame the measured phase velocity of drift waves is the vector sum of the electron diamagnetic and the $\mathbf{E}_0 \times \mathbf{B}$ drift velocities, Eq. (6.5). If the background pressure gradient and the electric field are anti-parallel, as in the experiments presented herein, so are the resulting drifts; the one dimensional approximation is valid also in the laboratory frame. The error in the estimate of the linear and quadratic coefficients will therefore be minimum if the probes are aligned along the direction of propagation. At midplane, at the position where \tilde{n} is maximum, the pressure gradient and the background electric field are mainly directed along R . The corresponding drifts are thus along z , as shown in Fig. 10.4. The strong convection at this location justifies the one-dimensional approximation for these plasma scenarios.

The model represented by Eq. (10.1) can be used as long as the turbulence is weakly developed, as discussed in Sec. 6.1.1 and in [57][64]. A measurement of the degree of turbulence associated with fluctuations at frequency ω is given by the second moment of the conditional wavenumber and frequency spectrum $p(k_z|\omega)$, Eq. (5.21). The conditional spectrum measured at midplane with two probes separated by $d_{\text{tip}} = 0.6$ cm, as well as the statistical dispersion relation $\bar{k}_z(\omega)$ are shown in Fig. 10.4. Density fluctuations with frequency in the range 10 to 60 kHz propagate along z with the same group velocity. The value of $\bar{\sigma}_{k_z}(\omega)$ is minimum at the frequency f_0 of the most coherent component of the spectrum and smoothly increases with increasing frequency, indicating a development of turbulence, also indicated by the broadening of $p(k_z|\omega)$ in k_z . For frequencies up to 60 kHz the degree of turbulence is low, *i.e.* $\bar{\sigma}_{k_z}(\omega) < \bar{k}_z(\omega)$. For frequencies $f \gtrsim 80$ kHz, the low signal-to-noise ratio precludes any clear conclusion. The estimate of the quadratic coefficients is therefore limited to fluctuations with $f \leq 60$ kHz.

10.2.2 Estimate of the nonlinear coupling coefficients

The linear and quadratic coefficients in Eq. (10.1) are estimated by means of multivariate regression techniques, as described in Sec. 6.3 and in [57]. The time sequences $\tilde{n}_1(t)$ and $\tilde{n}_2(t)$ are divided into M samples of length N , with 50% overlapping. The value of N is chosen in order to have the minimum frequency resolution required to resolve significant spectral components. After having calculated the Fourier components for each sample, the following system of M linear equations is built [57] for each value of the frequency:

$$Y_\omega = X_\omega A_\omega$$

with A_ω , X_ω and Y_ω defined by Eqs. (6.25)-(6.27). The choice of M strongly depends on the amplitude of the power spectrum, thus on the noise level. For simulated, noise-free, test signals, $M \approx N$ is sufficient to reconstruct the coupling coefficients with an accuracy of $\gamma_\omega^2 \simeq 99\%$, with γ_ω^2 defined by Eq. (6.30) (see Sec. 6.3.1). The required number of samples can significantly increase for real data, because of the slow convergence of the bispectrum for spectral power low with respect to the noise level. The mean value of the bicoherence, calculated in frequency ranges having negligible quadratic interactions, is approximately 7×10^{-4} , which is taken as background noise level. As a reference, the bicoherence of a gaussian signal, obtained by mixing up the phases of the measured signals, is 8×10^{-5} . The bicoherence measured at the midplane is approximately 12% at the frequency of the dominant mode f_0 , but decreases significantly for interactions involving spectral components with larger frequencies (see Fig. 10.3). For frequencies above 20 kHz the phase coherence is only 10 times larger than the background noise level, reducing the statistical significance of the estimate of the quadratic coefficients.

The coherence between the measured fluctuations, $n_{2,\omega}$, and the prediction of the model, Y_ω , is shown in Fig. 10.6 for measurements taken at midplane. The accuracy of the estimate is good at the frequency of the instability, then decreases with increasing frequency. The coherence saturates for M larger than a critical value that depends on the signal-to-noise ratio: increasing the number of samples over this value does not

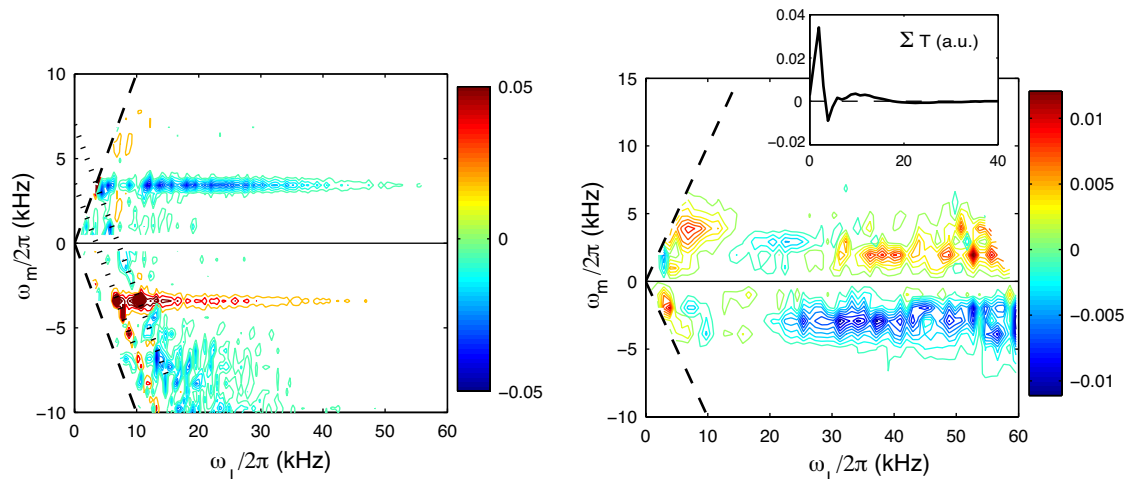


Figure 10.5: Left: Spectral power transfer due to quadratic interactions for \tilde{n} , measured at $R - R_0 = 5$ cm, $z = -15$ cm, using two probes with 0.1 cm separation along the azimuthal direction. The bispectrum measured at the same location is shown in Fig. 10.3(b). Scales of red indicate positive values of $T_\omega^{l,m}$, while scales of blue indicate negative values. Right: Relative spectral power transfer due to quadratic interactions measured at midplane, at $R - R_0 = 10$ cm, using two probes with 0.6 cm separation along z . The values of $T_\omega^{l,m}$ are normalized in this plot to the power spectral density of the sum component, P_ω , to highlight nonlocal interactions in the range from 20 to 60 kHz. The corresponding bispectrum is shown in Fig. 10.3(c). Scales of red indicate positive values of $T_\omega^{l,m}$, scales of blue indicate negative values. The insert shows the total contribution of quadratic interactions, $\Sigma T_\omega^{l,m}$.

lead to a better estimate (see Sec. 6.3.1). We believe the largest source of error in the estimate of the quadratic coupling stems from the low signal-to-noise ratio at large frequency, which affects the measurement of the phase, causing the error term ϵ_ω in Eq. (10.1) to increase with frequency. A concomitant effect is given by the increase of the degree of turbulence with frequency, which causes a spread of the distribution of the measured phases around the average value.

10.2.3 Spectral power transfer

A measure of how accurately the quadratic model describes the evolution of the fluctuating field is obtained by comparing the measured relative variation of spectral power, moving from z_1 to z_2 , with the predictions from the quadratic model, Eq. (6.14):

$$\frac{1}{2} \frac{dP_\omega}{dz} = \Re(\Gamma_\omega) P_\omega + \sum_{\substack{\omega_l \geq \omega_m \\ \omega = \omega_l + \omega_m}} \Re[\Gamma_\omega^{l,m} B(l, m)]. \quad (10.2)$$

Here $P_\omega = \langle |n_\omega|^2 \rangle$ is the power spectral density and the terms $T_\omega^{l,m} = \Re[\Gamma_\omega^{l,m} B(l, m)]$ quantify the spectral power transfer due to three-wave interaction processes. According to this model, the variation of P_ω at frequency ω occurring during propagation over the

distance dz is the result of the linear growth (or damping) of the mode plus the total contribution of quadratic interactions among triplets involving the same component ω . The amount of spectral transfer depends on the strength of the coupling coefficients $\Gamma_\omega^{l,m}$ and on the amount of coherent phase coupling, quantified by the bispectrum $B(l, m) = \langle n_l n_m n_{l+m}^* \rangle$. Positive $T_\omega^{l,m}$ values indicate a transfer of spectral power from the components ω_l, ω_m to the sum component $\omega = \omega_l + \omega_m$, while negative values indicate a transfer in the opposite direction, $\omega \rightarrow \omega_l, \omega_m$. Figure 10.5(a) shows the quadratic power transfer measured at the lower part of the plasma cross-section using two probes with 0.1 cm separation along the azimuthal direction. The corresponding bispectrum is shown in Fig. 10.3(b). A direct measurement of the background parameters is not available at this location, as shown in Fig. 10.1. The measured ion saturation current profile from an 86-tip LPs array and the statistical dispersion relation along the azimuthal direction, $\bar{k}_\theta(\omega)$, confirm that the propagation is mostly azimuthal at this location. The largest spectral power transfer occurs for interactions involving the first three harmonics, as expected by the amplitude of the measured bispectrum. The horizontal stripe corresponding to $\omega_m/2\pi = -|f_0|$, with $T_\omega^{l,m} > 0$, indicates that energy is transferred through difference interactions from components with frequency ω_l to components with frequency $\omega/2\pi \in [f_0, \omega_l/2\pi]$. These interactions are responsible for filling in the spectral valley between the first two harmonics, enclosed between dotted lines, and for the broadening of the frequency spectrum. The gain of spectral power at frequency ω reflects in a negative value of $T_\omega^{l,m}$ for interactions involving the partner components, as indicated by the horizontal stripe at $\omega_m/2\pi \simeq f_0$ and the region where $\omega_l \simeq |\omega_m|$, with $\omega_m < 0$.

Figure 10.5(b) shows the quadratic power transfer, measured at midplane at $R - R_0 = 10$ cm, using two probes with 0.6 cm separation along z . The pressure gradient and the electrostatic field at this location are mainly along R , giving rise to propagation along z . Local interactions among spectral components with $f < 10$ kHz and nonlocal interactions are measured, as discussed in Sec. 10.1, the power transfer due to the former being much larger.

To highlight nonlocal interactions, each coefficient $T_\omega^{l,m}$ in Fig. 10.5(b) is normalized to the power spectral density P_ω of the sum component. $T_\omega^{l,m}$ represents the relative contribution of the triplet $\omega_l, \omega_m, \omega$ to the power spectral density measured at frequency ω . The horizontal stripe with constant ω_m indicates that nonlocal interactions between spectral components with frequency $\omega_l \gg \omega_m$ transfer energy to frequency $\omega > \omega_l, \omega_m$. This gain of spectral power is reflected by the negative values of $T_\omega^{l,m}$ in the region corresponding to difference interactions.

The relative variation of spectral power along z due to quadratic coupling, $2\Sigma T_\omega^{l,m}/P_\omega$, is shown in Fig. 10.6(a) for measurements taken at midplane. It is negative at f_0 and positive for $\omega/2\pi < f_0$ and $f_0 < \omega/2\pi < 20$ kHz, indicating that in quadratic interactions involving the unstable mode f_0 , this loses energy on the partner components. The relative spectral transfer is negative for frequencies around 30 kHz, probably because of errors in the estimate of the coupling coefficients due to a low signal-to-noise ratio. In fact, this inversion is not observed in those cases where turbulence is more developed and the power spectral density is large up to higher frequencies.

This is observed, for example, when the injected microwave power is increased by a

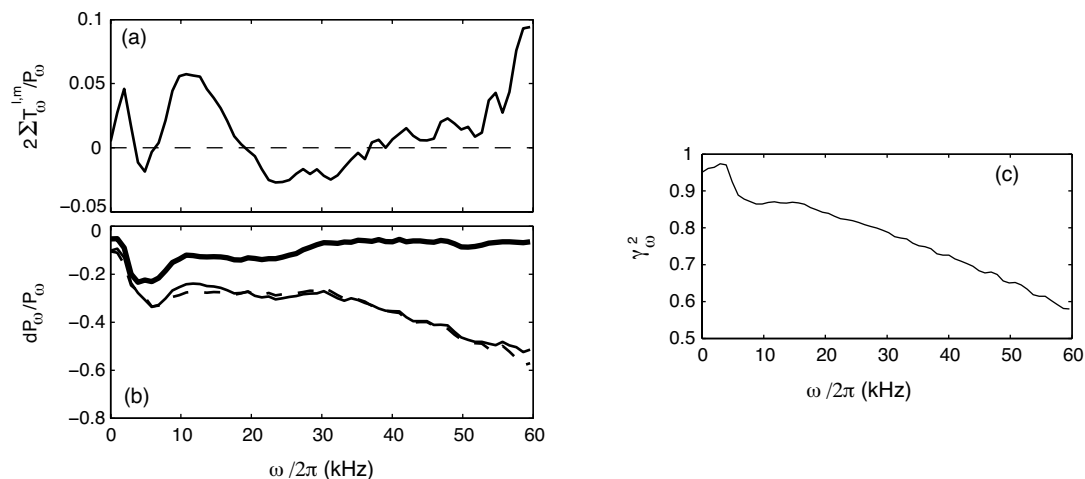


Figure 10.6: (a) Relative variation of power due to quadratic interactions, $2\Sigma T_{\omega}^{l,m}/P_{\omega}$, measured at $R - R_0 = 10$ cm, from two probes with vertical separation $\Delta z = 0.6$ cm. (b) Relative variation of power measured over Δz (solid thick line), compared with the relative variation estimated from Eq. (10.2) (solid thin line). The dashed line indicates the relative variation of power due to the linear term. (c) Coherence between the fluctuations measured at midplane, at $R - R_0 = 10$ cm, and the estimate from Eq. (10.1). The coefficients L_{ω} and $Q_{\omega}^{l,m}$ have been estimated from $M = 8655$ samples.

factor of three, and the magnetic field and neutral gas pressure are kept constant. The comparison between the relative variation of power, modeled by the right hand side of Eq. (10.2) and the measured variation, $\Delta P_{\omega}/P_{\omega} = 2(P_{\omega,2} - P_{\omega,1})/(P_{\omega,1} + P_{\omega,2})$, is shown in Fig. 10.6(b). Differences between probe tip size are estimated to affect $\Delta P_{\omega}/P_{\omega}$ by less than 5%, thus the variation of spectral power over the distance Δz , which is 20% at f_0 , must be interpreted as an effect of spatial inhomogeneity. The measured relative variation of power is qualitatively reproduced by the quadratic model. Nevertheless, the damping rate is overestimated, probably because of deviations of the dynamics from one dimensional. This can occur if the diamagnetic and the $\mathbf{E}_0 \times \mathbf{B}$ drift are not perfectly parallel, or if the probes are not exactly aligned along the direction of propagation. Both cases result in an underestimate of the coupling coefficients, as the energy redistribution along R is not taken into account.

10.3 From frequency to wavenumber cascade

Three-wave phase coupling is measured in the frequency domain at different locations of the plasma cross-section, along the direction of the $\mathbf{E}_0 \times \mathbf{B}$ convection, starting from the region where the observed drift-interchange instability is generated. It is shown that the frequency spectrum broadens mainly because of three-wave interactions, which make the unstable mode lose its energy to the partner components. Equation (10.1) is a particular case of a more general description of two-dimensional turbulence, where the resonance condition, considered here only in the frequency do-

main, is written as $\omega(\mathbf{k}_l + \mathbf{k}_m) = \omega(\mathbf{k}_l) + \omega(\mathbf{k}_m)$. Space and time derivatives are interchangeable in the Volterra representation, as discussed in Chap. 6 and, provided that the medium is homogeneous, an equation for the temporal dynamics of \tilde{n} can be derived using a Fourier representation in space. If probes are close enough that the amplitude variation of fluctuations over the probe separation due to nonlinear interactions is small, local homogeneity can be invoked. In this case, the measurement of a linear dispersion relation can be used to relate time and space dynamics and to interpret the cascade in frequency as a cascade in wavenumber.

Figure 10.7 shows the conditional spectrum $p(k_R|\omega)$ measured at midplane, at the position of maximum $|\tilde{n}|$, from two LPs with a radial separation of 1 cm. The value of $\bar{k}_R(\omega)$ reflects the scale length of density fluctuations at different frequencies. The fluctuations are coherent at frequency f_0 , with $\bar{k}_R(\omega) \sim 80 \text{ m}^{-1}$. This is consistent with the observations of macroscopic coherent structures in the time domain, which exhibit typical radial extensions $\sim 3 - 7 \text{ cm}$, and are advected in the vertical direction by the $\mathbf{E}_0 \times \mathbf{B}$ drift [28]. For larger frequencies the degree of turbulence is high, *i.e.* $\bar{\sigma}_R(\omega) > \bar{k}_R(\omega)$, and the measurement of $\bar{k}_R(\omega)$ becomes unreliable. In the experiments presented, the extension of the results from the frequency to the wavenumber domain is justified for fluctuations with $f > 10 \text{ kHz}$. In this range $\bar{k}_R(\omega)$ is almost independent of frequency, with $|\bar{k}_R(\omega)| \ll \bar{k}_z(\omega)$, and the forward cascade in frequency can be interpreted as a forward cascade in wavenumber, with transfer of energy from large to small scales. Conversely, for frequencies below 10 kHz, *i.e.* for interactions local in frequency involving large scale fluctuations, both $\bar{k}_z(\omega)$ and $\bar{k}_R(\omega)$ vary with frequency, and it is impossible to infer the direction of the wavenumber cascade. A complete characterization of the nonlinear coupling should include measurements both in the frequency and in the wavenumber domain. This is particularly important in those cases where the turbulence is isotropic in k_R and k_z .

10.4 Nonlinear interactions between pure interchange and drift-interchange instabilities

As discussed in the previous Chapter (Sec. 9.5), interchange and drift-interchange instabilities can coexist on the low-field side. For $B_z \leq 1.0 \text{ mT}$ the interchange mode is not detected at the lower part of the plasma cross-section, its amplitude at midplane is lower than that of the drift-interchange mode and the associated frequency spectrum is broad. For $B_z \geq 1.2 \text{ mT}$ the interchange mode is detected also at the bottom of the plasma cross-section and its amplitude at midplane is larger than that of the drift-interchange mode. If the frequencies of the two modes are sufficiently far apart, they maintain their individual spectral properties and are both convected by the $\mathbf{E}_0 \times \mathbf{B}$ field. Conversely, if the frequencies of the modes are comparable, as in the case of $B_z = 1.6 \text{ mT}$ (Fig. 9.15), there are indications that the drift-interchange mode becomes dominated by the interchange mode. At the upper part of the plasma cross-section, in fact, the drift-interchange mode cannot be detected.

The question arises whether or not the two instabilities interact nonlinearly and if there exists a significant energy transfer from one to the other. The answer to this

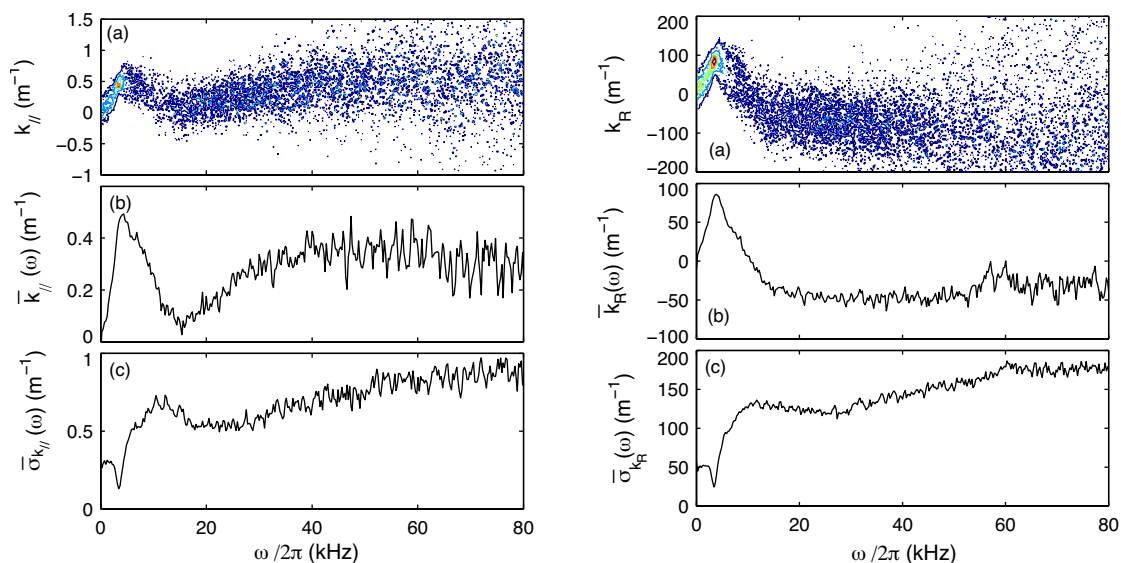


Figure 10.7: Left: (a) Conditional spectrum of density fluctuations, $p(k_R|\omega)$, estimated from two probes located at $R - R_0 = 10$ cm, with radial separation $\Delta R = 1$ cm. (b)-(c) statistical dispersion relation and wavenumber spectral width, Eq. (5.21). Right: (a) $p(k_{\parallel}, \omega)$ estimated from two probes located at $R - R_0 = 10$ cm, and toroidally separated by $\pi/2$. The probes are misaligned with respect to the magnetic field line by approximately 0.5 cm, the measured k is therefore an upper limit of k_{\parallel} . (b)-(c) statistical dispersion relation and wavenumber spectral width.

question can be found in the bispectra shown in Figs. 10.8-10.10. Figure 10.8 refers to measurements at midplane, for some values of the vertical field in the range $[0.8, 1.8]$ mT, while Fig. 10.9 and Fig. 10.10 refer to measurements done at the lower part of the plasma cross-section for $B_z = 1.4$ and 1.6 mT respectively. Nonlinear coupling between the two modes is measured at midplane, for $B_z \leq 1.4$ mT, with a stronger phase coherence for larger vertical field values. This is possibly related to the increase in amplitude and coherence of the interchange mode when B_z increases.

However, nonlinear coupling between modes is significantly weaker than between each mode and its harmonics, as indicated by the value of the bicoherence. This is seen in particular at the lower part of the plasma cross-section (see Fig. 10.9). Moving from the high to the low field side along the azimuthal direction, the value of the bicoherence decreases from 15% to approximately 5%, then increases again. The regions where the bicoherence is large correspond to geometrical locations where only one of the two modes is detected, while the regions where the bicoherence is low correspond to locations where both modes are detected. The phase coupling between the two modes is lower than the phase coupling between the interchange mode and its harmonics also at $B_z = 1.6$ mT, as shown in Fig. 10.10. Note that, for $B_z = 1.4$ mT, the frequency of the interchange instability is comparable to the frequency of the second harmonic of the interchange instability. Care should be taken in the interpretation of the bispectrum.

These preliminary results suggest that weak nonlinear interactions take place between the two modes. Although the nonlinear coupling increases when the two frequen-

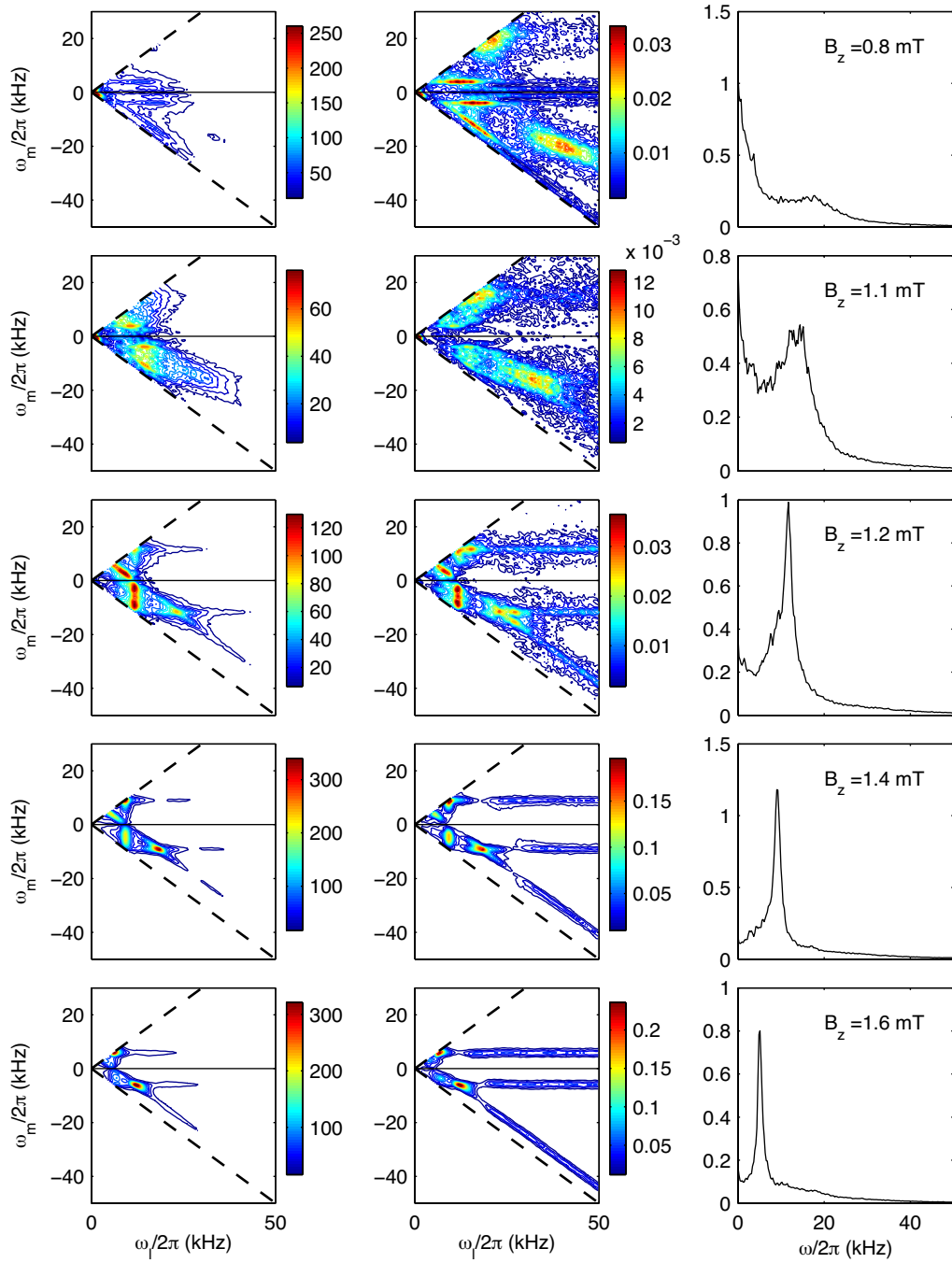


Figure 10.8: Bispectrum (left), bicoherence (center) and power spectrum (right), measured at midplane for different values of the vertical field, increasing from top to bottom in the figure.

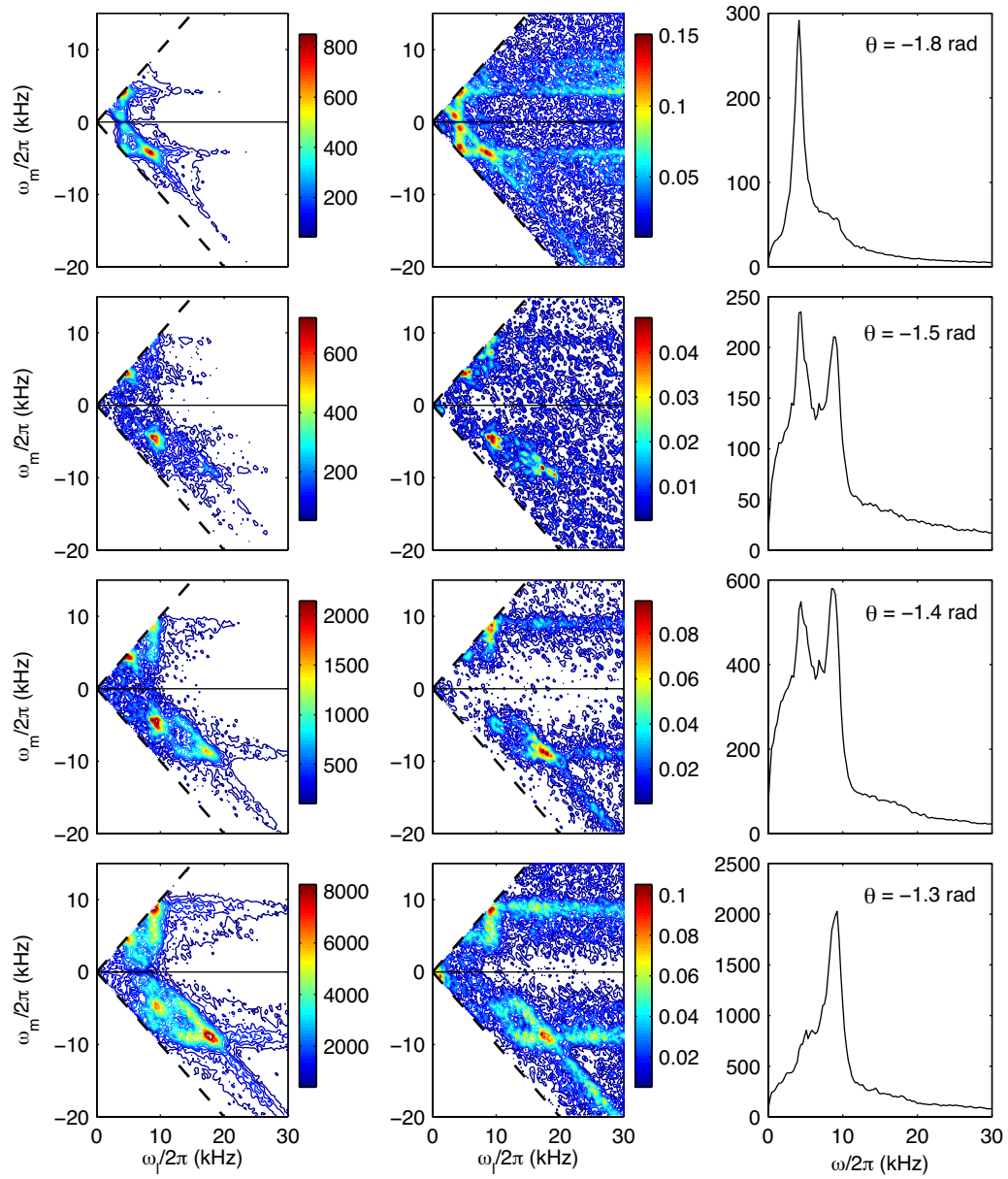


Figure 10.9: Bispectrum (left), bicoherence (center) and power spectrum (right), measured for $B_z = 1.4$ mT at the bottom part of the plasma cross-section.

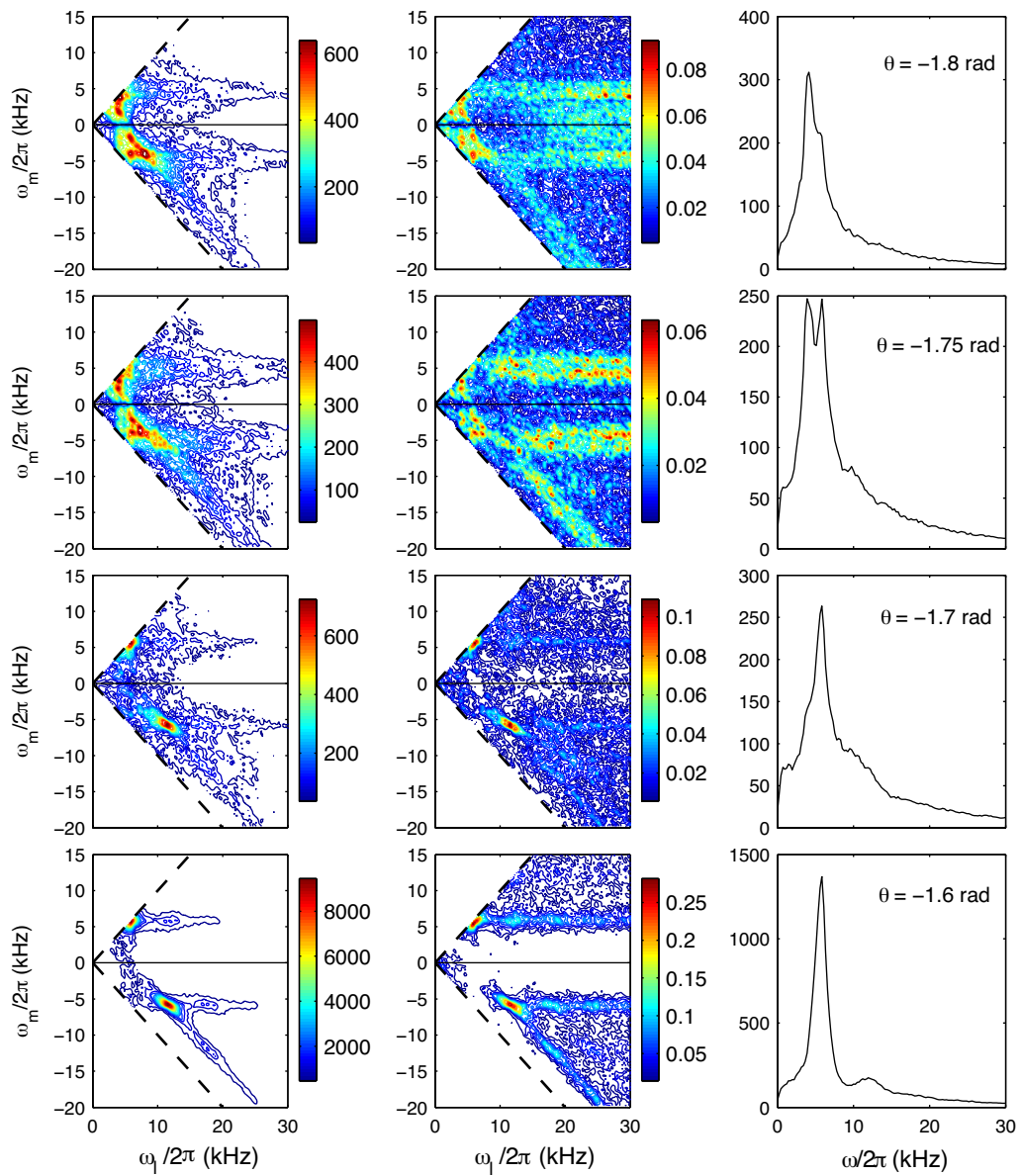


Figure 10.10: Same as Fig. 10.9, but for $B_z = 1.6$ mT.

cies are sufficiently close, the two modes maintain their individual character throughout the interaction. No clear indications of energy transfer from one mode to the other are provided by the analyzed data.

In general, the mechanism leading to a turbulent spectrum from an interchange instability, regardless of its nonlinear interactions with drift-interchange modes, seems to be similar to the mechanism described in the previous Sections for the drift-interchange mode. As shown in Fig. 10.10, generation of harmonics occurs when the amplitude of the mode is sufficiently large and the dominant interactions are those between lowest order harmonics. Proceeding along the convection path, the dominant instability interacts nonlinearly with spectral components with significantly larger frequencies.

10.5 Spectral features versus spatio-temporal dynamics

In most experimental situations on TORPEX, the amplitude of density fluctuations peaks on the low field side of the maximum of n_0 . In the case of drift-interchange instabilities the region of maximum amplitude of \tilde{n} is usually localized at $z < 0$ and on the low field side, as shown in Fig. 8.4 and Fig. 10.2. In the case of interchange instabilities, the region of maximum amplitude is usually vertically elongated, as shown in Fig. 9.4.

The region of maximum amplitude corresponds also to the location where large-scale coherent structures are detected in the density fluctuations [28]. These structures have a bipolar nature, with alternate negative and positive maxima, and propagate in the $\mathbf{E}_0 \times \mathbf{B}$ direction.

Figure 10.11 shows two examples of the profile of \tilde{n} measured with the HEX TIP array in Hydrogen plasmas, respectively at $B_z = 0.6$ mT and $B_z = 1.2$ mT. The time traces of I_{sat} have been filtered in the range of [1, 20] kHz to eliminate the contribution of the time-averaged part and of the high frequency spectral components. In this frequency range the power spectrum of \tilde{n} is dominated in one case by a drift-interchange instability, in the other by a pure interchange instability. The fluctuation amplitude is large enough on the low field side that the propagation of wave crests are observed directly in the time evolution of the \tilde{n} profile or at any individual time frame.

The statistical properties of structures, including size, velocity and trajectories can be reconstructed by means of a pattern-recognition method [34][47]. The global statistical space-time properties can then be compared to the local statistical spectral features of fluctuations.

For example, the geometrical orientation of structures in Fig. 10.11 seems to be related to the direction of the background pressure gradients. The structures appear in fact elongated and are oblique in the case of lower B_z , while they are almost horizontal for larger B_z , when the pressure profiles appear more slab-like. In the latter case the propagation is essentially vertical, consistent with the $\mathbf{E}_0 \times \mathbf{B}$ calculated from the measured background electric field along R (see Fig. 9.1).

This is confirmed by the statistical reconstruction of the trajectories of their center of mass, shown in Fig. 10.11. The velocity field of the structures (*i.e.* the trajectories)

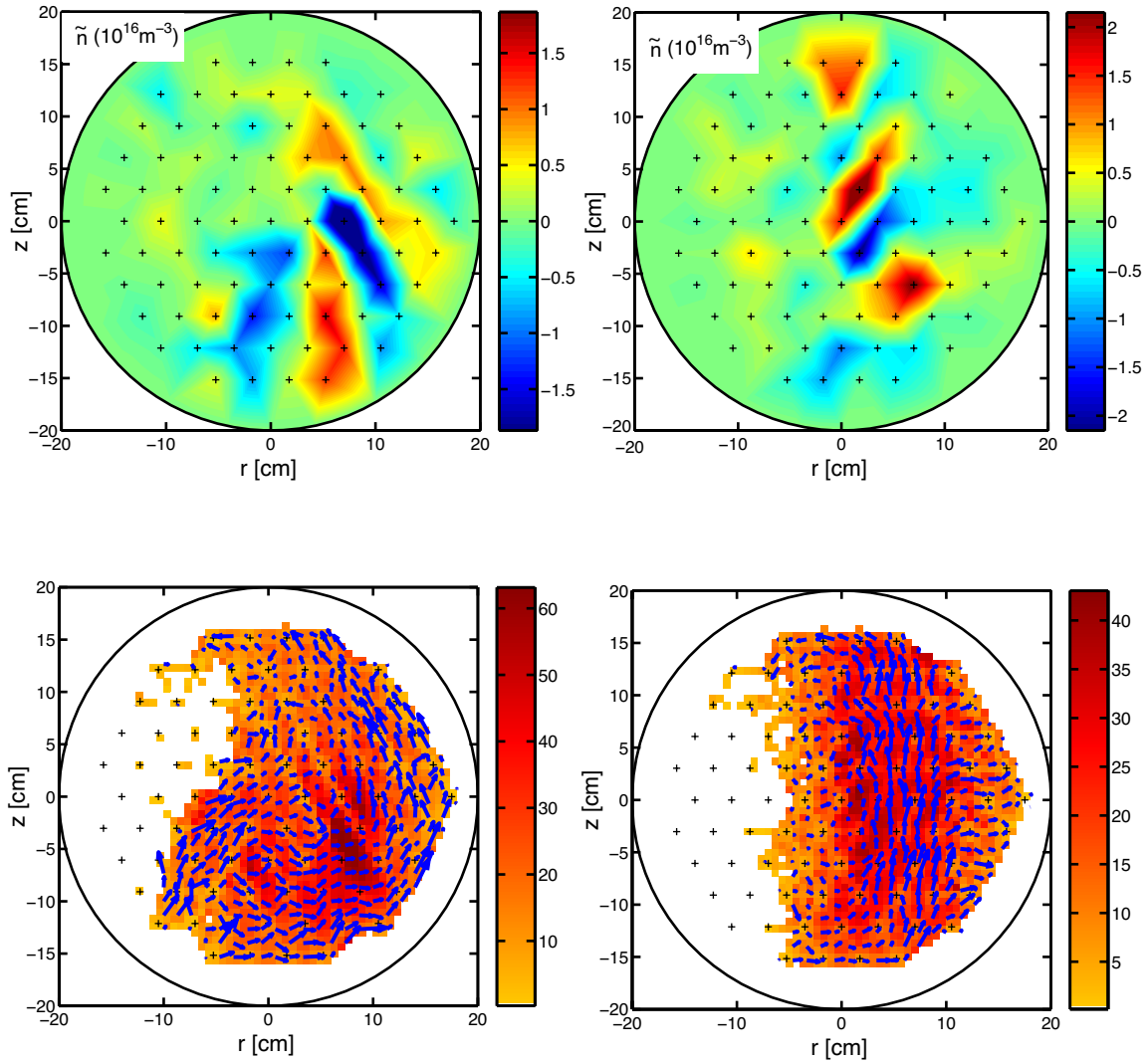


Figure 10.11: Top: Instantaneous profile of density fluctuations, measured in Hydrogen plasmas, for $B_z = 0.6 \text{ mT}$ (left) and $B_z = 1.2 \text{ mT}$ (right). The profile of the amplitude of \tilde{n} associated with the dominant mode is shown in Fig. 8.4 for $B_z = 0.6 \text{ mT}$ and in Fig. 9.4 for $B_z = 1.2 \text{ mT}$. Bottom: Statistical reconstruction of the trajectories of structures for $B_z = 0.6 \text{ mT}$ (left) and $B_z = 1.2 \text{ mT}$ (right). Color bars indicate the area of the structures in cm^2 .

is mainly vertical in the case of larger B_z and in both cases follows the direction of the $\mathbf{E}_0 \times \mathbf{B}$ convection, as can be seen comparing the case at $B_z = 0.6$ in Fig. 10.11 with the profile of the phase velocity in Fig. 10.4.

The detection of finite size structures on the low field side is also consistent with the measurement of a finite k_R at this location, cfr Fig. 10.7. Their extension is comparable to the half wavelength of the mode π/k_\perp and there are indications that their size is related to the degree of turbulence of the spectrum [28][34].

We showed in Sec. 7.5.1 (Fig. 7.11) that the wavenumber spectrum broadens with increasing neutral gas pressure and that $P(k)$ peaks at larger k . The broadening of the spectrum was ascribed to the effect of collisions with neutrals, which increase with the gas pressure, as discussed in [28]. The effect is even more pronounced if the level of absorbed microwave power is increased, as in the experiments presented in [28]. Increasing the pressure from 2.5×10^{-5} to 1.4×10^{-4} mbar results in a decreasing of the correlation length of almost a factor of three, from 25 to 8 cm, and in larger wavenumbers, as shown in Fig. 7.11, consistently with the detection of smaller size structures, whose average area shrinks from approximately 45 to 30 cm².

In experimental scenarios where a drift-instability is observed, the structures fade away approaching the equatorial plane and the probability of finding them in the upper half plane drastically reduces. This is possibly related to the cascade of energy measured in the Fourier domain, from the mode to spectral components with larger frequency and, according to the interpretation given in Sec. 10.3, to larger wavenumbers. If the energy is transferred to small scales we expect the probability of observing large scale structures to lower with increasing distance from the region where they are generated. Note that the space resolution of HEX TIP prevents detecting structures with area smaller than approximately 14 cm², which limits the extent of a quantitative analysis of structure decay.

In those situations where a strong $\mathbf{E} \times \mathbf{B}$ sheared profile exists, isolated density structures, or *blobs*, detach intermittently from the coherent mode and propagate radially towards the low field side edge. The dynamics of these blobs and the mechanism leading to their formation are investigated in detail in [40] [62] [66].

The presence of blobs may affect transport, as it adds a second particle transport mechanism in addition to the fluctuation induced, second order flux, $\Gamma = \langle \tilde{n}\tilde{v} \rangle$. Specific scenarios have been identified [40][62], akin to tokamak SOL, in which a clear distinction exists between the core plasma region (where the plasma itself and the instabilities originate), and a source-free region, where plasma is convected by blobs [40][62]. In these scenarios, transport is dominated by fluctuation-induced flux in the core region, and by the radial propagation of blobs in the source-free region [40].

10.6 Summary and discussion

In this Chapter we have addressed the transition from linearly unstable drift-interchange instabilities to turbulence. We have shown that three wave interactions are responsible for the transfer of spectral power from the unstable mode to spectral components with significantly larger frequency. It has been found that close to the region

where the mode has its maximum amplitude the dominant interactions are among the lowest order harmonics. Proceeding along the convection path the amplitude of the mode decreases, harmonics are not detected anymore and the spectral regions within harmonics are filled in.

These experimental results are consistent with a nonlinearity induced by the fluctuating $\tilde{\mathbf{E}} \times \mathbf{B}$ in the ion continuity equation [8][9][67]. This nonlinearity is expected to dominate for non adiabatic electrons and $k_{\perp}\rho_s \ll c_s/(L_n\nu_e) \equiv \delta$ (c_s is the ion acoustic speed and ν_e the electron collision rate) [67][68]. For the experiments described herein, $\delta \approx 0.7$ and $k_{\perp}\rho_s = 0.1$ for the unstable mode. We expect therefore the $\tilde{\mathbf{E}} \times \mathbf{B}$ nonlinearity to dominate for fluctuations with $k_{\perp} \lesssim 250 \text{ m}^{-1}$, *i.e.* for frequencies below 60 kHz, where most phase coupling is measured. Note that other mechanisms, such as temperature gradient effects, may introduce additional nonlinear terms in the continuity equation [69]. As the coupling coefficients are proportional to $(k_{\perp}L_{Te})^{-1}$, these terms are expected to dominate in the limit of small wavenumbers. Preliminary measurements of the nonlinear coupling for interchange instabilities suggest that the mechanism leading to the formation of a turbulent spectrum is independent of the nature of the instability.

We have interpreted the forward cascade in frequency as a cascade in wavenumber, from large to small scales. This hypothesis is supported by the measurement of a linear dispersion relation along z for frequencies larger than 10 kHz and by an almost constant $k_R(\omega)$ in the same frequency range. Conversely, around the frequency of the mode, the value of $k_R(\omega)$ strongly increases. In this frequency range the direction of cascade in wavenumber cannot be extracted from the measurements in frequency, but should be verified experimentally calculating the quadratic coupling coefficients in the wavenumber space, for example using the HEXTIP array.

It is worth mentioning that there are some limitations to this analysis and interpretation. The first is represented by the hypothesis of homogeneity, which is necessary to calculate the Fourier coefficients in the space domain, and fails in some regions of the plasma cross-section, close to the source region. This problem can be reduced limiting the analysis to those regions where the wave-packet assumptions, Eq. (5.15), are satisfied. Another solution would be to use wavelet transforms in space, with the advantage that homogeneity does not need to be invoked [70]. The other limitation comes from the low spatial resolution of the HEXTIP array, which limits wavelength resolution to 7 cm. As shown in Fig. 10.4, the energy cascade can be studied only in a limited range of wavenumbers, lower than 90 m^{-1} .

Chapter 11

Conclusions and outlook

This Thesis addresses two important problems in plasma physics, the identification and characterization of linear properties of electrostatic instabilities developing in toroidal magnetized plasmas, and their evolution to turbulence.

The first part of the research has been conducted by analyzing plasmas in a wide range of configurations and values of the external control parameters. The instabilities observed on TORPEX are found to have features that are common for different experimental scenarios, with density fluctuations peaking on the low field side, where the pressure gradient is large and co-linear to the magnetic field gradient. This indicates that the interchange mechanism is the dominant drive for the observed electrostatic instabilities. A theoretical dispersion relation based on the kinetic model has been calculated for TORPEX geometry and compared with the measured dispersion relation. Experiments presented in this Thesis are run primarily in Hydrogen plasmas, in which fluctuations have electrostatic nature. Increasing the ion mass would have two main effects. The first, as discussed in Sec. 7.1, would be to increase the ratio of β to m/M , the electron to ion mass ratio, and could lead to electromagnetic effects both on the dispersion properties and on the nonlinear developments. The second would be to give rise to finite Larmor radius effects, which would modify the dispersion relation of drift waves and the properties of turbulence for $k_{\perp}\rho_s \gtrsim 1$. These effects can be explored on TORPEX in plasmas from noble gases such as Argon, Neon or Xenon.

Both interchange and drift instabilities develop on TORPEX. Their complete identification and characterization is the first result of this Thesis [63]. The extended diagnostic coverage has been essential for the identification of the nature of the instabilities. Arrays of electrostatic probes have been developed for the measurement of the wavenumbers associated with density and potential fluctuations. The distance between probe tips was minimized in order to resolve small scale fluctuations and the dedicated electronics was designed to guarantee low amplitude and phase distortion in the whole range of measured frequencies. Some of these arrays are installed at fixed positions close to the edge and aligned along the azimuthal direction. Other arrays are installed on movable systems and are used to measure the radial profile of the parallel and the perpendicular wavenumbers, at positions that are varied shot by shot, with an almost arbitrarily good spatial resolution.

The nature of the electrostatic instabilities has been identified on the basis of a

number of measurements. First, the region where instabilities are driven has been identified, by reconstructing the profile of the amplitude of fluctuations associated with individual modes (Sec. 5.3). Second, the dispersion relation both perpendicularly and parallel to the magnetic field has been measured at different locations over the plasma cross section and compared to predictions of linear theory. The role of the phase shift between density and potential fluctuations in the identification of the nature of low frequency electrostatic instabilities has been explored. We find that in TORPEX the measurement of the phase shift, though extended over the entire plasma region, is not crucial for the identification of the nature of the instabilities, neither is the ratio between normalized density and electrostatic potential fluctuations. The radial profile of the phase shift depends on the local background parameters and on the degree of turbulence in the spectrum, but seems to be independent on the nature of the instabilities. Many factors can affect the value of the phase shift between \tilde{n} and $\tilde{\phi}_p$, usually not taken into account in linear theories. In particular, temperature fluctuations may have major effects on the measurement of electrostatic potential fluctuations and thus on the value of the phase shift between \tilde{n} and $\tilde{\phi}_p$, as our results demonstrate. For both pure interchange and drift-interchange instabilities, the normalized density fluctuations are larger than normalized electrostatic potential fluctuations.

Most of the results presented in this Thesis are based on a Fourier representation of the fluctuations in the frequency domain, justified by the stationarity of the physical quantities at play. The distribution of fluctuations in the wavenumber space has been reconstructed using standard statistical methods applied to the time traces from two probes with small separation. The reconstruction of the distribution of fluctuations both in the frequency and in the wavenumber domain is important to quantify the degree of turbulence. Information on the development of turbulence was inferred from the broadening of the spectra measured at different locations over the plasma cross-section. Moreover, by comparing the wavenumber spectra measured perpendicularly to the magnetic field, along crossed directions, the question of the turbulence anisotropy was addressed.

The power spectrum of density fluctuations is found to be narrow both in the frequency and the wavenumber close to the location where the instabilities are generated, then to broaden during convection, suggesting development of turbulence. The identification of the mechanism behind the generation of a turbulent spectrum represents the second main result of this work [71]. The analysis has focused on weakly turbulent plasmas to highlight the first stage of the transition from a coherent to a turbulent spectrum, although stronger turbulence can be achieved in TORPEX by increasing, for example, the neutral gas pressure or the level of injected power. The measurement of the bispectrum at different locations along the convection path has revealed the occurrence of three-wave nonlinear interactions between drift-interchange instabilities and spectral components with significantly larger frequencies. In these interactions the unstable mode loses its energy on the partner components causing the filling of the spectrum at large frequencies.

There are indications that the mechanisms leading to the development of turbulence do not depend on the nature of the instabilities. In plasmas dominated respectively by drift-interchange or interchange instabilities the generation of higher order harmonics

is the first step in the process. Strong nonlinear coupling is measured in both cases between the dominant mode and harmonics up to the third order. These interactions are responsible for the filling of the spectral regions intermediate to harmonics. Proceeding along the direction of convection, the unstable mode interacts with spectral components with larger frequencies. These results can be extended from the frequency to the wavenumber domain, leading to an interpretation of the forward cascade in frequency as a cascade in wavenumber, with transfer of energy from large to small scale fluctuations. This extension is justified for interactions nonlocal in frequency, which involve the unstable mode and spectral components with significantly larger frequencies. In this range, in fact, propagation is mainly along the $\mathbf{E}_0 \times \mathbf{B}$ direction. Conversely, around the frequency of the mode, the wavenumber measured along the drift direction is lower than that measured perpendicularly to it. For fluctuations with frequencies in this range one cannot conclude that a forward cascade in frequency corresponds to a forward cascade in wavenumber. In such case the coupling coefficients should be directly calculated in the wavenumber domain.

The measurement of a finite wavenumber along the radial direction is consistent with the detection of large scale coherent structures in the density fluctuations on the low field side. These structures have sizes that are comparable to the half wavelength of the mode, originate in the region of unfavourable curvature and propagate according to the $\mathbf{E}_0 \times \mathbf{B}$ drift direction. The spatio-temporal properties of the structures are related to the spectral properties of the instabilities detected in the spectrum of density fluctuations, suggesting that the structures detected on the low field side may be the spatial representation of a saturated drift wave (either drift-interchange or interchange). For a correct interpretation of the nonlinear dynamics, the spectral properties of fluctuations cannot be separated from their spatio-temporal properties.

Measurements on TORPEX indicate that turbulence is mainly driven by the $\tilde{\mathbf{E}} \times \mathbf{B}$ term in the ion continuity equation [8][9][67], acting on density fluctuations through the convective derivative, although we cannot exclude that other mechanisms, such as the electron temperature gradient, may affect the nonlinear dynamics in the limit of small perpendicular wavenumbers [69]. Future research should include the investigation of regimes in the opposite limit, *e.g.* in terms of $k_{\perp} \rho_s \gtrsim 1$, where a nonlinearity induced by the polarization drift is expected to dominate [67][68][7]. The comparison between the two regimes could give insight into the competition between direct and inverse cascade and the role of the observed structures in the transfer of energy.

The plasma conditions investigated on TORPEX have similarities with those of tokamak Scrape Off Layer (SOL), for example in terms of high relative fluctuation levels, due to strong, localized pressure gradients, or in terms of plasma parameters and even of magnetic field configuration, with open field lines characterized by long connection lengths. Although electrostatic fluctuations, the related turbulence and the resulting structures (or plasma blobs) are observed to play a dominant role in the SOL dynamics, *e.g.* in terms of particle transport, the limitations in the diagnostic coverage and resolution in high performance tokamaks and stellarators, prevents conclusive investigations. For example, the turbulence level measured at the edge can possibly be traced to one of the low frequency linear instabilities that develop in tokamaks, for example electron and ion drift waves or electromagnetic drift-Alfvén waves. However,

because the measured spectra are generally broad [2], a conclusive identification is not possible.

By providing a direct reconstruction of the dynamics of the development of drift waves into turbulence in a magnetized toroidal plasma, the results of this Thesis provide an extensive reference for the development and the benchmarking of numerical codes for electrostatic turbulence in magnetic fusion plasmas. An effort in this direction is being conducted at CRPP, with the implementation of a two-fluid code [72][34], based on the Braginskii equations for transport [73] with a semi-empirical model for the particle source term [40][43]. The model is two-dimensional and takes into account the curvature of the magnetic field lines and the contribution of electron temperature fluctuations. Density, temperature and plasma potential are evolved independently.

The measured plasma source and background profiles and the linear properties of fluctuations can be used as input parameters for the code, while the same linear and nonlinear analysis techniques developed for experimental data can be applied to the output of the code. The result could be a fully quantitative theory-experiment comparison, necessary for the identification of the essential ingredients in the theoretical model to account for the measured spatio-temporal dynamics of the turbulence.

Appendix A

Typical plasma parameters on TORPEX

SYMBOL	PARAMETER	H ₂	Ar
n_0 (m ⁻³)	background density	$\lesssim 10^{17}$	$\lesssim 10^{17}$
T_{e0} (eV)	electron temperature	$\lesssim 5$	$\lesssim 5$
T_{i0} (eV)	ion temperature	< 1	< 1
β	thermal/magnetic energy ratio	$10^{-5} - 10^{-4}$	
Frequencies (Hz)			
$\omega_{pe}/2\pi$	electron plasma frequency	1.3×10^9	2.8×10^9
$\omega_{pi}/2\pi$	ion plasma frequency	2.0×10^8	1.0×10^7
$\omega_{ce}/2\pi$	electron cyclotron frequency	2.45×10^9	2.45×10^9
$\omega_{ci}/2\pi$	ion cyclotron frequency	1.3×10^6	30×10^3
Lengths (m)			
λ_{De}	electron Debye length	1.0×10^{-4}	0.5×10^{-4}
λ_{Di}	ion Debye length	2.0×10^{-5}	0.7×10^{-5}
ρ_e	electron Larmor radius	0.5×10^{-4}	0.5×10^{-4}
ρ_i	ion Larmor radius	0.4×10^{-3}	2.3×10^{-3}
ρ_s	drift scale length	0.3×10^{-2}	2×10^{-2}
Velocities (m/s)			
$v_{th,e}$	electron thermal velocity	0.8×10^6	0.8×10^6
$v_{th,i}$	ion thermal velocity	3×10^3	0.5×10^3
c_s	ion sound speed	2.5×10^4	0.4×10^4

Table A.1: Characteristic lengths, velocities and frequencies for electron and ion species measured on TORPEX. Physical quantities are calculated assuming $B_\varphi = 76.6$ mT, $T_{e0} = 4$ eV, $T_{i0} = 0.1$ eV and $n_0 = 2 \times 10^{16}$ m⁻³ for Hydrogen plasmas and $n_0 = 10^{17}$ m⁻³ for Argon plasmas.

Appendix B

Normalizations used in the dispersion relation

The kinetic dispersion relation described in Chap. 2 uses normalized quantities. Let's write here again the dispersion relation:

$$\epsilon(\mathbf{k}, \omega) = 1 + \sum_{\alpha} \frac{1}{(k\lambda_D)^2} \left[1 - (\omega_N + \omega'_T + \omega_F - \omega) \cdot \sum_{n=-\infty}^{+\infty} \int d\mathbf{v} \frac{f_{\alpha 0}}{N_{\alpha}} \frac{J_n^2\left(\frac{k_y v_{\perp}}{\Omega}\right)}{k_z v_z + n\Omega + \omega_F + \omega_B - \omega} \right]$$

The various terms are defined as follows:

$$\omega_N = \frac{T k_y}{q B_0} \frac{1}{L_N} \quad (\text{B.1a})$$

$$\omega'_T = \omega_T T \frac{\partial}{\partial T} \quad \text{with} \quad \frac{\partial f_0}{\partial T} = \left(\frac{H}{T} - \frac{3}{2} \right) f_0, \quad \omega_T = \frac{T k_y}{q B_0} \frac{1}{L_T} \quad (\text{B.1b})$$

$$\omega_F = k_y v_F = -\frac{F}{q B_0} k_y \quad (\text{B.1c})$$

$$\omega_B = k_y v_B \quad (\text{B.1d})$$

Frequencies are normalized to the ion cyclotron frequency $\Omega_i = ZeB/M$, $\bar{\omega} = \omega/\Omega_c$. Wavenumbers are normalized to the ion Larmor radius $\lambda_i = v_{thi}/\Omega_i$, $\bar{k}_z = k_z \lambda_i$, $\bar{k}_{\perp} = k_{\perp} \lambda_i$. Forces are in units of T_i/λ_i , $\bar{F} = F \lambda_i/T_i$. Using these normalizations and inserting the equilibrium distribution function f_0 , the dispersion relation is written in

the form:

$$\epsilon(\mathbf{k}, \omega) = 1 + \sum_{\alpha} \frac{\varepsilon_A}{\bar{k}^2} \left(\frac{\lambda_{Di}}{\lambda_D} \right)^2 \left\{ 1 - \frac{1}{\sqrt{2\pi}} \times \int_0^{+\infty} \bar{v}_{\perp} d\bar{v}_{\perp} \int_{-\infty}^{+\infty} d\bar{v}_z e^{-\bar{v}_{\perp}^2/2} e^{-\bar{v}_z^2/2} \left[\bar{\omega}_N + \bar{\omega}_N \eta \left(\frac{\bar{v}^2}{2} - \frac{3}{2} \right) + \bar{\omega}_F - \bar{\omega} \right] \times \sum_{n=-\infty}^{+\infty} \frac{J_n^2 \left(\bar{k}_y \frac{v_{\perp}}{v_{thi}} \frac{\Omega_i}{\Omega} \right)}{\bar{\omega}_F + \bar{\omega}_B + \bar{k}_z \bar{v}_z \sqrt{\frac{T}{T_i}} \sqrt{\frac{m_i}{m}} + n\bar{\Omega} - \bar{\omega}} \right\}$$

with normalized quantities indicated with a bar. Perpendicular and parallel velocities are normalised to the thermal velocity, $\bar{v}_{\perp} = v_{\perp}/v_{th}$, $\bar{v}_z = v_z/v_{th}$. The term ε_A is the squared ratio of the ion Larmor radius to the Debye length, $\varepsilon_A = (\lambda_i/\lambda_{Di})^2$. The various terms are defined as follows:

$$\bar{\omega}_N = \frac{\bar{k}_y}{\bar{L}_N} \frac{T}{T_i} \frac{q}{q_i} \quad (\text{B.2a})$$

$$\bar{\omega}'_T = \eta \bar{\omega}_N \left(\frac{\bar{v}^2}{2} - \frac{3}{2} \right) \quad \text{with} \quad \eta = \frac{L_N}{L_T} \quad (\text{B.2b})$$

$$\bar{\omega}_F = -\bar{F} \bar{k}_y \frac{q_i}{q} \quad (\text{B.2c})$$

$$\bar{\omega}_B = \left(\frac{\bar{v}_{\perp}^2}{2} + \bar{v}_z^2 \right) \frac{T}{T_i} \varepsilon_N \frac{\bar{k}_y}{\bar{L}_N} \frac{q_i}{q} \quad \text{with} \quad \varepsilon_N = \frac{L_N}{R} \quad (\text{B.2d})$$

In particular, if $\mathbf{F} = qE_0\mathbf{e}_x$, one has $\bar{\omega}_E = -\bar{E}_0\bar{k}_y$, with $\bar{E}_0 = q_iE_0\lambda_i/T_i$. Note that this contribution is the same for both ions and electrons. Introducing the ratio of the electron to ion temperature $\tau = T_e/T_i$, and using $q_i = Ze$, $q_e = -e$, the ion and electron terms are written as:

$$\begin{aligned} \bar{\omega}_{Ni} &= \bar{F}_i \bar{k}_y & \bar{\omega}_{Ne} &= -\bar{\omega}_{Ni} Z \tau \\ \bar{\omega}_{Fi} &= -\bar{F}_i \bar{k}_y & \bar{\omega}_{Fe} &= Z \bar{F}_e \bar{k}_y \\ \bar{\omega}_{Bi} &= \varepsilon_N \frac{\bar{k}_y}{\bar{L}_N} \left(\frac{\bar{v}_{\perp}^2}{2} + \bar{v}_z^2 \right) & \bar{\omega}_{Be} &= -Z \tau \varepsilon_N \frac{\bar{k}_y}{\bar{L}_N} \left(\frac{\bar{v}_{\perp}^2}{2} + \bar{v}_z^2 \right) \end{aligned}$$

Appendix C

Complements to Chap. 4

C.1 The FLP arrays

The layout of the FLP arrays is shown in Fig. C.1. The three array have been dubbed FLP-U, FLP-H and FLP-L, where U, H, L stay respectively for upper, horizontal and lower. Each array contains 11 pairs of Langmuir probes, numerated from 1 to 11 according to the clockwise direction, and the tips in each pair are indicated as A, B. With this convention, for example FLP-U 4AB denotes the second tip, in the seventh pair of the upper array. Data from the FLP arrays are acquired on the boards 2 and 3 of the D-TACQ and a list of the channels is given in Table C.1. The FLP-H array measures fluctuations at $r = 163 \pm 3$ mm from the center of the vessel, while the other two arrays measure at $r = 158 \pm 3$ mm; the value is taken at the center of the tip length, the error corresponds to the tip half length.

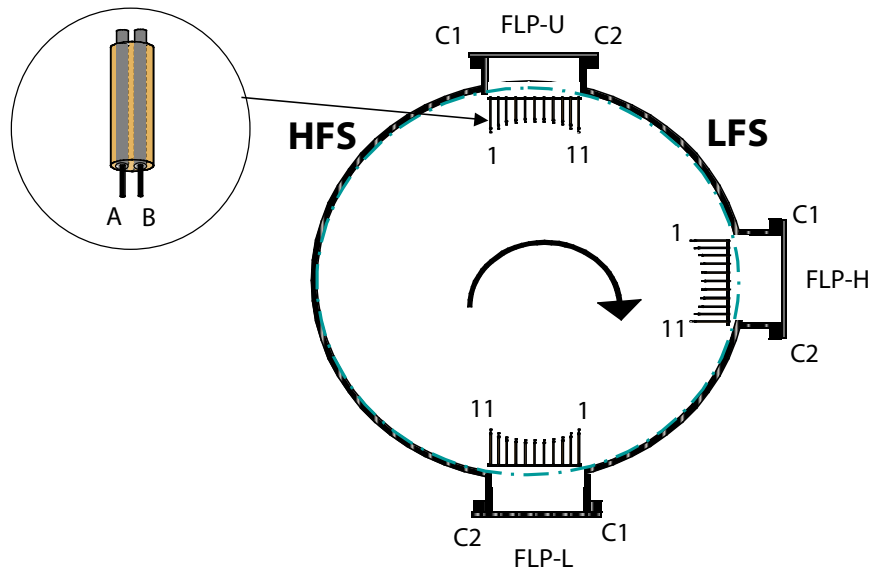


Figure C.1: Sketch of the layout of the FLP arrays and convention used for the numeration of tips.

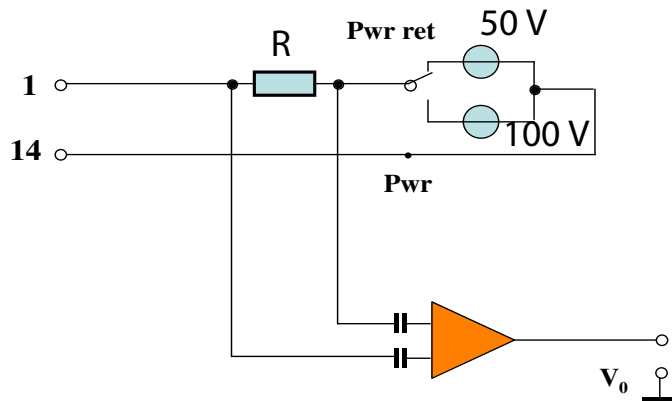


Figure C.2: Scheme of the circuit for the measurement of saturation current. Numbers 1 and 14 refer to the circuit for the measurement of the signal and of the ground respectively.

C.1.1 Transfer function of the FLP electronic modules

The probes on the FLP arrays are made of coaxial cables, the probe tip being the inner conductor. Both the inner conductor and the external shield are grounded to the vessel and the current measured from each probe is referred to its own shield. Figure C.2 shows a schematic of the circuit for the measurement of saturation current for one of the probes. The nominal amplification factor is 10 and the pass band is limited between 30 Hz and 250 kHz. The resistance R at the input of the system can be changed according to the amplitude of the saturation current, to avoid saturation of the signals. The output impedance of the electronic modules is 50 Ohm. This ensures the maximum transmission to the acquisition system.

The electric insulation between adjacent tips has been verified by applying a voltage of 1250 V between tips and measuring the corresponding current. Good insulation exists for all tips, with values of resistance well above 100 M Ω , apart for pair FLP-H 11 on the horizontal array, for which the resistance is 1 M Ω . Electrical insulation between signal and ground is particularly delicate, because crimping can damage the insulation of the coaxial cable (sometimes this was actually the case); the measured values are reported in Table C.2. The measured resistance varies in a wide range of values, because of the strength used to crimp. Taking into account that the insulation of THERMOCOAX cables is about 1 M Ω at 1250 V, with differences of 20% measured on individual tips, it is easy to deduce that insulation is damaged on those tips whose insulation is below this value. The broken tips are reported in italic in Table C.1.

The acquired time traces from different channels have different offset levels, which can be calculated from the part of the time series after the plasma discharge. This offset is usually not removed during shot downloading, because the mean average is in any case routinely subtracted before the calculation of the Fourier transforms.

The gain and the phase distortion for each signal have been first tested for each channel with a sinusoidal input signal with amplitude $V_0 = 500$ mV and frequency $f_0 = 50$ kHz. The amplification factor results to be 10, as expected, and the phase distortion

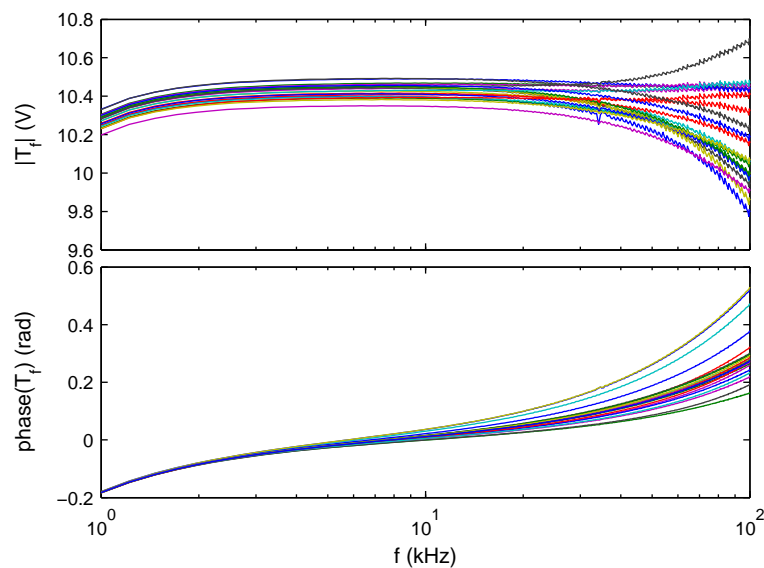


Figure C.3: Amplitude and phase of the transfer function for the electronic modules of the FLP-U array, in the frequency range $[1, 100]$ kHz.

negligible. These measurements have been done with a capacitor of $3.3 \mu F$ at the output of the function generator; the corresponding cutoff frequency is 1 kHz. The frequency response function in amplitude and phase has then been calibrated with an input sinusoidal signal whose frequency is varied logarithmically from 0.5 to 125 kHz. The resulting transfer function is shown in Figs. C.3-C.5. The deviation for frequencies above 30 kHz are an artifact of calibration when the sweeping frequency approaches the acquisition frequency. The deviations for frequencies below 2 kHz are due to the cutoff frequency of the capacitor used for the calibration. The frequency response is the same for all channels in a wide range of frequencies.

The wavenumber is routinely calculated applying the two-point correlation technique, described in Sec. 5.4. When applied to the FLP arrays, the value of k_θ is measured from two adjacent probes belonging to different pairs, with a distance of 0.8 cm. Neglecting the phase correction induces an error in the estimate of the wavenumber of approximately 1 m^{-1} at 20 kHz. The resulting shift of the wavenumber spectrum would be in any case negligible with respect to the measured broadening in wavenumber space (see for example Fig. 5.5).

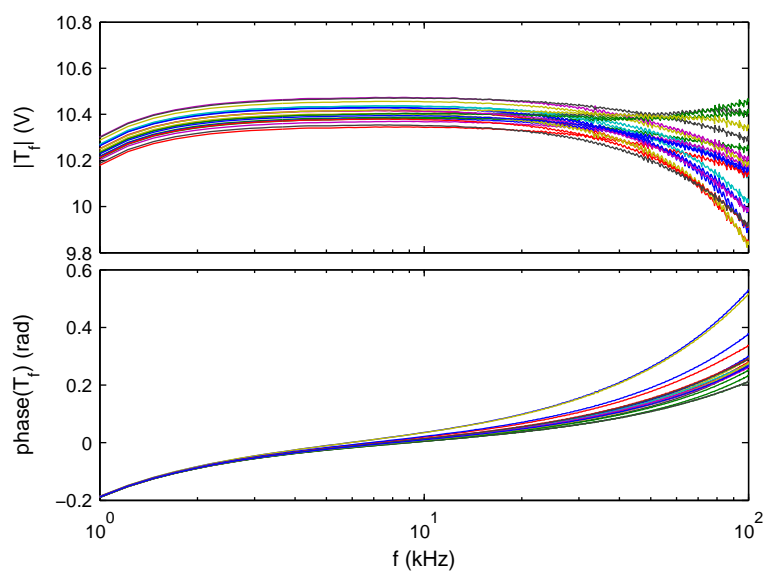


Figure C.4: Amplitude and phase of the transfer function for the electronic modules of the FLP-H array, in the frequency range [1, 100] kHz.

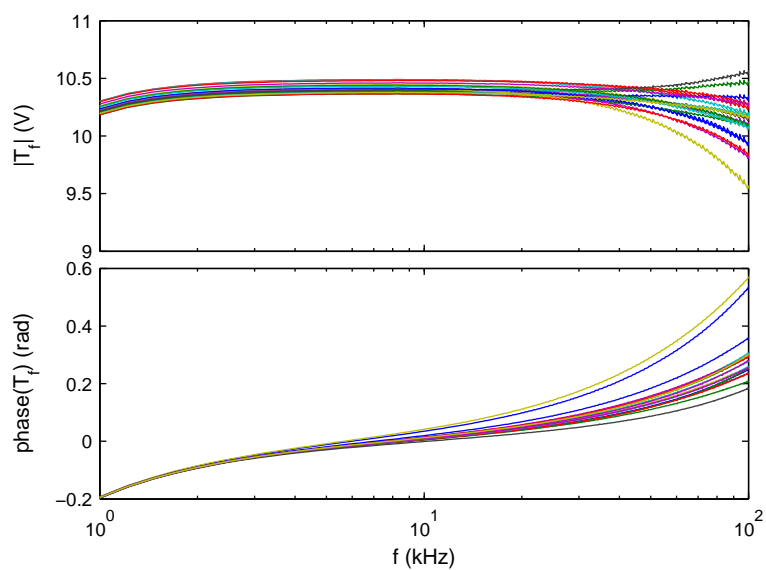


Figure C.5: Amplitude and phase of the transfer function for the electronic modules of the FLP-L array, in the frequency range [1, 100] kHz.

Table C.1: **List of channels on D-TACQ boards 2-3.**

ch	Board 2 probe	ch	Board 3 probe
1	LP-U 1A	1	LP-H 6A
2	LP-U 1B	2	LP-H 6B
3	LP-U 2A	3	LP-H 7A
4	LP-U 2B	4	LP-H 7B
5	LP-U 3A	5	LP-H 8A
6	LP-U 3B	6	LP-H 8B
7	LP-U 4A	7	LP-H 9A
8	LP-U 4B	8	LP-H 9B
9	LP-U 5A	9	LP-H 10A
10	LP-U 5B	10	LP-H 10B
11	LP-U 6A	11	LP-H 11A
12	LP-U 6B	12	LP-H 11B
13	LP-U 7A	13	LP-L 1A
14	LP-U 7B	14	LP-L 1B
15	LP-U 8A	15	LP-L 2A
16	LP-U 8B	16	LP-L 2B
17	LP-U 9A	17	LP-L 3A
18	LP-U 9B	18	LP-L 3B
19	LP-U 10A	19	LP-L 4A
20	LP-U 10B	20	LP-L 4B
21	LP-U 11A	21	LP-L 5A
22	LP-U 11B	22	LP-L 5B
23	LP-H 1A	23	LP-L 6A
24	LP-H 1B	24	LP-L 6B
25	LP-H 2A	25	LP-L 7A
26	LP-H 2B	26	LP-L 7B
27	LP-H 3A	27	LP-L 8A
28	LP-H 3B	28	LP-L 8B
29	LP-H 4A	29	LP-L 9A
30	LP-H 4B	30	LP-L 9B
31	LP-H 5A	31	LP-L 10A
32	LP-H 5B	32	LP-L 10B

Table C.2: **Insulation tests**

PIN	PAIR	R(M Ω)	PIN	PAIR	R(M Ω)
1-14	1A	25	1-14	7A	7
2-15	1B	8	2-15	7B	3
3-16	2A	12	3-16	8A	3.75
4-17	2B	4	4-17	8B	1
5-18	3A	1.5	5-18	9A	5
6-19	3B	2	6-19	9B	3
7-20	4A	6	7-20	10A	18
8-21	4B	1	8-21	10B	0.5
9-22	5A	7	9-22	11A	7.5
10-23	5B	0.5		11B	3.5
11-24	6A	1			
12-25	6B	1.5			
PIN	PAIR	R(M Ω)	PIN	PAIR	R(M Ω)
1-14	1A	20	1-14	7A	14
2-15	1B	16	2-15	7B	1
3-16	2A	25	3-16	8A	6
4-17	2B	18	4-17	8B	20
5-18	3A	22	5-18	9A	20
6-19	3B	9	6-19	9B	4.5
7-20	4A	25	7-20	10A	12
8-21	4B	6	8-21	10B	30
9-22	5A	22	9-22	11A	20
10-23	5B	14		11B	30
11-24	6A	22			
12-25	6B	18			
PIN	PAIR	R(M Ω)	PIN	PAIR	R(M Ω)
1-14	1A	6	1-14	7A	0.5
2-15	1B	16	2-15	7B	1.5
3-16	2A	18	3-16	8A	7.5
4-17	2B	20	4-17	8B	14
5-18	3A	1	5-18	9A	0.5
6-19	3B	20	6-19	9B	1.5
7-20	4A	16	7-20	10A	20
8-21	4B	20	8-21	10B	16
9-22	5A	1.5	9-22	11A	20
10-23	5B	25		11B	1
11-24	6A	20			
12-25	6B	1.5			

C.2 Transfer function of LP modules and HEXTIP modules

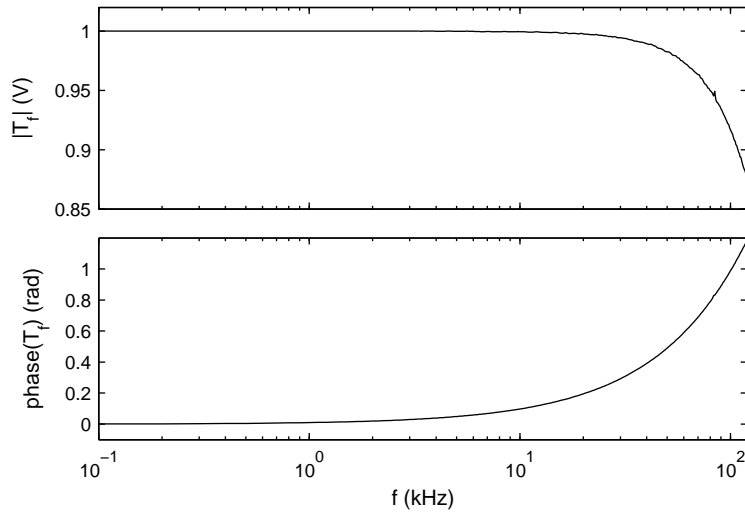


Figure C.6: Amplitude and phase of the transfer function of one of the Langmuir modules for the measurement of the ion saturation current.

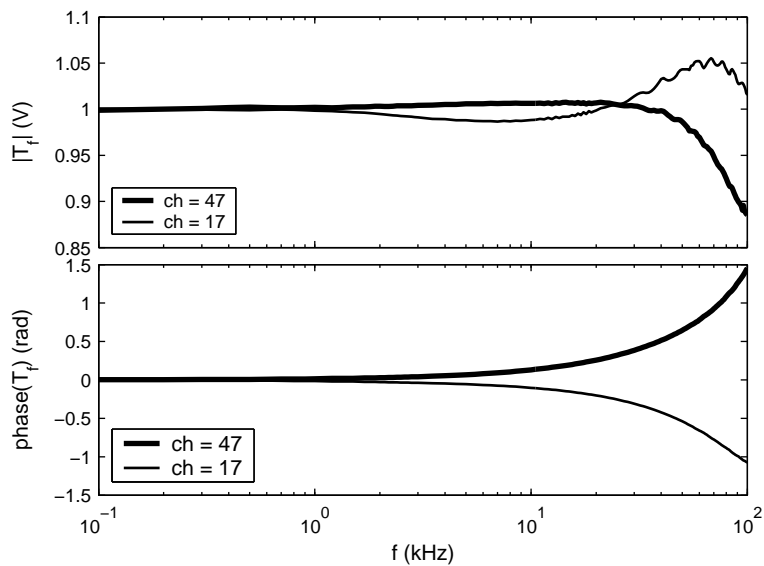


Figure C.7: Amplitude and phase of the transfer function of the HEXTIP array. Only two channels are shown here.

Table C.3: List of connections on feedthroughs C1-C2.

C1				C2			
PIN	SIGNAL	PIN	GROUND	PIN	SIGNAL	PIN	GROUND
1	1A	14	1A	1	7A	14	7A
2	1B	15	1B	2	7B	15	7B
3	2A	16	2A	3	8A	16	8A
4	2B	17	2B	4	8B	17	8B
5	3A	18	3A	5	9A	18	9A
6	3B	19	3B	6	9B	19	9B
7	4A	20	4A	7	10A	20	10A
8	4B	21	4B	8	10B	21	10B
9	5A	22	5A	9	11A	22	11A
10	5B	23	5B	10	11B	23	11B
11	6A	24	6A	11		24	
12	6B	25	6B	12		25	
13				13			

Appendix D

Geometrical effects on the measurement of k_{\parallel}

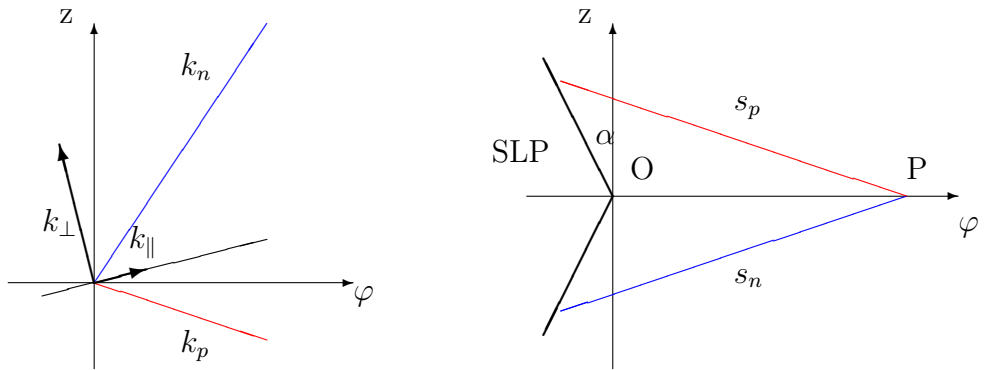


Figure D.1: Geometry of probes during the measurement of k_{\parallel} . φ and z denote respectively the toroidal and the vertical direction in our cylindrical reference, ψ is the pitch angle, with $\tan \psi = B_z/B_\varphi$, α is the angle formed by the SLP array with the z axis. The distance between the tips is indicated with s_n and s_p , respectively when the SLP array is oriented downward (along negative z) or upward (along positive z).

The parallel wavenumber is measured from the phase difference between two probes located at the same radial position and separated by $\Delta\varphi$ along the toroidal direction, aligned along the same field line.

A sketch of the probe geometry used for this measurement is shown in Fig. D.1. A picture of the arrangement was reported in Fig. 5.8. The TWEEDY array is located at the toroidal position indicated as P , while the SLP array is located at position O , with their axes both on the equatorial plane, separated by the distance $\overline{OP} = R\Delta\varphi$. The SLP can rotate around its axis, the angle α being measured with respect to the positive z axis. The directions of k_{\parallel} and k_{\perp} are shown in the figure, with k_{\parallel} along the

magnetic field line and k_{\perp} on the plane perpendicular to it.

Taking P as the reference position, there is a field line at P that intersects the SLP array; its z coordinate is calculated from Eq. (5.23):

$$z_0 = R\Delta\varphi \frac{B_z}{B_{\varphi}},$$

The SLP arrays contains eight tips with mutual separation of approximately 1.8 cm; there is good probability that at least one of them is close to this field line. The measured wavenumber, indicated in Fig. D.1 as k_n for the SLP oriented downward and as k_p when the SLP array is oriented upward, will be a combination of k_{\parallel} and k_{\perp} . Due to the low ratio of k_{\parallel} to k_{\perp} , the measurement can be strongly affected by the projection of k_{\perp} along the direction of measurement.

Indicating with γ_n and γ_p the angle between the direction of measurement and the z axis for $\alpha > 90^\circ$ and $\alpha < 90^\circ$, respectively, the measured wavenumbers can be expressed as:

$$k_n = k_{\parallel} \cos \gamma_n + k_z \sin \gamma_n \quad (\text{D.1})$$

$$k_p = k_{\parallel} \cos \gamma_p - k_z \sin \gamma_p \quad (\text{D.2})$$

where $\cos \gamma_n = (\mathbf{k}_n \cdot \hat{z})/|\mathbf{k}_n|$ and $\cos \gamma_p = (\mathbf{k}_p \cdot \hat{z})/|\mathbf{k}_p|$. After some algebra and using trigonometric relations, the measured wavenumber k_m can be written as:

$$k_m(z) = \frac{k_{\perp}}{\sqrt{1 + \left(\frac{z}{L}\right)^2} \sqrt{1 + \left(\frac{B_z}{B_{\varphi}}\right)^2}} \left[\frac{k_{\parallel}}{k_{\perp}} + \frac{B_z}{B_{\varphi}} - \frac{z}{L} \left(1 - \frac{B_z}{B_{\varphi}} \frac{k_{\parallel}}{k_{\perp}} \right) \right] \quad (\text{D.3})$$

where $L = R_0\Delta\varphi + z \tan \alpha$ is the toroidal distance between tips, measured at the midplane. In our experiments $B_z/B_{\varphi} \in [3 \times 10^{-3}, 2.4 \times 10^{-2}]$ for $B_z \in [0.2, 1.8]$ mT and typically $k_{\parallel}/k_{\perp} < 10^{-2}$. The term $(B_z/B_{\varphi})(k_{\parallel}/k_{\perp})$ can therefore be neglected with respect to unity. Moreover $\sqrt{1 + (z/L)^2} \cong 1$, as the correction to unity is $\approx 0.2\%$ at the maximum distance $z = 10$ cm. With these approximations the measured wavenumber finally results to be:

$$k_m \cong k_{\perp} \left(\frac{k_{\parallel}}{k_{\perp}} + \frac{B_z}{B_{\varphi}} \right) - \frac{k_{\perp}}{L} z \quad (\text{D.4})$$

Note that $k_m = k_{\parallel}$ when $z = z_0 = R_0\Delta\phi B_z/B_{\varphi}$. In particular, if $k_{\parallel} = 0$, the measured wavenumber changes its sign crossing the magnetic field line, as it can be easily proven replacing $z = z_0 \pm \zeta$ in Eq. (D.4). In this case the measured wavenumber is simply the projection of k_{\perp} along the direction of measurement:

$$k_m = -\frac{k_{\perp}}{L} \zeta \quad (\text{D.5})$$

In general, for $k_{\parallel}/k_z \ll 1$ and for measurements not taken along the field line, the measured wavenumber is dominated by the contribution of k_{\perp} . For $k_{\parallel} \neq 0$ the error on the measurement can be quantified as:

$$\frac{k_m - k_{\parallel}}{k_{\parallel}} \cong \frac{k_{\perp}}{k_{\parallel}} \frac{z - z_0}{L} \quad (\text{D.6})$$

For $k_{\parallel}/k_{\perp} \sim \times 10^{-2}$ and assuming that z_0 falls at exactly half the distance between two SLP tips, the relative error on the estimate of k_{\parallel} is 100%. It can be larger for a lower ratio k_{\parallel}/k_{\perp} . The error can be minimized by adjusting the angle of rotation of the probes. Note anyway that measurements with $\alpha = 110^\circ$ have revealed a strong shadowing effect. The best results are obtained with the SLP array kept almost vertical. Equation (D.4) can be used to infer the value of k_{\parallel} from a linear fit of k_m . Comparing with Eq. (D.4) it follows that the value of k_{\perp} and k_{\parallel} can be inferred from a and b ($k_m = az + b$):

$$\begin{aligned} k_{\perp} &= aL \\ k_{\parallel} &= b - aL \frac{B_z}{B_{\varphi}} \end{aligned}$$

The value of k_{\perp} can then be compared to independent measurements, such as the value of k_z measured during the same session with two tips of the TWEEDY array aligned along z . Alternatively, the angular coefficient from the linear fit can be used to interpolate the value of k_{\parallel} at z_0 . In this case, the error on the estimate of z_0 should be taken into account.

Error on the estimate of z_0

The optimal position z_0 is calculated as:

$$z_0 = \frac{B_z}{B_{\varphi}} R \Delta\varphi$$

where R is the radial position and $\Delta\varphi$ is the toroidal separation between probes, calculated at the midplane. The relative error on the estimate of z_0 is calculated as the sum of all relative errors:

$$\frac{\delta z_0}{z_0} = \frac{\delta R}{R} + \frac{\delta(\Delta\varphi)}{\Delta\varphi} + \frac{\delta B_z}{B_z} + \frac{\delta B_{\varphi}}{B_{\varphi}} \quad (\text{D.7})$$

with $\delta B_z/B_z = 0.02$ and $\delta B_{\varphi}/B_{\varphi} = 0.01$. The error on the radial position of the probes is given by the precision of the mechanical system, ± 0.2 cm, to which we add the uncertainty on the SLP tip length and on the tip diameter for TWEEDY. In total, $\delta R = 0.5$ cm.

The arrays are installed at fixed toroidal positions and their separation is calculated at the midplane, with respect to the center of the ports. Assuming that horizontal oscillations of the shaft are absent and that the array shafts are centered on the port, an upper limit to the error on $\Delta\varphi$ is given by the diameter of shafts, $\Delta\varphi = \pm 0.01$ rad. For $R = 1$ m and $\Delta\varphi = \pi/2$, the error on the estimate of z_0 is approximately $\delta z_0 = 0.04z_0$. The error due to δz_0 on the estimate of k_{\parallel} from a linear fit over the measured k_m is anyway negligible with respect to the broadening of the spectrum in wavenumber space.

Error on the measurement of k_{\parallel} due to the distance between tips

Wavenumbers are routinely measured by the ratio of the phase shift to the separation between probes. If probes are aligned along the magnetic field line, the error on the measurement of k_{\parallel} is mainly given by the uncertainty on the probe separation. The distance between tips is given by:

$$s^2 = L^2 + z^2$$

where $z = |z_T - z_S|$ is the vertical distance between tips and $L = R\Delta\varphi + l \sin \alpha$ their toroidal distance, z_T and z_S denote respectively the vertical coordinate of the tips belonging to the TWEEDY and the SLP array. The error on the estimate of s is given by the error propagation:

$$\delta s = \frac{L\delta L + z\delta z}{\sqrt{L^2 + z^2}}$$

where

$$\begin{aligned} \delta L &= R\delta(\Delta\varphi) + \delta R\Delta\varphi + l \cos \alpha \delta \alpha + \sin \alpha \delta l \\ \delta z &= \delta z_T + \delta z_S \quad \text{with} \quad \delta z_T = 0.2 \text{ cm} \end{aligned}$$

The error δz_S is calculated from $z_S = l \cos \alpha$, using the error propagation:

$$\delta z_S = l |\sin \alpha| \delta \alpha + |\cos \alpha| \delta l \tag{D.8}$$

where $\delta \alpha = 0.05 \text{ rad}$ is the error on the positioning of the mechanical system, and $\delta l = 0.1 \text{ cm}$ is the error on the position of tips along the support, estimated as the diameter of the tip. For $\alpha = \pi/4$, this gives $\delta z_S = 0.44 \text{ cm}$. Assuming $|z_T - z_S| \lesssim 12.8 \text{ cm}$ and $\alpha = \pi/2$, an upper estimate to the error is $\delta s = 1.2 \text{ cm}$. The error on the estimate of the distance between probes induces an error lower than 6% in the measurement of the wavenumber, much lower than the width in k -space commonly measured applying the two-point correlation technique. The latter should be therefore assumed as an estimate of the error in the measurement of k_{\parallel} .

Appendix E

Corrections due to temperature fluctuations

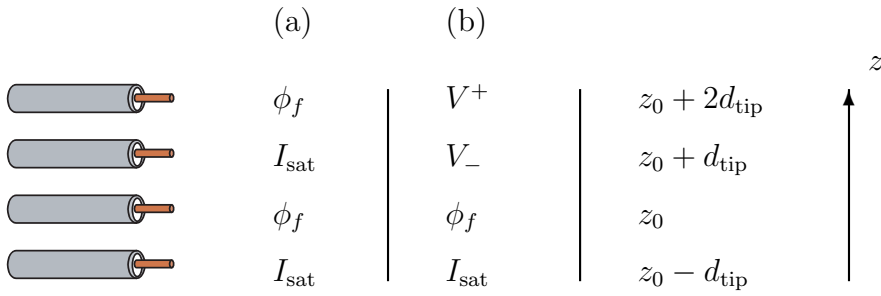


Figure E.1: Sketch of the TRIP probe with the configurations for the measurement of particle flux and the dispersion relation (a), and temperature and plasma potential fluctuations (b).

Figure E.1 illustrates the configuration used to measure the wavenumber associated with \tilde{n} and $\tilde{\phi}_f$ (a) and that used to measure the fluctuations of \tilde{n} , \tilde{T}_e and $\tilde{\phi}_p$ (b). In the configuration (b), the first and second tip from the top measured a positive and negative, constant voltage $\Delta V = V^+ - V^-$, such that $V^- < \phi_f < V^+$. The temperature is measured from the following equation:

$$2[1 + \beta(\phi_f - V^-)] = (1 + e^{-\frac{\Delta V}{T_e/e}}) \exp\left(\frac{V^+ - \phi_f}{T_e/e}\right) \quad (\text{E.1})$$

where β introduce a correction to the measurements in regimes of non complete ion saturation, and has been estimated experimentally to be ≈ -0.05 [40]. Good agreement with the temperature measured with the other probes is found for ΔV between 24 and 36 Volts.

E.1 Corrections to the measurement of $\tilde{\phi}_p$

The plasma potential ϕ_p is calculated from temperature and floating potential as:

$$\phi_p = \phi_f + \mu \frac{T_e}{e} \quad (\text{E.2})$$

The coefficient μ is estimated experimentally from the $I(V)$ curves, as described in [40][42]. The corresponding fluctuations can therefore be calculated as:

$$\tilde{\phi}_p = \tilde{\phi}_f + \mu \frac{\tilde{T}_e}{e} \quad (\text{E.3})$$

The power spectrum of $\tilde{\phi}_p$ is calculated as the ensemble average:

$$P_{\phi_p} = \langle \phi_{p,\omega}^* \phi_{p,\omega} \rangle = \left\langle \left(\phi_{f,\omega}^* + \frac{\mu}{e} T_{e,\omega}^* \right) \left(\phi_{f,\omega} + \frac{\mu}{e} T_{e,\omega} \right) \right\rangle \quad (\text{E.4})$$

where $\phi_{p,\omega}^*$, $\phi_{f,\omega}^*$, and $T_{e,\omega}$ denote the Fourier components in frequency of the corresponding fluctuating quantities. It follows that:

$$P_{\phi_p} = P_{\phi_f} + \frac{\mu^2}{e^2} P_{T_e} + 2 \frac{\mu}{e} \Re(P_{\phi_f T_e}) \quad (\text{E.5})$$

where P_{ϕ_f} and P_{T_e} are the power spectrum of $\tilde{\phi}_f$ and \tilde{T}_e and $P_{\phi_f T_e} = \langle \phi_{f,\omega}^* T_{e,\omega} \rangle$ is the cross spectrum between temperature and floating potential. If $\tilde{T}_e/e\tilde{\phi}_f = x$, the relative difference between P_{ϕ_p} and P_{ϕ_f} is given by:

$$\frac{P_{\phi_p} - P_{\phi_f}}{P_{\phi_p}} \simeq \mu^2 x^2 + 2\mu x \cos \theta_{\phi_f T_e} \quad (\text{E.6})$$

This correction depends on the sign of $\theta_{\phi_f T_e}$, the phase shift between $\tilde{\phi}_f$ and \tilde{T}_e . For Hydrogen plasmas and for $x = 0.25$, it can be 60% if $\theta_{\phi_f T_e} = \pi/2$ and up to 200% if $\tilde{\phi}_f$ and \tilde{T}_e are in phase.

E.2 Corrections to the measurement of \tilde{n}

For sufficiently large and negative applied voltage, V , the current collected by a Langmuir probe is independent on V , as discussed in Sec. 4.1, and proportional to the density. Writing density and electron temperature as the sum of an average and a fluctuating part, the ion saturation current can be written as:

$$I_{\text{sat}} = \frac{1}{2} e A (n_0 + \tilde{n}) \sqrt{\frac{T_{e0}}{M}} \sqrt{1 + \frac{\tilde{T}_e}{T_{e0}}}$$

Assuming ¹ $\tilde{T}_e/T_{e0} \ll 1$, the second square root can be expanded and the measured ion saturation current, $I_{\text{sat}} = I_0 + \tilde{I}$, finally written as:

$$I_0 + \tilde{I} = I_0 \left(1 + \frac{\tilde{n}}{n_0} + \frac{1}{2} \frac{\tilde{T}_e}{T_{e0}} + \frac{1}{2} \frac{\tilde{n}}{n_0} \frac{\tilde{T}_e}{T_{e0}} \right) \quad (\text{E.7})$$

¹In the experimental situations analyzed for this Thesis $\tilde{T}_e/T_{e0} \lesssim 20\%$.

where:

$$I_0 = \frac{1}{2} e A n_0 \sqrt{\frac{T_{e0}}{M}}$$

is the time-averaged value of I_{sat} . Neglecting the nonlinear term $\tilde{n}\tilde{T}_e$, density fluctuations are related to the measured \tilde{I} from:

$$\frac{\tilde{I}}{I_0} = \frac{\tilde{n}}{n_0} + \frac{1}{2} \frac{\tilde{T}_e}{T_{e0}} \quad (\text{E.8})$$

If temperature fluctuations are negligible, density fluctuations can be directly estimated from the power spectrum of \tilde{I} . The error done by neglecting \tilde{T}_e in Eq. (E.8) is smaller than $0.1 \tilde{n}/n_0$. It is worth noting that correction for temperature fluctuations includes the cross-spectrum between \tilde{n} and \tilde{T}_e , as can be easily proven multiplying Eq. (E.8) times \tilde{I}^* . The error introduced by the finite distance between tips on the measurement of the phase between \tilde{n} and \tilde{T}_e is in this case larger than the error done by neglecting \tilde{T}_e .

E.3 Corrections to the phase between \tilde{n} and $\tilde{\phi}_p$

The phase shift between density and potential fluctuations is one of the quantities commonly used for the identification of instabilities. Measurements should be done at the same location, but this is in practice impossible. To minimize the error due to the propagation of waves from one tip to the other, the separation between the probes that measure \tilde{n} and $\tilde{\phi}_p$ should be kept as small as possible. A further error is introduced by the temperature fluctuations, which are commonly neglected. Even when the amplitude of \tilde{T}_e is much lower than that of \tilde{n} or $\tilde{\phi}_p$, the correction in the measurement is not negligible due to the phase shift between \tilde{T}_e and \tilde{n} .

We assume that the phase shift between \tilde{n} and $\tilde{\phi}_p$ is ideally measured at z_0 and derive an expression that takes into account the corrections due to both \tilde{T}_e and d_{tip} . We start from the measured phase shift between \tilde{n} and $\tilde{\phi}_f$:

$$\theta_{\phi_f, \omega}(z_0) - \theta_{n, \omega}(z_0 - d_{\text{tip}}) = \theta_{\phi_f, \omega}(z_0) - \theta_{\phi_p, \omega}(z_0) + \theta_{\phi_p, \omega}(z_0) - \theta_{n, \omega}(z_0 - d_{\text{tip}}) \quad (\text{E.9})$$

where we have added and subtracted $\theta_{\phi_p, \omega}(z_0)$. The term $\theta_{\phi_f, \omega}(z_0) - \theta_{\phi_p, \omega}(z_0)$ is calculated from the cross-spectrum between $\phi_{f, \omega}$ and $\phi_{p, \omega}$, both measured at z_0 :

$$\phi_{p, \omega}^* \phi_{f, \omega} = \phi_{f, \omega}^* \phi_{f, \omega} - \frac{\mu}{e} \phi_{f, \omega}^* T_{e, \omega}, \quad (\text{E.10})$$

which gives:

$$\theta_{\phi_f, \omega}(z_0) - \theta_{\phi_p, \omega}(z_0) = \frac{\mu}{e} \frac{\Im [\langle \phi_f^* T_e \rangle]}{\Re [\langle \phi_f^* T_e \rangle] - P_{\phi_f}}. \quad (\text{E.11})$$

For $\tilde{T}_e/e\tilde{\phi}_f = x$, Eq. (E.11) can be approximated by:

$$\theta_{\phi_f, \omega}(z_0) - \theta_{\phi_p, \omega}(z_0) \simeq \frac{\mu}{e} \frac{x \sin(\theta_{\phi_f T_e})}{x \cos(\theta_{\phi_f T_e}) - 1}. \quad (\text{E.12})$$

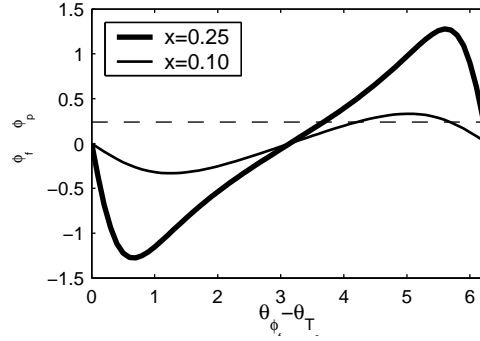


Figure E.2: Dependence of the phase shift between $\tilde{\phi}_f$ and $\tilde{\phi}_p$ on the phase shift between $\tilde{\phi}_f$ and \tilde{T}_e .

where $\theta_{\phi_f T_e} = \theta_{T_e, \omega}(z_0) - \theta_{\phi_f, \omega}(z_0)$. The dependence of $\theta_{\phi_f, \omega}(z_0) - \theta_{\phi_p, \omega}(z_0)$ on $\theta_{\phi_f T_e}$ is shown in Fig. E.2 for $x = 0.1$ and $x = 0.25$. The term $\theta_{\phi_p, \omega}(z_0) - \theta_{n, \omega}(z_0 - d_{\text{tip}})$ in Eq. (E.9), which accounts for the finite separation between tips, can be written as:

$$\theta_{\phi_p, \omega}(z_0) - \theta_{n, \omega}(z_0 - d_{\text{tip}}) = \theta_{\phi_p, \omega}(z_0) - \theta_{n, \omega}(z_0) + \theta_{n, \omega}(z_0) - \theta_{n, \omega}(z_0 - d_{\text{tip}}) = \theta_{n, \phi_p}(z_0) + k_{n, \omega} d_{\text{tip}} \quad (\text{E.13})$$

where $k_{n, \omega} = [\theta_{n, \omega}(z_0) - \theta_{n, \omega}(z_0 - d_{\text{tip}})]/d_{\text{tip}}$ is the wavenumber associated with density fluctuations. For the typical values of k_n measured on TORPEX, $k_n \lesssim 50 \text{ m}^{-1}$, the correction to the phase shift is smaller than 0.25 radians.

Using Eqs. (E.12)-(E.13), the difference between the phase shift measured between \tilde{n} and $\tilde{\phi}_p$ and that measured between \tilde{n} and $\tilde{\phi}_f$ can finally be written as:

$$\theta_{n, \phi_f}(z_0) - \theta_{n, \phi_p}(z_0) \simeq \frac{\mu}{e} \frac{x \sin \theta_{\phi_f T_e}}{e^{\frac{\mu}{e} x \cos \theta_{\phi_f T_e}} - 1} + k_n d_{\text{tip}} \quad (\text{E.14})$$

The second term can be reduced by keeping the tips as close as possible, while the first term depends on the phase shift between \tilde{T}_e and $e\tilde{\phi}_f$ and on the ratio of \tilde{T}_e to $e\tilde{\phi}_p$. The two contributions on the right hand side of Eq. (E.14) add when $\theta_{\phi_f T_e} > \pi$ and subtract in the opposite case. Note that the effect of finite separation can be eliminated by measuring $\tilde{\phi}_f$ at two positions, for example using the configuration for the measurement of particle flux. In this case, the measured phases are:

$$\theta_{\phi_2, n} = \theta_{\phi_f}(z_0 + 2d_{\text{tip}}) - \theta_n(z_0 + d_{\text{tip}}) \quad (\text{E.15a})$$

$$\theta_{\phi_1, n} = \theta_{\phi_f}(z_0) - \theta_n(z_0 + d_{\text{tip}}) \quad (\text{E.15b})$$

Using $k_\phi = [\theta_{\phi_f}(z_0 + 2d_{\text{tip}}) - \theta_{\phi_f}(z_0 + d_{\text{tip}})]/d_{\text{tip}}$, Eq. (E.15a) can be written as:

$$\theta_{\phi_2, n} = \theta_{\phi_f}(z_0 + d_{\text{tip}}) + k_\phi d_{\text{tip}} - \theta_n(z_0 + d_{\text{tip}}) \quad (\text{E.16a})$$

$$\theta_{\phi_1, n} = \theta_{\phi_f}(z_0 + d_{\text{tip}}) - k_\phi d_{\text{tip}} - \theta_n(z_0 + d_{\text{tip}}) \quad (\text{E.16b})$$

By taking the average value between $\theta_{\phi_2, n}$ and $\theta_{\phi_1, n}$, the term including k_ϕ cancels out.

E.4 Corrections to the wavenumber associated with $\tilde{\phi}_p$

Let's consider the typical configuration used for the measurement of flux, shown in Fig. E.1(a). The phase shift of potential fluctuations is measured from the argument of the cross-spectrum between $\phi_f(z_0 + 2\Delta)$ and $\phi_f(z_0)$, $\theta_{\phi_f}(z_0 + 2d_{\text{tip}}) - \theta_{\phi_f}(z_0)$. By adding and subtracting $\phi_p(z_0)$ and $\phi_p(z_0 + 2d_{\text{tip}})$, the phase shift can be written as:

$$\theta_{\phi_f}(z_0 + 2d_{\text{tip}}) - \theta_{\phi_f}(z_0) = k_{\phi_p} 2d_{\text{tip}} + \theta_{\phi_p}(z_0) - \theta_{\phi_f}(z_0) + \theta_{\phi_f}(z_0 + 2d_{\text{tip}}) - \theta_{\phi_p}(z_0 + 2d_{\text{tip}}) \quad (\text{E.17})$$

Replacing Eq. (E.11) into Eq. (E.17) gives:

$$\theta_{\phi_f}(z_0 + 2d_{\text{tip}}) - \theta_{\phi_f}(z_0) = k_{\phi_p} 2d_{\text{tip}} - \frac{\mu}{e} \frac{\Im(P_{\phi_f T_e})}{e^{\frac{\mu}{e} \Re(P_{\phi_f T_e})} - P_{\phi_f}} + \frac{\mu}{e} \frac{\Im(P_{\phi_f, 2T_{e,2}})}{e^{\frac{\mu}{e} \Re(P_{\phi_f, 2T_{e,2}})} - P_{\phi_f, 2}} \quad (\text{E.18})$$

where $P_{\phi_f T_e}$ is measured at z_0 and $P_{\phi_f, 2T_{e,2}}$ is measured at $z_0 + 2d_{\text{tip}}$. Let's indicate with x and x_2 the ratio of \tilde{T}_e to $\tilde{\phi}_f$ measured respectively at positions z_0 and $z_0 + 2d_{\text{tip}}$. The difference between k_{ϕ_f} and k_{ϕ_p} can be approximated as:

$$k_{\phi_f} - k_{\phi_p} \simeq -\frac{1}{2d_{\text{tip}}} \frac{\mu}{e} \left[\frac{x_2^2 \sin(\theta_{\phi_f T, 2})}{e^{\frac{\mu}{e} x_2^2 \cos(\theta_{\phi_f T, 2})} - 1} - \frac{x^2 \sin(\theta_{\phi_f T})}{e^{\frac{\mu}{e} x^2 \cos(\theta_{\phi_f T})} - 1} \right]. \quad (\text{E.19})$$

It is easy to prove that $k_{\phi_f} - k_{\phi_p} = 0$ when $\theta_{\phi_f T, 2} = \theta_{\phi_f T}$ and $x_2 = x$, *i.e.* if the amplitude and phase of fluctuations do not change with space, for example in the case of linear fluctuations. In the presence of turbulence, the amplitude and phase of fluctuations change because of nonlinear interactions and the presence of temperature fluctuations affects the difference $k_{\phi_f} - k_{\phi_p}$.

Bibliography

- [1] J. Wesson. *Tokamaks*. Oxford University Press, Cambridge (2004).
- [2] P. C. Liewer. *Nucl. Fusion*, **25**, 543 (1985).
- [3] W. Horton. *Rev. Mod. Phys.*, **71**, 735 (1999).
- [4] R. H. Kraichnan. *Phys. Fluids*, **10**, 1417 (1967).
- [5] A. Hasegawa and K. Mima. *Phys. Fluids*, **21**, 87 (1978).
- [6] A. Hasegawa, C. G. MacLennan, and Y. Kodama. *Phys. Fluids*, **22**, 2122 (1979).
- [7] M. Wakatani and A. Hasegawa. *Phys. Fluids*, **27**, 611 (1984).
- [8] P. W. Terry and W. Horton. *Phys. Fluids*, **26**, 106 (1983).
- [9] W. Horton and Y. H. Ichikawa. *Chaos and structures in nonlinear plasmas*, chapter 7, pages 278–286. World Scientific (1996).
- [10] Ch. P. Ritz, R. D. Bengtson, S. J. Levinson, and E. J. Powers. *Phys. Fluids*, **27**, 2956 (1984).
- [11] A. A. Ferreira, M. V. A. P. Heller, and I. L. Caldas. *Phys. of Plasmas*, **7**, 3567 (2000).
- [12] H. W. Hendel, T. K. Chu, and P. A. Politzer. *Phys. Fluids*, **11**, 2426 (1968).
- [13] A. Latten, T. Klinger, A. Piel, and T. Pierre. *Rev. Sci. Instrum.*, **66**, 3254 (1995).
- [14] F. Brochard, E. Gravier, and G. Bonhomme. *Phys. Plasmas*, **12**, 62104 (2005).
- [15] M. J. Burin, G. R. Tynan, G. Y. Antar, N. A. Crocker, and C. Holland. *Phys. Plasmas*, **12**, 52320 (2005).
- [16] C. Schröder, O. Grulke, T. Klinger, and V. Naulin. *Phys. Plasmas*, **12**, 42103 (2005).
- [17] T. Klinger, A. Latten, A. Piel, G. Bonhomme, T. Pierre, and T. Dudok de Wit. *Phys. Rev. Lett.*, **79**, 3913, 1997.

- [18] A. B. Mikhailovskii. *Basic plasma physics*, volume I, pages 587–610. A. Galeev and R. N. Sudan, North Holland, Amsterdam, 1983.
- [19] B. D. Scott. *Phys. Plasmas*, **12**, 623141 (2005).
- [20] J. C. Perez, W. Horton, K. Gentle W. L. Rowan, K. Lee, and R. B. Dahlburg. *Phys. Plasmas*, **13**, 32101 (2006).
- [21] F. Greiner, D. Block, and A. Piel. *Contrib. Plasma Phys.*, **44**, 335 (2004).
- [22] O. Grulke, F. Greiner, T. Klinger, and A. Piel. *Plasma Phys. Control. Fusion*, **43**, 525 (2001).
- [23] F. J. Oynes, O. M. Olsen, H. L. Pecselly, A. Fredriksen, and K. Rypdal. *Phys. Rev. E*, **57**, 2242 (1998).
- [24] F. Brochard, Windisch, O. Grulke, and T. Klinger. *Phys. Plasmas*, **13**, 122305 (2006).
- [25] U. Stroth, F. Greiner, C. Lechte, N. Mahdizadeh, K. Rahbarnia, and M. Ramisch. *Phys. Plasmas*, **11**, 2558 (2004).
- [26] S. Niedner, B. D. Scott, and U. Stroth. *Plasma Phys. Control. Fusion*, **44**, 397 (2002).
- [27] A. Fasoli, B. Labit, M. McGrath, S. H. Müller, M. Podestà, and F. M. Poli. *Bull. Amer. Phys. Soc.*, **48**, 119 (2003).
- [28] A. Fasoli, B. Labit, M. Mc Grath, S. H. Müller, G. Plyushchev, M. Podestà, and F. M. Poli. *Phys. of Plasmas*, **13**, 055902 (2006).
- [29] N. A. Krall. *Advances in Plasma Physics*. A.Simon and W.B.Thomson, Interscience, New York (1968).
- [30] S. Brunner. Waves and instabilities in inhomogeneous plasmas. Cours 3ème Cycle, CRPP-EPFL, Lausanne
- [31] M. Podestà, A. Diallo, A. Fasoli, I. Furno, B. Labit, S. H. Müller, G. Plyushchev, and F. M. Poli. *Plasma Phys. Control. Fusion*, **49**, 175 (2007).
- [32] M. Q. Tran, P. Kohler, P. J. Paris, and M. L. Sawley. The Linear Magnetised Plasma device (Imp). LRP 205/82, CRPP/EPFL, 1982.
- [33] P. J. Paris and N. Rynn. *Rev. Sci. Instrum.*, **61**, 1095 (1990).
- [34] S. H. Müller. *Turbulence in basic toroidal plasmas*. PhD thesis, EPFL (2006).
- [35] I. Furno, A. Diallo, A. Fasoli, B. Labit, S. H. Müller, G. Plyushchev, M. Podestà, and F. M. Poli. In *11th EU-US Transport Task Force Meeting* (2006).
- [36] T. T. Ribeiro and B. Scott. *Plasma Phys. Control. Fusion*, **47**, 1657 (2005).

- [37] S. H. Müller, A. Fasoli, B. Labit, M. McGrath, M. Podestà, and F. M. Poli. *Phys. Rev. Lett.*, **93**, 165003 (2004).
- [38] K. Rypdal, E. Grønvoll, F. Øynes, Å. Fredriksen and R. J. Armstrong, J. Trulsen, and H. L. Pécseli. *Plasma Phys. Control. Fusion*, **36**, 1099 (1994).
- [39] S. Yoshikawa, W. L. Harries, and R. M. Sinclair. *Phys. Fluids*, **6**, 1506 (1963).
- [40] M. Podestà. *Plasma production and transport in TORPEX*. PhD thesis, EPFL, 2007.
- [41] M. Bornatici, R. Cano, O. D. Barbieri, and F. Engelmann. *Nucl. Fusion*, **23**, 1153 (1983).
- [42] M. Podestà, A. Fasoli, B. Labit, M. McGrath, S. H. Müller, and F. M. Poli. *Plasma Phys. Control. Fusion*, **47**, 1989 (2005).
- [43] M. Podestà, A. Fasoli, B. Labit, M. McGrath, S. H. Müller, and F. M. Poli. *Plasma Phys. Control. Fusion*, **48**, 1053 (2006).
- [44] I. H. Hutchinson. *Principles of plasma diagnostics*. Cambridge University Press, New York (1987).
- [45] F. F. Chen. *Plasma diagnostic techniques*. R. H. Huddleston and S. L. Leonard, Academic Press, New York (1965).
- [46] S. H. Müller, A. Fasoli, B. Labit, M. McGrath, O. Pisaturo, G. Plyushchev, M. Podestà, and F.M. Poli. *Phys. Plasmas*, **12**, 090906 (2005).
- [47] S. H. Müller, A. Diallo, A. Fasoli, I. Furno, B. Labit, G. Plyushchev, M. Podestà, and F. M. Poli. *Phys. Plasmas*, **13**, 100701 (2006).
- [48] E. J. Powers. *Nucl. Fusion*, **14**, 749 (1974).
- [49] F. F. Chen and T. Sekiguchi. *J. Appl. Phys.*, **36**, 2363 (1965).
- [50] V. I. Demidov, S. V. Ratynskaia, and K. Rypdal. *Rev. Sci. Instrum.*, **73**, 3409 (2002).
- [51] G. Plyushchev and H. Boehmer *et al.* *Rev. Sci. Instrum.*, **77**, 10F506 (2006).
- [52] D. C. Champeney. *Fourier transforms and their physical applications*. Academic press (1973).
- [53] J. M. Beall, Y. C. Kim, and E. J. Powers. *J. Appl. Phys.*, **53**, 3933 (1982).
- [54] N. Iwama and T. Tsukishima. *Appl. Phys. Lett.*, **31**, 783 (1977).
- [55] S.J. Levinson, J.M. Beall, E.J. Powers, and R.D. Bengtson. *Nucl. Fusion*, **24**, 527 (1984).

- [56] N. Iwama Y. Ohba and T. Tsukishima. . *J. Appl. Phys.*, **50**, 3197 (1979).
- [57] T. Dudok de Wit, V. Krasnosel'skikh, M. Dunlop, and H. Lühr. *J. Geophys. Res.*, **104**, 17079 (1999).
- [58] Ch. P. Ritz, E. J. Powers, and R. D. Bengtson. *Phys. Fluids B*, **1**, 153 (1989).
- [59] Y. C. Kim and E. J. Powers. *IEEE trans. Plasma sci.*, **PS-7**, 120 (1979).
- [60] Ch. P. Ritz and E. J. Powers. *Physica*, **20D**, 320 (1986).
- [61] D.L. Jassby. *Phys. of Fluids*, **15**, 1590 (1972).
- [62] I. Furno, B. Labit, M. Podestà, and A. Fasoli *et al.* Mechanism for plasma blob generation from interchange waves. submitted to *Phys. Rev. Lett.* (2007).
- [63] F. M. Poli, S. Brunner, A. Diallo, A. Fasoli, I. Furno, B. Labit, S. H. Müller, G. Plyushchev, and M. Podestà. *Phys. of Plasmas*, **13**, 102104 (2006).
- [64] Ch. P. Ritz, E. J. Powers, and R. D. Bengtson. *Phys. Fluids B*, **1**, 153 (1988).
- [65] Y.C. Kim, J.M. Beall, E.J. Powers, and R.W. Miksad. *Phys. Fluids B*, **23**, 258 (1980).
- [66] C. Theiler. Electrostatic turbulent structures in torpex plasmas, Master Thesis, ETH (2007).
- [67] D. E. Newman, P. W. Terry, P. H. Diamond, and Y. M. Liang. *Phys. Fluids B*, **5**, 1140 (1993).
- [68] H. Xia and M. G. Shats. *Phys. of Plasmas*, **11**, 561 (2004).
- [69] V. N. Oraevsky, H. Tasso, and H. Wobig. In *proceedings of the 3rd IAEA Conf. on Plasma Physics and Nuclear Fusion research, Novosibirsk, 1968*, volume 1, page 671, Vienna, 1969. IAEA.
- [70] S. Mallat. *A wavelet tour of signal processing*, chapter 4. Academic Press, Cambridge (2001).
- [71] F. M. Poli, M. Podestà, and A. Fasoli. *Phys. Plasmas*, **14**, 052311 (2007).
- [72] O.E. Garcia, V. Naulin, A.H. Nielsen, and J. Juul Rasmussen. *Phys. Rev. Lett.*, **92**, 165003 (2004).
- [73] S. I. Braginskii. *Reviews of Plasma Physics*, **1**, 205 (1965).

Acknowledgments

Being an active witness of the conception, design and construction of a new experimental device is a unique and rewarding experience. I am grateful to the CRPP management and to my thesis advisor, Ambrogio Fasoli, for giving me an opportunity to join the newly formed Basic Plasma Physics Group at CRPP. Almost six years have passed since that day and the list of people I owe thanks is much too long to fit in just one page.

Every single person contributed to my personal and professional development. The perfect match of professional and human aspects makes CRPP a place of excellence where doing research is also having fun. Thanks a million to all of you, for discussions, for advice, for sharing with me your knowledge and experience, or just for chatting during lunch time. As great men are usually backed by greater women, I wish to thank the efficient staff of secretaries, in particular P. Halter and E. Grüter, for simplifying researchers' daily life and for guiding me during the first steps in the sea of Swiss bureaucracy. The *to-do list* Edith provided me at my arrival is my first souvenir as a PhD student.

Many colleagues at CRPP have contributed to the TORPEX 'dream' and worked hard since the early stages of the project. Some of them are still - efficiently - working on it, guaranteeing its maintenance, in particular D. Fasel, U. Siravo, A. Perez, P. Conti, O. Bartolomeoli, X. Llobet, C. Mourat, J-F. Mion. Thanks for your daily effort to keep TORPEX operational. This thesis is also yours and the results presented in these almost 150 pages have been made possible by the contribution from all the CRPP team. I wish to thank the engineers, the draftsmen and the staff of the *atelier mécanique*, who spent months in manufacturing pieces and setting up the whole structure.

I am grateful to all those people who supported me with their work in the design, conception and realization of the probes for the measurement of fluctuations. I own thanks to R. Pitts for his willingness to help and for his support and encouragement. Thanks to P. Gorgerat, who transformed my scratches in well designed and professional designs, to E. Bader who taught me how to use the machinery to cut ceramic without cutting my fingers, to P. Lavanchy and S. Antonioni, who took care of the electronics. I wish to thank P. Marmillod and B. Marletaz for their effort, not always successful, to introduce me to the secrets of electronics.

I wish to thank the members of my PhD Thesis Committee, Stephan Brunner, Richard Pitts and Stefano Coda, who followed with interest, curiosity and constructive criticism my scientific progresses during the last five years. In particular, I wish to thank S. Brunner, who patiently supported me during my 'theorist' period. I took

great advantage of the discussions I had with F. Skiff during his two-months sabbatical interlude at CRPP.

Heartfelt thanks to my closest colleagues, those who shared with me every single day from the beginning, Mario, Mark, Benoit, Stefan, and those who joined the group later on, Ahmed, Ivo, Gennady, Paolo and Davoud. Last, but far from least, I wish to thank our group leader, Ambrogio who, although weighed down by work, never closes the door of his office. I am indebted to him, because he always expected the maximum effort and the best performance from me. This, combined with my intrinsic curiosity and enthusiasm, has resulted in a continuous self improvement.

This work is supported in part by the Swiss National Science Foundation.

CURRICULUM VITAE

FRANCESCA MARIA POLI

Professional and Educational Background

- 04/2002 - 08/2007 - Assistant and Doctoral student at the CRPP-EPFL, Lausanne, Switzerland.
- 04/2000 - 03/2002 - EURATOM-ENEA Association, FTU, Frascati, Italy.
- 04/1998 - 03/1999 - CNR Padova, RFX, Italy.
- 12/1997 - University La Sapienza, Roma, Italy. Laurea in Fisica.

Refereed publications

F.M. Poli, M. Podestà, A. Fasoli, *Phys. Plasmas*, **14**, 052311 (2007).

B. Labit, I. Furno, A. Fasoli, A.Diallo, S.H. Müller, G. Plyushchev, M. Podestà, F.M. Poli, *Phys. Rev. Lett.*, **98**, 255002 (2007).

M.Podestà, A.Diallo, A.Fasoli, I.Furno, B.Labit, S.H.Müller, G.Plyushchev and F.M.Poli, *Plasma Phys. Control. Fusion* **49**, 1989 (2007)

F.M.Poli, S.Brunner, A.Diallo, A.Fasoli, I.Furno, B.Labit, S.H.Müller, G.Plyushchev and M.Podestà, *Phys. Plasmas* **13**, 102104 (2006)

S.H.Müller, A.Diallo, A.Fasoli, I.Furno, B.Labit, M.McGrath, G.Plyushchev, M.Podestà and F.M.Poli, *Phys. Plasmas* **13**, 100701 (2006)

M.Podestà, A.Fasoli, B.Labit, M.McGrath, S.H.Müller and F.M.Poli, *Plasma Phys. Control. Fusion* **48**, 1053 (2006)

J.R.Martin-Solis, B.Esposito, R.Sanchez, F.M.Poli and L.Panaccione, *Phys. Rev. Lett.* **97**, 165002 (2006)

A.Fasoli, B.Labit, M.McGrath, S.H.Müller, G.Plyushchev, M.Podestà and F.M.Poli, Phys. Plasmas **13**, 055902 (2006)

S.H.Müller, A.Fasoli, B.Labit, M.McGrath, S.H.Müller and F.M.Poli, Phys. of Plasmas, **12**, 090906 (2005)

M.Podestà, A.Fasoli, B.Labit, M.McGrath, S.H.Müller and F.M.Poli, Plasma Phys. Control. Fusion **47**, 1989 (2005)

S.H.Müller, A.Fasoli, B.Labit, M.McGrath, M.Podestà and F.M.Poli, Phys. Rev. Lett. **93**, 165003 (2004)

A.Zimbal, M.Reginato, H.Schuhmacher, L.Bertalot, B.Esposito, F.Poli, J.M.Adams, S.Popovichev, V.Kiptily, A.Murari. Rev. Sci. Instr. **75**, 3553 (2004)

B.Esposito, J.R. Martin-Solis, F.M. Poli, J.A. Mier, R. Sanchez and L. Panaccione. Phys. of Plasmas **10**, 2350 (2003)

Frigione D, Giovannozzi E, Gormezano C, Poli F. et al., Nucl. Fus. **45**, 1613-1618, (2001).

E.Brocato, V.Castellani, F.M.Poli and G.Raimondo, A&ASS **146**, 91 (2000).